

Preparation and Properties of $\text{Pb}(\text{Zr},\text{Ti})\text{O}_3$

Films Grown by
Metalorganic Chemical
Vapor Deposition

2002
MOMORET

Preparation and Properties of Pb(Zr, Ti)O₃

Films Grown
by
Metalorganic Chemical Vapor Deposition

Cover

Front:

Superimposition of a picture of a 6" diameter polycrystalline PZT wafer and the collage of different PZT film morphologies observed by SEM and AFM. In the hardcover version, these two pictures are combined to form a lenticular.

Back (softcover only):

PZT stereogram generated with 3D Miracle V1.30 software using a typical polycrystalline PZT film morphology as texture.

ISBN 90-9016155-4 (softcover)

ISBN 90-9016156-2 (hardcover)

Printed by PrintPartners Ipskamp in Enschede

Bound by Boekbinderij van Mierlo in Nijmegen

Lenticular on the hardcover produced by Harmonique in Edam

Preparation and Properties of Pb(Zr, Ti)O₃ Films Grown by Metalorganic Chemical Vapor Deposition

een wetenschappelijke proeve op het gebied
van de Natuurwetenschappen, Wiskunde, en
Informatica

Proefschrift

te verkrijging van de graad van doctor aan de
Katholieke Universiteit Nijmegen, op gezag van de
Rector Magnificus Prof. Dr. C.W.P.M. Blom, volgens
besluit van het College van Decanen in het openbaar
te verdedigen op donderdag 12 december des
voormiddags om 10.30 precies

door

Mona Pierrette Felicie Moret
geboren op 5 Augustus 1972 te Besançon

Promotor Prof. Dr. Poul K. Larsen
Co-promotor Dr. Paul R. Hageman

Manuscriptcommissie
Prof. Dr. Richard Zallen, Virginia Tech, USA
Prof. Dr. Ted Janssen
Dr. Hugo Meekes

The work described in this thesis was performed at the University of Nijmegen and financially supported by the Dutch Technology Foundation (STW).

Pour Mamou

et

pour papa

A c k n o w l e d g m e n t s

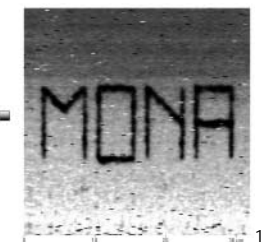
Several people contributed to the achievement of this thesis, directly and indirectly. Poul Larsen is known in the department to like ferroelectrics as he introduced this topic into the group. He gave me the freedom to do research my way and was always open to new developments for the project. The thesis is based on the investigation of thin films grown by MOCVD and there are therefore no results without any layers. The MOCVD reactor needed to be rebuilt at the beginning of the project. Paul Hageman was always ready to help with technical MOCVD subtleties and shared his long MOCVD experience with me since I started in the group. Additionally Paul was also always available to genuinely discuss any kind of other problems. Thank you for your continuous presence and support, even in the "Pt story" downs. Erik Haverkamp automated the whole reactor and spent lots of time with calibrations and electrical / electronical problems. Thank you for always being so motivated, efficient, and happy. Harry van der Linden helped with the Ferro reactor when it didn't work. As he often says that he is not interested in working machines, I guess that it was a nice one for him. Willy Corbeek saved me a lot of time making holders and other fancy things. I followed the instrumentmakerij cursus but once I got to know him, I realized it was not necessary. Marijn Devillers measured, by ellipsometry, essentially all the layers I have been growing from the beginning. He has been contributing to the project up to the end, in the ups and the downs. Marijn, thanks a lot and I hope this didn't delay your retirement too much. Gerard Bauhuis was brave enough to accept me as an officemate when I felt that I had to leave the "aquarium". It was nice to be able to repaint the world at times. Thanks for all the discussions about growth and your help with the XRD measurements. John Schermer has always been cheerful and motivating when I have shown him SEM pictures of crystals; he was the only one. He made a lot of useful suggestions, during coffee pauses and "volunteered" pauses, which helped me carry on. Thanks for your help with the PZ layers. Moreover I would like to thank Paul / Gerard / John together as the "trio van ouwe bakken": they didn't miss an occasion to annoy me but were always there to help out. Andy Zauner who joined the ferro project for a few months in 2001 was the only one who has grown PZT films with me. He clearly contributed to the start of the PZT growth on STO substrates. Frans Tichelaar (Technical University of Delft) performed all the TEM measurements. Frans, your cross-section studies and your reports were really precious in the analyses of the layers. There are several supporting university workshop groups, which have been just great. The glassblower lab with Jos Haerkens, Peter van Dijk, and Peter Walraven were always helpful and entertaining with the cleaning of the liner and the creation of the new liner. Gerard Dekkers and Dick van Aalst from the photo department have been supportive all these years fixing the 6" diameter wafers on paper and helping me with pictures-massage. SEM was used as a basic characterization tool and thanks to Huub Geurts, it is always in working condition. For the observations of smaller features, Edwin Aret has performed patiently all the AFM measurements I needed. Last but not least, Peter Mulder, the secret weapon from our group, was always around to help with everything

and cheer me up in the dark times and was a stimulating element during these years. Thank you for caring.

The work sphere is not the only one that was supporting. Henrik, since I met you, you always encouraged me carrying on with research. Thanks a lot for helping. Dick, thank you so much for listening when the PhD was tough and for all your continuous support since I left Virginia Tech. Thanks to Andy and Felix for being with me at home. Though Felix encourages me a lot, Andy also concretely helped with many problems in the completion of this thesis in the last years. The inhabitants of Muzenplaats, Iulia, Marius, Anamaria, and Cecilia were often around to chat and ready to take care of Felix. Additionally, thanks to my family especially my mum for her energy-bursting suggestions.

Finally, I would like to thank the people who helped me with the covers of my thesis for their professionalism and friendliness. The first one is my mum who came up with the lenticular idea (though it is apparently my sister's "fault") when I was struggling with stereograms. Lidwien van der Horst (Grafische Vormgeving department) was enthusiastic from the beginning with the lenticular project. Lidwien, you were very helpful and very creative for the files to be delivered. Monique Koopman (Harmonique) and Erik van Mierlo (Bindery) patiently helped out, and Yury Kraschnikov from Urry Software lab was helpful for the creation of text stereograms.

August 2002, Nijmegen



¹ Maria DeSanto is acknowledged for taking this EFM picture written in a polycrystalline MOCVD PZT film grown on Pt substrate.

Table of Contents

Acknowledgments	vii
Table of Contents	ix
Glossary	xii
Chapter 1.....	1
1 Introduction	2
1.1 Electroceramics.....	2
1.2 Ferroelectricity.....	2
1.3 Pb(Zr,Ti)O ₃	7
1.4 Ferroelectric thin film applications.....	9
1.4.1 Memories	10
1.4.2 Micro-ElectroMechanical Systems (MEMS)	11
1.4.3 Electro-optical applications.....	12
1.5 Aim of this study: MOCVD growth of PZT films	14
Chapter 2	15
2 Metalorganic Chemical Vapor Deposition	16
2.1 Introduction	16
2.2 Metalorganic Chemical Vapor Deposition - MOCVD	17
2.2.1 General	17
2.2.2 MOCVD and PZT	18
2.3 The MOCVD reactor for PZT deposition: The Ferro reactor.....	19
2.3.1 Description	19
2.3.2 Drawbacks of the Ferro Reactor	23
Chapter 3	27
3 Experimental Techniques	28
3.1 Characterization techniques.....	28
3.1.1 Color card	28
3.1.2 Ellipsometry	29
3.1.3 Optical reflectivity	31
3.1.4 X-ray diffraction.....	32
3.1.5 Raman.....	35
3.1.6 Morphology	38
3.1.7 Composition.....	38
3.1.8 Transmission Electron Microscopy	40
3.1.9 Ferroelectrics?	41

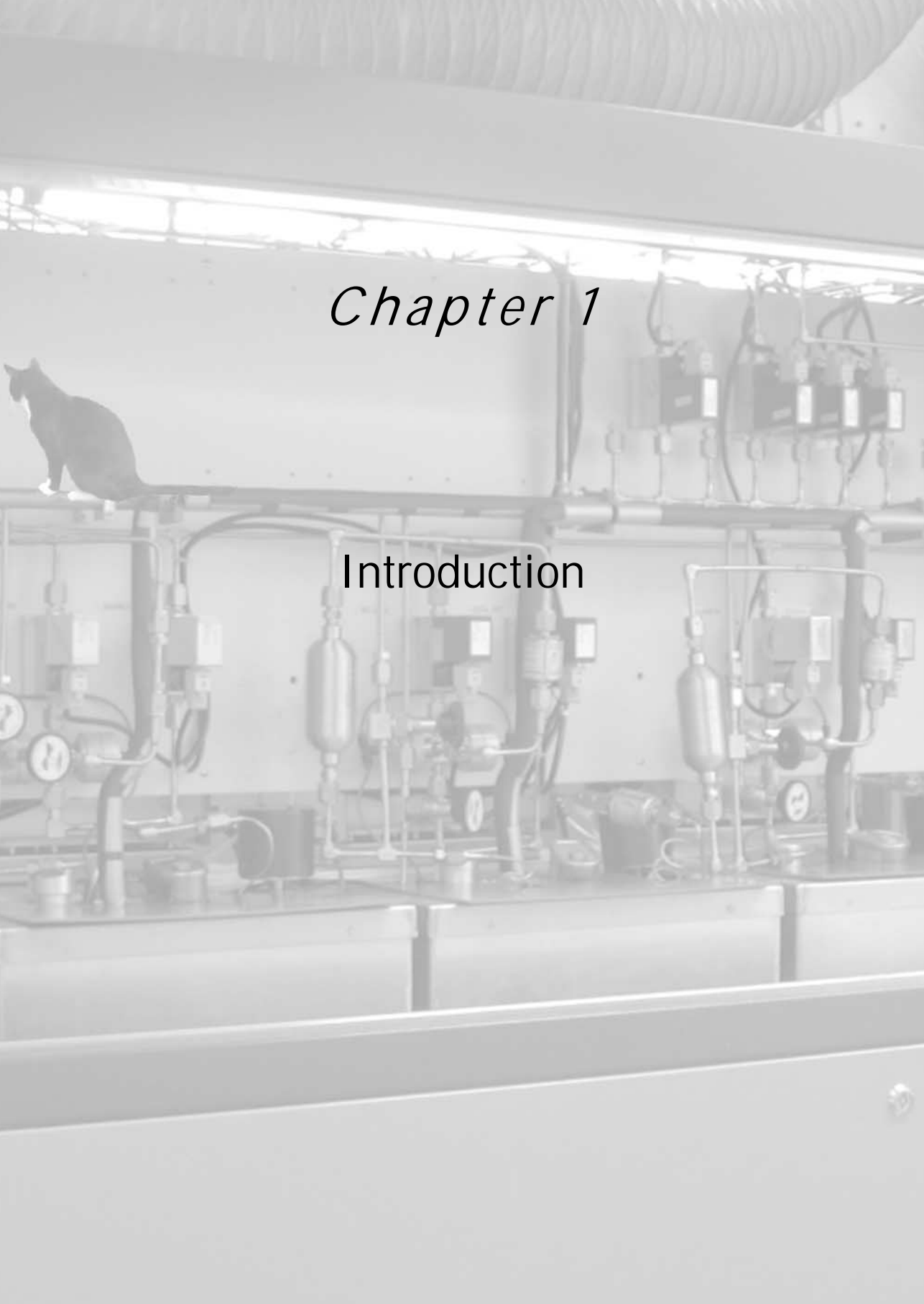
Chapter 4	43
4 Damage after Annealing and Aging at Room Temperature of the Platinized Silicon Substrates	44
4.1 Introduction	44
4.2 Results and Discussion.....	46
4.2.1 Pt wafers.....	46
4.2.2 Surface morphology	47
4.2.3 Cross-section and diffusion.....	51
4.2.4 Structure.....	58
4.2.5 Optical properties.....	61
4.2.6 Aging and roughening.....	66
4.3 Summary.....	68
4.4 Consequences for the MOCVD growth of PZT	70
Chapter 5	71
5 MOCVD Growth of Polycrystalline Pb(Zr,Ti)O ₃	72
5.1 Thickness determination.....	72
5.2 PZT films	73
5.2.1 Zr composition - thin films.....	73
5.2.2 Thickness series for PZT films with x _g = 0.24	74
5.2.3 Thick PZT layers	75
5.3 Morphology.....	75
5.4 Structure.....	81
5.4.1 XRD.....	81
5.4.2 Raman.....	87
5.5 Discussion and summary.....	91
5.5.1 Reproducibility of the runs.....	91
5.5.2 Morphology and texture	92
5.5.3 PT versus PZ and composition control	92
Chapter 6	97
6 Structure and Morphology of Epitaxial PbZrO ₃ Films	98
6.1 Introduction	98
6.2 PbZrO ₃ material properties	99
6.3 Samples	99
6.4 Results.....	101
6.4.1 Structure	101
6.4.2 Morphology	109
6.5 Discussion	114
6.6 Summary.....	117

Chapter 7	119
7 Influence of the Lead Stoichiometry on the Morphology and Structure of PZT Films.....	120
7.1 PZT lead-depleted crystals in a polycrystalline PZT film grown on platinized silicon wafers.....	120
7.1.1 Results	120
7.1.2 Discussion.....	126
7.1.3 Conclusion	127
7.2 Lead oxide crystals on semi-epitaxial PT films grown on STO and polycrystalline PT films grown on platinized silicon wafers.....	127
7.2.1 Results	128
7.2.2 Summary - conclusion.....	139
Chapter 8	141
8 Optical Properties of MOCVD $\text{Pb}(\text{Zr},\text{Ti})\text{O}_3$ Films.....	142
8.1 Refractive index	142
8.2 Bandgap (E_g) and Dispersion Energy (E_d).....	146
8.3 Waveguide experiments	150
8.4 Conclusion	150
Reference	152
Appendix 1: Color Figures.....	163
Samenvatting	175
Summary.....	179
Résumé	181
List of publications.....	183
Curriculum Vitae	185

G l o s s a r y

A (ratio)	$A = \frac{[\text{Pb}]}{[\text{Zr} + \text{Ti}]} \text{ for PZT films}$
	A=1, stoichiometric with respect to Pb
	A<1, Pb-deficient
AFE	Antiferroelectric
AFM	Atomic Force Microscopy
BE	Bottom Electrode
BF	Bright Field
CBED	Convergent Beam Electron Diffraction
CVD	Chemical Vapor Deposition
DF	Dark Field
DRAM	Dynamic Random Access Memory
EDS	Energy Dispersive Spectroscopy
EFM	Electrostatic Force Microscopy
FeRAM	Ferroelectric Random Access Memory
FWHM	Full Width Half Maximum
HREM	High Resolution Electron Microscopy
FE	Ferroelectric
ICP-AES	Inductive Coupled Plasma – Optical Emission Spectroscopy
ICSD	International Crystallographic System Database
MEMS	Micro-Electromechanical Systems
MOCVD	Metalorganic Chemical Vapor Deposition
MPB	Morphotropic Phase Boundary
PLZT	Lead Lanthanum Zirconate Titanate ($\text{Pb}_{1-y}\text{La}_y\text{Zr}_x\text{Ti}_{1-x}\text{O}_3$)
PT	Lead Titanate (PbTiO_3)
PTMHD	Pb(TMHD)_2 - Lead tetramethyl heptanedionate
PZ	Lead Zirconate (PbZrO_3)
PZT	Lead Zirconate Titanate ($\text{PbZr}_x\text{Ti}_{1-x}\text{O}_3$)

SADP	Selected Area Diffraction Pattern
SBT	<chem>SrBi2Ta2O9</chem>
SEM	Scanning Electron Microscopy
STO	Strontium Titanate (<chem>SrTiO3</chem>)
Tc	Curie temperature
TEL	<chem>Pb(C2H5)4</chem> - Tetraethyllead
TEM	Transmission Electron Microscopy
TIP	<chem>Ti(O-I-C3H7)4</chem> - Titanium isopropoxide
TTB	<chem>Ti(O-t-C4H9)4</chem> - Titanium tetra butoxide
X (ratio)	$x = \frac{[\text{Zr}]}{[\text{Zr} + \text{Ti}]} \text{ for PZT films}$
	x=1 : PZ
	x=0 : PT
x_g	X ratio in the gas phase
x_f	X ratio in the film
XRF	X-ray Fluorescence
XPS	X-ray Photoelectron Spectroscopy
XRD	X-ray Diffraction
WDS	Wavelength Dispersive Spectroscopy
ZTB	<chem>Zr(O-t-C4H9)4</chem> - Zirconium tetra butoxide

A black and white photograph of a black cat sitting atop a complex industrial control panel. The panel is filled with numerous mechanical components, including several large cylindrical tanks, various valves, and a network of pipes and hoses. The cat is positioned on the left side of the panel, looking towards the right. The background shows more of the industrial equipment and a ceiling with pipes and lighting fixtures.

Chapter 1

Introduction

1 INTRODUCTION

1.1 Electroceramics

Ceramics are broadly defined as inorganic nonmetallic materials processed at high temperature in their manufacturing cycle. The word ceramics comes from the Greek word "keramos" primarily used to mean "burnt stuff" (1). Ceramics, containing a large number of materials having different properties, are used (or are candidates) for a broad range of applications. They are generally resistant to chemicals (especially oxygen), and are strong, hard, and relatively thermally stable. The traditional ceramics relate to ceramic materials derived from naturally occurring raw materials such as clay, minerals, and quartz used in earthenware, porcelain, bricks, and some kinds of tile and stoneware. The advanced ceramics are defined by their specific properties and encompass some oxides, nitrides, carbides, and borides. There are two main application domains for advanced ceramics. In many tribological systems (automotive, aerospace...), advanced ceramics are used to complete or replace certain metallic parts (2). The advanced ceramics, mainly oxide ceramics, are also used in microelectronics, and then often called electroceramics. Figure 1-1 gives a very brief symbolic view of the properties / applications of advanced ceramics.

The development of advanced ceramics started in the 60's-70's when there was an increasing number of successful manufacturing routes for bulk ceramics. Twenty percent of the ceramic production in the 90's corresponded to advanced ceramics (3) with two-thirds of this production dedicated to electroceramics. The possibilities in the 70's-80's to develop electroceramics in thin film form increased the number of possibilities of applications of these materials: thin films are necessary for microelectronics and MEMS miniaturization.

1.2 Ferroelectricity

Some of the advanced ceramics are ferroelectrics, dielectric materials possessing specific properties. Ferroelectrics belong to the piezoelectric materials, more specifically to the pyroelectric materials (Figure 1-2). Piezoelectricity refers to the effect, which can be observed in these materials. An electrical polarization can be induced in the material by application of a force or a pressure (direct effect) or inversely, the sample dimensions can be changed by application of a voltage or an electric field (inverse effect). The pyroelectric effect is the modification of the spontaneous polarization of the material by temperature variation. Ferroelectrics possess both these two properties in addition to their electro-optic and dielectric properties. The electro-optic effect is the variation of the refractive index by an electric field (See chapter 1.4.3).

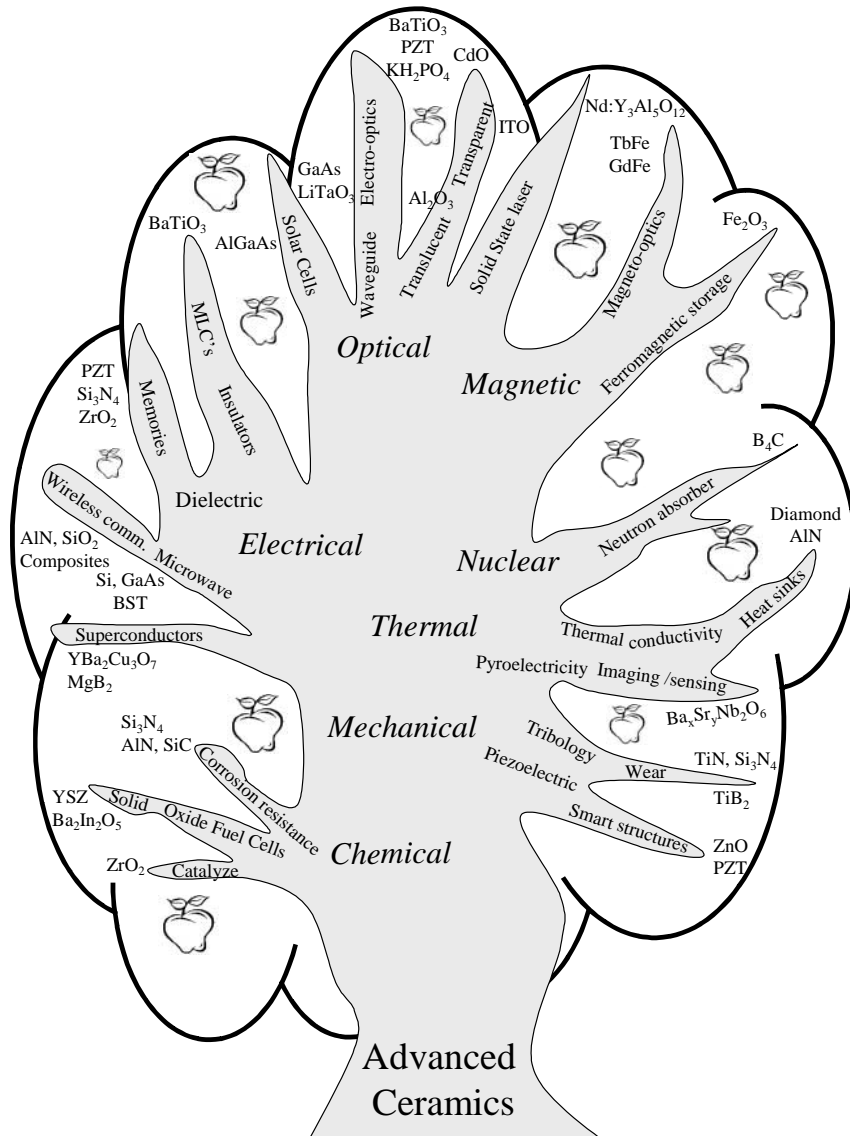


Figure 1-1: Advanced ceramic tree: a schematic non-exhaustive list of the properties of these ceramics leading to examples of applications / research orientations. Several of these properties are linked to each other, for example: for ceramics used in tribology, the chemical and mechanical properties are both of concern.

The specific ferroelectric properties can only occur within certain symmetry of the crystal lattice of the materials (4). Within the 32 crystallographic point groups, 21 are non-centrosymmetric. Non-centrosymmetry implies that there is one or more unique crystallographic direction. Twenty of these 21-point groups exhibit a piezoelectric effect in one direction. Piezoelectrics have polar axes but do not have a spontaneous

polarization, as the net result of electric moments along the polar axes may be zero. Only pyroelectric crystals, with a unique polar axis, can exhibit a spontaneous polarization. The non-centrosymmetry of the pyroelectric (therefore also the ferroelectric) materials only occurs within a limited temperature range. Above the upper or below the lower Curie temperature (specific to each compound), the pyroelectric materials become paraelectric. In the paraelectric phase, the crystal structure becomes symmetric and does not exhibit any of these specific properties (piezoelectricity, pyroelectricity, ferroelectricity). This is shown for PZT in the next section of this chapter (1.3).

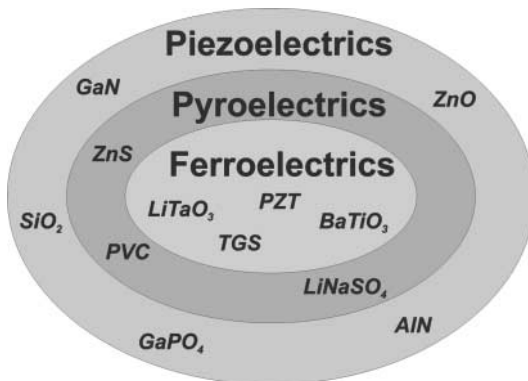


Figure 1-2: Ferroelectric materials group with respect to piezoelectric and pyroelectric materials. A few materials are given as examples in each group.

Ferroelectrics, a subgroup of pyroelectrics, possess special dielectric properties. They have a spontaneous polarization, which can be reoriented by an applied electric field. Ferroelectrics consist of different zones (called domains) with different local net polarizations. If an electric field is applied, ferroelectrics can be poled (the dipoles in the different domains are aligned in the same direction). The plot of the polarization versus the electric field leads to a hysteresis curve. It is one of the most distinctive features of a ferroelectric material. Typical hysteresis curves, measured on MOCVD PZT films of three different thicknesses, are shown in Figure 1-3 (5). As the electric field is increased, the dipoles in the domains orient within the electric field up to a maximum value (saturation polarization). When the electric field is removed, the dipole relaxes but not necessarily to their original position. At zero electric field, the ferroelectric crystal is left with a net polarization, called the remanent polarization (P_r). In the examples shown in Figure 1-3, it is roughly $35 - 40 \mu\text{C}/\text{cm}^2$. These are standard values for the polycrystalline PZT films studied in this work.

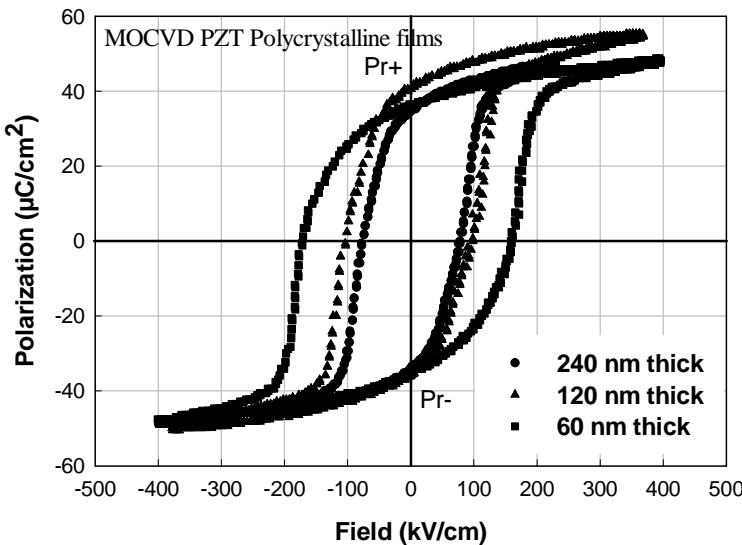


Figure 1-3: Typical hysteresis curves observed in ferroelectrics materials. These curves were measured on three MOCVD polycrystalline PZT films grown in this study. Pr stands for remanent polarization. A capacitor was formed by sputtering an additional top platinum electrode (0.05 mm^2) on the PZT film and using the platinized silicon substrate as bottom electrode. The polarization is measured by applying an AC voltage across the ferroelectric capacitor in series with a reference capacitor. By measuring the voltage across the reference capacitor, the polarization in the ferroelectric capacitor can be measured (Sawyer-Tower circuit).

Pyroelectricity was discovered as early as 314 BC in Tourmaline (mineral of the form $\text{XY}_3\text{Al}_5\text{B}_3\text{Si}_6(\text{OH})_4$) by Teophrast and named pyroelectricity by Brewster in 1824 (4). Piezoelectricity was discovered later, in 1880 by the Curie brothers (Jacques and Pierre). But it is not until 1921, that ferroelectricity was discovered by Vasalek in Rochelle salt (Potassium sodium tartrate, synthesized in 1655 in La Rochelle by Dr. Seignette, as a new mineral drug). While being called "Seignette electric effect" (6), the term ferroelectricity was finally coined for these materials after the ferromagnetic materials, simply due to the similar hysteresis loops they display.

The development of piezoelectric applications started to take off during the First World War. Langevin in France and Anderson, Cady, and Nicolson in the USA started to develop, using Quartz and Rochelle salt respectively, transducers used as depth sounding devices in submarines (6). Devices sensitive to displacement such as phonograph pickups could be developed with piezoelectric materials. The most

common application using the piezoelectric effect remains the quartz watch (1960-70's). A quartz crystal is used in the watch as a mechanically vibrating system and linked to the electric system via the piezoelectric effect. The piezoelectric resonator can then be used as frequency reference for an oscillator circuit. Piezoelectricity has also been observed in organic materials, synthetic as well as natural biological substances such as wood (observed in 1940's), and skin (4). This leads to the research on organic piezoelectrics and ferroelectrics.

Starting in the mid 1930's new ferroelectric materials were synthesized (KD_2PO_4 (KDP)); one of the well-known ferroelectric crystals (an oxide), $BaTiO_3$ was discovered in 1945 (respectively by Von Hippel at MIT and Vul and Goldman in the USSR). Synthesized ferroelectric ceramics (opposed to crystals) lead to similar type of applications as the piezoelectrics. Ferroelectrics can also be used as transducers since they have a spontaneous polarization as well as induced polarization (caused by an applied electric field) and can induce much higher electro-mechanical coupling than piezoelectrics. Ferroelectrics ceramics are used in numerous devices: as high dielectric materials in multilayer capacitors, in electro-optic ceramics, and pyroelectric detectors (7). A brief overview of these materials is given in Table 1-1.

Table 1-1: List of some ferroelectric material groups with some examples. (4, 8).

Oxygen Octahedra
Perovskite $BaTiO_3$, $SrTiO_3$, $PbTiO_3$
Layered perovskite structure - Aurivillius Compounds (Bismuth oxide layers with one or more perovskite layers in between) Bi_2MoO_6 , $SrBi_2Ta_2O_9$, $Bi_4Ti_3O_{12}$ - Strontium titanates: Sr_2TiO_4
Tungsten bronze (octahedra are oriented differently than in perovskite, leaving a different space in between them) $PbNb_2O_6$, $Ba_4Na_2Nb_{10}O_{30}$
Others
Aluminates, Germanates ($Pb_5Ge_3O_{11}$) "Salts" - Water sensitive – Hydrogen containing ferroelectrics Rochelle salt, KH_2PO_4 (KDP), TGS (Triglycine sulfate)
Organic ferroelectrics - Polymers PVDF-TrF (Polyvinylidene fluoride - Tetrafluoroethylene) Ferroelectric liquid crystals

The main ferroelectric group is by far the oxide group. It is called oxygen octahedra as the oxygen atoms form an octahedral shape around one of the cations, as illustrated for $SrTiO_3$ in Color Figure 1. The oxygen-octahedra perovskite as well as some

layered perovskite compounds are the most studied candidates for thin-film applications.

1.3 $\text{Pb}(\text{Zr},\text{Ti})\text{O}_3$

$\text{Pb}(\text{Zr},\text{Ti})\text{O}_3$ (PZT) is a synthetic compound. Bernard and Hans Jaffe introduced it in the 1950's as an improvement to BaTiO_3 to obtain a compound with higher and lower Curie temperatures (6). PbTiO_3 (PT) is also a mineral, macedonite, discovered later in Macedonia in 1971 (9). PT is a perovskite. Perovskite is named after a Russian mineralogist, Count Lev Aleksevich von Perovski (9). The mineral perovskite, CaTiO_3 , was first found by Gustave Rose in the Ural mountains in 1839. The perovskite group is defined by the compounds with the chemical formula RMX_3 , though many compounds with this formula do not have a cubic cell containing one chemical unit (10, 11). The general formula for oxygen-octahedra perovskite ferroelectrics is ABO_3 . The unit cell is cubic: A cations are at the cube corners (called "B-site"), B cations are at the center of the cube (called "A-site"), and the O anions in the cube faces as can be seen in Color Figure 1 (a). The oxygen atoms form an octahedral shape around the B cation, Color Figure 1 (b). A perovskite is really a network of these oxygen octahedra BO_6 all linked together by their corners as shown in Color Figure 1 (c).

Starting with PT, the Ti^{4+} cations can be replaced by Zr^{4+} cations leading to a binary compound, PZT. The Pb^{2+} cations can also be substituted by La^{2+} cations, for example to form PLT or PLZT compounds. PZT is not a unique example and several other binary and ternary compounds can be formed with perovskites, but not all of them exhibit ferroelectricity or piezoelectricity coefficients of a certain order (12). The phase diagram of the PZ-PT system is shown in Figure 1-4. One of the peculiarities of PZT is that, in the transition zone in between the two structures ($x = 0.53$), called the morphotropic phase boundary (MPB), high dielectric constants and piezoelectric coefficients are observed (12). PZT has been studied since the 1950's for these special properties. Recently, researchers updated this phase diagram (13) by studying PZT powder using synchrotron powder-diffraction to lower temperatures than room temperature. They discovered an extra monoclinic phase (inset in Figure 1-4) in between the tetragonal and rhombohedral-1 phases.

Several structures can be seen in the phase diagram. If the ideal perovskite structure is not distorted, the material is cubic (centro-symmetric) and there is no ferroelectricity as shown in cubic STO in Color Figure 1 (a). The cubic phase occurs above the Curie temperature (for PZ around 230°C , for PZT ($x = 0.6$) around 365°C , and for PT around 495°C). In the FE or AFE phase, the cubic structure is distorted in different manners depending on the x ratio in the material. The three different distortion directions of the phases below the Curie temperature are shown in Figure 1-4. These distortions correspond to the variation of three components, which do not have to be present together: the tilting of the oxygen octahedra, the displacements of the cations (Pb^{2+} , Ti^{4+} , and Zr^{4+}), and the distortion of the octahedra (14). The tetragonal PT / PZT structure is the easiest to visualize as the cubic structure is stretched along the $\langle 001 \rangle$

due to a cation shift along one the $<001>$ axes and leads to a tetragonal ferroelectric (space group 99). The unit cell of tetragonal PT and the oxygen octahedral network still contains one chemical unit and the oxygen octahedral network is similar to the one of an ideal cubic perovskite. Increasing the Zr composition leads to a parallel displacement of the Pb, Ti, and Zr cations along $<111>$ leading to a rhombohedral PZT (space group 160). This structure is indicated as "Rhom.1" in Figure 1-4 as there are two rhombohedral structures depending on the temperature and the Zr composition. Similarly as for PT, the PZT rhombohedral unit cell (1) contains one chemical unit and the oxygen octahedral network is similar to that of an ideal cubic perovskite. If the Zr content is higher (at room temperature), the structure is also rhombohedral and correspond to a stretch of the cubic structure along $<111>$ but, in addition to the ions displacement, the octahedra are also tilted along $<111>$, leading to a doubled unit cell (15). For PZ, the stretch from the cubic structure is along $<110>$ and leads to orthorhombic PZ. PZ exhibits different properties than PT or PZT. It is antiferroelectric (AFE). AFE materials do not have a spontaneous polarization but contain a chain of ions polarized in one direction with an adjacent ion chain polarized in the other direction, resulting in a zero net polarization, due to the antiparallel displacement of the Pb^{2+} ions along the a axis. These differences in properties are reflected in its structure. PZ is not an ideal perovskite: the unit cell is larger and contains 8 chemical units to accommodate both polarizations. The oxygen octahedra are arranged in a different way than for STO as shown in Color Figure 2, but the space in between them is still tetrahedral. LiNbO_3 is also a case of non-ideal perovskite. If the oxygen octahedra are linked in a peculiar way (4) leaving different spaces in between them, it can lead to another structure than perovskite, such as tungsten-bronze (listed in Table 1-1). AFE materials have a dielectric constant increase at the phase transition and the electric field can induce a "butterfly" hysteresis loop: at low field, there is no response and above a certain threshold field, the AFE behaves like a ferroelectric (8).

As the different coefficients (piezoelectric, electro-optic) are higher at the MPB, and as the film properties can be different than the bulk ones, it is important to be able to grow a whole range of PZT compositions to compare their properties. Once the MOCVD reactor was working, the composition study was the starting point of this work.

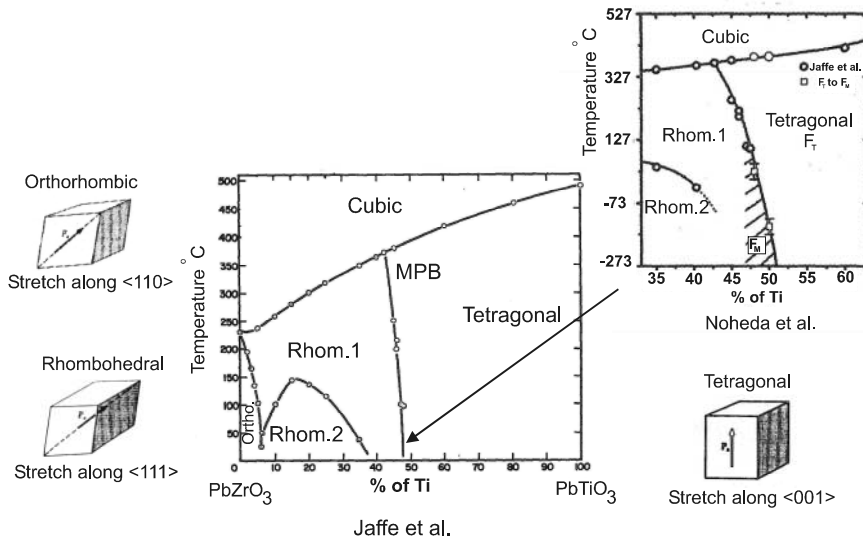


Figure 1-4: PZT phase diagram. In the middle, the standard phase diagram as defined by Jaffe et al. (12) is shown. The diagram around the MPB showing the monoclinic phase between the tetragonal and rhombohedral phases discovered recently by Noheda et al. (13) is shown at the upper right. F_M stands for ferroelectric monoclinic in the inset. The distortion from cubic is shown for tetragonal, rhombohedral, and orthorhombic (4).

1.4 Ferroelectric thin film applications

As ferroelectric materials have a special nature and possess a unique combination of properties, a broad spectrum of applications can be developed with these materials. Though the largest number of applications with ferroelectrics is still associated with bulk materials, important applications are under development for ferroelectric films. Figure 1-5 gives a schematic overview of these applications and some of them are detailed below. The feasibility of such applications is still dependent on the status of the film preparation, processing, and integration technologies. Each application has different requirements, which might be fulfilled by different techniques. For example, standard MOCVD growth fulfills certain requirements and not others (Chapter 2). Additionally, the ferroelectric film properties can differ largely from the bulk ones (4).

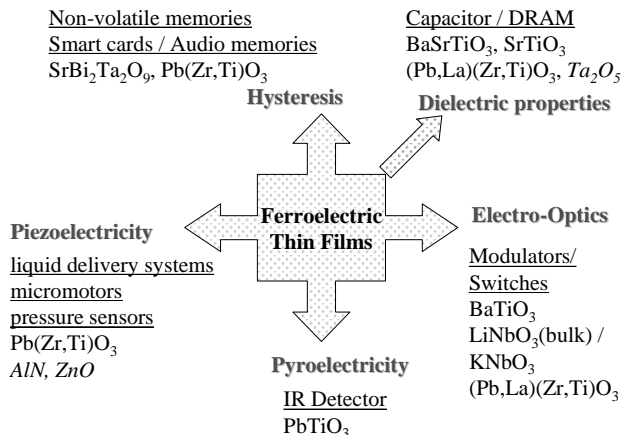


Figure 1-5: Overview of typical ferroelectric thin-film applications. The materials in *italic* are not ferroelectrics but are other candidates for these applications.

1.4.1 Memories

Ferroelectric films have attracted quite a lot of attention especially for their use in memories. The largest emphasis is probably on Nonvolatile Random-Access Memory (NVRAM or FeRAM) (16, 17). This application is based on the hysteresis properties of ferroelectrics, as the ones shown in Figure 1-3. The negative and positive remanent polarization (Pr, polarization without electric field) can be used as binary data storage. SBT and PZT are the two leading candidates: SBT offers low fatigue and low voltage while PZT seems to be more easily integrated (lower processing temperature) and possesses higher polarization values (18). Though ferroelectrics are not seen competitive for large-scale memory applications, some applications “niches” are thought of for these memories, as in smart cards (4kB) for example. Several companies are competing with the FeRAM technology and facing different integration issues (19).

Ferroelectrics are also being considered for other types of memories: Dynamic Random Access Memories (DRAM), which are volatile (the information is not retained without power supply). These are based on transistors tandemed with capacitors (17). Increasing miniaturization requires higher capacitance for smaller feature size. Though several designs have been introduced, new materials are considered to replace SiO₂ and Si₃N₄, which are scaled down to thicknesses of 15-20 Å (19). Ta₂O₅ is the replacement candidate but non-lead-based ferroelectrics, such as (Ba,Sr)TiO₃ (BST), are also candidates. As the dielectric constant is higher around the Curie temperature, Sr is added to BaTiO₃ to lower T_c below the operating

temperature and obtain higher dielectric constant (goes from 1000 to 10000 for BST) (17).

1.4.2 Micro-ElectroMechanical Systems (MEMS)

The MEMS technology is the integration of mechanical elements and electronics on a same substrate, usually silicon: micromachining and microelectronics are brought together to obtain a complete system on one chip (20). By adding sensors and actuators to MEMS, the aim is to transform MEMS into smart structures, which can sense and react to environment or stimuli. In this context, ferroelectrics are studied for their piezoelectric properties to be used as sensors and actuators in these types of systems. As an order of magnitude, an average value for piezoelectric coefficient of a ferroelectric material bulk is 100 pC/N. The converse piezoelectric effect would lead to a displacement ($\Delta l = dxV$) of 100 Å for V = 100 V. A piezoelectric coefficient (d_{31}) of 65 pC/N was measured (5) on a 200 nm thick MOCVD PZT layer grown for this study. One of the major problems is the integration of the ferroelectric layer into the MEMS (21). ZnO and AlN (piezoelectrics) are also studied for these types of applications. Though ferroelectrics might exhibit higher piezoelectric coefficients, there can be some drawbacks using them in specific context: in sensing mode, the piezoelectric effect can be disturbed by the pyroelectric effect and quartz stays a more stable option (4). The ferroelectrics and the piezoelectrics might be used in applications with different requirements (21). There are a rather large number of eventual applications in the literature and no overview will be given here. In Figure 1-6, a sensor and an example of actuator are shown. The microvalve could be used for example in micro-liquid systems (22); if three valves are used after each other, a pump could be made.

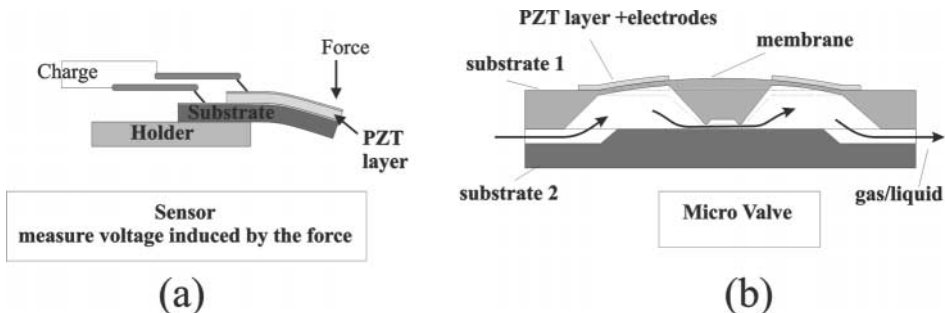


Figure 1-6: Example of a (a) sensor and (b) an actuator. A PZT layer is shown in these examples but it could be a different piezoelectric layer. The microvalve in (b) is based on reference (22).

1.4.3 Electro-optical applications

Though the use of ferroelectric thin films in electro-optical devices is often cited, there are few reports of such applications with respect to FeRAM applications. Ferroelectric films can be used in nonlinear optic applications to convert light to different wavelength (23), or in electro-optic modulators (24). The advantage of films is twofold. Waveguide electro-optic modulators require relatively low drive power in comparison to bulk modulators, because of the optical confinement in the film. Additionally, thin films produced on heterostructure substrates used in the semiconductor industry are more readily integrated than bulk hybrid technologies. Efforts are always directed to implement new technologies on Si wafers to integrate optical devices in existing silicon technology on a large scale. In one example, MgO was grown directly on Si in order to be able to later deposit BaTiO₃ for waveguide applications (25). Recently, GaAs has been grown on Si using an intermediate thin film of STO (26). Both of these structures could be used for ferroelectric thin film growth. This might become a major development, as next to the epitaxial growth challenge, one of the major inconveniences for oxide film growth is that only small-size-substrate crystals are available. There are several thin film candidates for electro-optic technology besides the III-V semiconductors and the dominant LiNbO₃ (27). These include other oxides, LiTaO₃ (24), BaTiO₃ (28), PLZT (7, 29, 30), as well as electro-optic polymers. All of these are highly transmissive at the infrared wavelengths used in optical communication networks. Additionally, the polymers can be deposited onto a wide variety of substrates (31).

Figure 1-7 shows a schematic overview of a possible waveguide modulator, which can be used as a light switch. The ferroelectric shown here is PZT as an example. There is one reference arm and one arm in which the PZT has a top contact to apply a transverse electric field with respect to the light propagation direction. When the light out of the activated arm is in 180° phase mismatch with the reference arm, the device is off (no light out). The mechanism of the device is based on the linear electro-optic effect (24). A large electro-optic effect is necessary to produce an optical phase shift of 180° over a path length of several microns. For LiNbO₃ or tetragonal PZT (001) or rhombohedral (111) crystals, the field-induced changes in refractive index are given by (24):

$$\Delta n_o = -\frac{1}{2} n_o^3 r_{13} E_3$$

$$\Delta n_e = -\frac{1}{2} n_e^3 r_{33} E_3$$

where n_o and n_e stand respectively for the real part of the ordinary and extraordinary refractive index, E for electric field, and r_{13} and r_{33} electro-optics coefficients.

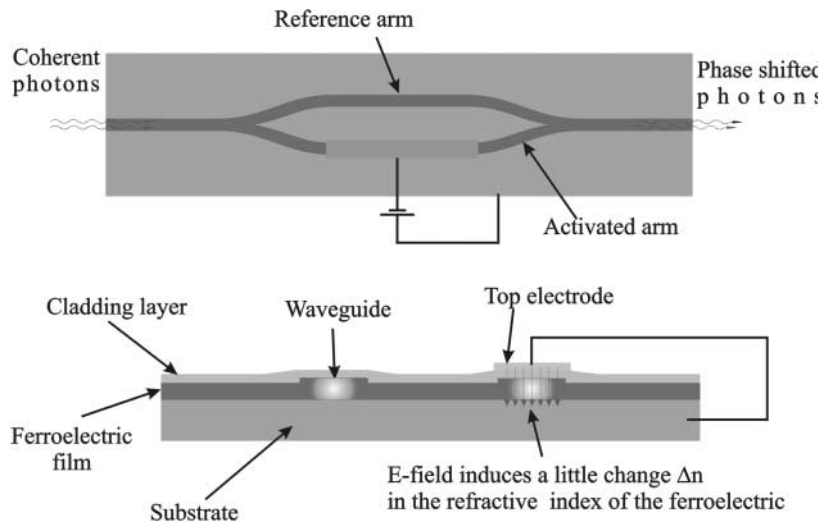


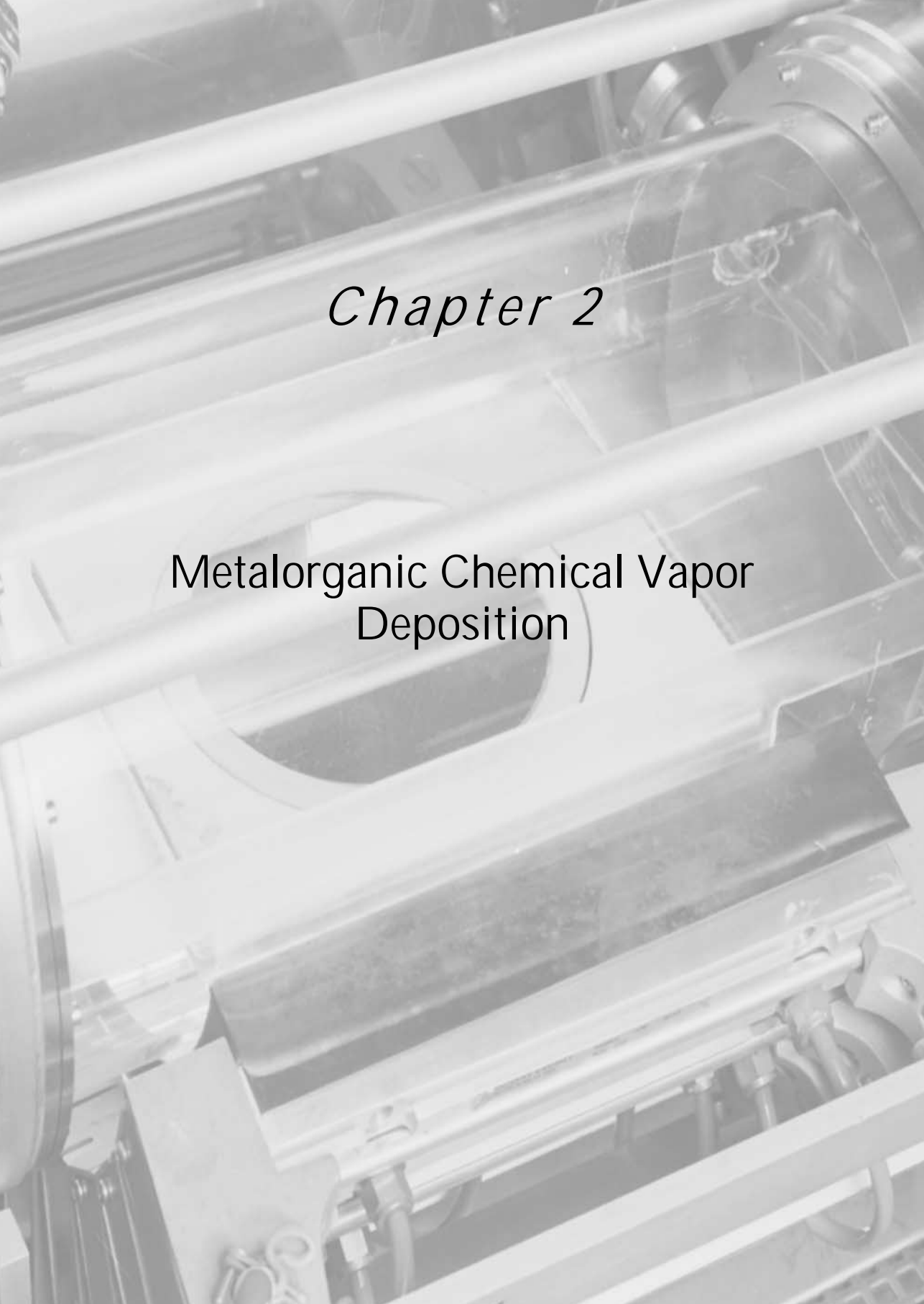
Figure 1-7: Example of an eventual use of a ferroelectric layer in an electro-optic devices: a Mach-Zehnder modulator used as an optical switch.

As an order of magnitude, the $\Delta n/n$ for a LiNbO_3 bulk ($r_{33} = 30.9 \text{ pm/V}$, $n_e = 2.2$, $V = 180 \text{ V}$, $\lambda = 0.6 \mu\text{m}$) is 1.35×10^{-5} for a modulator of 1 nm thickness and 10 mm length (24). This relative change in refractive index corresponds to 0.5 wavelength in this configuration. Electro-optical coefficients of some oxide films have been measured. Waveguides from BaTiO_3 thin films on MgO were successfully fabricated (28, 32) with $r_{\text{eff}} = 50 \text{ pm/V}$ and 5 dB/cm loss at 1.5 μm . Similarly, $(\text{Pb},\text{La})\text{TiO}_3$ sputtered films on sapphire have an r_{13} of 55 pm/V (29). The electro-optic coefficient of solid-phase-epitaxy $\text{PbZr}_{0.52}\text{Ti}_{0.48}\text{O}_3$ waveguide on $\text{Nb}-\text{SrTiO}_3$ is reported to be 53 pm/V (30). An earlier report of sol-gel $\text{PbZr}_{0.53}\text{Ti}_{0.47}\text{O}_3$ on glass substrates (33) indicated a larger electro-optic coefficient of 315 pm/V.

Ferroelectric films for waveguide-modulator applications should have a low optical loss and a low roughness for waveguiding and a high electro-optic coefficient for the refractive index modulation. The design of such devices was investigated in another work in the context of this project (34). In (23), it was shown that the rms surface roughness tends to be about 1% of the film thickness and that losses vary as the square of the rms roughness; the desired top roughness being $\text{rms} = 1 \text{ nm}$. In (28), a top-surface rms roughness of 2-5 nm, estimated with another approach, was also described as acceptable. Another source of loss is light scattering in the film, which can be due to inhomogeneities or domains of different crystallographic orientations (35, 36). Though hetero-epitaxial growth is the best option to produce low loss waveguides, one of the main challenges is the difficulty of growing high-quality thick films with low roughness. Several modulator demonstrations have been reported in literature: in (28) a waveguide of epitaxial BaTiO_3 grown by MOCVD has been fabricated with a loss of 4 dB/cm at 1.54 μm and an electro-optic coefficient of 50 pm/V.

1.5 Aim of this study: MOCVD growth of PZT films

This work is part of a four-year Dutch research project entitled "Ferroelectric Films for Optical and Micromechanical Applications" sponsored by the Dutch Science Foundation. The film development was carried out at the University of Nijmegen and the device development at the Technical University of Twente. The project was broad, ranging from the development of single ferroelectric layers to the development of demonstrators exploiting the ferroelectric properties of the layers. The motivation to grow ferroelectric films has been detailed in this introduction. The initial idea was to develop thick polycrystalline layers (a few microns) for MEMS application and relatively thinner (0.5 - 1.0 μm) hetero-epitaxial layers for electro-optic applications. Though PZT belongs to a class of materials with numerous interesting properties (ferroelectrics), and though it has been widely studied in its bulk form, it is not yet standard or straightforward to develop PZT films for MEMS and electro-optic applications. PZT films have been grown by several techniques since the 70's, but many growth aspects are not yet known, especially as a function of the x composition ratio. A large number of the current research efforts are oriented towards memory applications requiring film thickness in the range 60 – 200 nm and the improvement of the remanent polarization or the fatigue for FeRAM's. Polycrystalline films for MEMS were grown on platinized substrates and hetero-epitaxial films for optical devices were grown on STO. The work presented in this thesis deals with the MOCVD growth and a detailed investigation of both types of PZT films.



Chapter 2

Metalorganic Chemical Vapor
Deposition

2 METALORGANIC CHEMICAL VAPOR DEPOSITION

2.1 Introduction

PZT thin films can be produced by numerous techniques ranging from sol-gel (37), sputtering (38), laser-ablation (39), molecular beam epitaxy (38), to MOCVD (40). These techniques, all having different advantages and drawbacks, produce films of various qualities and the definite choice of the deposition technique might depend on the quality required by the application of the films. MOCVD is the dominant deposition technique for III-V films in the semiconductor industry as it has several advantages. Large wafers can be uniformly covered simultaneously (up to 5 wafers of 10" diameter in commercial systems), with an accurate control of the thin film composition. Additionally, films can be produced with high deposition rates, circa 2 $\mu\text{m}/\text{hour}$ (41) and good step coverage can be obtained. But these advantages exist for well-established MOCVD technologies with respect to reactor design, precursors, and growth of III-V materials on appropriate substrates. For these materials, the growth is homo-epitaxial (GaAs on GaAs) or hetero-epitaxial (for example InGaP on GaAs with a maximum mismatch of 0.1% below the critical thickness). Hetero-epitaxial MOCVD growth can also be successful with a higher lattice mismatch layer - substrate, as for GaN on sapphire with a 13.7% lattice mismatch (42). But for oxides, such as PZT, the MOCVD techniques (precursors, reactors) are not yet well established and the hetero-epitaxial growth of oxides, though the name of the film process is the same, is very different from III-V semiconductors with circa 5% lattice mismatch for PZT on STO. In addition to the growth difficulties, PZT films are grown in a cubic phase (above T_c) and the PZT structure changes during cooling, inducing domains in the layers (Chapter 6). For polycrystalline films, the growth is different as there is no epitaxy but some issues are similar, such as the composition control. Therefore the advantages commonly cited with respect to MOCVD and III-V materials do not necessarily apply to the oxide case. The strong interest in ferroelectric memories in thin film form has triggered research in growth techniques and there have been many reports in the literature on polycrystalline growth of PZT by MOCVD since the mid 1990's. Though more is now known about growth, no commercial MOCVD reactor systems are readily available to produce ferroelectric films of the same quality as semiconductor films. In this issue, the substrates (quality, lattice match, availability etc.) play a role as important as the growth techniques. The recent work of Ramdani et al. (26) reporting the growth of 12" GaAs wafers on Si substrates using a STO interlayer is a breakthrough in the substrate issue not only for III-V but also for oxides, as it might create extra possibilities for the growth of these compounds.

2.2 Metalorganic Chemical Vapor Deposition - MOCVD

2.2.1 General

Chemical Vapor Deposition (CVD) refers generally to the deposition of solid materials from precursors in the vapor phase. Growth of epitaxial thin films from the vapor phase started in the 1960's with the hetero-epitaxial growth of Ge on GaAs by Marinace and the epitaxial growth of GaAs films by Holonyak et al. as summarized in Ref. (43). The CVD technique can be enhanced and any derivatives of the CVD acronym refer to specificities in the deposition techniques. The term metalorganic, generally used to describe compounds where metal atoms are linked to organic groups, refers to the type of precursors used in MOCVD. Organometallic vapor-phase epitaxy (OMVPE) or Metalorganic vapor-phase epitaxy (MOVPE) are used as synonyms for MOCVD but directly imply an epitaxial growth. This is not the case for polycrystalline PZT on Pt substrates or semi hetero-epitaxial PZT on STO (Chapter 5), therefore the term MOCVD is used in this work. MOCVD was pioneered in 1968 with the work of Manasevit, who first grew hetero-epitaxial GaAs films on different oxide substrates by MOCVD (44) and then most of the III-V, II-VI, and IV-VI on oxide substrates (43).

For III-V materials, liquid and solid precursors have been developed with a relatively high vapor pressure at room temperature, but for most of the multi-metallic oxide materials, (e.g. ferroelectrics, superconductors), the metallic precursors have a low vapor pressure at room temperature as can be seen below in Figure 2-5 for our precursors. The solution to this problem was to increase the vapor pressure by heating the liquid or solid precursor to temperature above room temperature. The standard delivery system for liquid or solid precursors consists of a stainless steel bubbler containing the liquid precursor. The temperature of the bubbler can be controlled and determines the vapor pressure of the precursor. Additionally, the total pressure in the bubbler can be lowered below atmospheric pressure to increase the efficiency of the process. As shown in Figure 2-1, the precursor vapor is "carried" by the carrier gas bubbling through the bubbler. The term bubbler is more appropriate for liquid than solid precursors, but used for both. The efficiency of the process is determined by the amount of precursor that can be picked up by the carrier gas. If the bubbler is heated to obtain the required vapor pressure, the whole piping system from the bubbler up to the reactor also needs to be heated (for bubbler temperatures higher than ~ 25°C). In addition to technical problems, this can create reproducibility problems due to partial decomposition prior the reactor. To avoid the transport of the vapor at high temperature to the reactor, new evaporation technologies, for instance liquid source delivery, have been developed and are now used in modern commercial MOCVD reactors for oxides. There are several kinds of liquid source delivery systems patented in USA, Europe and Asia, but the principle is the same. The precursor, liquid eventually diluted or solid dissolved, is introduced (by mass flow controller or injector) into a hot cell, called vaporizer, often in the form of mist or droplets, where it quickly

evaporate (flash evaporation) to be introduced pure or diluted by a carrier gas into the reactor.

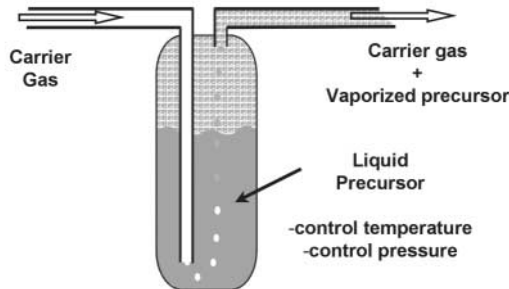


Figure 2-1: Schematic of a bubbler, standard delivery system for liquid or solid precursor. In this case, a liquid precursor is represented.

2.2.2 MOCVD and PZT

In an MOCVD PZT literature survey (up to 1995), Keijser (40) reports that the PT CVD deposition by Nakagawa et al (45) in 1982 started the research of PZT by MOCVD. Later in 1990, PZT was deposited by MOCVD for the first time by Okada et al. (46). The research on PZT MOCVD films was limited by the available number of precursors and the different types of reactor. A list of recent publications is shown in Table 2-1. There is now an increasing amount of research and information on different precursors. Earlier, the precursors were classified in three categories, β -diketonates, organometallics (e.g. TEL), and alkoxides (e.g. TIP) (47). As can be seen in Table 2-1, new various types of precursors, issued from a combination from these three categories (e.g. PTMH) are now used for PZT. Most of the layers in Table 2-1 were produced using bubblers and results on PZT layers grown with new delivery systems are recent. Most of the studies listed refer to FeRAM as applications. Though the list is non-exhaustive and some research projects are not focused on one specific type of application, there are very few research groups growing PZT by MOCVD for other purposes. This corresponds well to the relatively low layer thicknesses, on average below 500 nm as indicated in Table 2-1. The reactor types are not mentioned in Table 2-1, but two main types of reactor are often used, vertical or horizontal. The capacity of both types can vary considerably, that is from 0.5 cm^2 to 0.5 m^2 . Of course this will influence the amount of necessary precursor and carrier gas. Shower heads are also mounted on modern vertical reactors and used in combination with liquid source delivery to improve the distribution of the precursors uniformly over a large area.

2.3 The MOCVD reactor for PZT deposition: The Ferro reactor

2.3.1 Description

In the four years of research dedicated to this project, most of the time has been invested in the installation of the ferro reactor, its cleaning, its drawbacks, its simplifications, its modifications, and its maintenance; but only the most crucial aspects with respect to the growth will be summarized here. The Ferro reactor used was a second-hand Aixtron 200 MOCVD (for up to 6" diameter wafers), which had been briefly used previously (40) and was moved in non-working conditions to our lab.

The final system, after the necessary modifications, on which the layers described in this work were grown, is a standard horizontal cold-wall reactor equipped with three standard delivery systems. As can be seen in Figure 2-2, it is composed of several different units.

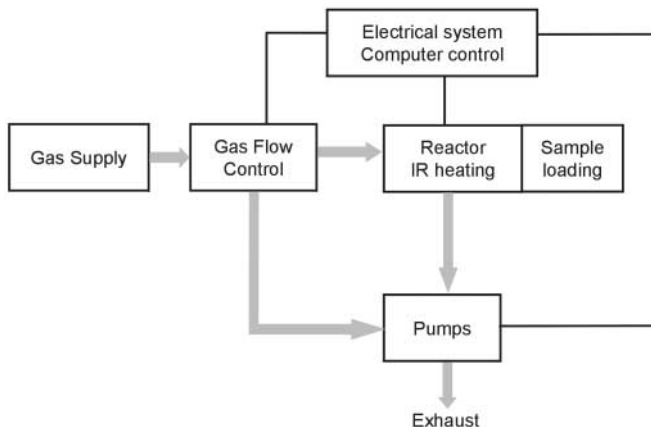


Figure 2-2: Schematic diagram of the Ferro reactor system.

The gas supply unit is composed of the nitrogen carrier gas, the oxygen gas, and the three precursor units for lead, zirconium, and titanium. These gases are brought to the reactor chamber or to the vent system through a network of piping and valves, schematized in Figure 2-3.

Table 2-1: Literature survey of different recent MOCVD PZT studies. References from the same lab are grouped together. For clarity, an indexing is used in the table and indicated below. If not specified, the type of the source is a bubbler.

Year	Pb source		Zr source		Ti source		Growth
	Precursor	T°C	Precursor	T°C	Precursor	T°C	T°C
1995	TEL	40 -90	ZTB	40 -90	TIP	40 -90	700
1999	PDPM	140	--	--	TIP	41	500-620
2000	TEPOL				TIP		490
2000	PDPM ^a		ZTB ^a		TIP ^a		620
2000	PDPM	140	ZTB	35	TIP	41	500(300-620)
2001	PDPM ^a		ZTB ^a		TIP ^a		415-580
1995	TEL	20-22			TIP	20-22	700-750
1997	TEL	28.5	ZTB	32	TIP	32	700
2000	TEL	45	ZTB	45	TIP	40	450-525
2000	PTMHD		ZTB		TIP		600
2000	PTMHD	118	ZTB	35	TIP	35	600
1998	TEL	0	ZTB	30	TIP	30	600
1999	TEL	0	ZTB	30	TIP	30	570-580
2000	TEL		ZTB		TIP		
2000	TEPOL	40	ZTB	35	TIP	30	580
1998	TEL	35			TIP	65	600
1999	TEL	35			TIP	65	650
2000	PDPM	135 ^b	ZTB	35	TIP	45	700
2000	PDPM	280 ^b	ZDPM	280 ^b	TIP	280 ^b	550-700
2001	PTMHD	130	--	--	TIP	45	300 -400
2002	PDPM ^c	130	ZBPM ^c		TDPM ^c	45	350-400
2002	TEL	45	ZTB	50	TTB	60	700

TEL - Pb(C₂H₅)₄ - Tetraethyllead

TEPOL - (C₂H₅)₃Pb(OC₅H₁₁) - Triethyl n-pentoxy lead

PDPM - Pb(DPM)₂ or Pb(C₁₁H₁₉O₂)₂ - Bis(2,2,6,6-tetramethyl-3,5-heptanedionato) lead

PTMHD - Pb(TMHD)₂ - Lead tetramethyl heptanedionate

ZTB - Zr(O-t-C₄H₉)₄ - Zirconium tetra butoxide

ZDPM - Zr(C₁₁H₁₉O₂)₄ - Tetrakis(2,2,6,6-tetramethyl-3,5-heptanedionato) zirconium

ZBPM - Zr(DIBM)₄/THF - Zirconium-isobutryl-pivoylmethane Tetrahydrofuran

TTB - Ti(O-t-C₄H₉)₄ - Titanium tetra butoxide

TIP - Ti(O-I-C₃H₇)₄ - Titanium isopropoxide

TDPM - Ti(OiPr)₂(DPM)₂/THF -

^a vapor pulsed introduced in the chamber, ^b solid delivery, ^c liquid source delivery

Table 2-1 (Ctd): Literature survey of different recent MOCVD PZT studies. References from the same lab are grouped together. For clarity, an indexing is used in the table and indicated below. If not specified, the type of the source is a bubbler.

Growth velocity (nm/min)	Layer thickness (nm)	Application	Substrate	Source
3.3		FeRAM	PSW; STO; SRO/STO	(40)
	50	FeRAM	PSW, PT, SRO/LaAlO ₃	Japan (48)
2	200		PSW	(49)
2.1	250	FeRAM	PSW	(50)
2.5-3.3	300-4000		MgO	(51)
	250	FeRAM	PSW, STO	(52)
2.5; 5-7	400-1000		MgO, LaAlO ₃ , STO	Argonne, Illinois (53)
2.5-5	50-1200	IO/MEMS	SRO/STO	(35)
5-7	200-700		PSW	(54)
	25	FeRAM	LaNiO ₃ /PSW	(55)
3-5	150-200	FeRAM	LaNiO ₃ /PSW	(56)
	40-400; 51-438	FeRAM	PSW	Japan, (57)
	40-440	FeRAM	SRO/STO, STO/SW	(58)
6-8	240-320	FeRAM	SRO/STO, STO/SW	(59)
			PSW	(60)
7.5?			Pt/STO	China (61)
5	100+100	transducers	Pt/STO, Pt/LaAlO ₃	(62)
25	700	MEMS	PSW (with TiN and TaN instead of Ti adhesion layer)	Japan (63)
-	210	FeRAM	PSW	Korea (64)
6.7-8	200-240		PSW	Korea (65)
11	440	FeRAM	PSW	Japan (66)
4.5	130 - 140; 800 - 1400	MEMS / IO	PSW; STO	Present work

PSW - Platinized silicon wafers

SRO - SrRuO₃

SW - Silicon wafers

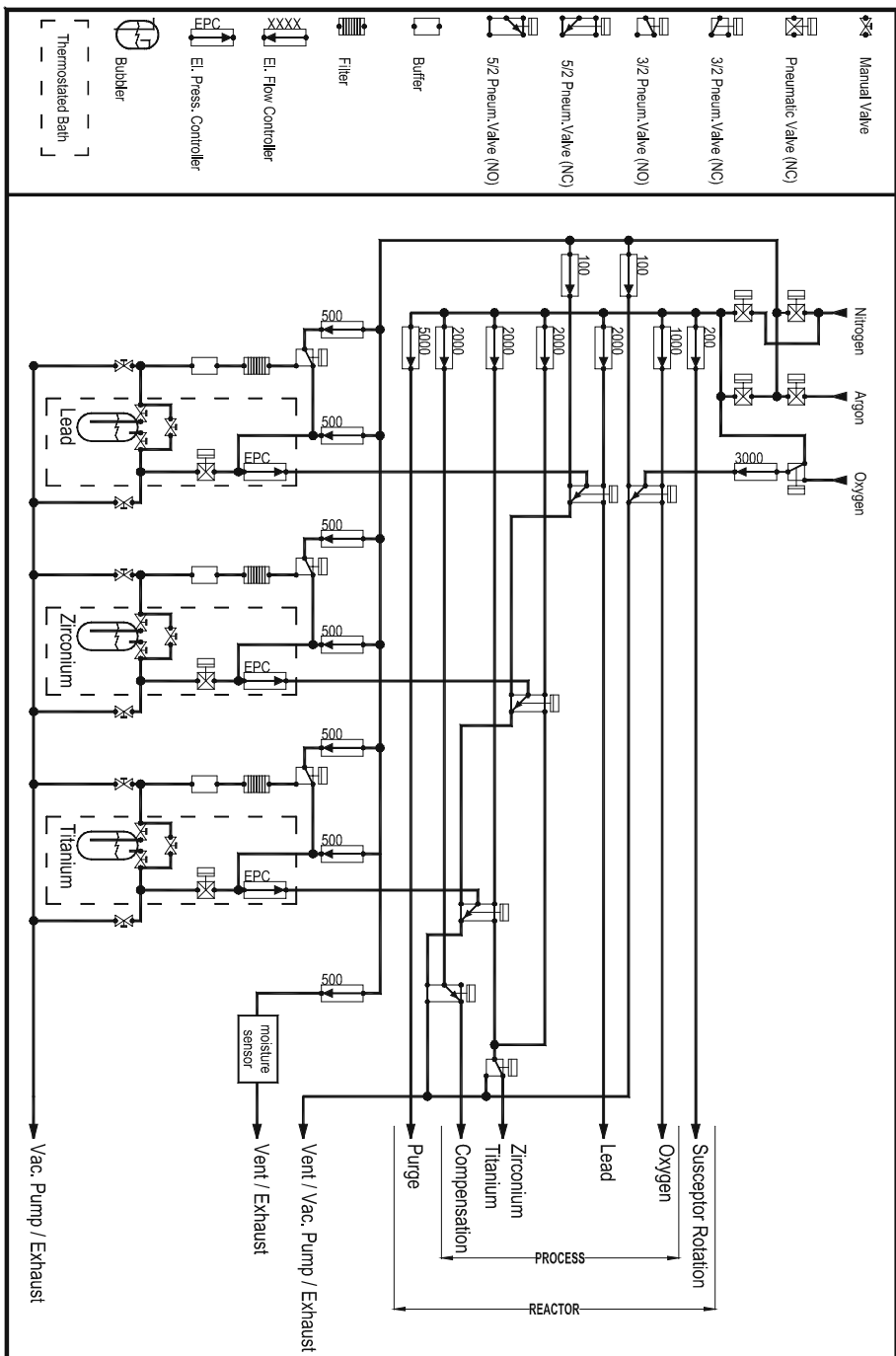


Figure 2-3: Ferro reactor - Gas flow system.

The growth takes place in the reactor chamber heated up to 700°C by infrared lamps and the substrate is set on a rotating disc (circa 30 rpm) to ensure an improved uniformity of the grown layer. The same type of precursors was used for all the layers, a metal-alkyl precursor for lead, tetraethyllead, and two metal alkoxides for zirconium and titanium, zirconium-t-butoxide and titanium-t-butoxide respectively. In Table 2-2, the parameters for the growth are summarized.

Table 2-2: Typical growth run parameters for both type of layers.

Parameter	Polycrystalline Growth	Hetero-epitaxial Growth
Substrate Temperature	700°C	700°C
Reactor pressure	5 – 10 mbar	5 – 10 mbar
Lead precursor $(Pb(C_2H_5)_4)$	30 µmole/min	80 µmole/min
Zirconium precursor $Zr(OC(CH_3)_3)_4$	0 to 30 µmole/min	0 to 80 µmole/min
Titanium precursor $Ti(OC(CH_3)_3)_4$	0 to 30 µmole/min	0 to 80 µmole/min
Oxygen flow	70 mmole/min	70 mmole/min
Total flow through reactor	3000 sccm	3000 sccm
Growth time thin film	15 - 30 min	60 min
Growth time thick films	60 - 120	300 min
Average growth rates	about 3 nm /min	0.8 - 4.7 nm /min x ratio and thickness dependent

In addition to the growth time to obtain the appropriate layer thickness, there is roughly 20 min necessary for the warming-up and up to 2 hours for cooling-down (not ramped or controlled) the reactor to room temperature as shown in Figure 2-4.

2.3.2 Drawbacks of the Ferro Reactor

Below some of the main problems are listed. None of them could definitely be solved and the Ferro reactor stays an exotic one. Though growth experiments could be performed, these problems often prevented the completion of many systematic studies.

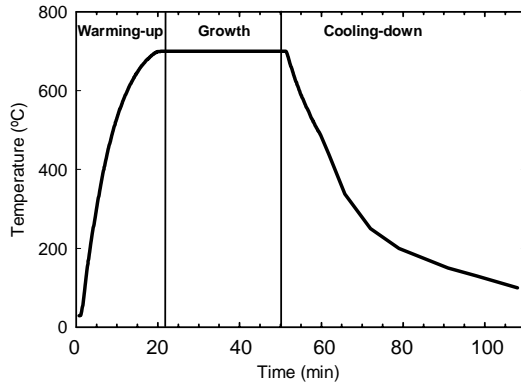


Figure 2-4: Typical heat cycle for a PZT growth run.

Precursors

The precursors used in this study had a low vapor pressure (Figure 2-5) and their delivery was ensured by a standard bubbler system. Therefore, as mentioned in Section 2.2.1, the bubblers as well as the whole precursor piping up to the reactor must be kept at a relatively high temperature and the heating of the piping leads to additional technical difficulties. The initial heating system did not consist of often-used, electrical wires around the piping, as they can induce hot or cold spots. Instead, a system of double piping was used to transport the precursor vapor from the bubbler to the reactor. An external circuit containing silicone oil was flowing at the right temperature around the internal pipe containing the gas. Though the idea of using a fluid to obtain homogenous heating was good, the silicone oil created lots of problems. The oil system constantly leaked and even leaked once in the reactor as the reactor inlet was also heated in a similar way. The system was modified and the final version made use of a flexible piping with flowing water rolled around the gas piping.

In addition to the low vapor pressure, the precursors were not widely available in standard bubblers, especially the lead precursor, which is considered toxic. Generally, the precursors used were moisture sensitive, ZTB being the most sensitive. The moisture of the carrier gas prior to the precursor inlet was measured to be circa 0.04 ppm when the reactor was in use and was as low as circa 0.015 ppm when in purging state. Nevertheless, the Zr precursor, being the most moisture sensitive, clogged regularly the piping system around the valve for the bubbler pressure control.

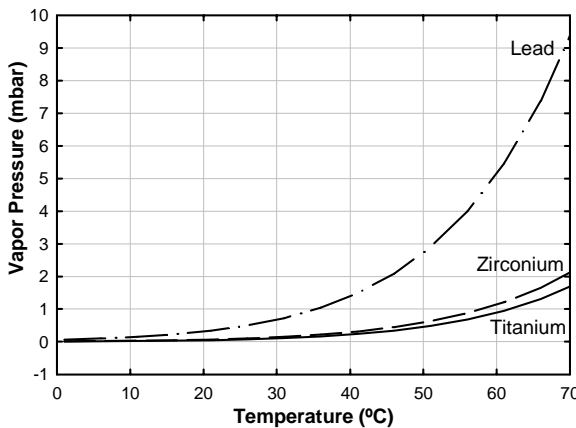


Figure 2-5: Vapor pressure of the precursors used for the growth of the PZT films. Lead (tetraethyllead), Zirconium (Zirconium-t-butoxide), and Titanium (Titanium-t-butoxide).

Reproducibility

To perform a study of the effect of one parameter, the others should stay constant and reproducible runs should be obtained. Sometimes, it was observed that runs could not be reproduced at all. In such conditions, unique wafers, such as the one shown in Section 7.1, could be obtained. The exact origin of these non-reproducible conditions is not exactly known. Therefore a standard run was repeated regularly to test the reactor, and a series of growth experiments was only performed once a standard run could be repeated a few times. The quality of some repeated runs is described in Chapter 5.

Non-uniformity

Optimization of the runs was performed to obtain PZT layers as uniform as possible. The initial layers were covered with colored rings (as seen on the cover of this thesis) representing different PZT thicknesses, increasing radially from the center to the edge of the wafer, as shown in Color Figure 3. By adjusting the flows, the runs were optimized to decrease the thickness inhomogeneity to an optimum value of 5 - 20 % difference in thickness as shown in Color Figure 4 for a circa 100 nm thick PZT layer. The wafers were not only inhomogeneous in thickness but also in the lateral composition (x ratio) (therefore also in morphology) with an x ratio, which could be doubled at the edge with respect to the center. But the thickness inhomogeneity is also present for PT films. This effect could not be suppressed and the PZT wafers were used as such. In addition to the flow, the inhomogeneity of the wafers could be due to

temperature inhomogeneity. The infrared lamps were manually adjusted but no improving effects have been observed on the growth.

Cleaning

The glassware (liner) was cleaned in a HF solution after each run and a run at higher temperature than the growth temperature was performed between runs to avoid contamination, from material at the susceptor surface, from one run to another. Nevertheless, even after this cleaning, there could still be contamination leading to a pre-growth or nucleation during the warming-up prior to growth as shown in Figure 2-6. This contamination comes from the carrier gas flow, containing eventually growth species, above the substrate, due to oxidized material in the piping. Extensive cleaning was mainly necessary after the hetero-epitaxial runs, which used higher partial pressure in the chamber and longer growth time. In these cases, in addition to the inlet piping, the reactor outlet could also be covered by different oxides causing back diffusion in the reactor.



Figure 2-6: Contamination during warming-up observed on a 4" Pt wafer heated up to 700°C for 1 min.



Chapter 3

Experimental Techniques

3 EXPERIMENTAL TECHNIQUES

3.1 Characterization techniques

The characterization techniques regularly used for this work are described below, along with the instruments used.

3.1.1 *Color card*

After a growth run, it is useful to be able to estimate some parameters of the grown layer rapidly. Thickness is one of these parameters. Weighing the sample prior to and after growth will give an indication of the thickness. But the polycrystalline films grown on large wafers (6" or 4" diameter) were not radially homogenous in thickness and composition (Chapters 2 and 5) and resulted in wafers with color rings. Rings were formed if the samples were rotated during growth, otherwise stripes were obtained. The thickness of the polycrystalline films could be evaluated by means of a color card. The color rings (or interference or Newton rings) are due to radially increasing film thickness from the center to the edge of the wafer. When light is reflected from a transparent thin film on an opaque substrate, interference colors appear because there is a path difference between the light reflected directly from the front surface (the air/film interface) and the light reflected from the back surface (film/substrate interface) of the film (67). The path difference p is given by:

$$p = 2 \cdot n \cdot d \cdot \cos \theta + \frac{\lambda}{2},$$

where n is the refractive index of the film, d is the thickness of the medium, θ is the angle that the beam makes with respect to the normal inside the film, and λ the wavelength of the incident light. The path difference between the reflected waves from the front and the back interfaces of the film lead to interference. As the samples are viewed with white light, a succession of colors is seen. If the sample would be viewed with a filter or illuminated with monochromatic light, only successive bright and dark rings would be seen, as there is no color overlapping. A color-card reference was established using a polycrystalline PZT layer grown on a 6" diameter platinized silicon substrate. In appendix 1, Color Figure 3, a PT film is shown with a thickness scale. The layer was etched in every zone and the thickness of the zones measured with a step profiler. The thickness in the different zones was also measured by ellipsometry. This color card provided an efficient way of determining the thickness rapidly. Nevertheless, the colors repeat each other regularly and if only two color rings are present, the technique can be misleading. Examples of such homogenous PZT

layers are shown in Color Figure 4. Additionally, the color card was only constructed for PT, as only PT and PZT films with low x ratios were grown in the first years of the project.

3.1.2 Ellipsometry

Ellipsometry is an optical characterization technique, which analyzes reflected light. The technique is sensitive to both phase and amplitude modification upon reflection. The measured quantities are Δ (phase modification) and Ψ (amplitude modification). Δ varies from 0 to 360° and is defined as:

$$\Delta = \delta_1 - \delta_2$$

with δ being the phase difference between the parallel component and the perpendicular component of the wave. The indices 1 and 2 stand for the incoming and outgoing waves respectively. Ψ varies from 0 to 90° and is defined as:

$$\tan \Psi = \frac{|R^p|}{|R^s|}$$

with $|R^p|$ and $|R^s|$ being the ratios of the outgoing wave amplitude to the incoming wave amplitude for the parallel (p) and perpendicular (s) (with respect to the plane of incidence) components respectively. Ellipsometry extracts relevant information from the complex quantity defined by the ratio ρ of the p-polarized reflectivity amplitude, r_p , and the s-polarized reflectivity amplitude, r_s :

$$\rho = \frac{r_p}{r_s} = \tan \Psi e^{i\Delta}$$

leading to (Δ, Ψ) contours. Each contour corresponds to a fixed set of optical constants, at a fixed wavelength. Along those contours, the film thickness varies. This is discussed in reference (68) where several examples are shown. The measured values of Ψ and Δ depend on the refractive index, its uniformity across the film, the thickness of the film, the refractive index of the substrate, and the roughness of both the film/substrate interface layer and the surface of the film. A model containing all these parameters is made to fit the experimental data. On the basis of published values of the refractive index versus PZT composition (35, 69) as well as on the basis of our own measurements (Chapter 8), we calculated (Δ, Ψ) contours for a number of PZT compositions on STO substrates using a linear extrapolation between the refractive index and the x ratio with $n_{PT} = (2.66, 0.0)$ and $n_{PZ} = (2.46, 0.0)$ at $\lambda=633$ nm. The near-zero value for the imaginary part of the refractive index (also called the extinction coefficient) corresponds to the optical transparency of PT and PZ to red light. Such

contours are shown in Figure 3-1 as a function of thickness for several PZT compositions. For the compositions shown in Figure 3-1(a), the curves are “degenerate”: the path is the same for different thicknesses. If an interface layer or a surface roughness layer is introduced, the curves become “non-degenerate”: the (Δ, Ψ) contours can split or shift considerably and the path is different for different thicknesses. This is shown in Figure 3-1(b) using the same interface with $n_{\text{interface}} = (2.45, 0.0)$ and $n_{\text{surface}} = (1.80, 0.0)$ representing approximately respectively 50% STO - 50% PZT ($x = 0.5$) and 50% PZT ($x = 0.5$) - 50% air, using $n_{\text{STO}} = (2.39, 0.0)$ at $\lambda = 633 \text{ nm}$ as given in (70). The non-degeneracy introduces extra difficulty to determine the exact refractive index of the layer; especially for the compositions shown in Figure 3-1(b) where the curves are very close to each other. One measurement is often not enough to obtain unambiguous information.

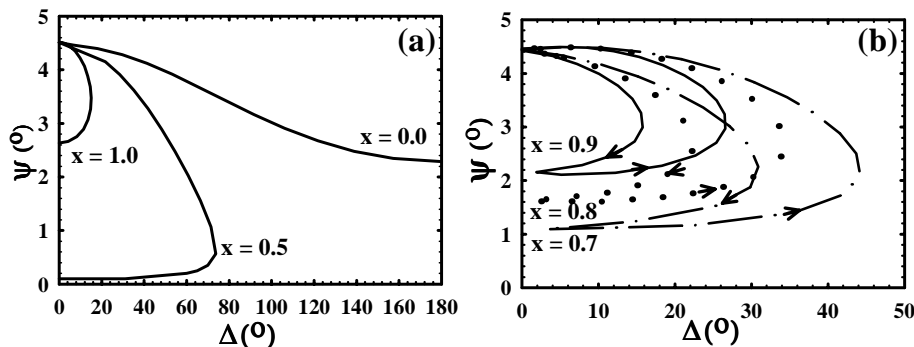


Figure 3-1: Calculated ellipsometry (Δ, Ψ) contours as a function of thickness at $\lambda = 633 \text{ nm}$ at $\varphi = 70^\circ$ for several $x = [\text{Zr}]/[\text{Zr}+\text{Ti}]$ ratios. The curves bounce back and forth every circa 60 nm, with the arrows indicating the increasing thickness direction on the contours. (a) For $x = 1.0, 0.5, 0.0$ with no interface nor surface roughness using 2.46, 2.56, and 2.66 as the respective values of the real part of the refractive index for these three compositions. (b) For $x = 0.9, 0.8, 0.7$ with 1 nm interface layer and 1 nm surface roughness. The respective values of the real part of the refractive index are 2.48, 2.50, and 2.52. The same values 2.45 and 1.80 of the refractive index were used respectively for the interface and the surface layers for the three compositions.

The determination of the refractive index based on a (Δ, Ψ) value therefore requires knowledge about other parameters. Other techniques, some of them described in this chapter, were used in parallel with ellipsometry to confirm the models used. Generally the surface roughness layer was measured by AFM, and the thickness was measured by various means. For the polycrystalline films, the thickness could be evaluated using the color card reference (Section 3.1.1) or measured by SEM cross-section (71). For the hetero-epitaxial films the thickness was measured by XRD reflectivity (Section 3.1.4), TEM cross-sections or by reflectivity (Section 3.1.3).

The interface layer between the substrate and the film leads to problems especially for the polycrystalline films. These layers always contain a substrate-film interface layer due to the Pt substrate modifications (Chapter 4) and the PZT growth. The morphology of the polycrystalline films is also more pronounced and leads to a higher surface roughness layer. These two roughnesses introduce too much uncertainty and only a rough refractive index determination (therefore a composition determination) was possible. For the ellipsometry measurements we have always made use of the fact that the growth conditions across the susceptor diameter during a MOCVD growth run are not radially homogeneous (see Section 2 and Chapter 5) and gathered extra information by measuring at different spots (having different thicknesses) on the wafers.

For the growth on STO, several samples were placed simultaneously on the susceptor in the same growth run, so we were able to measure samples of different thickness and composition. The interface layer thickness, in these types of samples, was smaller (a few nm) and the surface roughness also smaller than films grown on platinized silicon. The optical properties of PZ to PT were studied using hetero-epitaxial grown films on STO as described in Chapter 8.

Ellipsometry measurements were performed with a Gaertner L117C ellipsometer using a HeNe laser at 633 nm. The measurements of the ellipsometric angles Δ and Ψ were carried out at room temperature at 70° angle of incidence. A home-built system (similar to a Rotating Analyzer Ellipsometer (RAE)) was used for the wavelength-dependent ellipsometry measurements. Typical resolution for an ellipsometry measurement on an ideal specular reflecting and homogenous sample are $\Psi \pm 0.005^\circ$ and $\Delta \pm 0.05^\circ$. The absorption coefficient (k) was assumed to be zero. In all calculations the film anisotropy was neglected. Earlier studies reported the birefringence of PT films grown on MgO ($\sim 5 \times 10^{-3}$) and of PT crystals ($\sim 9 \times 10^{-3}$) (53).

Ellipsometry could be used to determine accurately the thickness of the films but also the refractive index of the films. From the refractive index, the PZT composition can be estimated as shown in Chapter 7.

3.1.3 Optical reflectivity

This technique was used to measure the refractive index dispersion of hetero-epitaxial PZT films thicker than 300 nm. The thick films were more easily measured by reflectivity than ellipsometry due to the smaller sensitivity to surface roughness for reflectivity. The reflectivity was measured as a function of wavelength from 300 nm to 800 nm. The measurements were performed using a Xenon lamp at 150 W with s-polarized light on the wavelength dependent ellipsometer described in Section 3.1.2. The resolution is estimated to be $\Delta\lambda \approx 1\text{nm}$. The obtained interference fringes were indexed by plotting N (fringe number) as a function of $1/\lambda$ through the origin and calibrating the refractive index at 633 nm using the ellipsometry measurement on the Gaertner. The dispersion of the refractive index could then be extracted. The reflectivity measurements

on these films lead to refractive index as function of the wavelength but also of the bandgap (E_g) of the films (Chapter 8). The bandgap (E_g) of STO is about 3.2 eV (70) and is lower than that of PZT ceramics (69), therefore direct bandgap determination of our PZT films by transmission measurements was not possible and the reflectivity measurements, on the thick films, were performed to measure the bandgap of the films. We estimated the bandgap as the photon energy at which, with increasing photon energy, the interference fringes disappeared (showing that the film was no longer transparent). For a film with a thickness of 700 nm, this occurs at an absorption coefficient of about 30000 cm^{-1} . At this high level of optical absorption, impurities are unlikely to have an appreciable influence, so that this procedure for estimating the bandgap is reasonable.

3.1.4 X-ray diffraction

Two X-ray diffractometers were used for the analysis of the films.

3.1.4.1 Powder diffractometer Philips PW1820

The first one, a Philips PW1820 powder diffractometer using a Cu target ($\lambda = 1.54060 \text{ \AA}$) dedicated to powder diffraction ($\theta - 2\theta$ scans) was used for routine phase control of the layers². Such a set-up ($\theta - 2\theta$ scans) used on thin films is sensitive to all the planes, satisfying Bragg's law (72), parallel to the substrate. The $\theta - 2\theta$ set-up is useful both for the polycrystalline and hetero-epitaxial layers to check the phases present in the layers. If a growth run goes wrong other oxides than PZT can be grown. The powder diffraction spectra of the PZT compounds are known from the literature (73, 74, 75, 76) but were also measured on powders³ in the same X-ray diffractometer as the one used for the layers. In Figure 3-2, the spectra of the powders are displayed showing the typical spectra of PZT used as reference. As seen for PZT ($x = 0.53$) both signals for rhombohedral and tetragonal are observed. For the layers, the position of the substrate peaks, Pt(111) and Si(004), were taken as reference to calibrate the 2θ axis. If other peaks were detected, they were indexed, using the ICSD database, by finding out to which different oxides they could correspond.

² René de Gelder and Jan Smits (Crystallography) are acknowledged for letting me use their X-ray diffractometer.

³ Ning Duan is acknowledged for kindly preparing the PZT powder pellets used as references.

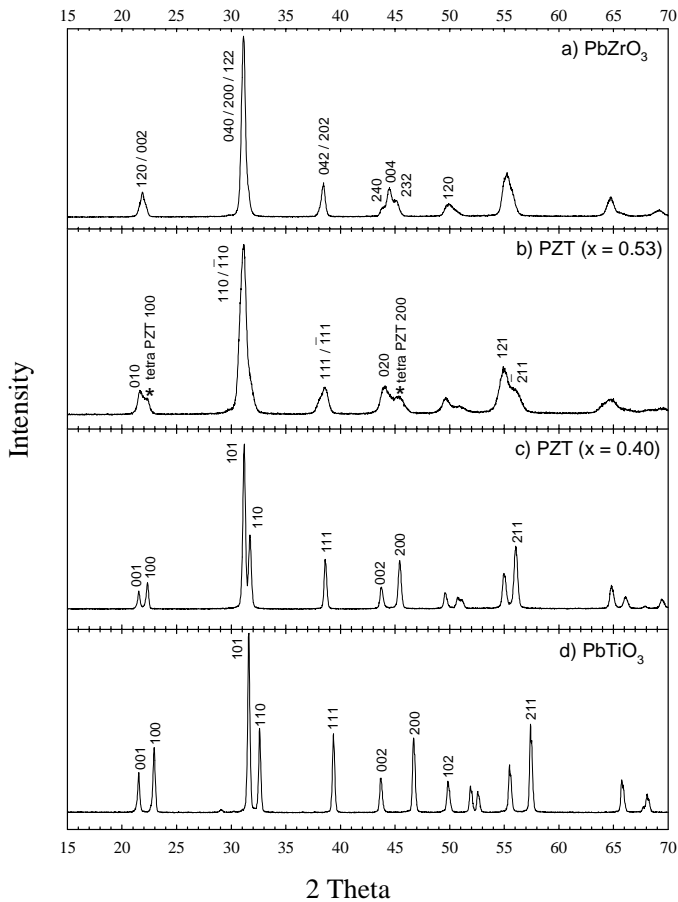


Figure 3-2: Powder diffraction spectra of PZT powders. a) PZ powder, b) PZT ($x = 0.53$) powder, c) PZT ($x = 0.40$) powder, and d) PT powder.

3.1.4.2 Bruker D8 discovery X-ray diffractometer

Rocking Curves

The second instrument used was a Bruker D8 discovery X-ray diffractometer using a Cu target ($\lambda=1.54060 \text{ \AA}$) and a 4-bounce monochromator Ge (022). This instrument allows the use of different configurations with the same system. It could be used for more flexible powder diffraction measurements; such as for example radial scans across the wafers. But this instrument was mainly used for rocking curves for the study of the hetero-epitaxial layers. Rocking curves (ω -scans) are different from powder diffraction

scans and provide extra information on epitaxial layers. These layers are textured as well as ordered in the plane of the substrate. For rocking curve measurements, the peak position of the substrate is known and verified. According to the offset found for the substrate and the theoretical peak position of the layer the software calculates the peak position of the layer. This procedure can be used for symmetric peaks (from planes parallel to the substrate, therefore the ones seen with $\theta - 2\theta$ scans) and for asymmetric peaks (planes not parallel to the substrates or off-specular reflections). It is also why the incidence angle is named omega (ω) and not theta (θ) anymore as:

$$\omega = \theta \quad \text{for symmetric peaks}$$

$$\omega_{\pm} = \theta \pm \tau \quad \text{for asymmetric peaks}$$

where τ corresponds to the lattice plane inclination and θ to the Bragg's angle. If both symmetric and asymmetric peaks can be found at the positions calculated by the software it means that there is an epitaxial relation between the substrate and the layer. As shown in Chapter 6, this relation is not straightforward for PZT layers, as PT and PZ layers form different crystallographic domains. The symmetric (002) and asymmetric (-103) peaks from STO were used for reference to calculate the offset due to sample mounting. In addition to epitaxiality information, accurate d-spacings can be measured with rocking curves using the Bond method (77), where rocking curves are performed at two opposite incidence angles to eliminate instrumental errors. The measurements were performed using one detector measuring the reflections at both standard incidence angle ω_1 and ω_2 where $\omega_2=180^\circ - \omega_1$. Chi-omega mapping was also performed. The mapping is based on a rocking curve repeated for different chi angles (the tilt angle of the holder). These measurements were used for the study of PT and tetragonal PZT having domains (of crystallographic orientation) which surface is not exactly in plane. Bragg's law is only fulfilled if the sample is a bit tilted and the peak can eventually be seen in the mapping.

It was possible to use the same diffractometer to measure the layer thickness by X-ray reflectivity, up to 200 - 300 nm. The geometry in reflection is different than in diffraction as X-ray reflectivity is a grazing incidence technique. A special knife-edge collimator is mounted at the top of the sample and no monochromator is used. The X-ray reflectivity data are fitted using the available software (78) as shown in Figure 3-3. The model is similar to the ones used for ellipsometry. The thickness, surface roughness, and film density can be extracted. The AFM-measured surface rms was also used in the model for the top-roughness.

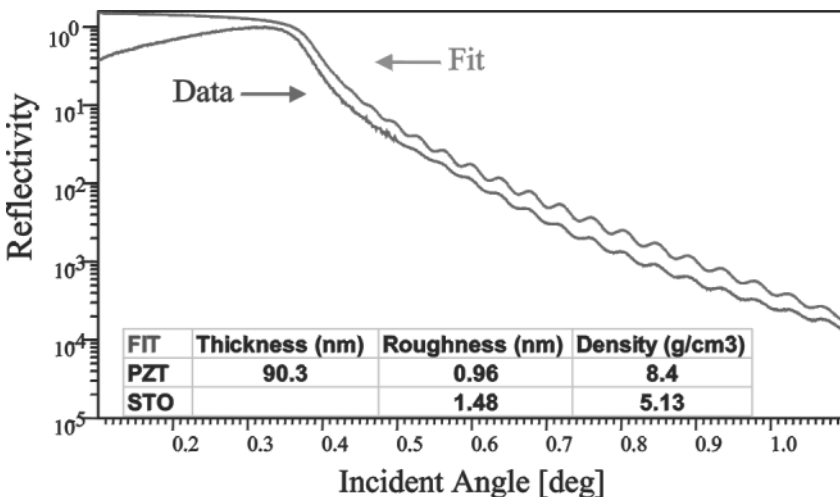


Figure 3-3: Example of X-ray reflectivity data with the fit to extract the thickness of a thin MOCVD PZT ($x = 0.4$) on STO. The data and fit curves are separated for clarity.

Only the thin hetero-epitaxial layers could be measured by this technique. The polycrystalline layers were too rough and did not show any fringes and the thick hetero-epitaxial films with thickness > 300 nm were too absorbing for these measurements.

3.1.5 Raman

A Renishaw 1000 Micro-Raman spectrometer with a laser at wavelength $\lambda = 514.8$ nm and 50 mW power was used to investigate the samples⁴. For all the spectra presented in the thesis, the measurements were performed at room temperature, a $\times 50$ magnification was used resulting in a spot size of $\sim 2 - 3 \mu\text{m}$ diameter. The acquisition times were typically 60 or 120 sec and the instrument resolution was 0.75 cm^{-1} . The Raman scattering signal of the PZT compounds has a relatively low intensity and some substrates are more favorable than others in thin film investigations. Platinized silicon substrates are ideal for these studies as the optically absorbing platinum prevents the laser beam from probing the silicon substrate, which is a strong Raman scatterer; additionally, the metal itself is a very weak Raman scatterer. On the other hand, the STO crystals have a very strong signal with large bands. The initial idea was to use Raman to detect eventual additional phases in the films and to determine the composition of the grown PZT layers. Therefore, similarly as for the XRD, the spectra of the powders were recorded for different compositions, as shown in Figure 3-4. As can be seen in Figure 3-4, the spectra are clearly modified from one composition to another but the peaks become rather broad towards the Zr-rich side of the PZT composition, rendering phase identification difficult.

⁴ Thanks to Yvan Buijnsters (Molecular and Laser Physics Department) for showing me how to use the Renishaw Raman instrument.

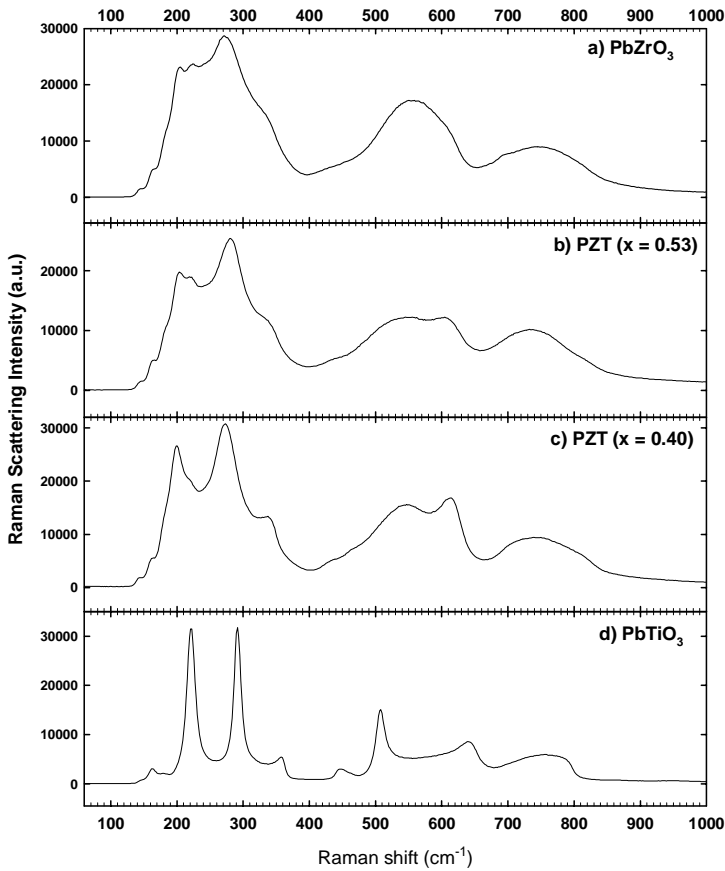


Figure 3-4: Raman spectra measured on PZT loose powders. a) PZ powder, b) PZT ($x = 0.53$) powder, c) PZT ($x = 0.40$) powder, and d) PT powder.

The PT Raman spectrum is known and has already been reported (79). The PT peaks observed in Figure 3-4 are listed in Table 3-1 and compared to single crystal and thin film PT data. The terminology used in the assignment refers to normal mode analysis, based on the space group and Raman selection rule analysis. LO and TO refer to longitudinal and transverse optical modes.

Raman is often used as a characterization technique and spectra are regularly reported for specific compositions, but few reports were found on PZT composition studies. Meng et al. (80) reported on Raman analysis of a composition series of nanocrystalline PZT powders. To ease the comparison of their spectra and the measured spectra on the loose powders, their results, containing data on additional compositions, are shown in Figure 3-5.

Table 3-1: Characteristic PT Raman bands (at RT) observed in the powders and compared with literature.

Bands observed in the PT loose powders	Bands reported in crystals (81)	Band assignment (79, 81)	Bands reported in sputtered PT film on MgO (82)
--	87.5	E(1TO)	80
--	128	A(1LO)	--
160	148.5	A ₁ (1TO)	147
--	194	A ₁ (1LO)	--
220	218.5	E(2TO)	212
290	289	B ₁ +E	288
360	359.5	A ₁ (2TO)	340
445	440.5	E(2LO)	--
--	465	A ₁ (2LO)	442
508	505	E(3TO)	503
640	647	A ₁ (3TO)	621
--	687	E(3LO)	~728
~750-790	795	A ₁ (3LO)	--

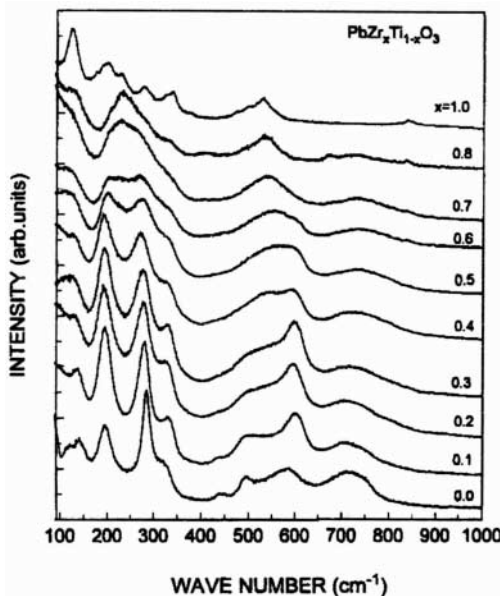


Figure 3-5: Raman spectra for PZT nanocrystalline powders (of size ~ 60 nm) as measured and published by Meng et al. (80).

Though there can be a shift for the peak positions between bulk and nanocrystalline powders, as for the A₁(3TO) peak in the nanocrystalline PT powder shifted down to ~ 580 cm⁻¹, the x ratio influences principally peak intensities. The peak intensity of

the strong peaks progressively decreases and the spectrum ends up being dominated by three broad bands for $x = 0.8$. But additional peaks become again visible in the PZ spectrum.

3.1.6 *Morphology*

3.1.6.1 Scanning electron microscopy

The grains and features of the polycrystalline films had an average diameter of 200 nm and were best observed with a SEM with a field emission source. With such an instrument it is possible to work with lower accelerating voltages than with a conventional thermo-ionic source as field emission sources permit higher image resolution, increases signal to noise ratio, and depth of field. The standard operating conditions were 3kV as accelerating voltage and 8 mm as working distance. Generally, coating the sample with a thin conductive layer would improve the image as it prevents the buildup of surface charge. But the as-grown surface of both polycrystalline and hetero-epitaxial films were properly seen without coatings. The SEM was therefore a non-destructive technique. The SEM used for these experiments was a Jeol JSM 6330F field emission microscope.

3.1.6.2 Atomic Force Microscopy

Most of the features from the hetero-epitaxial films could not be seen by SEM and AFM had to be used. Additional information such as surface roughness (rms) or feature height can be extracted from the AFM pictures. The measurements were performed with an AFM Dimension from Digital Instruments in contact mode. The sample stage allowed the study of 6" wafers, useful for the platinized substrates study (Chapter 4), with a scan range of 100 by 100 μm .

3.1.7 *Composition*

One of the principal parameters, which can be varied in a PZT growth run, is the x ratio. This ratio is controlled in the gas phase, but it does not necessarily correspond to the ratio in the thin film. Additionally, the A ratio should be 1 for the perovskite structure. Several techniques, depending on the layers and the instruments available to us, were used in this study to measure the A and x composition ratios of the layers. To be able to make growth tests or series, it is preferable to have relatively rapid feedback on the layer quality to modify / adjust reactor parameters.

3.1.7.1 Routine check

In the first years of the project, ICP-AES was used to estimate the film composition of polycrystalline growth tests (83). It is destructive and requires the preparation of identical size pieces of the wafer. The layer is completely etched away and the resulting solution is analyzed and provides the concentration of each element in the solution. Both A and x could be measured with an experimental error of ± 0.05 or ± 0.1 (determined by measurement repetition). Such a technique was only suitable for the large polycrystalline wafers where sufficient material was available for destructive characterization.

The most used technique, ellipsometry, was used to obtain an estimate of x in the layer using the value of the refractive index of the layer (Section 3.1.2 and Chapter 8). The experimental accuracy of these measurements was $x \pm 0.2$ and $x \pm 0.1$ for the polycrystalline and hetero-epitaxial layers respectively. This technique is very convenient as it is non-destructive and allows a rapid mapping of the wafers.

3.1.7.2 XRF

The composition of all thick hetero-epitaxial layers and specific polycrystalline layers was estimated by XRF. These measurements were performed at Philips in Eindhoven in a Rh-2400 XRF spectrometer with a spot size from 5 mm and the analysis software FPM⁵. With XRF, an X-ray beam is used to irradiate the sample, and the emitted fluorescent X-rays specific to the chosen elements are analyzed. XRF is wavelength dispersive and not energy dispersive. Energy dispersive spectroscopy, EDS, intensity as a function of energy, takes into account all the X-ray emitted by the sample and can scan the entire X-ray spectrum. It is convenient to detect unknown contamination quickly. Wavelength dispersive spectroscopy, WDS, intensity as a function of 2θ , is based on Bragg's law for X-ray. With WDS each element is measured separately. This technique is more practical to measure elements in small quantities or elements with overlapping energy. The relative error on the XRF measurements was estimated to be 0.5%.

3.1.7.3 EDS

Depth profiles of the elemental composition were measured on the cross-sections of the layers in the TEM analysis using a LINK local probe mounted on the TEM microscopes. An error up to 10% can be made on the atomic % determination.

Surface composition of films could also be measured in a SEM equipped with an EDS⁶. On an irregular basis, a Jeol JSM –6310 with an EDS (Voyager II from Noran

⁵ Harrie Jaspers (Philips Eindhoven) is acknowledged for making the XRF measurements.

⁶ Late Han Smits (Microbiology) is acknowledged for making the SEM / EDS system available and Bert Otter (Twente University) for his advices with EDS measurements.

Instruments) was used to compare compositions from specific crystals or zones from the same layer. The initially grown layers were relatively thin (50 to 200 nm) and were not ideal for EDS analysis. A compromise has to be found between the thickness of the layers, the elements to be detected, and the accelerating voltage to be certain to probe the appropriate volume. The minimum accelerating voltage is 7 kV to be able to detect Ti in the PZT layer. The penetration depth in PZT at this voltage is rather high and a 350 nm thick layer is necessary to avoid probing the substrate, as shown in Figure 3-6. If the substrate is also in the probed volumes, it creates problems as the substrates used for the polycrystalline growth contains Ti (Chapter 4) and can eventually lead to incorrectly high Ti values in the layer. Moreover the Pt and Zr lines in the energy spectrum are very close to each other and this leads to analysis problems. The technique was not absolutely quantitative as trend in measurements across the surface of one layer are much more reliable than comparison of composition from different layers.

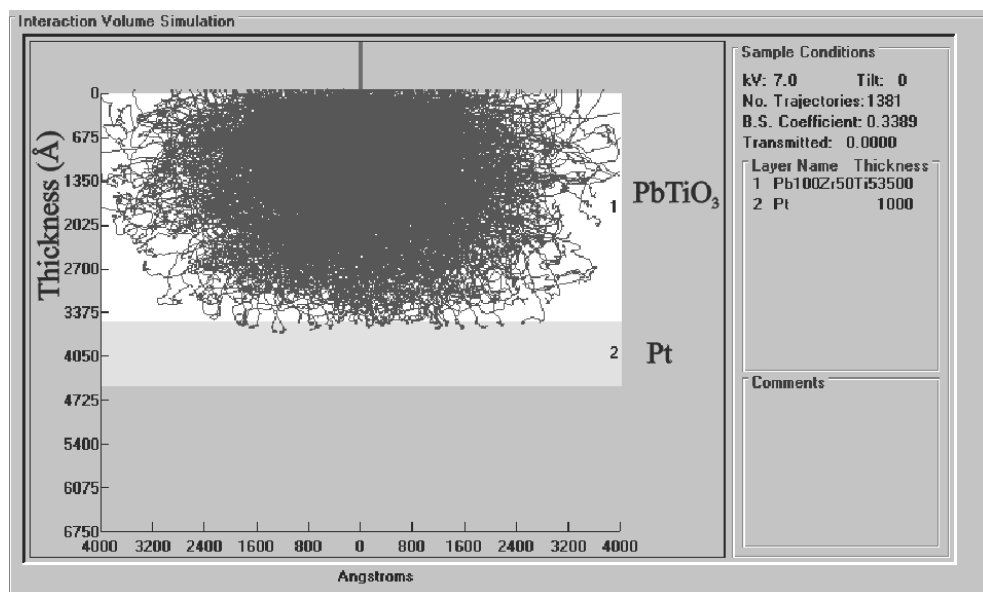


Figure 3-6: Simulation of the interaction volume for a 350 nm thick PZT layer with an accelerating voltage of 7 kV using Electron Flight Simulator⁷.

3.1.8 Transmission Electron Microscopy

The study of the Pt substrates and the thick hetero-epitaxial PZT films on STO were completed by cross-section studies performed by TEM. The samples were sent to the National Center for HREM at the Technical University of Delft. A CM30T and

⁷ Kees Kwakernaak (Delft University) is acknowledged for letting me use their program Electron Flight Simulator.

CM30UT Philips transmission electron microscopes (300kV) were used for imaging. The cross-sections of the layers were prepared according to the following sequence:

- Gluing glass on the film side of the material
 - Cutting a cross-section with a thickness of 0.5 - 1 mm with a diamond saw.
 - Mechanical grinding and polishing the cross-section to a thickness of ~10 µm.
 - Putting a piece of the cross-section on a Cu slot grid.
 - Thinning to electron transparency by a Gatan PIPS 691 ion mill, using Ar.
- Different types of images can be taken and their corresponding abbreviations are defined in the glossary.

3.1.9 Ferroelectrics?

The characterization techniques described above are general to thin film characterization and not specific to ferroelectric films. The work described in this thesis does not investigate the ferroelectric properties of the grown layers but is principally focused on the growth and investigation of the structure and morphology of the layers. In parallel to this work, electrical characterization of polycrystalline layers grown on platinized silicon wafers revealed that the layers were of standard quality: remanent polarizations of 35 - 40 µC/cm² were obtained for 50 000 µm² capacitors, as shown in Figure 1-3 showing three typical hysteresis curves from the MOCVD PZT films. But it was difficult to grow a layer on a 6" diameter wafer with these characteristics all across the wafer radius (Chapters 2 and 5). The hetero-epitaxial layers were not investigated by electrical characterization but by EFM⁸. EFM is an AFM with additional features. In addition to the standard morphology studies, extra information can be extracted by applying, with a conductive tip, an electric field between the tip and the sample. Applying an oscillating voltage to the tip and detecting the signal related to the subsequent electrostatic interaction between the tip and the sample, it is possible to simultaneously visualize the topography and the surface potential map of the sample surface (84). The photo displayed on page viii, is an example of such writing (with one type of voltage), in contact mode on a MOCVD PZ hetero-epitaxial film on STO. If an alternating positive and negative voltage is used, black and white stripes can be produced. No quantitative information was obtained yet but standard oxide surfaces, such as STO or Al₂O₃ do not display these features.

⁸ These measurements were performed by Maria DeSanto.

Chapter 4

Damage after Annealing and Aging at Room Temperature of the Platinized Silicon Substrates⁹

⁹ The work presented in this chapter is based on "Damage after Annealing and Aging at Room Temperature of Platinized Silicon Substrates" by M.P. Moret, M.A.C. Devillers, F.D. Tichelaar, E. Aret, P.R. Hageman, and P.K. Larsen, accepted in *Thin Solid Films*.

4 DAMAGE AFTER ANNEALING AND AGING AT ROOM TEMPERATURE OF THE PLATINIZED SILICON SUBSTRATES¹⁰

Platinum films to be used as a substrate and as a bottom electrode for the growth of ferroelectric materials should be able to withstand the temperature specific to the deposition method of the ferroelectric layer without being degraded. Annealing of platinized Si wafers in nitrogen and nitrogen : oxygen ambient conditions were performed in a similar fashion as prior to metalorganic chemical vapor deposition of ferroelectric thin films. The consequent induced modifications of the initial morphology, composition, and structure of the Pt wafers were studied respectively by AFM, TEM, XPS, and XRD. The observations were related to the optical properties of the annealed Pt wafer by creating a model fitting the ellipsometry data. Using this technique, the roughening at room temperature of a platinized wafer was monitored for 15 months starting shortly after the wafer was processed. These results indicate that the Pt wafers are also aging at room temperature.

4.1 Introduction

Ferroelectric thin films can be used in three main types of application: memories, microelectromechanical systems, and integrated-optics (Section 1.4). These applications are based on the dielectric, piezoelectric, and electro-optic properties of the materials. In order to measure and exploit these effects the ferroelectric is sandwiched in between two electrodes and the resulting capacitor forms the basic building block for active and passive ferroelectric devices. The electrode on which the thin film is deposited is called the Bottom Electrode (BE). Numerous studies are found in the literature on the choice of adequate bottom electrodes for the growth of ferroelectrics, as they need to remain stable under all the processing conditions of the thin films. Hetero-epitaxial growth is performed on crystals such as STO, SrRuO₃, and sapphire, whereas multi-layer substrates are used for polycrystalline growth.

Platinum is one of the favorite candidates and is widely used in the ferroelectric thin film community as it is chemically stable against oxidation, it has a high workfunction (5.65 eV) and a low resistivity (circa 18 $\mu\Omega\text{cm}$ at RT for our Pt films (5)) (85, 86). Early efforts to use Pt electrodes directly deposited on Si wafers were not successful (85) as Pt peeled off from the Si and lead silicate formation was reported after the PZT growth. Therefore the Si wafers are oxidized prior to electrode deposition to prevent silicate formation and Ti is used as an adhesion layer in between the SiO₂ and the Pt, as shown in Figure 4-1.

¹⁰ Han Gardeniers (Twente University) is acknowledged for sharing his previous results on Pt wafers and spending time reviewing them with me.

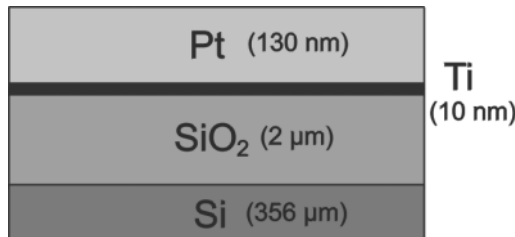


Figure 4-1: Schematic of platinized silicon wafers. The indicated layer thicknesses correspond to those used in this study.

One of the major problems with this type of Pt film as bottom electrode is its modification during the processing steps of thin film growth (85, 86, 87). Numerous studies are reported on Pt electrodes for ferroelectric applications, but the properties and transformation of the platinum are dependent on the properties of the starting Pt layer, which nature is defined by its deposition conditions. Several effects are expected upon annealing of platinized Si wafers as summarized in (85, 86) and the mechanisms must be known to understand the consequence on the growth of the ferroelectrics as well as to correctly characterize the system substrate-layer. Several mechanisms occurring in the BE are found to influence the growth of the ferroelectrics. Kim et al. (88) reported on the importance of the Pt thickness and roughness on respectively the texture and the perovskite formation of the MOCVD grown PZT. On the other hand, Afanas'ev et al. (89) reported that the Pt surface roughness hampered the perovskite phase formation. Several researchers found that Ti or TiO₂ at the surface of the Pt was beneficial to enhance the formation of perovskite (e.g. 90, 91). The transformation of the BE, as well as the formation of an interfacial layer between the Pt substrate and PZT influences the electrical (92) and other standard characterizations such as, in our case, ellipsometry (93, 94). The changes in the Pt layer are also referred as damage here and include alterations in structure and morphology and the formation of an interfacial layer between the Pt electrode and the ferroelectric layer. The modifications of the Pt film are also of interest for other applications, such as for highly reflective x-ray mirrors (95), platinum catalysts (96), high temperature metallizations for microelectromechanical devices (97), and/or protective coatings (98). For platinum used in catalyst systems, platinum – titanium interaction is studied in the context of degradations of catalytic systems due to encapsulation of the Pt layer. Sun et al. and Spencer et al. (96, 99) report negligible encapsulation of Pt evaporated on TiO₂ substrate but significant encapsulation on reduced TiO₂ and Ti.

This article makes an effort to detail the modifications observed in our sputtered platinum BE used as a substrate for MOCVD growth of PZT. As this growth technique imposes a pre-heat treatment of the substrate to reach the growth temperature, the effects of annealing on the Pt wafers were investigated. The effect of aging at room temperature and of the storing conditions on annealing were also studied. Surface morphology, cross-sections, diffusion processes in the layer stack, and structural properties are presented for the annealed layers. By developing an

appropriate roughness model, the different observations from the annealed layers are related to optical properties of all the Pt wafers measured by ellipsometry. Additionally, the aging of the Pt wafers at room temperature is reported for the first time and the effects of the storing conditions prior to annealing are presented.

4.2 Results and Discussion

4.2.1 Pt wafers

The Pt wafers were prepared according to the layer sequence shown in Figure 4-1. Silicon (100) wafers, of 6" and 4" diameter were thermally oxidized for 16 hours to obtain a 2 µm thick SiO₂ layer. Circa 10 nm Ti and 130 nm Pt were sequentially sputtered at room temperature in a Nordiko 2050. The background pressure in the chamber was 4×10^{-8} Torr and the sputter conditions for Ti and Pt were 250W RF / 10 mTorr Ar and 800W DC - 70W RF bias / 20mTorr Ar respectively. No cleaning steps were included except a sputter-etch on SiO₂ and Ti prior to deposition.

As-received Pt wafers were received and stored in different conditions. Six months old as-received 6" Pt substrates, from the same batch, which had been stored in air, were cut in ¼ wafer pieces and annealed in the MOCVD reactor. This annealing is a simulation of the MOCVD heating-up prior to growth. Two different heating-up procedures were applied to these platinum wafers, one in nitrogen environment and one in nitrogen : oxygen (1 : 1) environment as shown in Table 4-1. All the annealing runs were performed in the same flow conditions. No specific heating-up ramp was programmed, simply the same warming-up as the one used for the PZT growth (Figure 2-4). The substrates were kept for 1 min at the growth temperature of our ferroelectric films and then cooled down to room temperature within 2 hours with a rate of ~ 25° C/min from 700°C to 300°C and with a rate of ~ 3°C/min from 300°C to room temperature.

Table 4-1: Annealed Pt wafers samples.

Sample	Substrate Temperature (°C)	Environment at 5mbar
0	--	--
1	500	N ₂
2	500	N ₂ : O ₂ (1:1)
3	550	N ₂
4	550	N ₂ : O ₂ (1:1)
5	600	N ₂
6	600	N ₂ : O ₂ (1:1)
7	650	N ₂
8	650	N ₂ : O ₂ (1:1)
9	700	N ₂
10	700	N ₂ : O ₂ (1:1)

4.2.2 Surface morphology

4.2.2.1 At room temperature

The surface morphology of the Pt wafers kept for different times in different ambient conditions was studied by AFM. Sample 0, the reference sample of the annealed series, is shown in Figure 4-2a. This wafer was kept for 6 months in air prior to investigation. The surface is composed of triangular shaped grains, circa 30 nm wide and the rms roughness of the wafer is 0.9 nm. Unfortunately, no Pt wafers were examined by AFM directly after reception and thus we assume that the initial Pt columns are triangular. When stored for a longer time at room temperature either in air or in nitrogen environment, the triangular shapes seen at the surface are slightly rounded off. For a Pt wafer aged in air for 16 months, shown in Figure 4-2b, the triangular grains became totally round and appeared to be smeared out with a larger diameter of circa 60 nm and a rms roughness of circa 0.8 nm. Though the morphology is modified, the rms roughness of the Pt wafers stored longer than 6 months in air or nitrogen environment is similar (0.9 ± 0.1 nm) to sample 0, as measured by AFM.

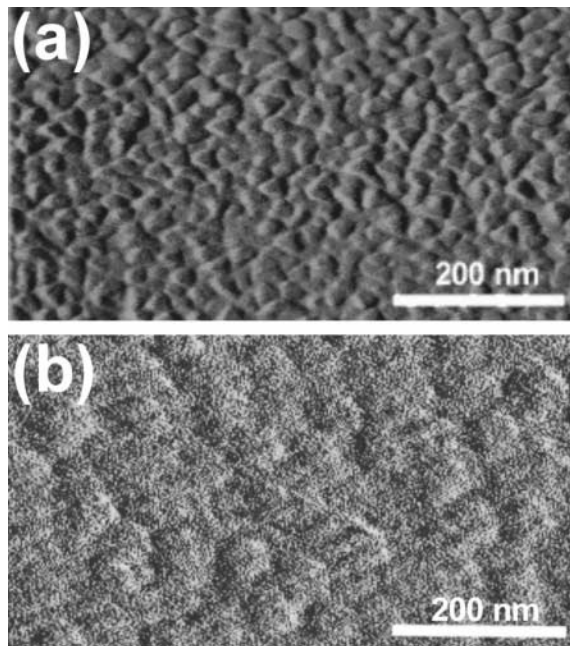


Figure 4-2: AFM deflection picture of the surface morphology of (a) the as-received Pt wafer kept in air for 6 months (sample 0) and (b) a Pt wafer kept in air for 16 months.

4.2.2.2 After annealing

The morphologies of the Pt wafers stocked for 6 months in air and annealed in N₂ and N₂ : O₂ environments at different temperatures were compared. Observed by SEM, the morphology of the oxygen-rich environment consists of small grains with different heights in contrast to the morphology of the nitrogen environment consisting of a smooth pitted surface as shown in Figure 4-3. The Pt wafer heated at 700°C in oxygen rich environment looked similar to the one heated up to 650°C in the same environment. The morphologies of the other annealed Pt wafers were too smooth to be observed by SEM.

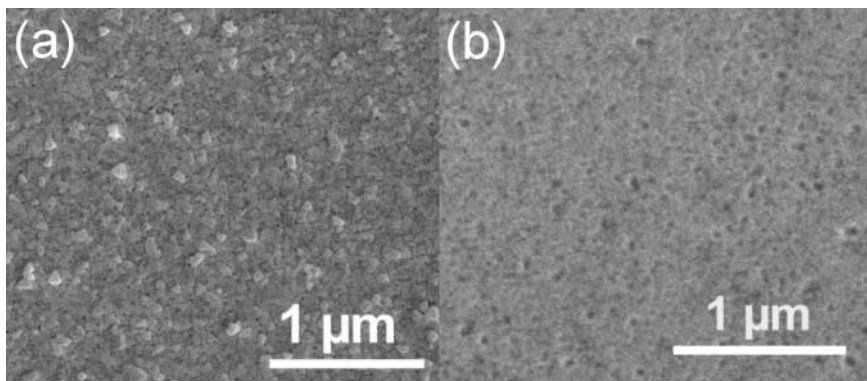


Figure 4-3: Morphologies observed by SEM for (a) a Pt wafer heated at 700°C in N₂ : O₂ (1 : 1) and (b) a Pt wafer heated at 700°C in N₂.

By AFM, it was possible to study all the wafers. The morphologies of the wafers heated at 500°C, 600°C, 650°C and 700°C are shown in Figure 4-4. The pits and hillocks observed by SEM, are confirmed by the height pictures (not shown here) corresponding to the deflection pictures shown in Figure 4-4. The initial triangular pattern on the Pt wafer (Figure 4-2a) is changed after all annealing experiments. In the N₂ environment at 500°C and 600°C, the small triangular grains disappear and smooth, larger grains of about 50 - 100 nm diameter are visible. At 650°C, small grains reappear and pits are formed. On the other hand, triangular grains do not smear out in the oxygen-rich environment but coalesce steadily into elongated polyhedral shapes ending up into rounded mounds at 700°C. Other studies reported high hillocks (about the height of the Pt film, i.e. 100 - 200 nm) protruding at the wafer surface after annealing (85), but the surface of our wafers, observed after annealing in the oxygen-rich environment, does not contain such peculiar hillocks. The initial morphology of the Pt wafers has drastically changed upon annealing in both environments, but the roughness is not modified directly at the lowest annealed temperature. As can be seen in Figure 4-4 and Figure 4-5, the roughness (rms) starts increasing respectively at 650°C and 550°C for substrates heated in N₂ and N₂ : O₂. It corresponds well to the vertical modifications such as the irregular coalescences (or grain growth) of the Pt grains observed in the N₂ : O₂ environment and to the pit formation for the N₂ annealing.

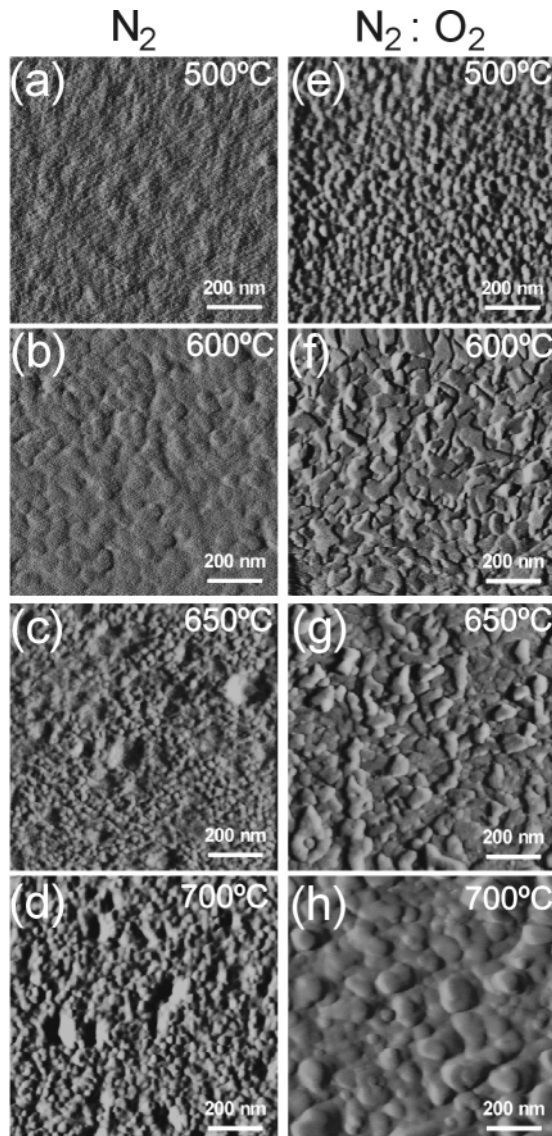


Figure 4-4: AFM deflection pictures showing the surface morphology of the annealed Pt wafers. a) wafer heated to 500°C in N_2 , b) wafer heated to 600°C in N_2 , c) wafer heated to 650°C in N_2 , d) wafer heated to 700°C in N_2 , e) wafer heated to 500°C in $\text{N}_2 : \text{O}_2$ f) wafer heated to 600°C in $\text{N}_2 : \text{O}_2$ g) wafer heated to 650°C in $\text{N}_2 : \text{O}_2$ h) wafer heated to 700°C in $\text{N}_2 : \text{O}_2$. The height pictures are not shown but none of them revealed triangular shapes as for the reference sample of this series.

Table 4-2: Morphology features observed by AFM at the surface of the annealed Pt wafers.

Sample	Grain size diameter (nm) - form - other
0	30 - triangular
1	circa 50 - 100 nm - round but grains barely not distinguishable
2	30 - round
5	50-100 - round
6	50 - 100 - elongated
7	20 - 40 - round - pits (100 nm)
8	50 - 100 - elongated
9	20 - 40 - round - pits (100 nm)
10	20-150 - round

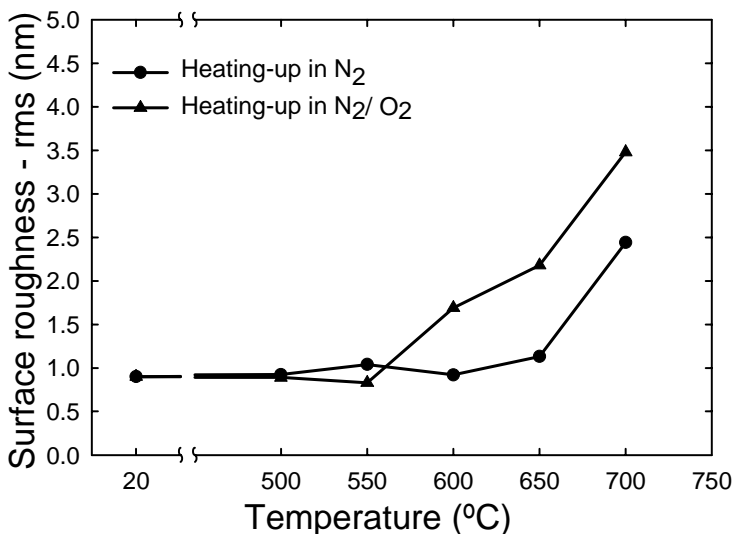


Figure 4-5: Surface roughness (rms) measured by AFM on the Pt wafers.

Identical N₂ annealing procedures have been performed on wafers stocked for longer periods in air or in N₂ prior to annealing. For wafers stocked 8 months in N₂, the morphology after a N₂ annealing at 700°C corresponds to the N₂ annealing observed in Figure 4-4d, as for Pt wafers stocked 6 months in air prior to annealing. On the other hand, for wafers kept for 10 months in air and then 10 months in N₂, the morphologies after the N₂ annealing correspond to the N₂ : O₂ annealing shown in Figure 4-4h for Pt wafers stocked 6 months in air prior to annealing. This observation indicates that a process is already initiated at room temperature in air and that oxygen

(or moisture) influences the later annealing behavior in N₂. There is an incubation time of ~ 6 - 10 months in air before that the effects are visible after annealing in N₂.

The rounding and smearing out of the grains indicate surface diffusion. This is supported by a recent study by Michely et al. (100) who observed that triangular adatom islands, covered partially by a second layer, are formed at the start of Pt deposition on Pt (111). Upon annealing at 357°C, the triangular shapes are replaced by hexagonal shapes and at 427°C the second layer disappeared indicating that diffusion by step atom detachment occurs in this temperature range. As the surface morphology of the wafers stocked for 16 months in air corresponds to the annealed Pt wafers in N₂ up to 600°C, Figure 4-2b and Figure 4-4a, it indicates that there is also surface diffusion at room temperature.

The measure of the damage observed in the morphology, increases as function (in ascendant order of importance) of time, temperature, and oxygen content in the environment. This means that the different effects observed after the N₂ : O₂ annealing are preceding, in time, the ones observed in N₂ annealing as the oxygen rich ambient conditions enhance the pace of the different mechanisms taking place. If the annealing in N₂ is performed for a longer time than 1 min similar degradations, as after the 1 min annealing in N₂ : O₂, would be observed. The N₂ : O₂ annealing environment contains 50 % oxygen and the surface of the wafer is directly exposed to oxygen. In the nitrogen ambient, there is no oxygen flow present but there is still a low partial pressure of oxygen present due to traces of impurities. Assuming that to get a monolayer of oxygen, there is one O atom necessary for each Pt atom at the Pt wafer surface, that the carrier gas contains roughly 0.05 ppm of oxygen (the moisture in the carrier gas is measured as roughly 0.05 ppm), and that the sticking coefficient is 1, the minimum time it takes in the flow conditions to supply enough molecules for a monolayer oxygen on a 6" diameter Pt wafer is circa 60 min. In the literature, a similar pit-like morphology as the one observed for the annealing in N₂ at 650°C (Figure 4-4c) has been reported in Ref. (97) for 100 nm Pt films with a 10 nm Ti adhesion layer. For annealing at 900°C from 2 to 9 hours, an initial grooving of the surface was observed, followed by the cutting of the grooves through the layer until the Pt layer became a set of Pt islands. This phenomenon was attributed mainly to Pt surface diffusion. A thicker adhesion layer, a higher annealing temperature, and an oxygen-rich environment aggravated the degradation of the Pt layers. It is well known in the literature that different annealing ambient conditions can reduce or enhance diffusion reactions and / or grain growth (101). For a 30 nm thin Pt film used as bottom electrode in cup-type structure DRAM, Tsuzumitani et al. (102) observed a Pt grain segregation similar to the grain growth observed in Figure 4-4h after N₂ - 5% O₂ annealing at 500°C. This grain segregation was not observed for Pt film annealed in Ar - 4%H₂.

4.2.3 Cross-section and diffusion

4.2.3.1 Transmission Electron Microscopy

Cross-sections of the samples 0, 1, 2, 7, 8, 9 10 from Table 4-1 were studied by TEM. The as-received Pt layer (sample 0) has a columnar structure, as shown in Figure 4-6a, with a column size of 15 - 28 nm and a peak-to-peak surface roughness of 3.0 ± 0.7 nm. Both observations agree well with the grain size of ~ 30 nm and the peak-to-peak roughness of circa 2.8 nm measured by AFM. The Ti layer is the zone with a low contrast below the Pt grains. Lattice imaging of the Ti layer showed a nanocrystalline structure and a d-spacing value of 2.54 Å, corresponding to hexagonal Ti. The (111) texture of the Pt layer was determined with selected area diffraction patterns.

The cross-sections of two differently annealed samples are shown in Figure 4-6b-c and the major changes are summarized in Table 4-3 for all the samples studied. The Pt column widths, the Pt thickness, the Pt grain boundaries, and the Ti interface layer have been modified after annealing. The Pt columns widen up to 110 nm for the annealed substrate at 700° C in N₂ : O₂ but barely increased for samples annealed in N₂. Only for the samples annealed in an oxygen-rich environment, the width of the columns corresponds to the surface grain diameters measured by AFM as can be seen in Table 4-3. The Pt grain widening in the oxygen-rich environment corresponds therefore to a grain coalescence or grain growth over the whole Pt thickness, as can be seen in Figure 4-4h and Figure 4-6c. On the other hand, for Pt films annealed in N₂, the large grain diameters observed in Figure 4-4a-b do not correspond to the column diameters observed in cross-section, confirming that the "grain smearing" is only a surface phenomenon. Additionally, the pits observed by AFM on the N₂ annealed samples were not directly observable by TEM. Similarly to the Pt column diameter widening, the thickness of the Pt layer stays constant for the N₂ annealing (~ 145 nm) but large thickness variation are observed (up to 24%) for the N₂ : O₂ annealing as can be seen in Table 4-3.

In addition to the column widening, the grain boundaries in between the columns from the Pt wafers annealed in N₂ : O₂ widen irregularly from 0.8 nm to 10 nm forming irregular pockets (see Figure 4-6c). But no grain boundary widening could be observed for the N₂ annealing. The sizes of the different features observed in cross-section are summarized in Table 4-3.

The Ti layer between the Pt and the SiO₂, which can be seen well in the non-annealed sample (Figure 4-6a) as a zone of constant thickness with a lower contrast, is clearly modified upon annealing and changes into a zone with mixed contrasts. Energy Dispersive Spectroscopy (EDS) was performed in the different contrasts of the modified Ti layer, indicated by "Ti" in Figure 4-6b-c. The results indicated the presence of O and Ti in the light area and Pt in the dark areas. Weak reflections with d-spacing values ($\pm 2\%$) of 3.54 Å, 3.08 Å, and 3.76 Å were visible in the diffraction patterns in the light areas. These d-spacing values could be from different Ti_xO_y compounds such as TiO₂ anatase (3.52 Å for (101)).

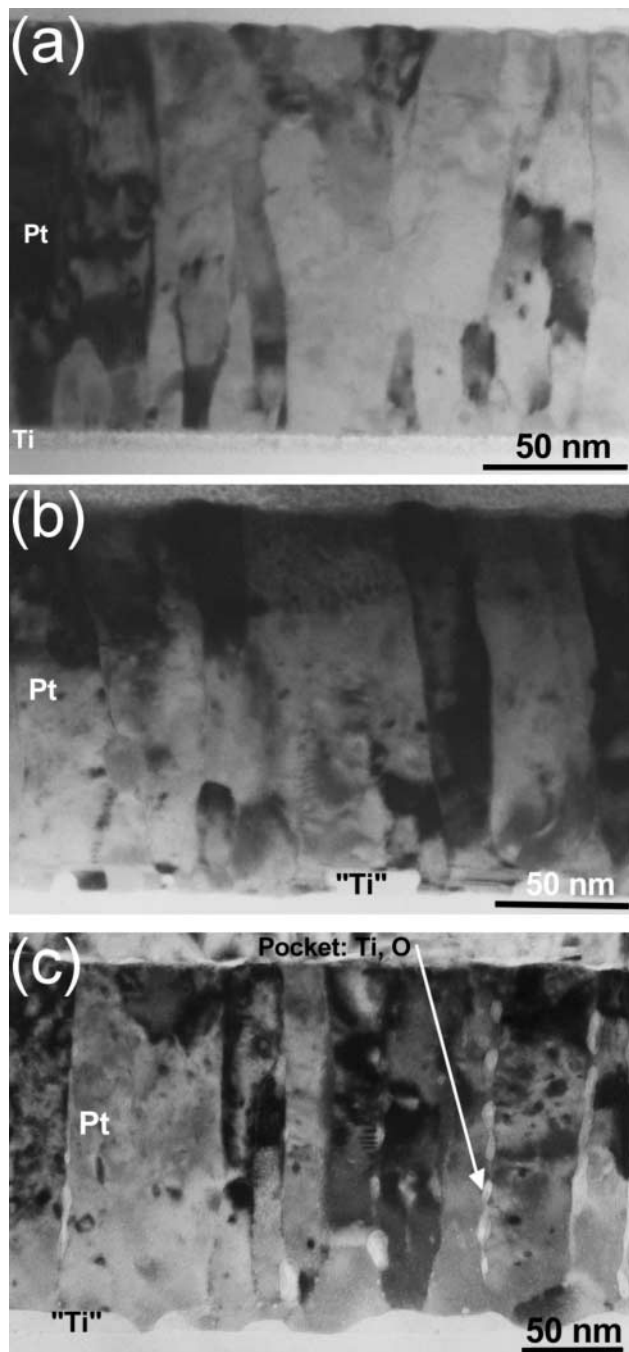


Figure 4-6: Bright field TEM cross-section images of different Pt wafers. "Ti" indicates the position of the initial Ti layer. (a) As-received Pt wafer (sample 0); (b) Pt wafer annealed at 650°C in N₂ (sample 7) ; and (c) Pt wafer annealed at 700°C in N₂ : O₂ (sample 10).

Table 4-3: Features from Pt wafers observed in TEM cross-sections pictures.

Wafer	Pt column width (nm)	- Width grain boundary (nm) - EDS in grain boundary	Pt Thickness (nm)	Ti Thickness (or Ti / Pt mix) (nm)
As rec. Sample 0	15 – 28	- 0 - no Ti	145 (± 5) regular	7.8 / regular
500 N ₂ Sample 1	20 – 35	- 0 - no Ti and O	145 (± 2) regular	locally 9 nm
500 N ₂ : O ₂ Sample 2	20 - 55	- 0.8 – 1.5 regular - Ti and O	180 (± 4) regular	13 nm (Ti _x O _y and Pt)
650 N ₂ Sample 7	20 – 35 (17 – 43)	- 0.8 - no Ti and O	142 (nm ± 2) regular (133 ± 5)	--
650 N ₂ : O ₂ Sample 8	25 - 45	- 0.8 – 10 irregular pockets - Ti and O	116 (± 2) regular	--
700 N ₂ Sample 9	30 - 40	- 0 - 0.8 - no Ti and O	149 (± 2) regular	Locally 8 nm
700 N ₂ : O ₂ Sample 10	20 - 110	- 1 – 10 irregular pockets - Ti and O	177 – 190 irregular; Pt insertion in Ti layer	10 – 13 Ti _x O _y and Pt

Observations at the interface were similar for all layers except for the Pt wafer annealed at 500°C in nitrogen, which did not contain any O at the interface. In the N₂ : O₂ annealed samples, EDS detected Ti and O in the pockets at the Pt grain boundaries but not within the Pt grains. From the Selected Area Diffraction Pattern pictures, it is found that most of the Ti - O material found in the pocket was amorphous. Some crystalline material was detected with a d-spacing value of 3.32 \pm 0.12 Å, which can correspond to several titanium oxide compounds. In the N₂ annealed samples, pockets were absent in the grain boundaries and almost no grain boundary widening was observed. Neither Ti nor O was detected by EDS at the grain boundaries or within the Pt grains of the N₂ annealed samples. In a similar way as for the interface and the grain boundaries, the top surface of the Pt grains was examined to detect possible diffusion or special features. For the Pt wafers annealed in an oxygen-rich environment, bright field and high-resolution electron micrographs suggest the presence of a locally amorphous layer a few nm's thick. However, EDS on these layers did not confirm the presence of oxides here. On some samples, the intersection Pt grain boundary - Pt surface layer is very clear, as shown in Figure 4-7 where a layer with a vague contrast can be seen at the top of the Pt grains for a Pt wafer annealed at 500°C in N₂ : O₂. In addition to the locally amorphous layer at the

top of the grains, lateral stretches of the Pt grain could be observed at the top surface of the Pt columns. This phenomenon was only weakly observed for the series of annealed wafers but is very clear in the cross-sections of the Pt wafers covered by our ferroelectric layer as shown in Figure 4-8. The effect is more important here as these last Pt wafers were held for 20 min instead of 1 min at the growth temperature. This observation agrees with the morphology studies showing a progressive effect of time and temperature. However an enhancing effect of the ferroelectric layer containing oxygen cannot be excluded.

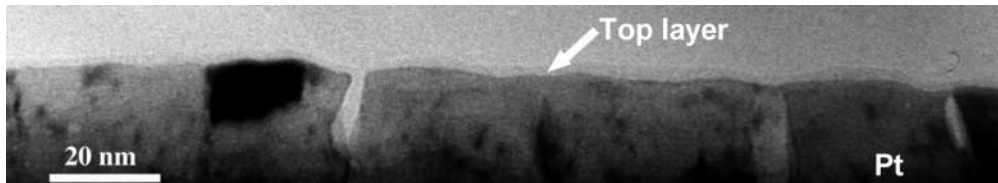


Figure 4-7: Bright field TEM cross-section micrograph near the surface of the Pt wafer annealed in $N_2 : O_2$ at 500°C. A very vague contrast layer is present near the Pt surface, with the same intensity as the Ti-O inclusion at the grain boundary near the surface.

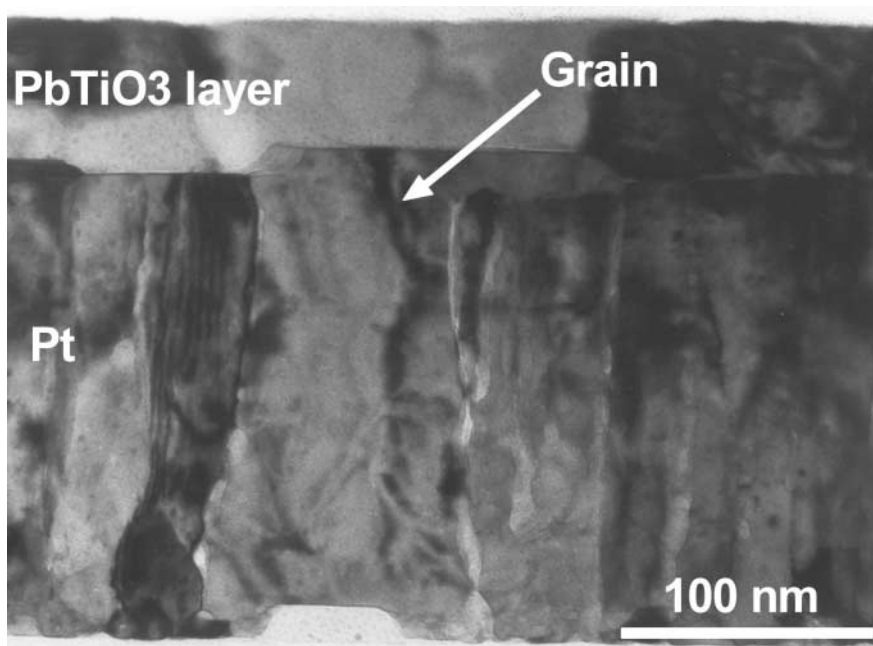


Figure 4-8: TEM cross-section from a Pt wafer with a PT layer. A surface lateral stretch is clearly visible at the top of one of the Pt column indicated by the arrow.

Combining the Ti / Pt interface and grain boundary composition observations, the morphology changes in the N₂: O₂ annealed samples can be described as follows. The Pt grain size increased in the lateral direction of the layer and at the same time grew within the Ti layer. Simultaneously, Ti diffused along the Pt grain boundaries towards the surface and O diffused along the same path from the surface towards the interface. The Ti, which reached the Pt top-surface, did not form a fully oxidized top layer in the studied samples.

The possible presence of Si in the different areas of the Pt cross-section was examined with EDS. Due to the background Si signal caused by stray electrons hitting the Si / SiO₂ substrate and also due to the overlap of the Pt and Si line in the spectrum, absolute Si contents could not be determined. However, relative measurements on different positions gave the following indications. Measurements, performed with a 15 nm spot on all the analyzed Pt wafers, consistently indicate a larger amount of Si in pockets of the former Ti layer and in the dark contrast zones (extended Pt grains) in the former Ti layer. The Si signal seemed to be stronger in the Pt grains and in the pockets between the Pt grains indicating the presence of Si. Since a solid solution of Si in Pt can only contain at maximum 1.4 at% Si at 830°C (103), a second phase, like Pt₃Si is expected when the Si content in Pt is higher. No such phase could be observed in the diffraction and bright field analyses and no Si-rich contrasting to Si-poor zones could be observed in the Pt grains. Therefore, the Si content in the Pt grains is expected to be lower than 1.4 at%.

4.2.3.2 X-ray Photoelectron Spectroscopy

Pt wafers 0, 2, 3, 4, 9, 10 were studied analyzing the Si(2s), Pt(4f7/2), O(1s), and Ti(2p) peaks in the XPS depth profiles. The measured energies were compared to the binding energies tabulated in a database (104) to identify the nature of the chemical bonding of the different elements detected. In Figure 4-9a, the depth profile of the non-annealed Pt wafer (sample 0) is shown and in Figure 4-9b that of the Pt wafer annealed at 700°C in N₂ (sample 9). The depth profiles of all annealed samples looked similar to Figure 4-9b for both annealing environments and no difference in the atomic concentration was detected, indicating that Ti diffused from the interface to the Pt surface for all the samples except in the as-received Pt wafers. In the TEM analysis, Ti diffusion through the Pt grain boundaries was only detected after the N₂ : O₂ annealing but is clearly visible for both ambient conditions by XPS.

A Ti atomic concentration up to 5 at% was present in the Pt layer of all the annealed samples. Though atomic concentrations were similar for both annealing ambient conditions, the measured binding energies were different. The Ti(2p) measured at 455 eV, at the interface of the as-received wafer, corresponds to the Ti(2p) peak from Ti tabulated as 453.2 - 454.3 eV. For the N₂ annealing, the Ti(2p) at the interface is only shifted to higher energies after annealing at 700°C. On the other hand, for the N₂ : O₂ annealing, the Ti(2p), at the interface and at the surface, is clearly shifted progressively to higher energies up to 459 - 460 eV as shown in Table 4-4. The Ti(2p) peak shifted

to higher energies, 459 - 460 eV, corresponds well to the Ti(2p) peak from TiO_2 tabulated as 458.3 - 459.2 eV. The shifting effect observed here cannot be due to charging effect as the shift was not observed systematically for all elements at the same depth and the shift was different for all elements. The oxygen peak intensity has a maximum at the same depth at the interface in the profiles as the Ti peak intensity. Additionally the binding energy of the O(1s) peak at 530 eV corresponds also to O(1s) as in TiO_2 . Both Ti(2p) and O(1s) peak indicate that TiO_2 is formed at the interface. This is clear for the $\text{N}_2 : \text{O}_2$ annealing at all temperatures but only above 550°C in the N_2 environment. In agreement with the TEM results, the oxidation of Ti(2p) is very clear for the wafers annealed in oxygen-rich environment but not in the nitrogen environment.

Both Si and O could be detected at the surface of all samples. The origin of the Si at the surface is not clear but might eventually come from contamination after the sputter process or from the XPS measurements. No Si was consistently detected in the bulk Pt layer in agreement with the EDS results indicating a low Si content in this zone, expected to be lower than 1.4 at%. The Si(2s) peak position in the bulk SiO_2 was around 155 eV, in good agreement with Si tabulated values for SiO_2 . At the Pt surface the peak position was 152 - 153 eV, which may correspond to Si/SiO_x compounds. At the interface, the Si(2s) peak is shifted to higher values 156 - 157 eV but is not positioned at the depth corresponding to the maximal Ti intensity. Similarly to Si(2s), the Pt(4f_{7/2}) peak is shifted from 70 - 72 eV (at the Pt surface and within the Pt layer) to 73 - 74 eV at the interface, indicating the possible formation of Pt_xSi_y compounds. This is consistent with the EDS observation indicating the presence of Pt and Si in the former Ti layer in the annealed samples. In the literature, Pt diffusion through SiO_2 pinholes and reaction with Si have been observed by TEM on Pt (10 nm) / SiO_2 (0-2.2 nm) / Si structures in Ref. (105), but no direct reaction of Pt with the SiO_2 forming Pt_xSi_y compounds was found. In our samples, TEM and XPS indicate Pt diffusion towards the SiO_2 and eventual reaction of Pt and Si in the dark contrast zones of the former Ti layer.

Table 4-4: Binding energies (eV) of the Ti2p peak observed in the XPS depth profiles of the Pt wafers

Pt wafer	Interface	Surface
As-received	455	--
500°C - $\text{N}_2:\text{O}_2$	456 - 459 (weak)	458
550°C - N_2	456	456 (weak)
550°C - $\text{N}_2:\text{O}_2$	456 - 459	459
700°C - N_2	456 - 459 (weak)	456
700°C - $\text{N}_2:\text{O}_2$	459 - 460	459

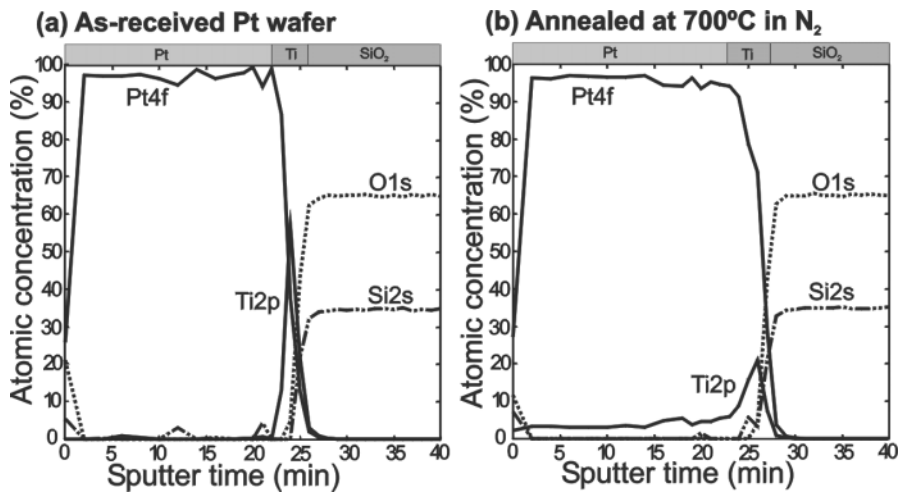


Figure 4-9: Atomic concentration depth profiles measured by XPS. (a) in the as-received sample (sample 0); and (b) in the Pt wafer annealed at 700°C in nitrogen (sample 9).

4.2.4 Structure

Pole figure measurement (Figure 4-10) confirmed the Pt (111) texture of the layers. As observed by TEM, the texture of the films did not seem to be altered by the annealing procedure, as a similar pole figure were obtained for the different Pt wafer. The θ - 2 θ XRD spectra of the films all looked similar and only displayed the Pt (111) and Si (400) peaks. The position of the Pt (111) was consistently shifted in both annealing series but the Si (400) was at the same position for all Pt wafers.

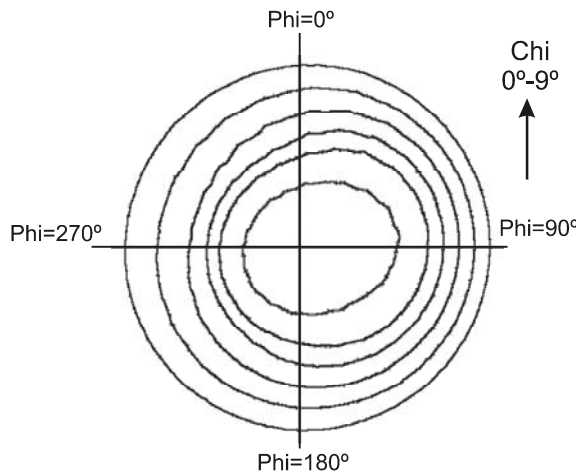


Figure 4-10: Pole figure of the as-received Pt wafer. The dark lines are intensity contour.

The Pt wafers were deposited at 800W (See section 4.2.1) leading to the largest compressive stress of -700 to -750 MPa, as measured with a stress analyzer (106). This corresponds with the value of -500 MPa found from the 2θ position of the Pt(111) peak for the as-received Pt wafer in the θ - 2θ spectrum. The stress in the film is calculated as follow:

$$d = \frac{n\lambda}{2\sin\theta}$$

using Bragg's law (72) to extract the spacing in between the plane from the XRD spectrum.

$$\varepsilon = \frac{d - d_0}{d_0}$$

where ε is the strain of the d spacing with respect to d_0 , the relaxed value. For Pt, $d_0(111)=2.2650 \text{ \AA}$ (107).

$$\sigma = -\frac{E}{2\nu} \varepsilon$$

where σ is the resulting stress in the layer, E is Young's modulus, and ν is Poisson's ratio (108, eq. 9-23). The E and ν values for Pt were respectively taken as 170 GPa and 0.39 as in Ref. (106). Upon annealing, the d -spacing of the Pt(111) decreased indicating that the stress state at room temperature of the film changed from compressive (negative) to tensile (positive) as can be seen from Figure 4-11. The trend observed for the $N_2 : O_2$ annealing corresponds well with the one reported in (106, 109) with similar Pt wafers. Spierings et al. measured the stress cycle of such wafer from RT to 700°C to RT in N_2 . They found that the linear stress behavior from compressive to tensile stress during cooling down was due to thermal stresses as the expansion coefficient of Pt is circa three times larger than that of Si. On the other hand, the stress behavior upon annealing is fluctuating and cannot be due to thermal stress only. Spierings et al. suggested that high protruding hillocks in combination with additional Pt (200) orientation in the XRD spectra could be associated to relaxation mechanisms in the films leading to stress fluctuations. Though it has been observed in other studies (85, 110), none of these phenomena have been observed in our films as mentioned earlier. This might be due to our Pt film thickness, circa twice thicker than the one in Ref. (106).

Additionally Spierings et al. found similar stress behavior for both annealing in N_2 and in $N_2 : O_2$ and we observe a different stress behavior for the two annealing ambient as shown in Figure 4-11. This suggests that different mechanisms are present or that the same mechanisms are in different stages. The stress state after annealing in N_2 reached directly circa 1.5 GPa and remains constant for all temperatures indicating small compressive stress variations upon annealing. On the other hand, our annealing in oxygen-rich environment is similar to their results with the stress state increasing with temperature. The rapid filling of the grain boundaries with Ti and O as observed by TEM might be related to the compressive stress variations in oxygen-rich environment for our Pt wafers.

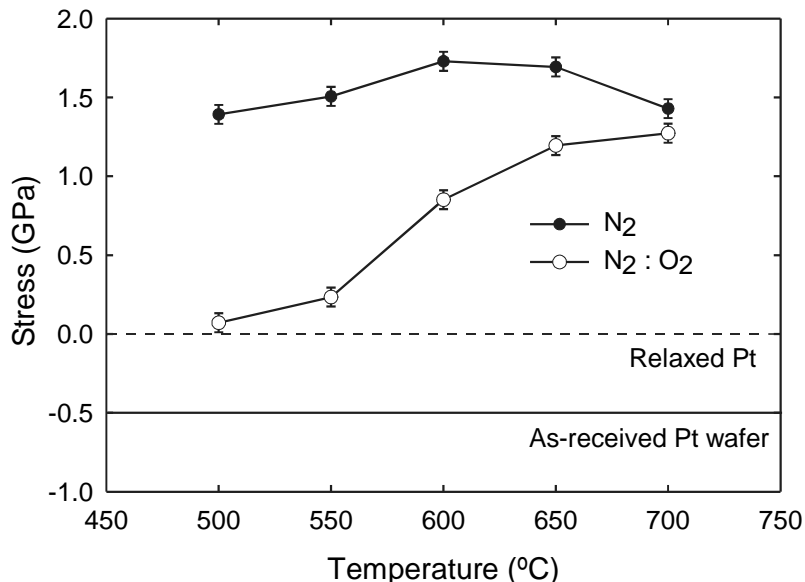


Figure 4-11: Room temperature stress of the Pt wafers as calculated from the 2θ position of the Pt(111) in the XRD θ - 2θ spectra. The error bars indicate the error in the stress for a $\pm 0.01^\circ$ error in 2θ .

In the θ - 2θ spectra, the FWHM's of the Pt (111) peaks decreased from 0.36° for the as-received wafer to $0.27^\circ \pm 0.02$ and $0.29^\circ \pm 0.03$ respectively for the N_2 annealing and for the $N_2 : O_2$ annealing. The FWHM's of the Pt (111) peaks measured in the rocking curves were modified differently as shown in Figure 4-12. The FWHM's in the θ - 2θ and the rocking curve are not sensitive to the same properties of the layer, and the values are very different for textured layers. The FWHM-rocking curve is sensitive to the columns of the textured Pt layer and the FWHM- θ - 2θ spectrum to variation for planes with a normal perpendicular to the surface. But the strain variation measured in Figure 4-11 is not reflected in the Pt (111) FWHM's in the θ - 2θ spectra. The FWHM of the as-received Pt wafer measured in the rocking curve (5.19°), circa 14 times larger than the FWHM measured in the θ - 2θ spectrum, indicates little strain in the layer with respect to the tilt distribution (111), which is consistent with the fact that the Pt layer is textured and not epitaxial. No texture differences were detected in the pole figures in between the non-annealed sample and the Pt wafer annealed at $700^\circ C$ in N_2 but Figure 4-12 indicates that the Pt columns are re-arranged upon annealing as the rocking curve FWHM's decreases from 5.1° to circa 3° . This is in agreement with previous measurements (90). The rearrangement seem to be temperature dependent and not ambient dependent as both series display the same trends.

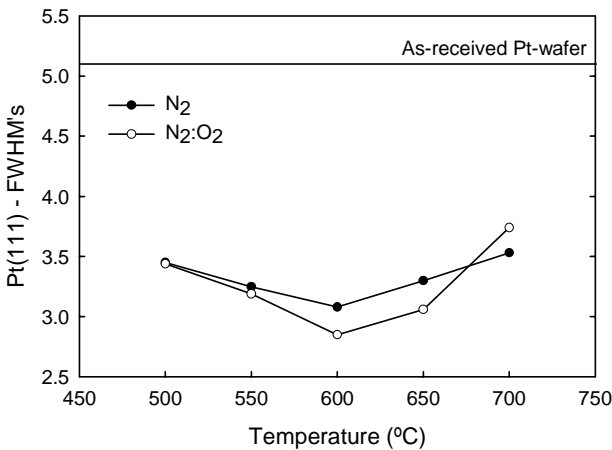


Figure 4-12: FWHM's of Pt (111) measured from the rocking curves for the different wafers.

4.2.5 Optical properties

In addition to morphology modifications, the optical properties of the Pt wafers were also affected by the warming-up procedure (Figure 4-13). The refractive index $n = (n_1, n_2)$ at $\lambda = 633$ nm of the 6-months-old-non-treated Pt wafer was measured by ellipsometry as n_{Pt} (2.12, 4.92). Upon heating in nitrogen, n_1 increased steadily with temperature up to 2.45 for 700°C. For the substrates heated up in oxygen, n_1 increased at 500 - 550°C up to 2.35 and then decreased. On the other hand n_2 remained relatively constant. The larger error bars for the higher annealing temperatures in N₂: O₂ are due to the large diffuse scattering coming from a higher surface roughness (as directly observed in Figure 4-4h).

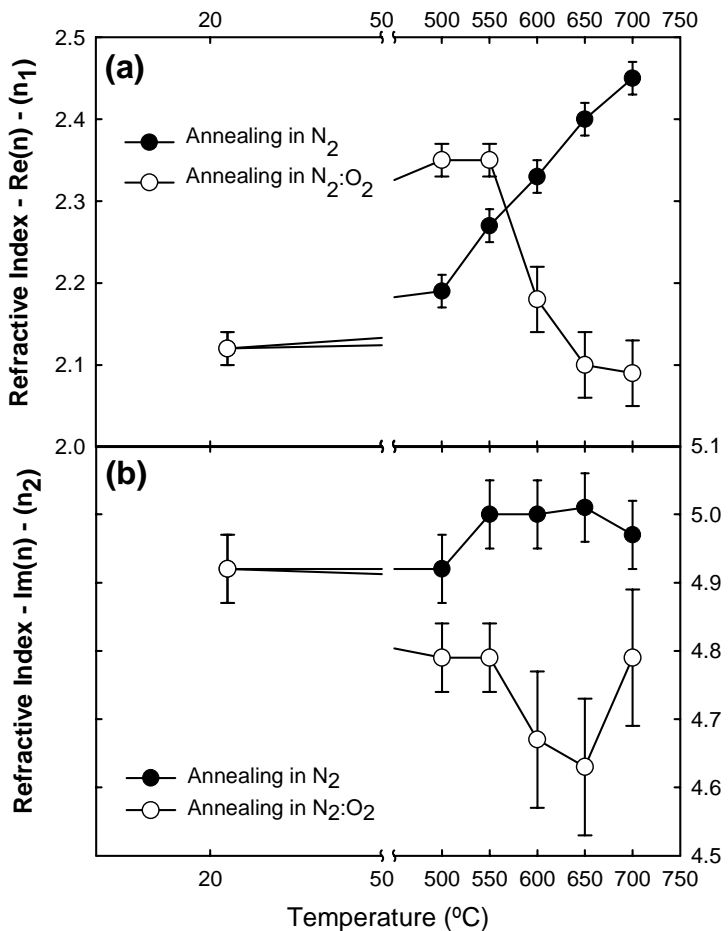


Figure 4-13: Optical properties of the annealed Pt wafers. (a) Real part of the refractive index. (b) Imaginary part of the refractive index.

Modifications upon annealing of the optical constants of different Pt layers have already been observed earlier (87) but are not easily interpreted in terms of optical constants. Therefore, we try to interpret our data as a function of the volume probed by ellipsometry. From surface morphology and cross-sections results, two main parameters will influence the ellipsometry measurements: the roughening of the Pt and the eventual appearance of Ti_xO_y as shown in the TEM cross-sections (Figure 4-6c) and the XPS analysis (Figure 4-9 and Table 4-4). The measured (Ψ , Δ) ellipsometry data are plotted in Figure 4-14, where the filled and opened circles are for the annealing respectively in N_2 and $N_2 : O_2$ and the opened triangles are for the aging studies to be discussed later.

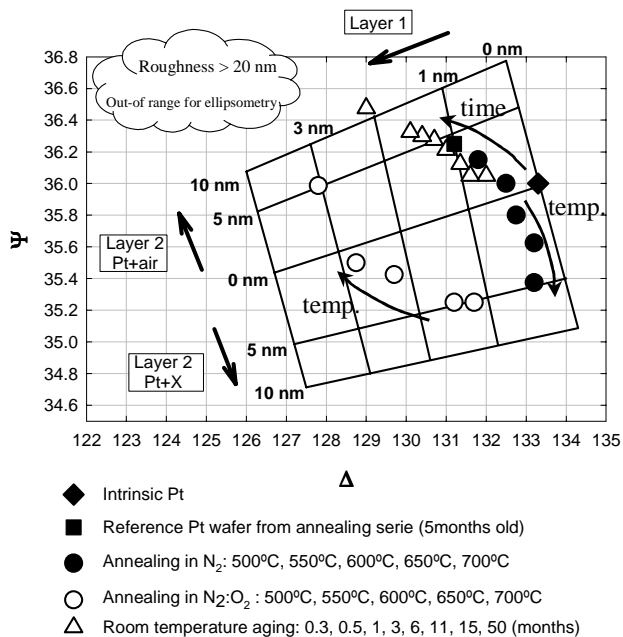


Figure 4-14: Ellipsometry data Ψ versus Δ at $\lambda = 633\text{nm}$ and $\varphi = 70.0^\circ$. The filled and opened round symbols correspond respectively to the annealed series in N_2 and $N_2 : O_2$, the square symbol to the Pt wafer non-annealed, and the triangle symbol to the Pt wafer measured as a function of time directly after reception. The diamond symbol corresponds to the value of intrinsic Pt determined from our values. The thickness of the roughness layer from the Pt wafer as well as the dominant factor (ellipsometry sensitive) can be read directly from the plot. The tilted grid corresponds to values computed from the model as shown in Figure 4-15. Straight lines have been drawn for clarity in between the points. The semi-horizontal direction corresponds to layer 1 roughness and the semi-vertical one to layer-2 roughness. The vertical direction is dependent on the composition of the layer 2.

As can be directly seen in Figure 4-14, a different trend is visible for each series. These ellipsometry data were analyzed by creating a two-layer model having a suitable refractive index fitting our data. The model is shown schematically in Figure 4-15. Layer 1 with $n_{layer1} = (1.8, 2.5)$ for the horizontal variation in Figure 4-14 and layer 2 : type 1 with $n_{type1} = (2.1, 5.0)$ for the upwards vertical variation in Figure 4-14, and layer 2 : type 2 with $n_{type2} = (2.7, 5.0)$ for the downwards vertical variation in Figure 4-14. A grid of (Ψ, Δ) ellipsometry data sets computed for Pt films with these layers as described in the model above, was drawn in Figure 4-14 using a thickness from 0 to 10 nm for each layer. The grids are superimposed to the measured (Ψ, Δ) data for our Pt wafers as shown in Figure 4-14 and the thickness and composition of each layer were read directly from the grid for each Pt wafer. Following the grid representation

of the model, in the N_2 environment, the thickness of layer 2 - type 2 steadily increases up to 5 nm with the temperature, whereas layer 1 barely increases. In the $N_2 : O_2$ environment, layer 2 - type 2 reached directly 5 nm at 500°C and as the temperature increases, layer 1 thickness increases.

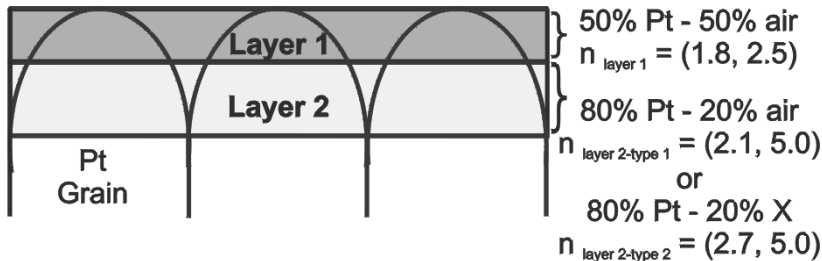


Figure 4-15: Schematic cross-section of the top surface of the Pt layer and the two layers used for the roughness model.

To define the nature of the layers used in the model, we first defined the intrinsic optical constants of our Pt layer as a dense and isotropic Pt layer with zero roughness. In Table 4-5, optical constants for Pt from different sources show that there are significant differences in reported values in the literature. The optical properties of bulk Pt or Pt films deposited in different ways might differ from each other (70, 112) but the refractive index of Pt, after the corrections (e.g. roughness) specific to each layer, should be the same. Using several of our Pt layers, we plotted their optical constants as a function of roughness and extrapolated to 0 roughness to obtain our intrinsic value of $n_{Pt} = (2.34, 5.05)$.

Layer 1 is therefore a typical roughness layer, which contains roughly 50% Pt and 50% air with $n_{layer1} = (1.8, 2.5)$. Both the real part and the imaginary part of the Pt optical constants are affected in layer 1. Layer 2 is representative of the columnar structure of the Pt film and the grain boundaries. For this layer, we have two structures: type 1 contains 80 % Pt and 20 % air with $n_{type1}=(2.1, 5.0)$ and type 2 contains 80 % Pt and 20 % X with $n_{type2}=(2.7, 5.0)$. For both types of layer 2, only the real part of the Pt optical constant is affected.

There are several possibilities for material X but only materials with a high refractive index, circa (3.8, 0.0), can explain the optical constants of layer 2 : type 2 (80% Pt + 20% X). From the diffusion analysis, we know that Ti diffuses to the top surface and that ellipsometry is sensitive to a material filling the grain boundaries. Therefore, the compound X should contain Ti. TiN was not a candidate as it has a too low (n) refractive index (113) and the two values 455.2 and 455.8 eV for the Ti binding energy as TiN (104) are lower than the extra peak observed in the XPS studies as shown in Table 4-4. Si has a high refractive index (3.85, 0.02) (70) but it was detected by XPS at the surface of all wafers, including the reference wafer. Therefore, if its presence is

real, it is not due to our annealing experiments and it is already included in our intrinsic Pt values.

Table 4-5: Optical properties from Pt at 633 nm (1.96 eV).

Sample	n_1	n_2	Reflectivity (%)
Compilation of reflectance and transmittance data (70)	2.35	4.15	67
Evaporated Pt films (112)	~2.25	~4.65	72
As received Pt-wafer measured directly after reception	2.30 ±0.05	5.0 ±0.1	74.4
"Intrinsic" value extrapolated from our data	2.34 ±0.05	5.05 ±0.1	74.5

It is difficult to find the ideal material X, which agrees with the three investigation techniques, but the most plausible material from the cross-sections analysis is a Ti_xO_y compound. The optical constants of TiO_2 films were measured as $n_{rutile} = (3.1, 0.0)$ and $n_{anatase} = (2.82-2.95, 0)$ at $\lambda = 633$ nm (114) and the optical constants of TiO_2 rutile crystals as $n_{//} = (2.87, 0.0)$ and $n_{\perp} = (2.59, 0.0)$ at $\lambda = 633$ nm (70). The optical constants of rutile are lower than values required for the ellipsometry model material X, but a Ti_xO_y compound corresponds well to both the grain boundaries evolution observed in TEM and the Ti diffusion observed by XPS. For the samples annealed in N_2 there is as a progressive diffusion and oxidation of the Ti in the Pt grain boundaries, corresponding to the progression seen in Figure 4-14. On the other hand, for the annealing in the O_2 -rich environment, the grain boundaries are filled much more rapidly with this oxidized material and annealing at higher temperatures in this ambient condition mainly increases the Pt roughening (layer 1). This roughening is in agreement with the Pt grains coalescence and the Pt layer thickness variations observed after the $N_2 : O_2$ annealing in the TEM cross-sections. Therefore we assume that X is a Ti_xO_y compound, which cannot be clearly identified with these analyses and that EDS in TEM is less sensitive to the Ti in the grain boundaries than XPS or ellipsometry as Ti was not observed by EDS for samples annealed in N_2 .

The rms roughness values measured by AFM do not coincide directly with the roughness measured by ellipsometry. AFM is sensitive to vertical changes at the surface whereas ellipsometry is sensitive to both vertical and lateral variations on a depth thickness of circa 80 nm. If layer 1 + layer 2 in the ellipsometry model is defined as the total roughness, it does not correspond to the physical thickness rms measured by AFM as shown in Table 4-6. For the annealing in nitrogen, the trend is similar but the values do not match as well as for the as-received Pt wafer. For the oxygen-rich annealing, the thickness increases and decreases, whereas the rms (AFM) steadily increases. If the rms (ellipsometry) is defined without the layer 2 - model 2, it matches better with the AFM values, especially for the annealing in $N_2 : O_2$. AFM (rms) and ellipsometry are not in disagreement but ellipsometry is sensitive to certain

dominant factors in the layer and vice versa. For example, the pits observed in the N₂ annealed Pt wafers are not “detected” by ellipsometry as they create too much diffuse scattering but AFM is very sensitive to the pits. Additionally, the ellipsometry model can help to understand additional mechanisms qualitatively (even though relative large error bars results from the model) and other ellipsometry data on Pt wafers at $\lambda = 633$ nm can be read directly from our plot.

Table 4-6: Comparison of the ellipsometry roughness for the annealed layers and the AFM roughness in terms of rms. The roughness of the ellipsometry model is read directly from Figure 4-14.

T(°C)	N ₂ environment				N ₂ :O ₂ environment			
	Layer 1	Layer 2	Total	AFM	Layer 1	Layer 2	Total	AFM
500	0.32	1.06	1.4	0.92	0.39	1.78	2.17	0.89
550	0.18	0.35	0.53	0.92	0.42	1.78	2.20	0.83
600	0.18	0.35	0.53	0.92	0.78	0.88	1.66	1.69
650	0.18	1.06	1.24	1.13	0.99	0.35	1.34	2.18
700	0.18	1.78	1.96	2.44	1.06	1.77	2.83	3.48

4.2.6 Aging and roughening

The optical constants of sample 0 (2.12; 4.92), measured by ellipsometry 6 months after reception (Figure 4-13a-b), differ from the optical constants of a Pt wafer measured directly after reception (2.30, 5.00), as listed in Table 4-5. It was therefore supposed that the wafers start aging after reception. To verify this assumption, aging and roughening studies were carried out at room temperature. A Pt wafer was monitored, directly after its reception, by measuring it regularly for 15 months. The sample was kept in air and therefore exposed to oxygen and moisture. The as-measured (Ψ , Δ) ellipsometry data, plotted in Figure 4-14 as opened triangles, show a trend different from both annealing experiments. The layer 1 and layer 2 : type 2 thicknesses increase and no layer 2 composed of X compound influences the data, indicating that the dominant mechanism in the room temperature aging is the Pt roughening. If the Ti diffusion already started along the grain boundaries, it is not yet detectable by ellipsometry.

The peak-to-peak ellipsometry roughness, defined here as (layer 1 + layer 2) is plotted versus time in Figure 4-16, for wafers kept in air. For clarity, not all these ellipsometry (Ψ , Δ) data were shown in Figure 4-14. AFM measurements on the wafer aged for 16 months (shown in Figure 4-2b) indicate an rms roughness of 0.8 nm whereas ellipsometry indicates circa 2.8 nm. Therefore a direct comparison of the AFM and ellipsometry rms is not possible for the sample aging at room temperature and roughness measurements performed only by AFM would not have detected the aging. AFM is sensitive to vertical changes at the surface whereas ellipsometry is sensitive to both lateral and vertical variations up to 80 nm below the surface.

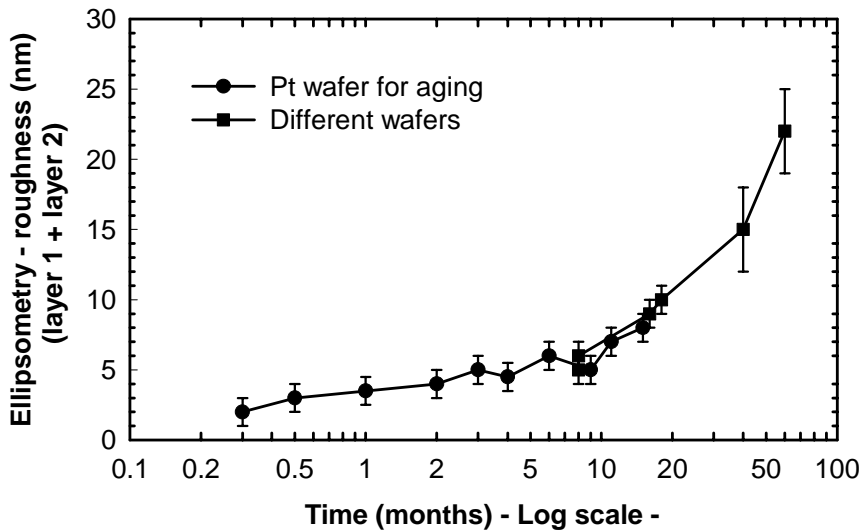


Figure 4-16: Evolution of the roughness layer (layer 1 + layer 2 as defined in Figure 4-15) estimated by ellipsometry (at $\lambda=633\text{nm}$) for a Pt wafer kept in air versus time in months on a logarithmic scale. The ellipsometry data of some points are also visible in Figure 4-14 as open triangles.

Below 10 months the roughness increases slowly and above 10 months more sharply. If it is assumed that the thickness layer 1 + layer 2 is proportional to diffusion, it might indicate that two diffusion mechanisms occur or that the intake of oxygen is only apparent after 10 months. This 10-month period corresponds well to the incubation time of 6 - 10 months in air as observed by AFM after annealing. Wafers kept longer than 6 - 10 months in air prior to annealing displayed a $\text{N}_2 : \text{O}_2$ morphology not dependant on the annealing ambient conditions. Additionally, a Pt wafer kept in air and a Pt wafer kept in a N_2 environment for the same period, do not have the same optical properties. The Pt wafer kept in an N_2 environment for 21 months has the same (Ψ , Δ) values as a Pt wafer kept for 6 to 12 months in air, therefore the mechanism responsible for the layer 1 (defined in the ellipsometry model) is enhanced by oxygen.

It would have been interesting to make a standard curve of the ellipsometry roughness evolution as a function of temperature and time to compare the time necessary for similar damage at different temperatures. Such a plot is unfortunately not possible in our case, as the roughening factors influencing the ellipsometry measurements are not easily compared, as can be directly seen from Figure 4-14. Additionally, there are no sufficient data points from the same wafer available for the plot in Figure 4-16.

4.3 Summary

The changes in the Pt wafers used as a bottom electrode and substrate for ferroelectric layers were monitored as a function of time, annealing temperature, and ambient atmosphere (N_2 or $N_2 : O_2$). In addition to the Ti diffusion along the Pt grain boundaries observed in previous studies (85, 86), and grain growth subsequent to annealing (115), these mechanisms were observed as a function of the ambient conditions and correlated using different investigation techniques. The observations, summarized in Figure 4-17, are qualitative and do not lead to a general quantitative description of the different diffusion mechanisms. It is believed that the less severe damage observed after aging, at lower temperature, or in N_2 annealing, are not qualitatively different than the most severe damage observed at $700^\circ C$ in oxygen-rich environment, but correspond to an earlier stage of the damage as time, temperature, and an oxygen-rich environment progressively enhance the damage mechanisms. In addition to the annealing conditions, the ambient stocking conditions play an important role, as illustrated schematically by the arrows in Figure 4-17. If the Pt wafers were kept longer than 6 - 10 months in air, Pt-wafer degradation was similar to that produced by $N_2 : O_2$ annealing, even if they were only annealed in N_2 . The incubation time is confirmed by the aging studies showing an increase in the ellipsometry-roughness after 10 months for Pt wafers kept in air.

The TEM and XRF cross-section observations were used to fit the optical data obtained by ellipsometry and interpret the different optical properties. Aging in time of such wafers is reported for the first time. A roughness model was developed and other Pt ellipsometry data can be directly interpreted using our grid based on this model.

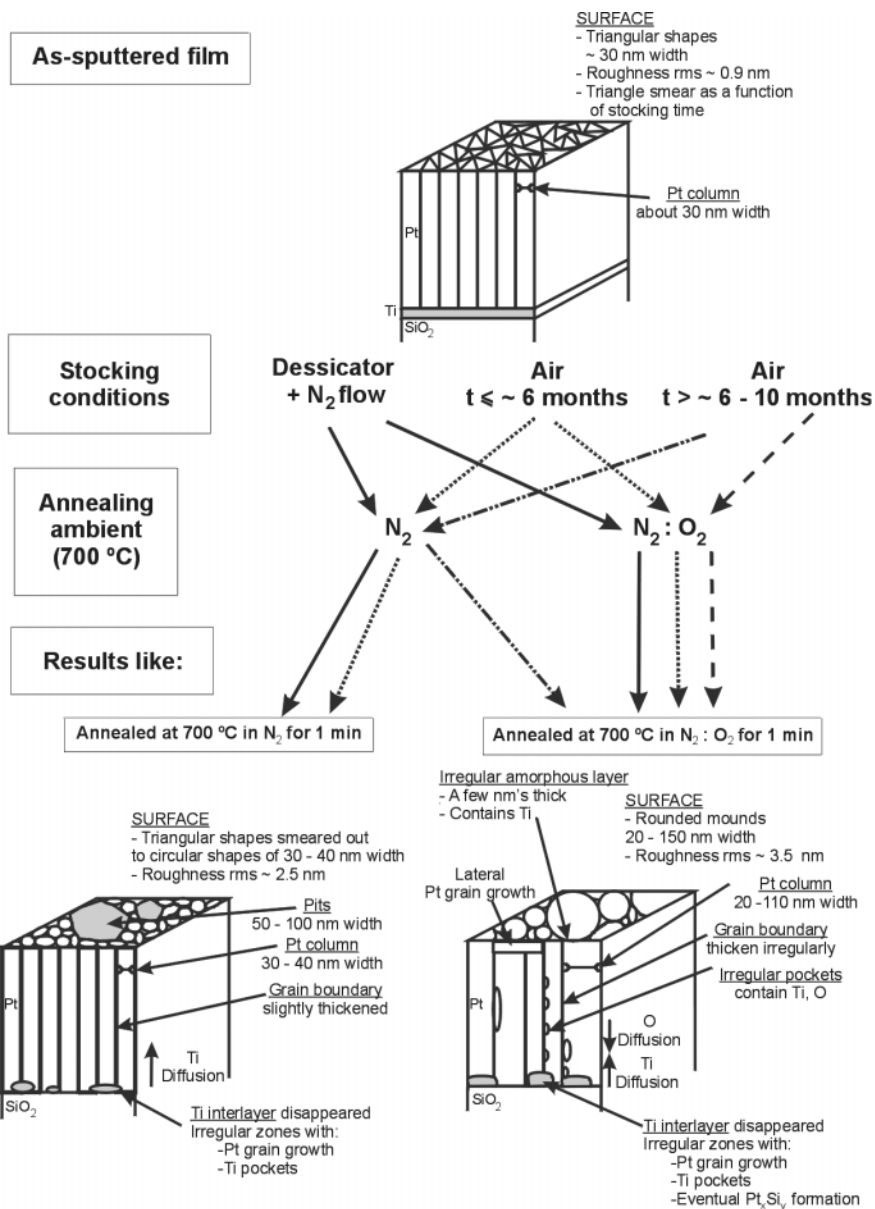


Figure 4-17: Schematic summary (not to scale) of the degradations observed on Pt wafers. The morphology - cross sections after annealing are for 700°C only.

4.4 Consequences for the MOCVD growth of PZT

Pt wafers should be used as rapidly as possible and if they are stocked, they should be stocked in a N₂ dessicator. It should also be kept in mind that a small partial pressure of O or an O₂-rich environment during stocking can lead to more severe than expected modifications of the interface Ti - Pt after annealing. The Pt layers are clearly modified upon annealing prior to the PZT deposition. The Pt wafer modifications are more severe in the N₂: O₂ environment therefore the standard warming-up procedure was always in N₂. The effects of the Pt wafers degradations subsequent to N₂ annealing on the PZT growth have not been investigated. Additionally, once the growth starts, it is not clear if the PZT can act as a barrier layer and stop the degradations. Spierings et al. (106) and Madsen et al. (116) have seen that Pt substrates were further modified even when covered with a layer. On the other hand, Fox et al. (87) concluded the opposite, noticing that PT or PZT layer will help retain the starting Pt properties. No specific studies have been performed to find out if the degradations were stopped or reduced once the Pt layers were covered by a PZT layer, but observations on our PZT / Pt system indicate that the degradations carry on during the PZT deposition. XPS analysis on a film grown for 30 min indicates that there is no more Ti left at the Pt - SiO₂ interface. Additionally, the very thick PZT layers grown for 5 hours on Pt, peeled off easily and were covered by large blisters (Figure 7-7) coming apparently from the Pt, indicating that the Pt wafers couldn't stand long annealing procedures. These Pt electrodes are therefore not useable for the long growth time at high temperature. In the literature, several studies were performed on alternative adhesion layers to replace Ti, such as Ta and TiO₂ (117), which might be more suitable. For memories applications, thinner films are required and Pt films are used on a regular basis and some of the effects in their initial stage might not be limiting.

Once the Pt surface modifications are known, it is possible to integrate them in the PZT layers analysis. PZT layers grown on Pt were regularly characterized by ellipsometry. The roughness model described above (section 4.2.5) was the same but the air in layer 1 was replaced by PZT to calculate the thickness of the interface layer. In addition to ellipsometry characterization, the BE modifications could eventually influence the electrical properties of the top electrode / PZT / BE stack. The resistivities of the annealed wafers increased steadily from 18 $\mu\Omega\cdot\text{cm}$ up to 23.5 $\mu\Omega\cdot\text{cm}$ in nitrogen and fluctuate from 18 $\mu\Omega\cdot\text{cm}$ to 23 $\mu\Omega\cdot\text{cm}$ in oxygen-rich environment (5).

Chapter 5

MOCVD Growth of Polycrystalline $\text{Pb}(\text{Zr},\text{Ti})\text{O}_3$ ¹¹

¹¹ Some parts of the work presented in this chapter are based on "MOCVD $\text{PbZr}_x\text{Ti}_{1-x}\text{O}_3$ Thin Films on Platinized Silicon Wafers and SrTiO_3 Crystals: Growth and Optical Properties", Mona P. Moret, Marijn A.C. Devillers, Andy R.A. Zauner, Edwin Aret, Paul R. Hageman, Poul K. Larsen, Integrated Ferroelectrics 36, 265-274, (2001).

5 MOCVD GROWTH OF POLYCRYSTALLINE Pb(Zr,Ti)O₃

All the layers presented in this thesis are grown above T_c, in the cubic PZT structure. For hetero-epitaxial growth, this is very important as, during growth, cube-on-cube deposition of PZT on STO takes place. During cooling-down the cubic PZT structure is deformed as temperatures below T_c are reached. Depending on the deformation of the cubic structure, which can be predicted by the PZT composition as seen in the phase diagram in Figure 1-4, domains of different crystallographic orientations will be introduced to accommodate the deformation in hetero-epitaxial films. This is also true for polycrystalline films, but as they do not have any epitaxial relations with the substrate, they can deform easily and the PE - FE/AFE transition is not crucial on their resulting structure. In this work, the domain formation in thin PT / PZT films resembles the results already presented in the literature for tetragonal (40, 118, 119, 120) and rhombohedral (121) PT / PZT and the obtained data will not be presented in this thesis. The formation of domains in hetero-epitaxial PZ films was not found in the literature and is therefore described separately in detail in Chapter 6.

There were numerous polycrystalline PZT films grown on 6" and 4" diameter wafers for this study. A typical run of 30 min, using $x_g = 0.24$, was used as a reference to test the reproducibility when some modifications were carried out on the reactor. The appearance of this layer is shown in Color Figure 4. Besides test purposes, several growth series were based on this run and three main series are presented below to observe the modifications of the layers as a function of composition and thickness. One composition series for ~ 100 nm thick films, one thickness series (from ~ 20 nm to 300 nm) for $x_f = 0.4$, and a series of thick PT, PZT ($x_f = 0.6$), and PZ layers of respectively 890, 870, and 2600 nm, are presented. The morphology and structure of these layers are shown in this section, but more specific studies are detailed in Chapter 7. The morphology and the structure of the MOCVD PZT thin films are presented and the major results and growth difficulties for this reactor are highlighted.

5.1 Thickness determination

It is difficult to measure or estimate the thickness of the polycrystalline layers, as they are inhomogeneous, usually with an increasing thickness from the center to the edge. Therefore the thickness was evaluated by several means. By weighing the wafer prior to and after each run, an average thickness could be estimated using the theoretical density (122). The color card, defined in Section 3.1.1, was also used in combination with the mass method. If an additional technique is not used, it is difficult to estimate the thickness with only the color card. Especially since the color card is shown for PT only, and since it does not take into account the extra phase problem (as for PZ) or an excessive roughness (PT). The thickness of the layers was also estimated using ellipsometry on certain layers, as many polycrystalline layers were not suitable for this technique due to a large interface and top roughness for relatively thin layers. A step,

etched using a buffered HF solution or using dry etching, was measured in different zones using a Tencor alphasteppeper. Additionally, the thickness was confirmed for a few samples by SEM cross-section.

5.2 PZT films

Three main series of polycrystalline MOCVD PZT layers are presented. One thin composition series, a series for different growth time for one composition, and thick films for three different compositions.

5.2.1 *Zr composition - thin films*

Using the growth conditions for polycrystalline films shown in Table 2-2, five films were produced by adjusting the x ratio in the gas phase from 0.00 to 1.00 with a fixed A ratio of 1.00. The thickness and growth rate of the films are shown in Table 5-1.

Table 5-1: Polycrystalline films grown for the composition series of the thin layers. The average thickness is estimated with the mass of the layer and the theoretical density of PZT powders (122). The -- symbols means that there is no data available.

x_g	x_f edge (ICP) ± 0.1	Mass (mg)	Average Thickness (nm) ± 20	Thickness (nm) Stepprofiler ± 20		Growth rate (nm/min) ± 0.7
				Edge	Center	
0.00	0.00	13.7	95	--	--	3.2
0.24	0.40	17.2	127	170	--	4.2
0.52	0.60	16.7	123	130	125	4.1
0.76	0.70	16.3	120	150	130	4.0
1.00	--	15.8	124 ($\rho=7$) 116 ($\rho=7.5$)	145	110	3.9

As can be seen in Color Figure 5 and Table 5-1, the colors displayed on these wafers correspond to first order colors, whereas both orders can be seen in the color card in Color Figure 3. This illustrates that if an additional technique is not used, it is difficult to estimate the thickness with only the color card. The $x_g = 0.24$ layer should, in principle, be identical to the one shown in Color Figure 4a, but it is clearly thicker than the reference run. There is also a slight difference in morphology, discussed in the following section.

Additionally, when the thickness of the PZ film is estimated with the mass and the theoretical density, it is larger than estimated with the color card (more blue) and the stepprofiler measurements. Therefore the density of the grown film is higher than the theoretical one, circa 7.5 g/cm³ to obtain an average thickness of ~116 nm corresponding to a PZ film thinner than the PZT. This PZ film density trend is in

agreement with our measurements on semi-epitaxial PZ layers, which have a density of $9.1 \pm 0.5 \text{ g/cm}^3$ (Section 6.3). But the thin PZ film (Table 5-1) contains a second phase, which might induce additional difficulties in color interpretation as well as for the density (note, the additional phase is a ZrO_2 phase with a relatively low density around 6 g/cm^3).

5.2.2 Thickness series for PZT films with $x_g = 0.24$

Layers grown for shorter and longer times than the 30 min reference run were studied to follow the evolution of the grains. The run with a ratio $x_g = 0.24$ was again taken as reference and the growth time varied from 1 to 120 min using the gas conditions described for polycrystalline films as shown in Table 2-2. The thickness and growth rate of the films are shown in Table 5-2. The thickness of the 120 min sample was confirmed by etching it progressively to see the second order (green layer) of the color. Additionally, TEM cross-section measurements were performed on this layer and among other information, the thickness could be obtained. There are three films of 30 min described in this series. Film N°1 is the reference run, and the two others are repeated runs on different days. The thickness, and as seen below the morphology, were not exactly reproduced in these two films.

Table 5-2: Polycrystalline films grown for the thickness series ($x_g = 0.24$). The average thickness is calculated using $\rho = 7.5 \text{ g/cm}^3$, the density of powder PZT ($x = 0.74$) (122). The -- symbols means that there is no data available.

Growth time (min)	Mass (mg)	Av. thickness (nm) ± 20	Thickness Stepprofiler		Growth rate (nm/min) ± 0.7	x_f at edge (ICP) ± 0.1
			Edge	Center		
1	3.1	23	--	--	23	--
5	3.6	26	--	--	13	--
15	9.5	70	--	--	4.7	0.36
30 N° 1 (ref run)	15.4	113	110	105	3.8	0.41
30 N° 2 (Film $x_g = 0.24$ Table 5-1)	17.2	127	170	--	4.2	0.40
30 N° 3	14.1	103	--	--	3.4	--
60	29	213	145	100	3.5	0.43
120	52.6	386	285	190	3.2	0.45

5.2.3 Thick PZT layers

Thick layers of three different compositions were produced (Table 5-3). The semi-epitaxial gas phase conditions, as described in Table 2-2, were used whereas the other runs shown in Table 5-1 and Table 5-2 were grown in the polycrystalline gas phase conditions. Thick PZT layers were grown simultaneously on STO and platinized silicon substrates. For this experiment, one by one cm Pt substrates, were cleaved out of a 6" diameter platinized wafer. But it was noticed that for the PZT layers grown on these platinized silicon substrates, the layers + Pt adhere really poorly to the silicon wafer and that features consisted of high hillocks as well as "bellies" (such as the one shown in Figure 7-7c) were observed at the surface of the layer, eventually coming from the platinum substrates.

The growth rates of both the thick and thin PT / PZT films are similar, around 3 nm/min. But for the thick PZ film, there is a clear growth rate increase. Three densities were used to estimate the PZ film thickness, the $x = 0.98$ powder density, the density used for the thin film, and the density determined for the hetero-epitaxial films in the same run (Section 6.3). If the density is the same for the polycrystalline PZ as for the hetero-epitaxial film, the average growth rate is 2.25 higher for the 300 min run than for the 30 min run. The quality of the thick PZ layer is also better, as will be shown below.

Table 5-3: List of thick polycrystalline films grown with the semi-epitaxial films. The -- symbol indicates that the data is not available.

x_g	Mass (mg)	x_f	Average thickness (nm) ± 20	Growth rate (nm/min) ± 0.7
0.00	--	0.00	870 (estimated by ellipsometry)	2.9
0.24	0.71	0.60	890	3.0
1.00	2.37	1.00	3386 ($\varrho=7$) 3160 ($\varrho=7.5$) 2633 ($\varrho=9.1$)	10.5 8.8

5.3 Morphology

An overview of the thin PZT wafers (Table 5-1) is shown in Color Figure 5 and a SEM picture of the morphology (near the edge) is shown in an inset next to each wafer. The radial inhomogeneity is relatively similar to the reference run, but the edges of the wafer with a high Zr ratio are very inhomogeneous. The PT film was very rough and had a "milky/cloudy" haze as the layer is discontinuous with $\sim 100 - 200$

nm wide grains. On the other hand, all the Zr-containing films appear smooth and shiny, as the layers are continuous with relatively regular flat grains.

The morphology of the layers is highly influenced by the Zr composition. As can be seen in the SEM photograph in Color Figure 5a, the PT film is composed of slightly faceted "round" grains, ~100 - 200 nm in diameter, separated from each other and randomly oriented. For a ratio $x_g = 0.24$, the layer is continuous (except at the middle of the wafer), and the grains, ~ 150 nm wide, tend to develop a facet parallel to the surface. For a ratio $x_g = 0.52$, the "bulky" grains are not visible anymore and very flat grains, ~ 100 - 300 nm wide, appear. Bulky grains have been totally replaced by angular platelets of ~ 250 nm width, tilted in different directions in the PZT film of $x_g = 0.76$ (Color Figure 5d). The PZ film contains clearly two morphologies: crystals of different shapes or clusters, which are embedded in a fine-grain matrix. In Color Figure 5e, different SEM photographs are shown for different zones across the PZ wafer.

Regularly, some polycrystalline MOCVD PZT film morphology is reported in the context of film study (usually electrical properties), but no complete morphology study as a function of composition has been found in the literature. Usually, the grains are relatively small and no specific facets can be distinguished. There are fewer reports for Zr-rich compositions (54, 123, Chapter 6), therefore even less morphology photographs are available. In an earlier report, Keijser et al. (40) performed a composition series on 4" diameter platinized silicon wafers using the same precursors as used in this study. A similar grain modification, from round to platelet-like grains from PT to Zr-rich PZ film can be distinguished in the reported SEM pictures. Some other microstructure / orientation reports are available. Kim et al. (124) reported on the morphology and structure of MOCVD grown PZT films on platinized silicon substrates with $x_f = 0.35$, 0.50, and 0.65. They observed the morphology and orientation variation for $x = 0.35$ as a function of temperature. From 540°C to 600°C, the morphology transforms from "round" grains to flat crystals, nicely aligned parallel to the surface. Additionally, these flat in-plane grains progressively transform to tilted platelets for an x ratio from 0.35 to 0.65, which correspond fairly well to the microstructure change observed in Color Figure 5 from $x_g = 0.52$ to $x_g = 0.76$. They indexed the flat in-plane crystals as (111) and indicated that (100) planes in the XRD patterns originate from the tilted platelets. Moreover, Kim et al. argued that the flat crystals had a triangular form, but this is not visible in the reported photographs. PZT flat triangular crystals have also been reported on MOCVD films grown on platinized silicon wafers by Fujisawa et al. (60) in PZT ($x = 0.24$ and 0.74) and by Shimizu et al. (125) on PT buffer layers. Shimizu et al. showed that the orientation of PZT layers could be controlled by using a PT buffer layer. The orientation of the buffer layer was controlled by modifying the A ratio from 0.5 to 0.6 in the gas phase, leading respectively to (111) and (001)/(100) orientation. The (111) grains were flat triangles and the (001) / (100) grains looked more round. More recently, Fujisawa et al. (60) observed the triangular islands evolution at the initial growth stage for both $x_f = 0.26$ and 0.76. Similar triangular flat PZT crystals have also occasionally been observed in

our polycrystalline PZT films, but in the 30 min Film N°3 most of the observed grains were triangular as shown in Figure 5-1. This is a repeated reference run, which displayed a similar thickness inhomogeneity, but its morphology is different from the reference run (Figure 5-2f). It might indicate that the A ratio was different from one run to another. The importance of the A - ratio on the morphology of the PZT crystal has also been observed in this study and is further developed in Section 7.1.

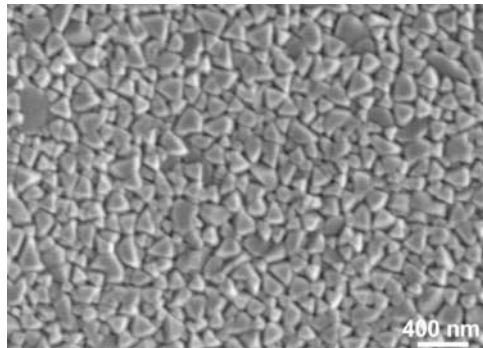


Figure 5-1: Triangular grains observed in a polycrystalline PZT layer grown on platinized silicon wafer (30 min Film N°3). This morphology was mainly observed at the center of the wafer.

No overview pictures of the wafers for the thickness series are shown but the wafers displayed similar radial inhomogeneities as the wafers previously described, especially a few mm at the wafer edges. After 1 min growth the wafer is already densely covered by small nuclei (~ 90 nm diameter at the edge), which coalesce together with increasing growth time. After 5 min, the nuclei coalescence and some bean-shaped grains are formed. After 15 min, the elongated coalesced nuclei start to form grains and after 30 min growth, the grains develop facets. After 120 min growth, clear grain shapes can be observed: hexagonal and triangular platelets (tilted or in-plane), four-fold symmetry shapes, and multi-shape bulky grains, as shown in Figure 5-2a-b.

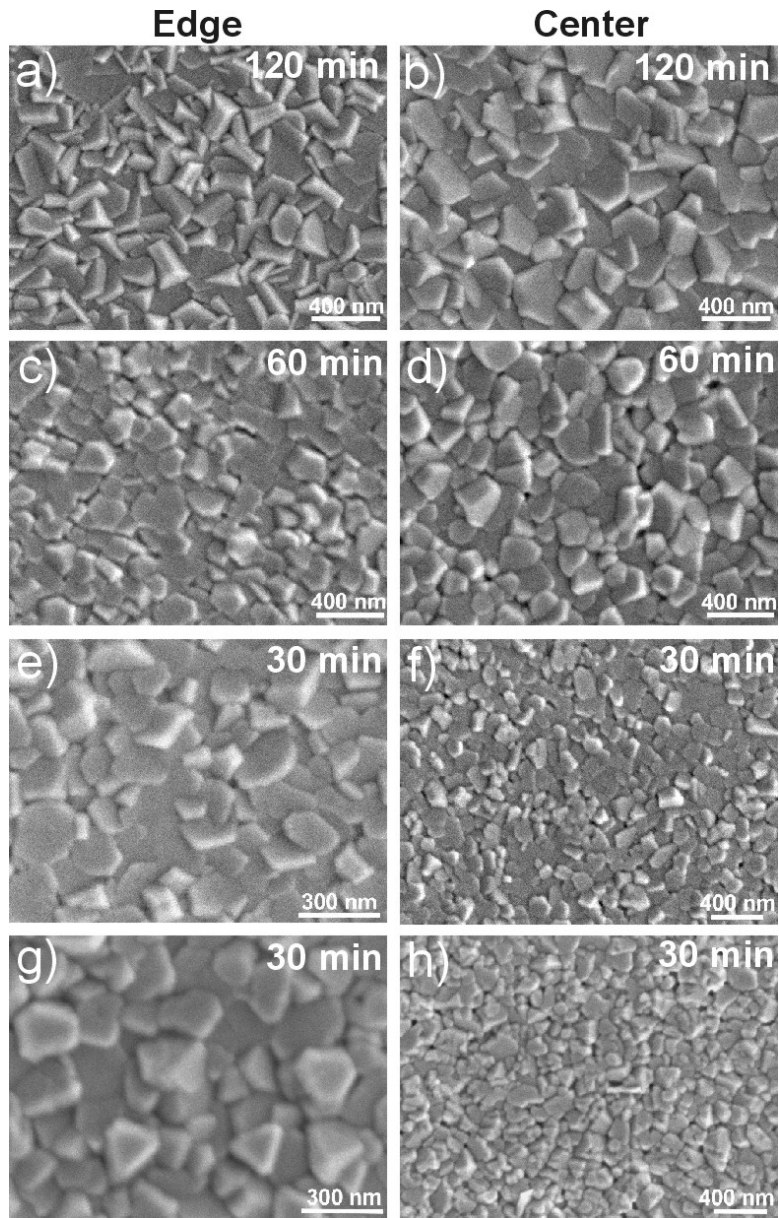


Figure 5-2: SEM photographs of the morphology from 120 to 30 min runs with $x_g = 0.24$. a) 120 min run, edge of the wafer, b) 120 min run, center of the wafer, c) 60 min run, edge of the wafer, d) 60 min, center of the wafer, e) 30 min (reference run), edge of the wafer, f) 30 min (reference run), center of the wafer, g) 30 min, edge of the wafer, and h) 30 min, center of the wafer.

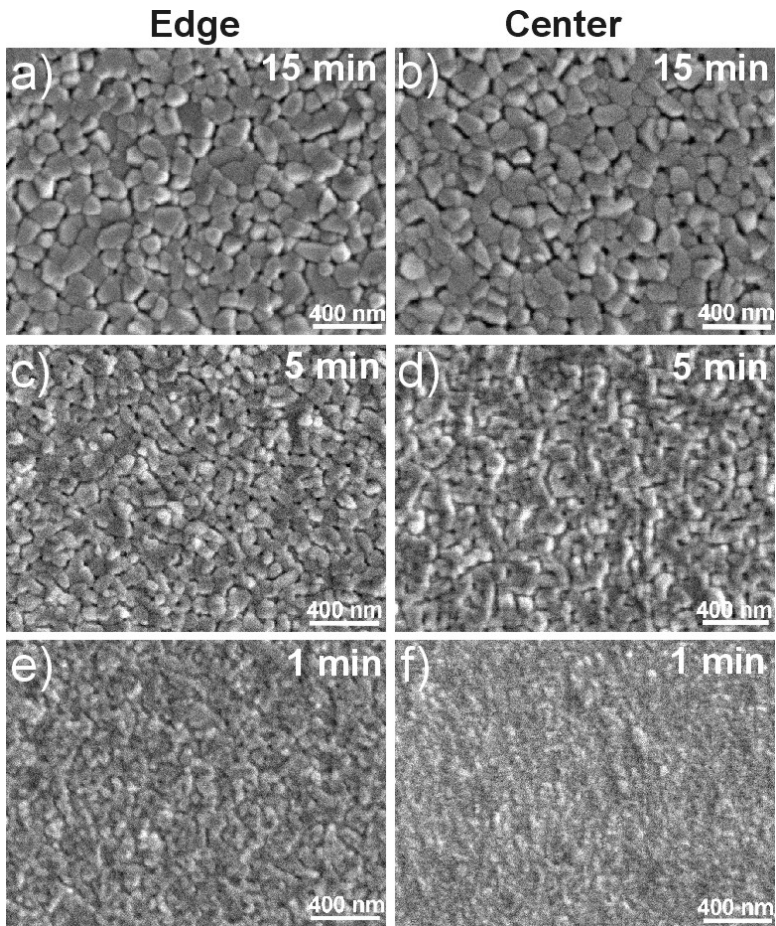


Figure 5-3: SEM photographs of the morphology from 15 to 1 min runs with $x_g = 0.24$.
a) 15 min run, edge of the wafer, b) 15 min, center of the wafer, c) 5 min, edge of the wafer, d) 5 min, center of the wafer, e) 1 min, edge of the wafer, and f) 1 min, center of the wafer.

The average size of the nuclei was measured, both at the edge and the center of the PZT layers of the thickness series, from the SEM pictures and plotted as a function of time. As can be seen in Figure 5-4, the evolution of the lateral grain growth progresses in two steps up to 120 min at both the edge and the center of the layers. The lateral grain growth, estimated from the slopes, and the transition time from one lateral growth type to the other, are summarized in Table 5-4. In the first growth stages, nuclei are formed and lateral growth takes place. The initial lateral growth at the edge, 4.2 nm/min corresponds well to the layer (vertical) growth rate estimated from the thickness for $x_g = 0.24$ for 30 min (Table 5-1). The lateral growth rate is 25% lower at the center. The composition at the edge of the layers of the thickness series is $x_f \sim 0.4$ and at the center $x_f \sim 0.2$. Therefore the lower lateral growth rate at the center, 3.2 nm/min, similar to the PT vertical growth rate of 3.2 nm (Table 5-1), is consistent with composition measurements. The morphology of the PT film in Color Figure 5a

also showed a lower nucleation density than Zr containing films. PT runs from 1 to 30 min were performed, and only after 5 min growth, the substrate is covered with nuclei as after 1 min for PZT (Figure 5-3f). Though PT and PZT grow through similar mechanisms, PT nucleates clearly less easily than PZT.

The growth rate at the center in the second stage is higher than at the edge because the grains can grow laterally for longer times without completely touching each other prior to the formation of a continuous layer due to the lower nucleation density. Both observations at the center and the edge indicate that in the initial growth stage, the growth rate is vertically and horizontally similar and is lowered horizontally as the layer becomes continuous. On all pictures, larger and smaller grains are visible corresponding to nuclei formed at different times, the larger being first.

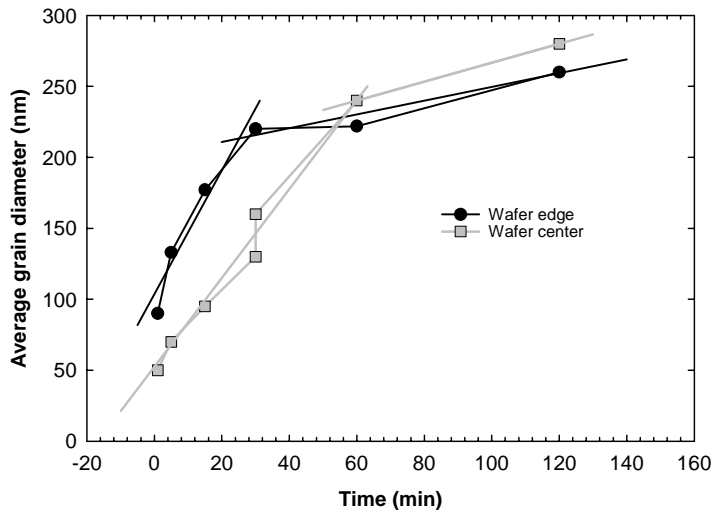


Figure 5-4: Average grain diameter versus time for the thickness series with $x_g = 0.24$ from 1 to 120 min.

Table 5-4: Lateral grain growth rates measured on the thickness series with $x_g = 0.24$ from 1 to 120 min.

	Lateral grain growth 1 (nm/min)	Lateral grain growth 2 (nm/min)	Transition time (min)
Edge	4.2	0.5	22
Center	3.2	0.7	60

The morphology of thicker films (grown for more than 120 min) has also been investigated and the principal surface aspects are shown in Figure 5-5. All the PZT

films grown for a long time on platinized silicon wafers, had a milky "haze" due to roughness, peeled off relatively easily, and contained high features ("bellies" (Figure 7-7a) or high hillocks (Figure 5-5h)). The protruding features and the poor adhesion are most likely due to the Pt damage, reinforcing the non-suitability of the platinized silicon wafers for the growth of thick PZT films at 700°C in the Ferro reactor (Chapter 4). The thick PT film, shown in Figure 5-5a, contains PT and lead oxide grains. The lead oxide phases, type and morphology, are discussed in Section 7.2. The PT crystals are flat (in-plane) multishaped crystals, 0.3 - 2 μm wide. The 300 nm thick PZT film ($x = 0.4$) in Figure 5-5b, also shown in Figure 5-2a, is composed of smaller regular platelet crystals, 300 nm wide. The thicker PZT film ($x_f = 0.6$), Figure 5-5c-e, is composed of different type crystals: flat triangular crystals in plane or tilted forming pyramids (on average 500 nm width base). In certain zones, the pyramids have an unclear base and flat top as in Figure 5-5e. Assuming that the growth behavior of PZT films ($x_f = 0.4$ and 0.6) is similar, then it is expected that the average grain size in the 300 min growth run would be 350 nm using the lateral grain growth 2 (Table 5-4). The average grain in this film and in the PT film are larger than 350 nm, indicating that the growth might not be compared, or that there might be a third growth stadium above 300 nm or that there is a different texture in the thick layers.

The PZ layer is composed of pyramids and flat triangular crystals, appearing like the edge of the pyramids tilted in plane. The growth of the pyramids in PZ films is discussed in Chapter 6 for PZ films on STO. For polycrystalline PZ films, the pyramids, also originating from (002) or (120) texture (as confirmed by XRD below) are randomly oriented in plane, in contrast to semi-epitaxial PZ films.

5.4 Structure

The structure of the films was studied both by XRD and Raman.

5.4.1 XRD

In the XRD, the substrate signal is dominated by the strong Pt (111) - α peak at $\sim 2\theta = 39.9^\circ$. All the peaks coming from the platinized silicon substrates are labeled by an asterisk. The XRD spectra presented below are typically measured at the edge of the wafers but measurements were also performed at the center. The spectra at the center, never completely similar to the edge, tend to show lower x ratio than the edge according to lattice constants evaluated from d-spacings (these observations are in agreement with the ICP measurements). The XRD spectra are all indexed with respect to their symmetry by comparing the measured d-spacings with references (73, 74, 75, and 76).

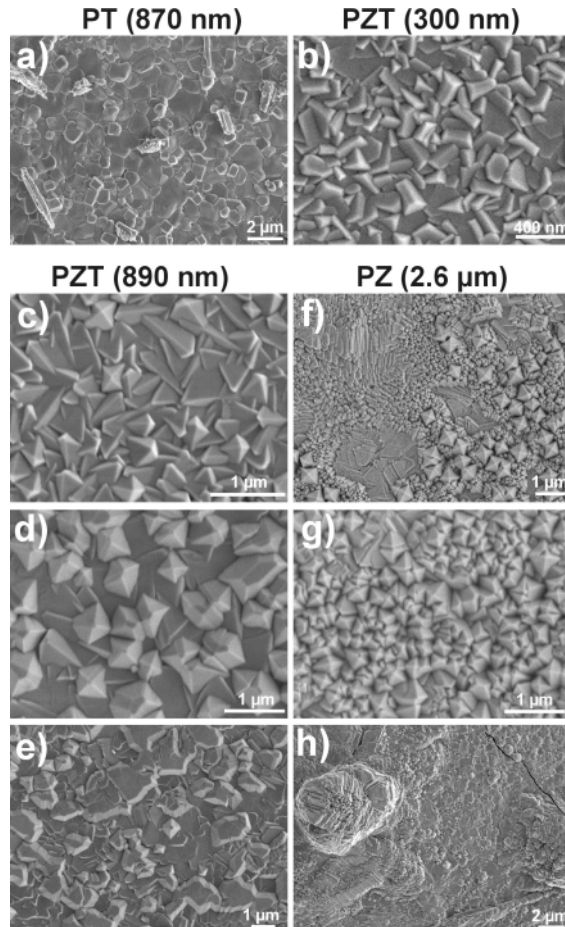


Figure 5-5: SEM photographs of the thick PZT films. a) a 870 nm thick PT film, b) a ~300 nm thick PZT film, c-e) a 890 nm thick PZT film, and f-g) a 2.6 μm thick PZ film.

In Figure 5-6, the XRD spectra of the thin films are presented. The peaks of the PZ film are broad and weak and the spectrum contains one clear non -PZ peak at $2\theta = 34.38^\circ$ ($d = 2.61 \pm 0.05$). A similar peak was also detected in polycrystalline Zr-rich films (Section 7.1) and indexed as (111) orthorhombic ZrO_2 (136); therefore the same indexing has been used here. Additionally, the XRD similarities correspond also to the morphology similarities as zirconium oxide appear as a fine grain compound in the MOCVD films in this study. In Color Figure 5e, clearly different morphologies are seen and it is expected that the fine grains are the zirconium oxides and the large clusters and crystals are PZ crystals. The peak at $2\theta = 35.15^\circ$ could be from the PZ layer (plane (132)) or from another zirconium oxide form. It is only observed at the edge of the wafer tending to indicate that it is due to a Zr-rich phase. The same peak is visible in the PZT film ($x_g = 0.76$) in Figure 5-6b, also at the edge of the wafer, but the origin of the peak cannot be determined on the basis of these results. The PZT peaks observed in the PZT $x_g = 0.76$ indicate the rhombohedral 2 structure. The

XRD spectrum of PZT $x_g = 0.52$ (Figure 5-6c) contains both the rhombohedral 1 and the tetragonal PZT phases together. Similar multi-phase films have been reported at these compositions (40). In the tetragonal PZT ($x_g = 0.24$), tetragonal PZT structures with different d-spacings are present. The PZ/PZT films are only slightly textured compared to powders (Figure 3-2) with a light 100/001 texture. This corresponds well to the tilted platelet morphology and the report of Kim et al. indicating that tilted platelet corresponds to (100) texture. On the other hand, the PT film, corresponding well to the PT powder pattern shown in Figure 3-2, is randomly oriented in plane and in the vertical direction. It also corresponds well to the morphology of randomly oriented bulky grains (Color Figure 5a).

It is possible to estimate the lattice constant values obtained for the films using the (100) and (001) related peaks. There is relatively large error bar on these measurements due to a poor calibration on the Si (004) (See section 3.1.4.1) and the presence of both α_1 and α_2 radiations. The values are reported in Table 5-5 and compared to the reference values for powders (122). The lattice constants measured for the gas phase composition do not correspond directly to the powder lattice constants for the same composition.

There is no (111) signal visible in these spectra, but there might be a PZT(111) peak embedded between the Pt(111) - α and W peaks. The films from the Zr series were therefore not textured, but the films grown for the thickness series were clearly (111) textured as can be seen in Figure 5-7, where the XRD spectra of the films grown from 120 to 30 min are shown. After 30 min, there is an XRD signal and a clear (111) texture is observed. This corresponds to the appearance of facets in the grains.

Table 5-5: Lattice-constant estimates for the thin PZT films compared to powder data. The ** indicate that the peaks cannot be resolved in the film to estimate the lattice constants.

Film	Lattice constants in films (Å) ± 0.05		Lattice constants - values from phase diagram		
	a	c	x	a	c
$x_g = 0.00$	3.92	4.15	0.00	3.90	4.15
$x_g = 0.24$	3.94	4.04	0.20	3.94	4.13
$x_g = 0.52$	R1 = 4.12 T = 3.92	-- **	0.60	4.06	--
$x_g = 0.76$	4.13	--	0.80	4.11	--
$x_g = 1.00$	**	**	1.00	4.15	4.11

The two films grown for 30 min are not equivalent. In Film N°1, there are clear peaks from (001) and (101) diffraction planes, whereas there is only one peak from (111) diffraction plane in Film N°3. There is in agreement with the observed morphology and with reports in the literature. The Film N°1 contains flat platelets (3 and 4 fold symmetry), tilted and in-plane, whereas Film N°3 contains mainly flat triangular grains.

This is in agreement with the observation of Shimizu et al. (125) reporting that the flat triangular grains are (111) oriented. The films grown for 60 and 120 min display similar morphology as Film N°1 and these films are also mainly (111) textured with some (001) / (101) orientation. Good electrical measurements could be performed on these continuous (111) textured PZT layers. The hysteresis curves, shown in Figure 1-3, are measured on these films grown for 120 min, 60min, and 30 min. The non-textured films, usually not so continuous, resulted in poor electrical properties.

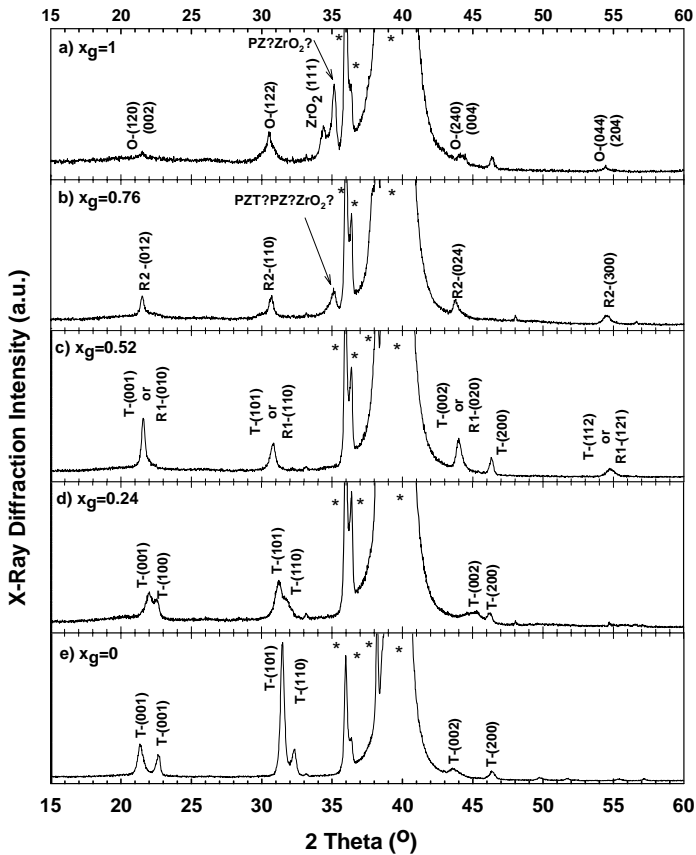


Figure 5-6: XRD spectra of the thin PZT films. a) $x_g = 1.00$, b) $x_g = 0.76$, c) $x_g = 0.52$, d) $x_g = 0.24$, and e) $x_g = 0.00$. Prior to each indexing the letter stands for the structure of the PZT: O for orthorhombic, R2 for rhombohedral 2, R1 for rhombohedral 1, and T for tetragonal as shown in Figure 1-4.

It is important to note that there was no control on the texture of the films in this study as both the composition series and the thickness series were performed with the same gas phase conditions. The Film N°2, grown for 30 min with an $x_g = 0.24$, displays a different morphology and a random orientation, whereas the two others are

(111) textured. As the (111) texture is clearly influenced by the A ratio, and the $x_f \sim 0.4$ was similar for all films grown at $x_g = 0.24$, there might have been uncontrolled variation in the lead flow. Flat crystals were also observed for the thin film $x_g = 0.52$, but no strong (111) diffraction peaks was visible, indicating that not all flat crystals correspond to (111) texture.

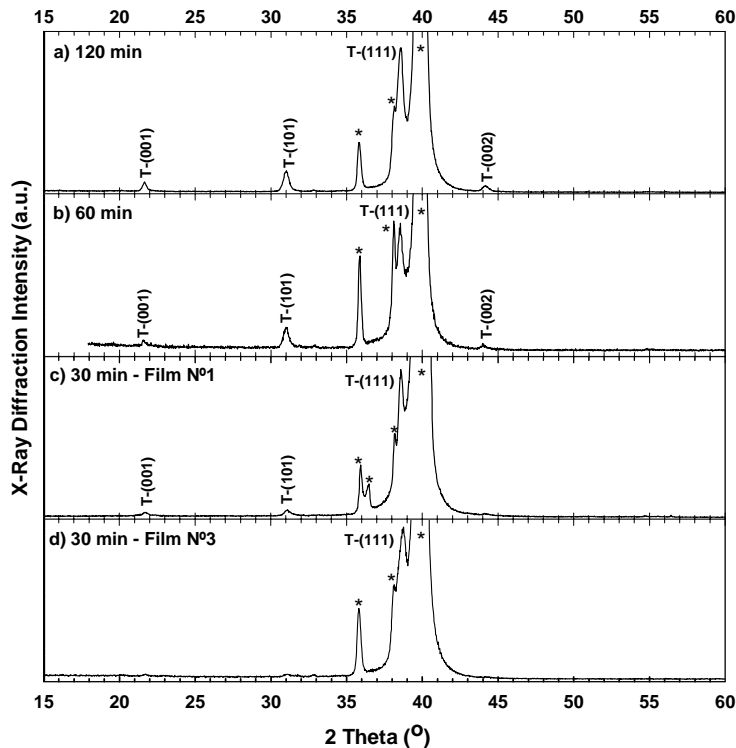


Figure 5-7: XRD spectra of the thickness series. a) Film grown for 120 min, b) Film grown for 60 min, c) Film N°1 grown for 30 min, Reference run corresponding to the morphology shown in Figure 5-2e,f; b) Film N°3 grown for 30 min, the morphology of this run is shown in Figure 5-1. Prior to each indexing the letter stands for the structure of the PZT: O for orthorhombic, R2 for rhombohedral 2, R1 for rhombohedral 1, and T for tetragonal as shown in Figure 1-4.

The structure of the thick PZT films was also investigated and is shown in Figure 5-8. The lattice constants of the thick films are reported in Table 5-7. The spectrum of the thick PT films is not presented in this section but in section 7.2 because these thick PT films contain additional lead oxide by-phases and were studied separately in detail.

Table 5-6: Lattice-constant estimates for the thin PZT films. The ** indicate that the peaks cannot be resolved in the film to estimate the lattice constants. The c-value lattice constant of 4.10 Å corresponds to a powder $x = 0.49$ with $a = 4.04$ Å.

PZT Film	Lattice constants in films in Å ± 0.05	
	a	c
380 nm (120 min)	4.01	4.10
210 nm (60 min)	4.01	4.12
110 nm (30 min - N°1)	4.02	4.09
100 nm (30 min - N°3)	**	**

The diffraction pattern of the thick PZ film is very clear and indicates two main textures, (120) and (002), in the film (Figure 5-8a). This corresponds to a (100)/(001) equivalent in tetragonal terminology. The texture (120)/(002) is in agreement with the morphology (Figure 5-5f-g), showing mainly pyramids, which can grow from both (120) or (002) texture. Pyramids have also been observed on the hetero-epitaxial PZ films, similarly textured but also oriented in plane, and their formation is detailed in Chapter 6. There are no ZrO_2 by-phases detected by XRD for the thick PZ film, but ZrO_2 by-phases were detected in the thin PZ film. The ratios A and x were the same in the gas phase for both runs, but the amount of material in the reactor was higher for the thicker film. It is interesting to note that the situation is the opposite for PT films: the thin PT films were single phase, and the thick PT films contained Pb_xO_y by-phases. The lattice constants of the thick PZ film correspond well to powder PZ, indicating no stress in the film (Table 5-7). In the morphology picture in Figure 5-5h, cracks are also clearly seen.

The thick PZT film, Figure 5-8b, is strongly (012) textured and contains no extra phase. The morphology of the thick PZT film (Figure 5-5c-e) shows zones with triangular tilted platelets, pyramids, and flat topped pyramids. The pyramids might be due to the R2-(012) texture, equivalent to the O- (120)/(002) in PZ and also triggering pyramid formation. The XRD pattern of the thick PZT film was indexed as a R2-PZT structure, as the composition was also determined by other means. The x_f value was determined by XRF and EDS as ~ 0.6 on thick semi-epitaxial films grown on STO in the same run as the thick PZT film. It is in agreement with the data of Keijser et al. (40) who reported that films had a higher a- value of the lattice constant than powders.

According to the film lattice parameters versus composition, the PZT film composition is around $x_f \sim 0.6$. For the 300 nm thick PZT film (Figure 5-7a) both rhombohedral and tetragonal indexing were also possible, nevertheless, ICP measurements and Raman (shown below) indicated a ratio x_f of ~ 0.40 at the edge of the wafer. Similarly as for PT and PZ, the composition of the thick PZT films grown in hetero-epitaxial conditions is different from the thin film grown in polycrystalline conditions: the same x_g (0.24) for both PZT films resulted in two different x_f : about

0.4 for the 300 nm thick PZT film grown in polycrystalline conditions and 0.6 for the 890 nm thick PZT film grown in hetero-epitaxial conditions.

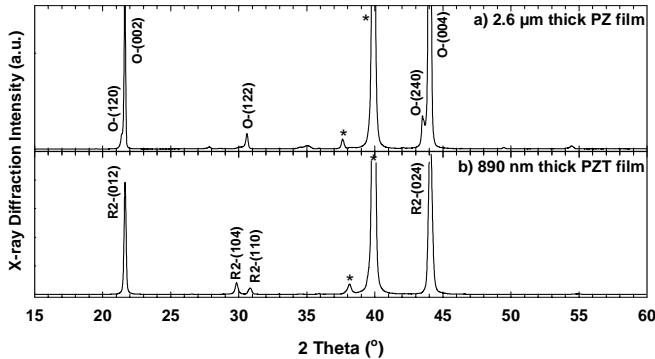


Figure 5-8: XRD spectra of the thick PZT films. a) a ~ 2.6 μm thick PZT film, b) 890 nm thick PZT film. Prior to each indexing the letter stands for the structure of the PZT: O for orthorhombic, R2 for rhombohedral 2 in Figure 1-4.

Table 5-7: Lattice-constant estimates for the thick PZT films compared to powder data. The -- symbol indicates that there are no data available.

Film	Lattice constants in films (\AA) ± 0.05		Lattice constants - values from phase diagram - powders (122)			Lattice constants - values from phase diagram - films (40)		
	a	c	x	a	c	x	a	c
1 μm PZT film $x_g = 0.24$	4.11	--	0.85	4.11	--	0.63	4.11	--
1 μm PZ film $x_g = 1.00$	4.16	4.11	1.00	4.15	4.11	--	--	--

5.4.2 Raman

Raman spectra were taken in the different zones across the radius of the different layers, but only the spectra taken at the edge of the wafers are displayed in Figure 5-9 with the Raman shift indicated above each peak. The PT spectrum corresponds well to that of the loose powder, as shown in Figure 3-4. But the signal intensity is very weak for the ~ 100 nm thick non-PT films and thicker films are required to obtain stronger signals.

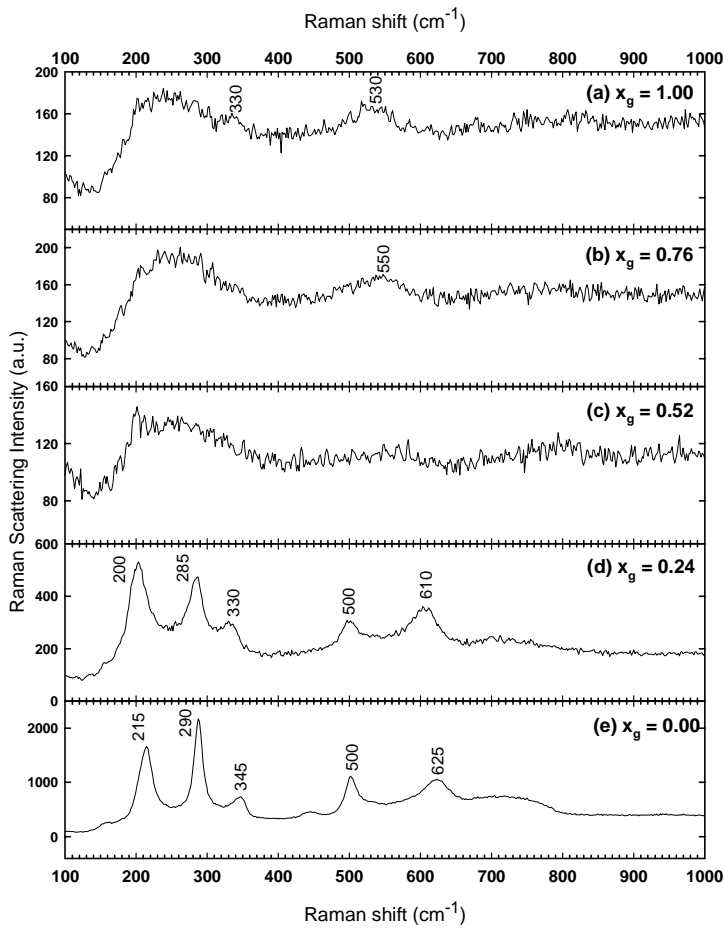


Figure 5-9: Raman spectra of the thin PZT films grown in the composition series. The spectra shown here are taken at the edge of the wafers, where the layer is thicker to obtain a stronger signal. a) $x_g = 1.00$ (PZ), b) $x_g = 0.76$, c) $x_g = 0.52$, d) $x_g = 0.24$, and e) $x_g = 0.00$ (PT).

The intensity of the MOCVD PZT films for different compositions is compared to powders as shown in Figure 5-10. The absolute intensity, is defined as:

$$\text{absolute intensity} = \frac{\text{counts (max)}}{\text{laser power (mW)} \times \text{acquisition time (s)}}$$

and when comparing films of different thickness (as for the thick films below), the intensity is divided by the film thickness. The stronger Raman scattering signal for the thin PT film might have been due to the rough surface morphology of the films

resulting in poor specular reflection whereas the other films are continuous and smooth. But as a similar trend is observed with the loose powders, the stronger Raman signal for PT is due to an intrinsic property of PT. PT is a stronger scatterer (~10 times better) than PZT or PZ. Covalent materials have a strong Raman signature (e.g. diamond) but ionic materials have a very low-intensity signature. In section 8.2, it is indicated that, according to the calculated Wemple DiDomenico parameters, PT is more covalent than ionic. The observation of the decrease of the absolute Raman intensity with decreasing Ti concentration supports this idea.

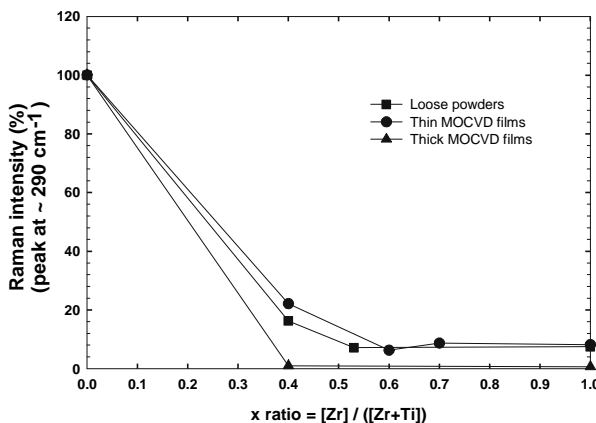


Figure 5-10: Composition dependence of the intensity of the Raman peak at $\sim 290 \text{ cm}^{-1}$ for loose powders (Figure 3-4), thin MOCVD films ($\sim 100 \text{ nm}$) (Figure 5-9) and thick MOCVD films (Figure 5-11). The absolute-intensity results are normalized to the intensity observed for PT, which is seen to be a much stronger Raman scatterer than PZ or PZT.

The composition was estimated by comparing the peak position and shape of the spectra with the powder spectra (Figure 3-4 and Figure 3-5) and by comparing it with ICP results (Table 5-8). Both techniques agree but the Raman analysis is rather subjective (as the peak position depends on the particle size as well as on chemical composition) and both techniques have a large error ± 0.1 . Two weak PZ peaks at 330 and 530 cm^{-1} can be distinguished in the thin PZ film. In contrast with XRD, the zirconium dioxide phase is not observed in the thin PZ layer by Raman and might indicate that the zirconium dioxide phase also has a low intensity Raman signal or that it was not present in the probed volume.

Table 5-8: Estimation of the film composition using the Raman spectra. The -- symbol indicates non-available data.

x_g	x_f as estimated by Raman ± 0.1	x_f as estimated by ICP (edge of the wafers) ± 0.1
Thin Films		
0.00	0.00	0.00
0.24	0.30	0.40
0.52	0.60	0.60
0.78	0.80	0.70
1.00	1.00	--
Thick films		
0.00 (890 nm)	0.00 + lead oxides	--
0.24 (300 nm)	0.40	--
1.00 2.6 μm	1.00	--

The Raman PZ spectrum measured on the thick PZ film (Figure 5-11a) contains more details than the measured spectrum on PZ loose powder (Figure 3-4) and is clearer than the reported spectrum on PZ nanocrystals (Figure 3-5). As for the thin films, the PT Raman signal is clearly stronger on 890 nm PT films than the 2.6 μm PZ films. The intensity of the peak at 290 cm^{-1} for the thick films has also been plotted in Figure 5-10, and the absolute Raman intensity is roughly 100 times stronger in PT than in PZ and not 10 times as for thin films and powders. This is due to the strength of the 290 cm^{-1} peak in the thick PT film being much larger than in the powder and the thin film. If the peaks at $\sim 215 \text{ cm}^{-1}$ are chosen, the PT signal is 10 - 20 % stronger than the PZ signal as for powders and thin films. The peaks in the PZ spectrum correspond to the peaks in the PT spectrum but split in pairs and are clearly visible in this spectrum. For the thick PT film (Figure 5-11), additional lead oxide phases are detected and further discussed in Section 7.2. The shift of the Raman peak in the film with respect to PT powder Raman spectrum is attributed to size effects. The spectrum of the 300 nm thick PZT film (Figure 5-11b) contains 4 clear peaks at 200, 280, 335, and 620 cm^{-1} corresponding well to peaks measured on loose powders with $x = 0.4$.

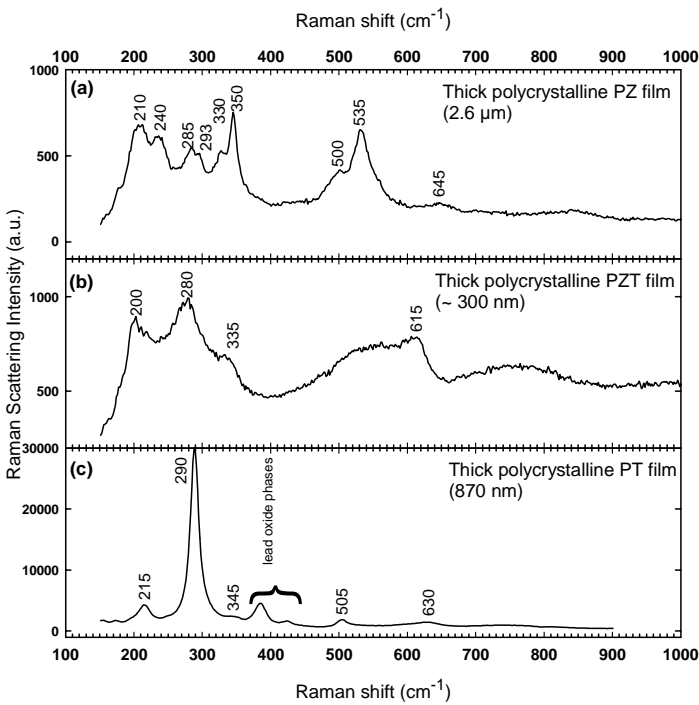


Figure 5-11: Raman spectra of the thick PZT films. a) a 2.6 μm thick PZ film, b) a ~ 300 nm thick PZT film, and c) a 870 nm thick PT film.

5.5 Discussion and summary

Several issues on the growth of polycrystalline PZT layers with the MOCVD reactor are summarized and discussed below and separated into small section for clarity.

5.5.1 Reproducibility of the runs

Perfectly homogenous (in thickness and composition) films of 6" and 4" diameter could not be grown. Therefore, the run having the best quality (homogeneity, electrical properties) was finally chosen as a reference run. The run was still inhomogeneous in thickness (10 % thicker at the edge) and composition (50% more zirconium at the edge). This run was reproduced several times; nevertheless the reproducibility is not exact. The thickness and the texture were different from one reference run to another. Because the radial inhomogeneity is mainly due to Zr variation, it was supposed that the main problem was the Zr flow. Nevertheless, for fully (111) textured film, the x composition ratio in the film was the same as in the

reference indicating that there is also a problem with the lead flow, as the (111) texture is induced by a lower A ratio as reported in literature (125).

5.5.2 Morphology and texture

Using reports from the literature, morphology observations, and XRD, the appearance of different PZT film morphologies and their texture can be summarized. An overview is shown for four PZT compositions and films of different thickness in Figure 5-12. It is a useful summary as the morphology of PZT films is rarely shown in the literature, due to the fact that the crystals are not large and that growth over the whole PZT composition range is still a challenge.

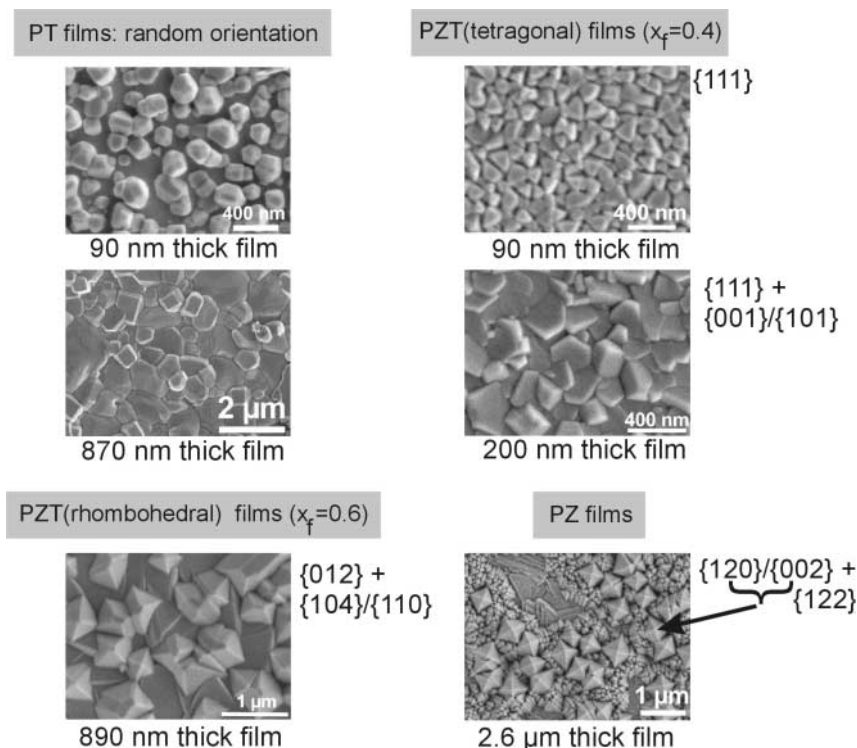


Figure 5-12: Overview of the different surface morphology and texture for PZT films with different compositions. The planes parallel to the substrate (texture) are indicated next to the SEM micrographs.

5.5.3 PT versus PZ and composition control

Composition control is a key element in the preparation of thin films, but it is not trivial for PZT. For all runs, the values of the A and x ratios in the gas phase were set

as the intended A and x ratios in the solid phase. Nevertheless there was no one-to-one relationship between them and the composition control is difficult. The growth runs detailed in this thesis are all performed at 700°C, but the precursor flows in the hetero-epitaxial conditions was 2.67 times higher than in the polycrystalline conditions (Table 2-2). Several observations resulting from the analysis of these three series grown in different gas conditions are listed below, compared with the literature, and summarized to have a better overview of the MOCVD PZT growth in this work.

- Lower nucleation rate of PT versus PZ

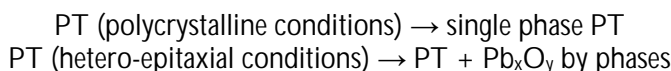
It is clear that the growth mechanisms are different for the different PZT compositions. This is first observed radially on PZT layers grown on 6" diameter platinized substrates. For a ~ 100 nm thick tetragonal PZT layer, the layer at the center is not continuous (corresponding typically to $x_f = 0.2$ and the layer at the edge of the wafer is continuous corresponding to $x_f = 0.4$). Similarly, in the PT to PZ growth series, for the same growth time, the Zr rich layers are continuous whereas the PT layers are not.

There is not so much clear information in the literature on the growth mechanisms of the different PZT compositions. Recently, Shimizu et al. (126) reported on the growth differences between PT and PZT on different type of substrates, and observed for both compositions island growth on platinized silicon wafers. In their study (126), it was also observed that the PZT film start from small nuclei, which coalesce together, indicating island growth.

As all the Zr containing PZT layers grown in this study were continuous, it can be concluded that the Zr (or ZrO_2) nucleated more easily than Ti (or TiO_2) on the platinized silicon substrates. This is in clear disagreement with some reports in literature. After growing PbO , ZrO_2 , and TiO_2 separately at different temperatures, Keijser (40) showed that Ti has a deposition rate 2.5 higher than Zr at 700°C. On the other hand, Nagashima et al. (51) reported that the deposition rates of Pb, Zr, and Ti in the PZT film were considerably different from those of the corresponding single-oxide films, indicating a strong interaction between the depositions of Pb, Zr, and Ti in PZT films. Fujisawa et al. (60) who reported that, at 580°C, the lateral growth for Zr - rich PZT films is higher whereas nucleation and growth of PZT islands progress simultaneously for Ti-rich composition.

- Different film compositions obtained when higher partial pressures are used in reactor

The growth of the PZT end compositions in both type of runs behaved differently and the composition control is different in both cases:



PZ (polycrystalline conditions) → PZ + ZrO₂ by phases
 PZ (hetero-epitaxial conditions) → single phase PZ
 PZT $x_g = 0.24$ polycrystalline conditions → $x_f = 0.40$
 PZT $x_g = 0.24$ heteroepitaxial conditions → $x_f = 0.60$
 PZT $x_g = 0.10$ heteroepitaxial conditions → $x_f = 0.40$

For higher supply rates, the ZrO₂ is more efficiently integrated to PbO than TiO₂ and vice versa. Though the growth rates on PT and STO are different (not discussed in the thesis), these effects were also observed on the STO substrates and are not particular for platinized silicon wafers (See Section 7.2 for the Pb_xO_y formation on both types of substrates). The relationship between x_g and x_f at 700°C for this study and results from other groups are shown in Figure 5-13. Foster et al. showed that stoichiometric films could be obtained over the whole PZT composition and that x_g was roughly equivalent to the x_f for every composition. On the other hand, Keiser et al. (40) obtained different results with a systematic lower x_f than x_g for a growth at 700°C. The observations, in the polycrystalline conditions, indicate, with respect to x_g , a larger x_f at the edge of the wafer and lower at the center.

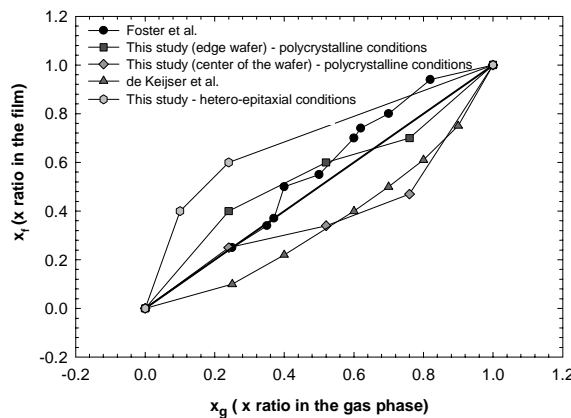


Figure 5-13: x ratio in the film versus the gas ratio in the gas phase. The data from Foster et al. were reported in ref. (47) and from Keijser et al. in ref. (40). For the measurements in this study, the x_f at the end composition PT and PZ are shown to be fictitious, since PbO is obtained in PT (hetero-epitaxy conditions) and ZrO₂ in PZ (polycrystalline conditions).

- Only PZ has a higher growth rate in higher partial pressures conditions

It is surprising to see that the growth rate of PT and PZT films on Pt was not changed by using 2.67 higher precursor partial pressures in the hetero-epitaxial conditions. On the other hand, it is different for PZ films. The growth rate is 2.25 higher by

increasing the partial pressures by 2.67 assuming a $\rho \sim 9 \text{ g/cm}^3$ for the PZ polycrystalline films. If the powder PZ density (7 g/cm^3 is used, the growth rate is 2.9 higher. To obtain a 2.67 growth rate, the density is 7.6 g/cm^3 , similar to the thin PZ film. These data indicate that the PZ growth rate on Pt is proportional to the precursor partial pressure in the reactor, in contrast with the titanium composition.

- Overview

Some growth models and descriptions are available in the literature and De Keiser et al. (40) reported the important point, that a rich A ratio in the gas phase was controlled by self-regulation process for substrate temperature $T \geq 700^\circ\text{C}$, due to the desorption rate of unreacted PbO. Usually single-phase PZ films are difficult to grow and some researchers have commented on that fact. Chen et al. (123) reported that, "the difficulty in preparing single-phase PZ probably arises from the fact that the rate of formation of PZ is much lower than that of PT and also that the adhesion of ZrO_2 on the substrate during the growth would disrupt the growth of PZT". Additionally, Bai et al. (127) reported that, "in comparison with the growth of PT thin films by MOCVD, it was found that the reaction rate of PbO with ZrO_2 was much lower than that of PbO with TiO_2 . In order to grow stoichiometric PZ epitaxial films, the partial pressure of PbO in the gas phase must be higher than the stoichiometric value to compensate for the evaporation of PbO from the substrate surface."

Here, it cannot be determined if the reaction rate of PbO and ZrO_2 is lower than PbO and TiO_2 , but according to the series described here, the nucleation rate of ZrO_2 is the controlling factor. Zr (or ZrO_2) nucleates much more easily than PT. If relatively low partial pressures are used (polycrystalline conditions), ZrO_2 will nucleate but as the PbO tends to desorb, it cannot fully react to from PZ (or PZT) and ZrO_2 phases are grown. It is not the case for PT. TiO_2 nucleates much less easily and there is enough PbO to react and form PT. On the other hand, if 2.67 higher partial pressures are used, the opposite happens. There is enough PbO to react with the ZrO_2 and PZ is formed. For PT, not all the PbO can desorb and evaporate and Pb_xO_y by-phases are formed. If PZT is grown, there is a competition between the ZrO_2 and TiO_2 to form PZT. In both partial pressure conditions, the ZrO_2 is more competitive as higher x_f are obtained than x_g but as the partial pressures are increased, Zr clearly dominates. The growth mechanisms are complex and several steps occur in the gas phase, as well as at the surface and they cannot be summarized in a qualitative summary. For example, it is not known when the single oxides react to form PZT and if they are adsorbed and nucleate as single oxides or as PZT. But it is clear that the PZT growth is issued from a competitive process between ZrO_2 and TiO_2 with PbO and that ZrO_2 nucleates (eventually with PbO) more easily than TiO_2 . The MOCVD PZT growth is very dependent on gas phase composition and the radial inhomogeneity on our wafers is mainly due to a non-homogenous flow across the wafer.

Chapter 6

Structure and Morphology of Epitaxial PbZrO_3 Films¹²

¹² The work presented in this chapter is based on "Structure and Morphology of Epitaxial PbZrO_3 Films Grown by Metalorganic Chemical Vapor Deposition" by M.P. Moret, J.J. Schermer, F.D. Tichelaar, E. Aret, and P.R. Hageman, *J.Appl.Phys.* 97, 3947-3957, (2002).

6 STRUCTURE AND MORPHOLOGY OF EPITAXIAL PbZrO₃ FILMS

PZ films of different thickness have been grown by metalorganic chemical vapor deposition on STO substrates. The structure of the films was determined by XRD and TEM. At the deposition temperature, the growth is cube-on-cube and is therefore hetero-epitaxial. During cool-down, PZ goes through a phase transformation from paraelectric to anti-ferroelectric at the Curie temperature and its cubic structure is stretched to orthorhombic. This results in domain formation in the PZ films corresponding to the different stretching directions. At room temperature, the thin PZ film consists of at least two different (120) domain variants and the thin-film substrate relation can be described as (120)[002] PZ//(100)[001] STO for one of these variants. By etching down a thick film, it was observed that circa 260 nm is the threshold thickness, above which two additional different (002) domain variants appear in addition to the (120) domain variants. For one of the (002) domain variant, the thin-film substrate relation can be described as (002)[100] PZ//(100)[011] STO. The surface morphology of the thick films, studied by scanning electron and atomic force microscopy, is partly covered with pyramids. These pyramids can originate from both (120) or (002) domains and are due to a higher growth rate of these two planes compared to the rest of the layer. A suggestion is made for pyramid-facet indexing for both domains.

6.1 Introduction

PZT thin films are candidates for several applications such as memories, piezoelectric devices, and electro-optic devices (Section 1.4.3). Of particular interest are the materials with compositions around the morphotropic phase boundary ($x=0.53$), as they show large piezoelectric effects and dielectric constants. PZ ($x = 1$) is antiferroelectric (AFE) and has received significantly less attention. Its AFE phase can be switched to the FE phase by applying an electric field (128) and the relatively large strain increase accompanying this phase change could be used in devices requiring on/off strain states (128). For these applications, PZ thin films seem more interesting than bulk materials as they have higher breakdown strength. In addition to phase switching, other applications related to the PZ electro-optical properties are reported in the literature (129).

FE / AFE films are usually grown above the Curie temperature, at which the antiferroelectric or ferroelectric phase transforms to paraelectric. Therefore, the hetero-epitaxial growth of ferroelectric material leads to the formation of domains during cool-down after deposition. This phenomenon has been investigated for tetragonal PT and PZT (119, 120) as well as for rhombohedral PZT (121), but not for orthorhombic PZ. The growth of polycrystalline PZ films on platinized substrates by

different techniques (magnetron sputtering, sol-gel, laser ablation) and their electrical properties have been reported (128, 130). Although some applications, such as electro-optical applications, might require epitaxial films (single crystals) as they have a higher potential than poled polycrystalline structures (35), no investigations on epitaxially deposited PZ films were encountered. In this paper, we present data on the structure and morphology of thin and thick PZ films hetero-epitaxially deposited on STO substrates. The structure of these films, measured by XRD, is compared and related to the TEM cross-section results and the film surface morphology. These observations are further discussed in relation to the processes that occur during growth and cool-down.

6.2 PbZrO₃ material properties

Above the Curie temperature, around 230°C, PZ is paraelectric with a cubic structure and below it is antiferroelectric with an orthorhombic structure. A schematic representation of the corresponding unit cells is shown in Figure 6-1. Upon cooling, cubic PZ is deformed by stretching the cubic structure along <110>. The stretch along the <110> induces a small angle difference of 5'28" with respect to the original unit cell structure. The distortion of the cube leads to a monoclinic cell, which can be described more conveniently as an orthorhombic unit cell. AFE materials have a zero net polarization as they contain ion chains displaced in one direction with adjacent ion chains displaced in the other direction, leading to a large unit cell containing 8 chemical units. For clarity, the films studied in this work will be described starting from the unit cell axes, as shown in the orthorhombic unit cell in Figure 6-1.

6.3 Samples

A thin PZ film was obtained in a deposition run of 60 min while 9 thick films (7 and 2) were obtained successively in two separate deposition runs of 300 min. In Table 6-1, data with respect to the composition, thickness, and surface roughness of the PZ films are summarized. The difference in growth rates for the thin and the thick films will be discussed later on. The XRF, the EDS, and ellipsometry analyses of these PZ

films (Chapter 8) indicate that the ratio $\frac{[\text{Pb}]}{[\text{Zr}]}$ in the film was relatively close to 1 as

expected for a perovskite. The EDS measurements are less accurate than the XRF ones as TEM sample thickness is not exactly known. The ratio $\frac{[\text{Pb}]}{[\text{Zr}]}$ did not vary

from the interface to the surface as measured by EDS in the TEM cross-section. This indicates that the growth environment was successfully kept constant during the 300 min growth run. By measuring the weight of the films prior to and after growth and using the thickness determined by ellipsometry and cross-section TEM, an average density of the PZ films was estimated as $\rho = 9.1 \pm 0.5 \text{ g/cm}^3$, which is relatively high compared to 6.98 g/cm³ for PZT ($x=0.98$) sintered ceramics (122). This difference

might be due to the fact that our estimated density is for fully continuous crystalline MOCVD films, which are denser than ceramics.

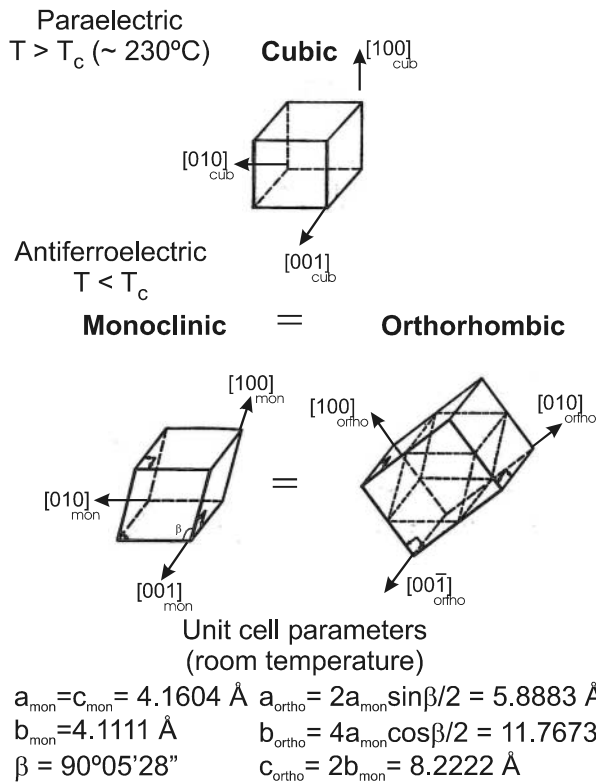


Figure 6-1: Schematic representation (not on scale) of the unit cell transformation of PZ from a cubic to an orthorhombic structure with the relationships between the cell parameters of the different symmetry (4, 7, 12).

Table 6-1: Growth rates, layer thickness, roughnesses, and composition ($\frac{[\text{Pb}]}{[\text{Zr}]}$) of the MOCVD PZ films investigated.

PZ Film	Growth rate nm/min	Thick. (nm)	Rough. rms (nm)	XRF Surface composition	EDS (TEM) average composition (across thickness)	Ellipsometry average surface composition (Chapter 8)
Thin film	1.75 ± 0.08	105 ± 5	0.59	--	--	≈ 1.0
Thick films	4.3 ± 0.2	1292 ± 66	30-50	0.90 ± 0.05	0.820 ± 0.10	≈ 1.0

6.4 Results

6.4.1 Structure

The XRD patterns of the films are shown in Figure 6-2. The PZ spectra were indexed according to orthorhombic PZ at room temperature (122, 131). For the thin PZ film on STO, Figure 6-2a, only the orientation (120) is seen. In contrast, for films roughly ten times thicker deposited on similar STO substrates, two orientations, (002) and (120), can be identified (Figure 6-2b). The peak positions are listed in Table 6-2. The peaks observed in the thin film are not split as the peaks measured in the thick films, but they are quite broad. The FWHM of the two high intensity (240) peaks from the thick films are respectively 0.05° and 0.06° , and the FWHM of the (240) peak of the thin film of 0.2° and hides an eventual peak splitting as discussed later.

One thick PZ film was dry etched four times to perform a depth analysis by XRD of the layer. The etching was performed in an Alcatel GIR300 at 50W at a pressure of 5 mTorr with a SF₆ flow of 15 ml/min resulting in an average etch rate of 20 nm/min. The XRD 2θ spectrum of the etched film was measured after each etch step. The film thickness was estimated by weighing the film prior to and after etching and using the estimated PZ density. The XRD spectra are shown in Figure 6-2c-f. The intensity of the {002}-related peaks as well as the {120} splitting progressively decreased and nearly disappeared at the last etch step for a film thickness of about 260 nm. The {120} - related peaks are not clearly visible in Figure 6-2f, but low intensity peaks can still be distinguished as shoulder peaks from the {002}-related peaks. Such weak shoulder peaks are not visible for the 100 nm thin film, but as its XRD spectrum and that of the 100 nm thin film are similar, it indicates that 260 nm is roughly the threshold thickness for the formation of (002) domains.

All thick PZ films displayed the same features in the in-plane XRD spectra. There are two observable orientations, (120) and (002), each with multiple splitting. Both (120) and (002) consist of two peaks whereas (240) and (004) consist of two high intensity peaks separated by two (and eventually three, although not visible on the displayed spectrum in Figure 6-2b) lower intensity peaks with varying intensity from film to film. The high intensity (120) or (002) peaks do not correspond directly to the respective (240) and (004) high intensity peaks as seen from the peak positions in Table 6-2 but to peaks between each (240) and (004) high-intensity-peak pairs.

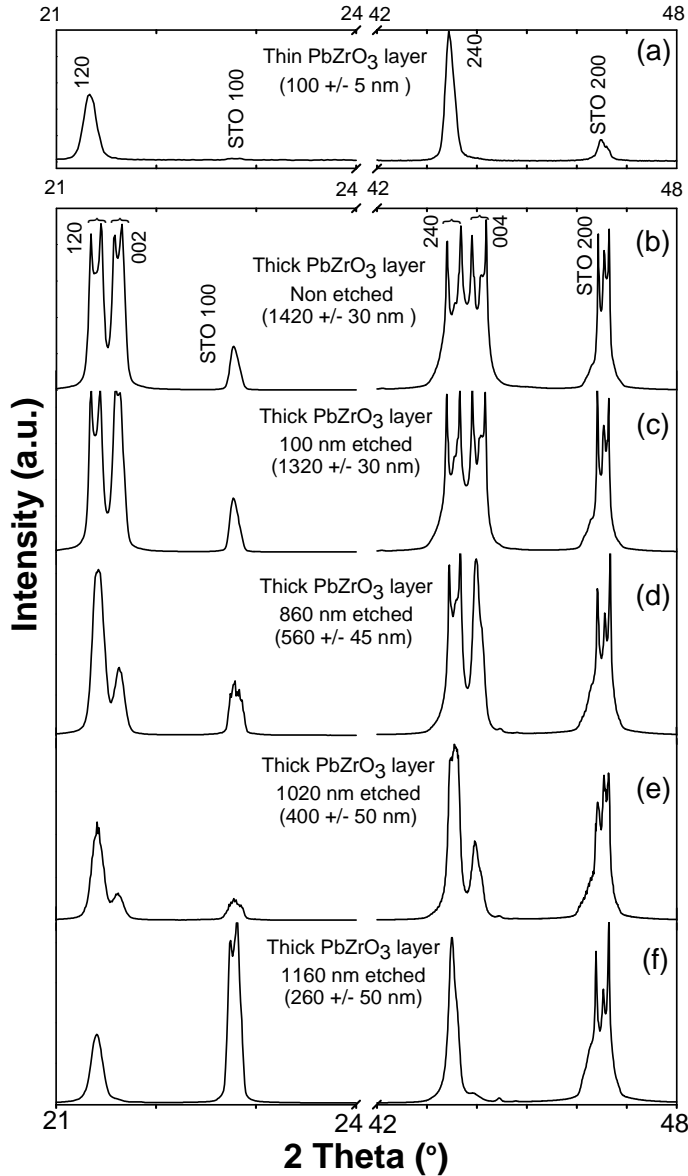


Figure 6-2: XRD spectra (θ - 2θ scan) of (a) a thin PZ film on STO and (b) a thick PZ film on STO. (c)-(f) The thick film was dry etched four times and the XRD were successively measured. As the film becomes thinner, the {002} peaks disappeared and only one peak for {120} planes survives.

Table 6-2: Position of the 2θ peaks in the PZ films on STO and the ICSD reference (76).

Reference Powder data ICSD 75-1607		MOCVD PbZrO ₃ Films			
		100 nm Thick	1450 nm thick	1450 nm thick etched down to 260 nm	2θ
2θ	(hkl)	2θ	2θ min	2θ max	2θ
21.339	(120)	21.30	21.35	21.44	21.40
21.605	(002)	--	21.58	21.65	--
43.466	(240)	43.41	43.40	43.68	43.50
44.029	(400)	--	43.90	44.19	

The STO peaks in the XRD spectra shown in Figure 6-2 also displayed similar types of peak splitting. Additionally, STO crystals identical to the substrates used for this study, also show splitting in θ - 2θ spectra and rocking curves from these peaks indicate a kind of mosaic structure in the STO substrate. Pole-figure measurements, performed with a monochromator to avoid eventual peaks originating from Cu K_{α2}, around the symmetric (240) peak confirmed that there are clearly 2 to 3 tilts as shown in Figure 6-3a-c. The peak splitting observed in the θ - 2θ spectra correspond to these tilts in the pole figures. Though the θ - 2θ spectra in Figure 6-2a from the thin film indicate a single (240) peak in the film, the pole figure shows that there are actually two (240) tilts in the thin film causing the relatively large FWHM of the peak. A similar multi-tilt structure was found for the (004) peak in the thick PZ film (Figure 6-3d). The tilts observed in the pole figure do not seem to be correlated to the in-plane STO axis for the thick film but eventually aligned along [010] and [0̄10] for the thin film.

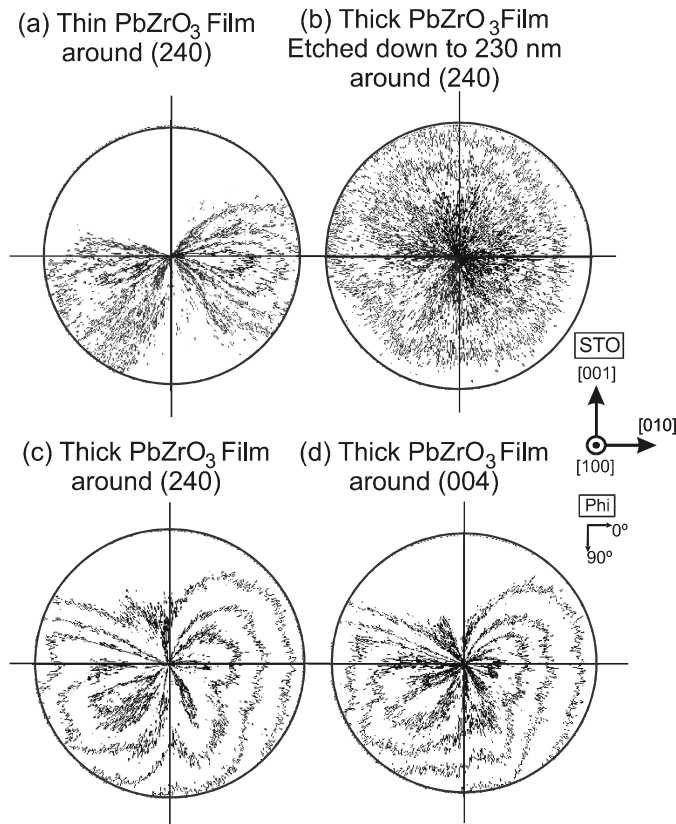


Figure 6-3: (a-c) Pole figures around the symmetric (240) peak in the PZ films and (d) around the symmetric (004) peak in the thick PbZrO₃ film. For a pole figure, a Phi scan is performed in the $\theta - 2\theta$ diffraction condition of the peak for different Chi values (0° to 3° for all pole figures shown here).

Assuming an epitaxial relationship between film and substrate, the observed (120) and (002) domains in the PZ films are oriented in-plane to minimize the lattice misfit with the substrate as shown for both domains in Figure 6-4a. Note that the lattice misfit is not visible in this schematic figure. Depending on the orientations of the in-plane components, different variants for each of these two domains can occur as is shown in cross section views in Figure 6-4b. There are four main variants for the (120) domains, Figure 6-4b₁-b₄, and two main variants for the (002) domains, Figure 6-4b₅-b₆. All the variants are composed of two sub-variants leading to a total of 12 possibilities. In Figure 6-5, X-ray Phi scans performed around the asymmetric (362) peak of the (120) domains are shown. The scans for the thin and thick PZ films are similar and show peaks at Phi = 0 and 180° corresponding to variant 1 and/or 2 and peaks at Phi = 90 and 270° corresponding to variant 3 and/or 4. This indicates that two variants of the (120) domain are present in the thick as well as in the thin films.

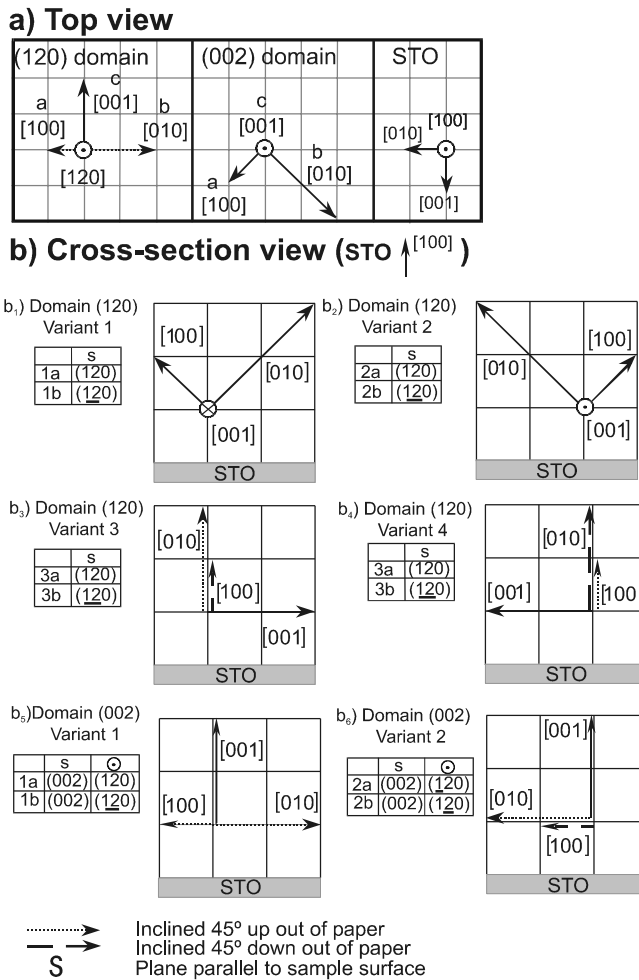


Figure 6-4: Schematic representations of the epitaxial relations between the orthorhombic PZ unit cell (vectors) and the cubic STO. For both top and cross-section views, the STO orientation is given. Dotted and dashed lines represent vectors pointing 45° respectively out of and in to the paper. (a) Representation of (120) and (002) domains in top view. (b) Representation of the different possible variants for each domain in cross-section view. The first variant of each domain corresponds directly to the top-view.

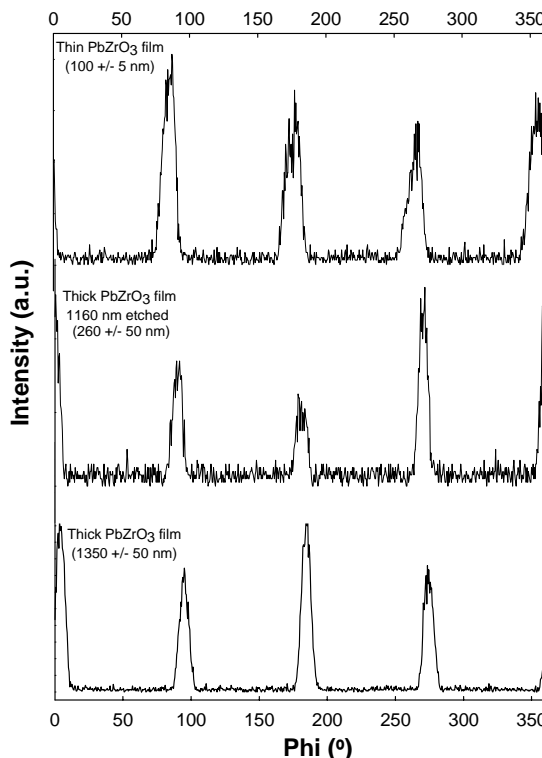


Figure 6-5: Phi scan around the asymmetric (362) peak of the (120) domain for the thin PZ film, the thick PZ film etched down to 260 nm, and for a thick PZ film.

The occurrence of different domain variants was confirmed by cross-section analyses of a thick PZ film by TEM. A general overview of the cross-section is given in Figure 6-6. SADP and HREM images were analyzed to differentiate one variant from another. By checking if the b axis (for PZ) was in the plane of the SADP, and the lattice plane spacing values in the SADP plane, differentiation between the variants was possible. Within the limited sample volume addressed by TEM, (120) domain variants 1 and 2 occurred most frequently and very few of the other variants were observed. High electron-dose exposure caused a front like boundary to move from the edge of the specimens towards the thicker foil areas indicating that the variants are beam sensitive. In one area, diffraction on both sides of the growth front showed that variants with the b-axis out of the image plane ((120) for variants 3 or 4, and/or (002) for variants 1 or 2) were growing at the expense of (120) variants 1 or 2 (b-axis in the image plane). The d-spacing values of the (120) and (002) planes are in agreement with XRD measurements, as can be seen in Table 6-3. The d-spacing values of the thick PZ films obtained directly from the 2θ spectra were confirmed by the Bond technique at two opposite incidence angles to eliminate instrumental errors. Table 6-3 shows

that, within the experimental error, the measured d-spacing values correspond well to powder PZ data (76). The peak splitting observed in the XRD spectra could not be observed in the SADP's since with an instrumental error of circa 1%, the selected area diffraction technique is less sensitive than XRD.

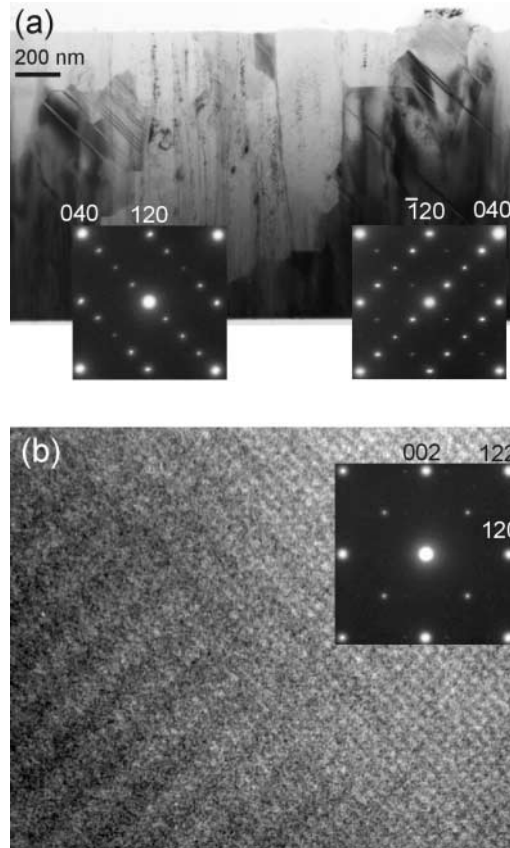


Figure 6-6: (a) Bright field transmission electron micrograph of the PZ layer imaged with a 040 reflection in the dark regions. Light and dark areas correspond to different variants in the layer, as demonstrated by the inserted Selected Area Diffracted Patterns (SADP). They were taken from the corresponding areas after tilting the specimen about 20° to the [001] beam direction. Note that in the right SADP a variant with the b-axis in the plane of paper inclined to the left is also partly present. (b) High Resolution Electron Micrograph image of the PZ layer showing three different variants. The surface normal is directed in the vertical direction of the figure. The two variants with the b-axis in the plane of the paper are recognized from the 11.8 Å spacing, present in two directions in two different areas respectively. A variant with the b-axis inclined to the image plane can be seen in the right part of the image. A SADP from such an area is inserted. Note that the SADP is consistent with different variants, for example as indexed in the figure, but an indexing with a (120) plane parallel to the surface is also possible.

Table 6-3: d -spacing values of the (120) and (002) planes determined by SADP (TEM) and XRD, and compared to powder PZ (131).

	d (120) (Å)	d (002) (Å)	d(240) (Å)	d(004) (Å)
TEM - thick Film (± 0.4)	4.19	4.14	--	--
XRD - thick film (± 0.005)	4.15/4.16	4.11/4.12	2.07/2.09	2.05/2.0 6
XRD - thin film (± 0.01)	4.17	--	2.09	--
Powder (131)	4.16	4.11	2.08	2.06

In the XRD-crystallographic reference (76), the intensity ratio of $I(120)/I(002)$ and $I(240)/I(004)$ for a random PZ powder are stated to be 1.50 and 1.75 respectively. On the other hand, the XRD spectrum in Figure 6-2b shows similar intensities for both the (120) and (002) related peaks. It therefore indicates that a majority of (002) domains is present, which is in contrast with the TEM analysis, indicating a majority of (120) domains. As the etch experiments show that the majority of the (002) domains is present in the upper 600 nm of the layer, the larger (002) domain percentage detected by XRD can be explained by its depth sensitivity. For PZ, with an X-ray absorption factor of about 3600 cm^{-1} , the XRD peak intensity is 3 times stronger at the surface of the material than at a depth of 550 - 600 nm (72).

In agreement with the present findings, a single crystallographic domain film has been reported by Bai et al. (127) for 100 - 200 nm thick MOCVD PZ films on STO, analyzed by XRD and TEM measurements. However, in contrast to the present work, they assign their layer, which shows two peaks at $2\theta = 21.5^\circ$ and 43.8° in the $\theta - 2\theta$ XRD spectrum, as being (002) oriented. Based on the additional information presented above, we tend to believe that this is an incorrect assignment. Foster et al. (35) report on MOCVD grown 500 - 1200 thick PZ films on STO. Their films have two main orientations in the XRD at roughly $2\theta = 43.5$ and 44.1° attributed respectively to (240) and (004). The additional splitting from the (240) and (004) was further attributed to Cu $K_{\alpha 1}$ and $K_{\alpha 2}$. The peak positions match the ones of our films as listed in Table 6-2. Our peak splitting, however, cannot be due to Cu $K_{\alpha 1}$ and $K_{\alpha 2}$ splitting as the maximum 2θ spacing is higher than 0.1° as expected in between Cu $K_{\alpha 1}$ and $K_{\alpha 2}$ for $2\theta=43.5^\circ$. Additionally, the pole figures recorded with a monochromator confirmed that both (120) and (002) related peaks were tilted. The main origin of the peak splitting of both (240) and (004) (or tilting) is likely to be due to the mosaic structure of the substrate described above. However, domain tilting might be expected in the (120) domains of a PZ film grown on a perfect STO substrate. In the room temperature PZ structure, the (120) planes are not completely parallel to the substrate. The normal of the (120) planes is tilted by $5'28''$, with respect to the STO substrate.

surface, due to the stretch leading to the orthorhombic structure (Figure 6-1). The stretching in different directions corresponding to the formation of the different (120) domain variants is therefore expected to result in peak splitting. But the tilt results in a maximal 2θ difference of $4 \times 5'28'' = 0.3644^\circ$, larger than the maximal measured 2θ difference 0.28° for (240) (Table 6-2). Additionally, it was reported in the literature that the tilts of (200) and (002) domains in PT films increased when relatively slow cooling rates were used after growth (132). In our work, the non-controlled cooling rate of $\sim 25^\circ\text{C}/\text{min}$ from 700°C to 300°C and of $\sim 3^\circ\text{C}/\text{min}$ from 300°C to room temperature might be compared to the standard ($30^\circ\text{C}/\text{min}$) and slow ($5^\circ\text{C}/\text{min}$) cooling rates as used by Foster et al. (132). Therefore, the tilt of the (120) domains might be influenced in a similar fashion as reported by Foster et al.

The STO-PZ interface was studied using cross-section TEM analyses. The PZ composition did not vary at the interface but a highly defective zone of roughly 10 nm thickness was identified. Voids and misfit dislocations were detected in this zone by respectively taking bright field (BF) electron micrographs in underfocus and by tilting the sample position. Additionally, threading dislocations extending from the interface to the sample surface are observed in most of the micrographs. A threading dislocation density in the order of 10^{10} cm^{-2} was estimated using a TEM foil-specimen thickness of $0.1\mu\text{m}$. This dislocation density is comparable to the threading dislocation density of $10^9\text{-}10^{10}\text{ cm}^{-2}$ observed by plane view TEM for a PT film grown on MgO (53). PT films on MgO have similarities with PZ films on STO as they grow with a relatively high lattice mismatch (6.8% at 700°C) and go through a phase transformation upon cooling.

6.4.2 Morphology

The as-grown thick PZ film surfaces are peculiar. They consist of a flat surface partly covered with pyramidal structures, all oriented in the same fashion with respect to the substrate, as shown in the SEM photo in Figure 6-7a. It is possible to distinguish fully-grown well-shaped pyramids with similar lateral dimensions and an average height of about 250 nm. In some areas, appearing opaque to the naked eye, the film surface was fully covered with pyramids (Figure 6-7b). The pyramids in these areas are significantly smaller and usually irregularly shaped as they hamper each other's development or grow together as shown in Figure 6-7b and c. Occasionally flat square crystals, rotated 45° in plane with respect to the pyramids, were observed next to or below the pyramids as shown in Figure 6-7d. The side facets of the pyramids have an inclination of about 50° with the substrate surface, as shown in the crystal drawings in Figure 6-7 displaying the angles, determined using AFM, between the facets of the pyramids and the surface of the film. The morphologies of the thin film and the etched thick film, observed by AFM, did not display specific features. The rms roughness of the successively etched film was reduced from 30 - 50 nm to around 20 nm, due to the disappearance of the pyramids. The thin PZ film has an rms roughness below 1 nm.

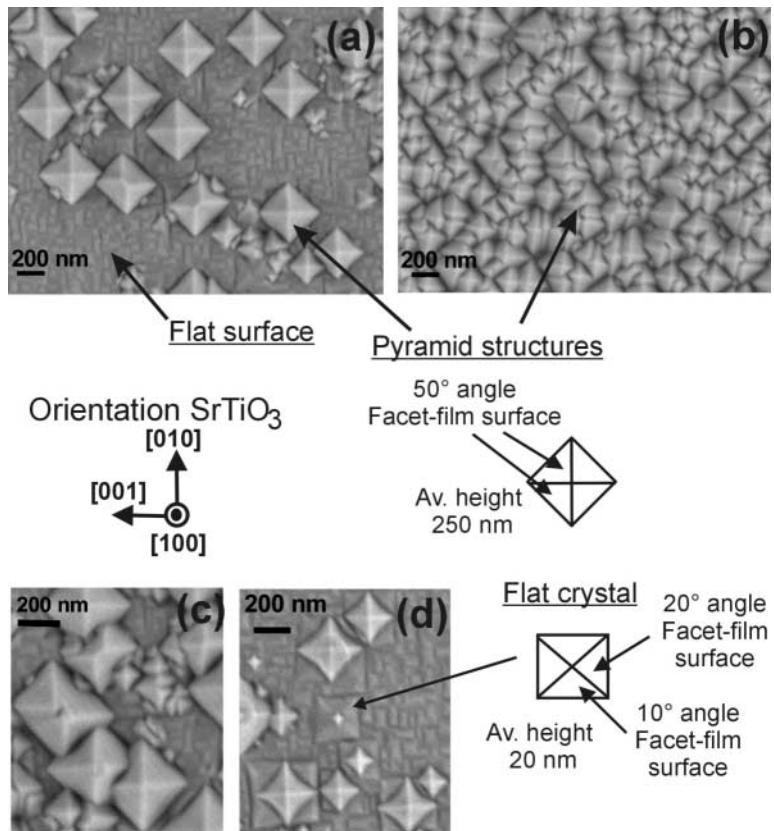


Figure 6-7: SEM photos and schematic representations of the surface morphologies of the PZ films on STO substrates. (a) SEM photo of a PZ surface partly covered with pyramids, (b) SEM photo of a PZ surface densely covered with pyramids, (c) Details of a SEM photo showing coalescent pyramids, and (d) SEM photo of the PZ surface displaying superposition of a pyramid on a square crystal. The schematic representation of the pyramid and the flat crystal are based on AFM data.

As both the second crystallographic domain and the pyramids were exclusively found on the thick films, one might speculate that these two features are correlated. The pyramids might eventually be outgrowths from the (002) domains. To check this assumption, local XRD $\theta - 2\theta$ measurements were performed in zones with a high pyramid density and in zones with a low pyramid density. However, no difference in the XRD intensity ratios of (120) and (002) peaks was observed. Figure 6-8a shows that the pyramids are easily observed in cross-section TEM photographs. The detailed photograph in Figure 6-8b shows a typical V-shaped area under the pyramids. However, for the area shown in Figure 6-8b, no differences in crystallographic domains were observed between the V-shape zone and directly adjacent areas. Only variant 1, corresponding to a (120) domain, was observed. Compared to the rest of the

layer, the V-shaped area has a higher density of dislocation loops, as shown in Figure 6-9. Furthermore, large voids, confirmed in under and over focus experiments, were found around the V-shapes. Enlargements of the pyramid areas reveal that about half of them do not have a uniform structure. For example, the pyramid imaged in Figure 6-8b is build up in layers. Local electron diffraction analyses on different locations in the pyramid itself, using Convergent Beam Electron Diffraction (CBED) with a probe of 20 nm, indicate that slightly different orientations are present in the pyramids as is shown in Figure 6-8b. The CBED analyses reveal a weak and a strong pattern in area 2 of Figure 6-8b. The patterns are mutually tilted by 5° and have slightly different d-spacing normal to the surface (4.15 \AA and 4.10 \AA) indicating the formation of local (002) domains at the top of the pyramid.

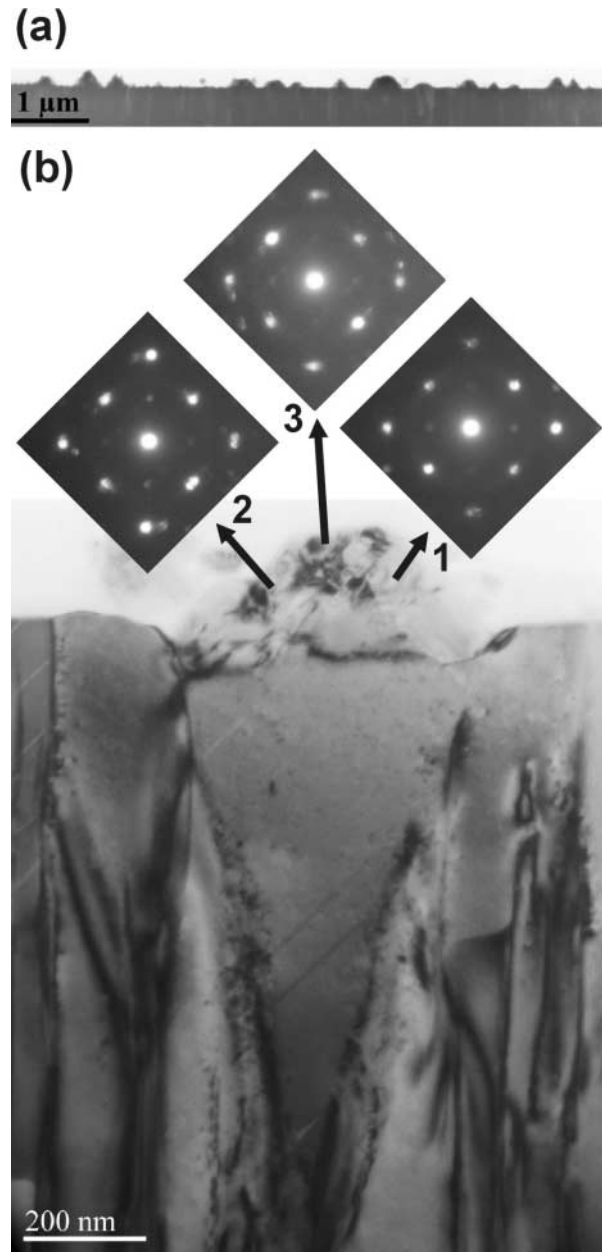


Figure 6-8: Cross-section transmission electron micrographs of a PZ film on STO. (a) The pyramids seen at the top of the surface correspond to those observed at the surface in top-view by SEM, and (b) Detailed cross-section of a pyramid with the typical V-shaped area observed under the pyramid. The inserted CBED of area 2 shows that at least two variants are present in area 2.

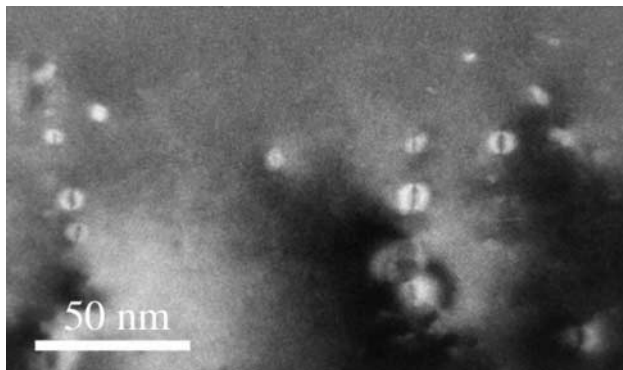


Figure 6-9: Bright field transmission electron micrograph of the typical dislocation loops observed in the V-shaped area located under the pyramid.

The results described above indicate that the pyramids are certainly not originating exclusively from (002) domains. Using a crystal morphology editor/viewer (133), it is possible to simulate (002) or (120) textured pyramids with circa 50° inclined low indices planes, corresponding to the SEM and AFM observations. In Figure 6-10b and d, it is shown that fully developed pyramids are obtained if the growth rate of the (120) and (002) top facets is at least 1.8 times larger than that of the pyramid side facets. An eventual facet indexing for the pyramids, based on the in-plane orientation of PZ on STO and the angles in between the facets measured by AFM, is given in Figure 6-10. The angles of roughly 54° between the indexed facets (Table 6-4) correspond well to the 50° angle observed by AFM (Fig. 7). The facets of the pyramids originating from (120) or (002) domains are the same but occur in a different order. It comes from the fact that there is only a rotation of 90° around the $\bar{[2}10]$ axis between a (002) oriented pyramid and (120) oriented one, and vice versa, as can be seen in Fig. 1 and Fig. 10. The occasionally observed square flat crystals might result from different growth rates from other facets leading to different square-like flat pyramids.

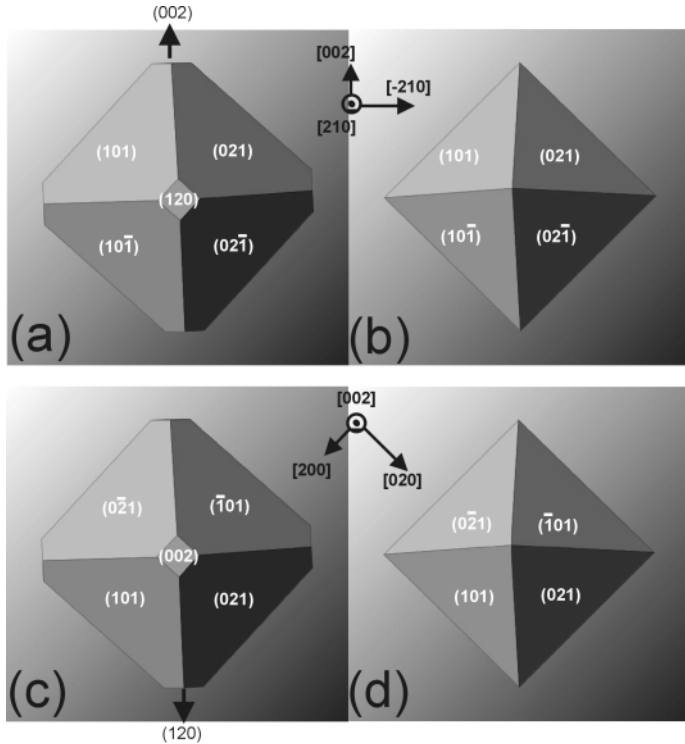


Figure 6-10: Simulated crystal shapes using Jcrystalsoft (133) to visualize the pyramids. (a) Pyramid issued from a (120) domain with a {120} and {002} growth rate of 1.5. (b) Pyramid issued from a (120) domain with a {120} and {002} growth rate of 1.8. (c) Pyramid issued from a (002) domain with a {120} and {002} growth rate of 1.5. (d) Pyramid issued from a (002) domain with a {120} and {002} growth rate of 1.8.

Table 6-4: Angles in between the facets as calculated with a crystal morphology editor / viewer (133).

	(120)	(002)
(101)	54.9	54.4
(021)	54.9	54.4

6.5 Discussion

At 700°C, cubic PZ grows epitaxially on the cubic STO crystal structure. As shown in Figure 6-1, upon cooling, cubic PZ is deformed to an orthorhombic PZ structure by stretching the cubic structure along one of its 12 edges, i.e. along one of the $\langle 110 \rangle$ directions. These 12 deformation possibilities result in a maximum of six different geometries of the PZ structure with respect to the STO substrate (see Figure 6-4b).

For a stretch along $[1\bar{1}0]$, as shown in Figure 6-1, the thin film-substrate relation is, by using pseudo-cubic notation for the PZ structure, $(100)[010]PZ//(100)[010]STO$ corresponding to $(120)[002]PZ//(100)[00\bar{1}] STO$ using the orthorhombic notation. However, the thin PZ film obtained in the present study shows the presence of several (120) domain variants. This means that the elongation has occurred along several out-of plane $<110>$ directions of the pseudo-cubic structure, namely $[1\bar{1}0]$, $[110]$, $[101]$, and, $[10\bar{1}]$, corresponding respectively to variant 1, 2, 3, and 4 of (120) domains. Stretching along the four other out-of plane $[\bar{1}10]$, $[\bar{1}\bar{1}0]$, $[\bar{1}01]$, $[\bar{1}0\bar{1}]$ directions is physically identical to stretching along $[1\bar{1}0]$, $[110]$, $[101]$, and, $[10\bar{1}]$, leading to a $(\bar{1}20)$ oriented domain instead of a (120) domain. Therefore they are not really different variants and are called sub-variants as shown in Figure 6-4b. At room temperature, the thin PZ film is not hetero-epitaxial as there is an orthorhombic structure on a cubic structure and the film contains one crystallographic domain composed of a maximum of four variants. The film is therefore not epitaxial in the way it is usually mentioned in the context of III-V materials, but possesses much more than a local epitaxy, therefore the film is defined as semi-epitaxial.

The structure of PZ films thicker than circa 260 nm deviates even more from an epitaxial structure since (002) domains are formed in addition to (120) domains. It is clear that above the threshold thickness (circa 260 nm), the impact of the STO substrate is smaller and the cubic structure can be stretched along the in-plane $<011>$ directions leading to (002) domains. Referring to Figure 6-4b, a stretch along $[0\bar{1}1]$ and $[01\bar{1}]$ leads respectively to (002) domain variants 1 and 2. For a stretch along $[0\bar{1}1]$ the thin film-substrate relation is, by using pseudo-cubic notation for the PZ structure, $(0\bar{1}1)[010]PZ//(100)[010]STO$ corresponding to $(002)[100]PZ///(100)[011] STO$ using the orthorhombic notation. Elongations along $[0\bar{1}1]$ and $[01\bar{1}]$ are directly equivalent leading to the sub-variants of (002) domains, just as for the (120) domains. In fact, a (002) domain corresponds simply to a (120) domain rotated by 90° from in and out of plane, as can be seen in Figure 6-1 and Figure 6-4a. The relation between the (120) and (002) domains is clearly seen with the pyramids at the sample surface, which can originate from both types of domains. Figure 6-10 shows that, if a (120) oriented pyramid is rotated by 90° around the $[\bar{2}10]$ axis, such that the $[002]$ orientation becomes normal to the surface, it becomes a (002) oriented pyramid. Pyramids from both (120) domain variant 1 and (002) domain variant 1 have the $(\bar{1}20)$ or $(\bar{1}20)$ side planes in common as can be seen in Figure 6-10. The development of pyramids at the PZ surface is due to a locally higher growth rate of the (120) and (002) planes with respect to the pyramid facets and to the (120) and (002) planes of the surrounding flat surface domains. Initially, the higher growth rate might be triggered by some kind of defect, and then it grows out as a V-shaped zones.

The V-shaped area under the pyramid contains a higher density of dislocation loops than the adjacent areas. Since growth of the V-shaped crystal volumes did not proceed along {120} and {002} planes, as for the rest of the layer, but took place through the {101} and {021} sides facets of the pyramids, this might result in a different defect level with respect to the rest of the layer. Alternatively, the higher defect level is expected to result in the increased growth rate of the (120) and (002) top faces of the V-shaped area. The growth rate can be estimated to be 1.2 times higher than in the flat domains, by considering that the largest pyramids have a height of roughly 250 nm and that the largest pyramids start roughly at the threshold thickness of 260 nm for a circa 1400 nm thick PZ layer. This higher growth rate of the (120) and (002) in the pyramids, might be a contributing factor to the 2.5 larger growth rate of the thick films with respect to the thin films (Table 6-1) as the thick films contain many pyramids. Nevertheless, the major factor for the higher growth rate of the thick film is that the PZ seem to grow faster once the substrate is covered by PZ as we observed a similar behavior for the other PZT composition grown.

The room temperature lattice mismatch (f) for (120) oriented domains is determined by

$$f(120) = \frac{2a_{\text{STO}} - c_{\text{PZ}}}{c_{\text{PZ}}} = -5.0\%,$$

and the lattice mismatch for the (002) oriented domains is determined by

$$f(002) \text{ along } [010] = \frac{2\sqrt{2}a_{\text{STO}} - b_{\text{PZ}}}{b_{\text{PZ}}} = -6.1\%,$$

$$f(002) \text{ along } [100] = \frac{\sqrt{2}a_{\text{STO}} - a_{\text{PZ}}}{a_{\text{PZ}}} = -6.2\%.$$

For both domains, the calculated lattice mismatch at room temperature indicates a PZ film in compression. Nevertheless the 2θ peaks observed in the XRD spectra of Figure 6-2b and listed in Table 6-2 and Table 6-3 indicate that only the thin film is in compressive stress with the d(120) lattice planes 0.2% in tensile stress. As can be seen in Table 6-5, the lattice mismatch is roughly constant at all temperatures. It is expected that most of the lattice mismatch is absorbed in the defective intermediate layer of roughly 10 nm observed at the interface STO-PZ containing numerous misfit dislocations and voids. Additionally, the threading dislocation, observable in most BE micrographs, originate from this layer. Their presence might be correlated to misfit dislocations and stress release (108). Nevertheless, additional minor factors also contribute to the stress release as no stress is observed in the thick layers. The formation of all possible domain variants above the threshold thickness might be one of these minor factors. The thermal expansion coefficients (134) difference between STO and PZ is not large with respect to the lattice misfit, therefore, as can be seen in Table 6-5, its role is minor. But below the Curie temperature, the expansion coefficient along the pseudo-cubic c-axis is $28 \times 10^{-6} \text{ K}^{-1}$ and $-0.5 \times 10^{-6} \text{ K}^{-1}$ along the

two other axes (122), therefore when the c-axis is in-plane, as for (120) domains, tensile stress will form and might compensate for compressive mismatch stress.

Table 6-5: Mismatch and thermal strain in PZ films on STO substrates as a function of temperatures. Mismatch: $f = (a_{\text{STO}} - a_{\text{PZ}})/a_{\text{PZ}}$ above T_c and as described above for temperature lower than T_c . Thermal strain: $\epsilon_T = (\alpha_{\text{STO}} - \alpha_{\text{PZ}})\Delta T$.

Temp (°C)	PZ Lattice Constants (Å)	PZ Thermal Expansion Coeff. (10^{-6} K^{-1})	STO Lattice Constants (Å)	STO Thermal Expansion Coeff. (10^{-6} K^{-1}) (134)	Mismatch f (%)
700	4.161	7.7 (134)	3.934	11.7	-5.5
500	4.155	7.7 (134)	3.925	11.2	-5.5
230 ($\approx T_c$)	4.146 (122)	7.7 (134)	3.913	10.4	-5.6
150	$a \approx 5.87$ $b \approx 11.73$ $c \approx 8.24$	-0.5 (a' , b') (122) * 28 (c') (122) *	3.910	10.6	-5.1 for (120) up and -5.7 and -5.8 for (002) up
RT	$a = 5.884$ $b = 11.768$ $c = 8.220$	-0.5 (a' , b') (122) * 28 (c') (122) *	3.905	10.3	-5.0 for (120) up and -6.1 and 6.2 for (002) up

Temperature range	Thermal strain
700 – 230	circa $1.6 \cdot 10^{-3}$ (compressive upon cooling)
230 – RT	along a' pseudo-tetra $2.2 \cdot 10^{-3}$ (compressive upon cooling) along c' pseudo-tetra $-3.6 \cdot 10^{-3}$ (tensile upon cooling)

* the expansion coefficients are given for a' , b' , and c' being the pseudo tetragonal unit cell parameters.

6.6 Summary

The structure and the morphology of PZ films grown on STO by MOCVD have been investigated for the first time. A schematic overview of the different observed features is shown in Figure 6-11. At 700°C, the PZ films are epitaxially grown in their cubic paraelectric phase on cubic STO substrates. During cool - down, the cubic PZ structure is transformed to orthorhombic as it goes through the paraelectric-antiferroelectric phase transition. For a film thinner than the threshold thickness of circa 260 nm, the stretching of the cubic structure responsible of the orthorhombic structure is limited to four pseudo-cubic directions [110], [110], [101], and, [101], and results in a semi-epitaxial PZ film composed of a maximum of four (120) domain variants. For films thicker than the threshold thickness, the stretching of the cubic structure can also occur along the [011] and [011] directions due to a smaller impact of the substrate. The resulting PZ layer is composed of (002) as well as (120) oriented domains, with respectively 2 and 4 variants each. These variants correspond to the 6 different elongation directions (along the 12 cube edges from the cube) of the paraelectric cubic structure to form the antiferroelectric orthorhombic structure. The lattice misfit is roughly -5% at all temperatures, but only the 100 nm thick PZ layer is

in slight compression. At the interface STO-PZ, a layer of roughly 10 nm thickness, containing voids, misfit dislocations, and the origins of the threading dislocations growing up to the film surface, was observed. The defective intermediate layer formation and its associated mechanisms probably accommodate most of the lattice misfit. For layers thicker than the threshold thickness of 260 nm and relaxed at room temperature, the additional formation of (002) domains might also contribute to release the remaining lattice misfit stress. In addition to (002) domain formation, peculiar pyramids of different sizes are observable at the surface of films thicker than the threshold thickness of circa 260 nm. Pyramids can originate from (120) and (002) domains and develop due to a circa 1.2 higher growth rate of the {120} and {002} planes in the pyramids with respect to the rest of the layer. Initially, the higher growth rate might be triggered by any kind of defect. The formation of pyramids leads to V-shaped zones growing from {101} and {021} facets containing a high dislocations density with respect to the rest of the layer growing from {120} and {002} planes, indicating eventual differences in the layer growth mechanisms between {101}, {021} and {120}, {002} planes.

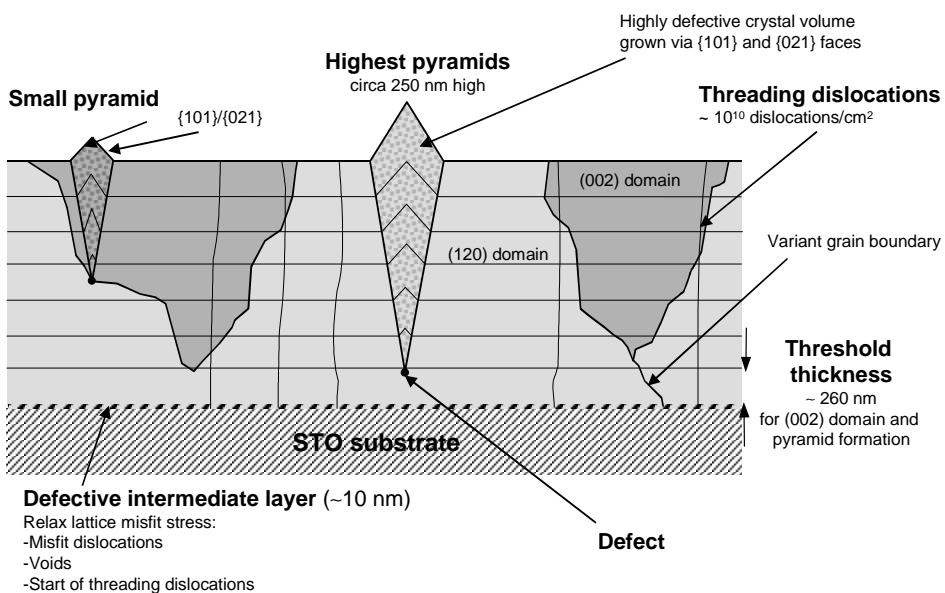


Figure 6-11: Schematic cross-section of a thick PZ film detailing the different features of these films as observed and discussed in the present work.

Chapter 7

Influence of the Lead Stoichiometry on the Morphology and Structure of the PZT Films

7 INFLUENCE OF THE LEAD STOICHIOMETRY ON THE MORPHOLOGY AND STRUCTURE OF PZT FILMS

In this section, not all the grown films were smooth and consist of a single phase but some of them display unique crystals. These films cannot be used to produce devices, such as the ones described in Section 1.4, but detailed information on these crystals provides additional feedback for the growth problems and guidance to more rapid interpretation of the PZT film morphology. Additionally, on a long term, sufficient and accurate knowledge on PZT crystal growth might lead to new developments, such as growing larger crystals, to broaden application possibilities.

To illustrate this point, one polycrystalline PZT film grown on a platinized substrate and a PT film grown on STO are detailed below. The surface morphology, the structure, and possible origins of the different crystal morphologies and compositions are studied. The lead-poor / Zr-rich crystals were observed in a polycrystalline PZT film and the lead-rich crystals in semi-epitaxial PT films and polycrystalline PT films.

7.1 PZT lead-depleted crystals in a polycrystalline PZT film grown on platinized silicon wafers

The PZT layer was grown on a 6" diameter platinized silicon wafer with the same gas conditions as described in Table 2-2 and Section 5.2, but unexpectedly a different type of PZT layer than the one shown in Color Figure 4 was obtained. The wafer's morphology was studied by SEM and its composition by EDS and XRF. The structure was determined by XRD and thickness measurements were performed by stepprofiler measurements after etching a step in the different zones of the layer.

7.1.1 *Results*

7.1.1.1 Morphology, composition, and thickness

An overview of a quarter of the wafer is shown in Color Figure 6. Seven color rings can be observed from the edge to the center of the wafer. These different colors correspond mainly to thickness inhomogeneities as observed for other wafers (Color Figure 3) but also to different crystal morphologies. Zone 1 and zone 3 display a typical polycrystalline PZT morphology with crystals shaped differently, respectively circa 200 - 300 nm wide in zone 3 and circa 100 - 200 nm wide in zone 1. On the other hand, zone 2 contains large (circa 1 μm width) flat triangle crystals embedded in a fine granular matrix of small round crystals (circa 30 nm width). From zone 3 to zone 7, the crystals become more and more disparate and form a discontinuous layer.

The transition from zone 1 to zone 2 (or zone 2 to zone 3) is relatively sharp with a width of ~ 1mm and is shown from zone 1 to zone 2 in Figure 7-1. The PZT crystals of different shapes transform progressively to large (500 - 800 nm) flat triangular crystals. At the transition between the two zones, the density of the triangles is high as can be seen in Figure 7-1d, but is low at the middle of zone 2 as can be seen in Color Figure 6 (inset zone 2).

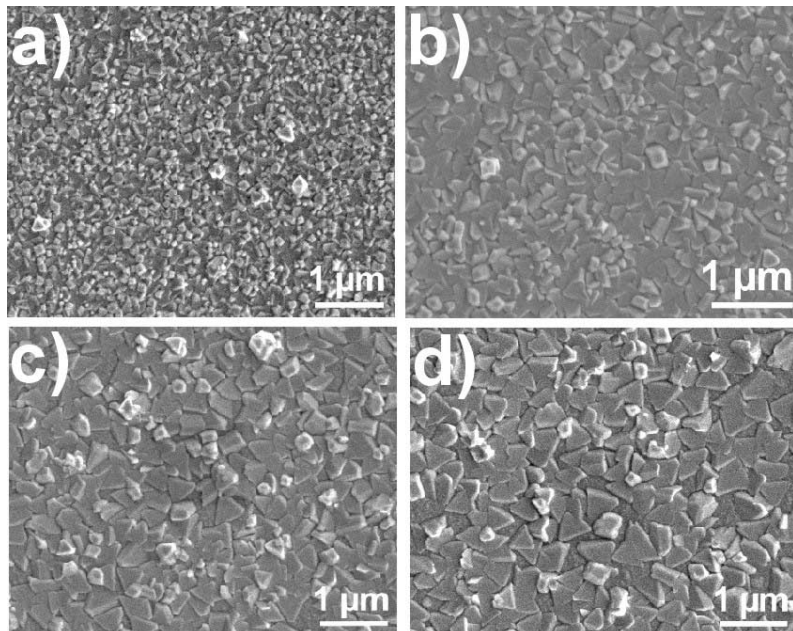


Figure 7-1: Morphology transition from zone 1 to zone 2 for the non-homogenous PZT film on platinized silicon wafer. a) Zone 1, b) zone 1 to zone 2, c) zone 1 to zone 2, and d) zone 2.

The composition of the different zones was measured by XRF for all zones and by EDS from zone 1 to zone 3 in the different features. XRF measures the average composition in the different zones, but features such as the flat triangles can be measured independently by EDS. The results are summarized in Table 7-1.

The stoichiometry in the film phase is very different from the gas phase, which was set as $A = 1$ and $x = 0.24$ for this run. As seen in Section 5.2, for a standard film, the x ratio in the solid phase is roughly twice as that of the gas phase, but for this film it is about 3 times higher. Therefore a large Zr concentration is present in these non-reproducible conditions compared to a standard run. In addition to the high Zr composition, zone 1 is lead-rich (A ratio = 1.40 (XRF) and 1.00 (EDS)) and zone 2 is on average lead poor (A ratio = 0.66 (XRF) and 0.44 (EDS average of both features)). In zone 2, the different features have a different composition: the flat triangles contain

more lead (A ratio = 0.51) and the granular matrix of the layer contains very little lead (A ratio = 0.37). The error on the XRF measurements is smaller than with EDS (refer to Section 3.1.7), but both techniques are in agreement for zone 3. For zone 1 and zone 2, XRF indicates a higher lead content in the layer.

Table 7-1: Composition measured by XRF and EDS on the inhomogeneous PZT film.

Zones	XRF		EDS	
	A ratio	X ratio	A ratio	X ratio
Zone 1	1.40	0.76	1.0	0.76
Zone 2 - granular matrix	0.66	0.72	--	--
	--	--	0.37	0.51
	--	--	0.51	0.74
Zone 3	0.90	0.67	0.91	0.72
Zone 4	1.03	0.7	--	--
Zone 5	1.03 - 0.87	0.70 - 0.64	--	--
Zone 6	0.87	0.64	--	--
Zone 7	0.86	0.55	--	--

The thickness of the various zones was measured with a Veeco Dektak ST stepprofiler¹³ after etching a step in the different zones. The measurements are not so accurate as the heights to be measured were relatively small, the surfaces not really smooth, and there is a 5% instrumental error. The thickness was also estimated by XRF for zones 6 and 7 only, the other samples being too small for thickness estimation with this technique. As shown in Figure 7-2, the thickness profile of the layer is not smooth and the stepprofiler and XRF measurements are not in agreement in zone 6. Zone 2 is thinner than its neighboring zones according to stepprofiler measurements.

7.1.1.2 Structure

Raman measurements were performed in each zone of the wafer, but the signals were too weak, due to the small layer thickness, to detect clear peaks. The three characteristic PZT bands (as shown in Section 3.1.5) were visible in zone 1 and 3 but not in zone 2 (having a featureless spectrum), indicating a phase difference in zone 2.

¹³ Bert Otter (Twente University) is acknowledged for letting me use their stepprofiler.

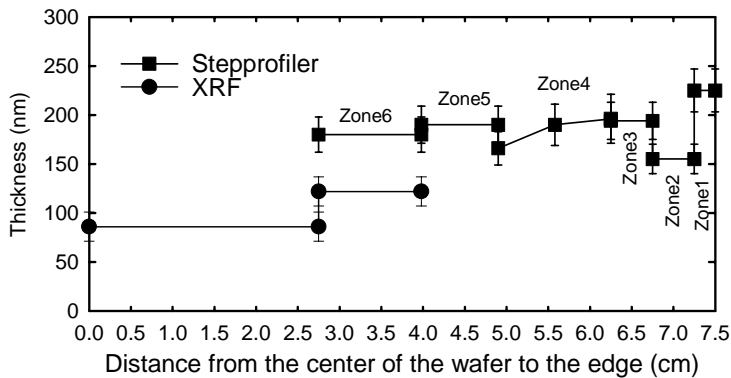


Figure 7-2: Thickness profile of the PZT film.

XRD measurements of each zone can be seen in Figure 7-3. Similarly as for Raman, the XRD peaks have a low intensity. The Pt (111) - α peak at $2\theta = 39.80^\circ$ correspond well to the Pt peak for the annealed wafer and the Pt (111)- β peak is clearly visible on all spectra as well as the Pt (111)-W peak. An asterisk indicates all the XRD peaks due to the platinized silicon substrate. The XRD spectra from all the zones contain peaks originating from PZT tetragonal and rhombohedral phases, indicated respectively by filled and opened triangles. It agrees well with the composition measurements indicating a high x ratio in the film and the fact that both the tetragonal and the rhombohedral phases are observed in high x ratio films (as already discussed in Section 5.4).

Zone 2, shown in Figure 7-3b, displays smaller intensity PZT peaks than those shown in the other zones and two additional high intensity peaks at $2\theta = 30.00^\circ$ and 34.70° , of respectively 85% and 100% intensity. These peaks, indicated by a filled circle in Figure 7-3b, do not correspond to PZT peaks. The peak at $2\theta = 34.70^\circ$ also appears slightly in zone 3 and clearly in zones 4 to 7, shifting progressively from circa 0.09° to lower d-spacing from zone 2 to the center.

The second phase in zone 2 can originate from many oxides, but as the wafer composition is Zr rich, the XRD spectrum of zone 2 was first compared to that of a MOCVD Zr_xO_y film deposited in a single oxide growth series. The XRD spectrum and the morphology of the Zr_xO_y film are shown in Figure 7-4. The additional peaks observed in Figure 7-3b correspond relatively well to the peaks of the Zr_xO_y film (Figure 7-4) but the respective intensity 100% and 30% is different, as shown in Table 7-2. The stoichiometry of this Zr_xO_y film was deduced by comparing the d-spacing values with values tabulated for different Zirconium oxides in the ICSD and listed in Table 7-2. The Zr_xO_y phase observed in these films is not ZrO , Zr_3O , neither ZrO_2 baddeleyite with a monoclinic structure, but can be ZrO_2 tetragonal (135) or

orthorhombic (136) (Table 7-2). Orthorhombic ZrO_2 (ICSD 83-809) has the closest d-spacing difference for both films.

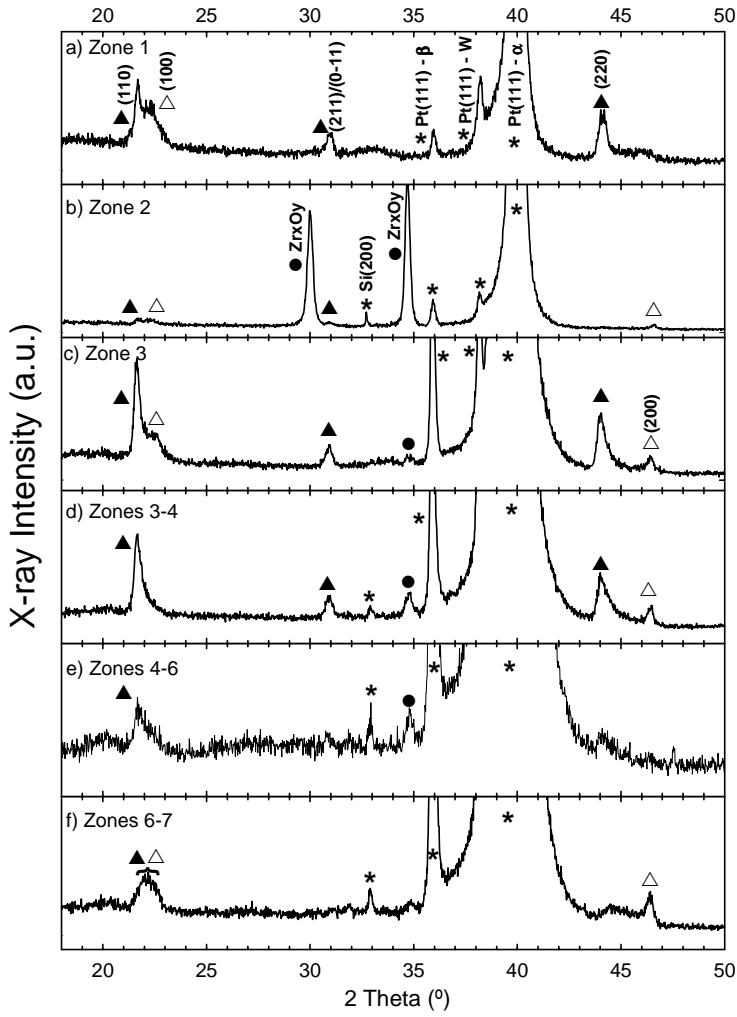


Figure 7-3: XRD spectrum from the different zones observed in the wafer. a) Zone 1; b) Zone 2; c) Zone 3; d) Zone 3-4; e) Zone 4-6, and f) Zone 6-7. The asterisks indicate peaks due the substrate, opened and filled triangles indicate respectively the PZT tetragonal and rhombohedral phase, and the filled circles indicate the Zr_xO_y phase.

The additional peaks in zone 2 do not correspond to pyrochlore structure ($\text{Pb}_2(\text{Zr}_{x}\text{Ti}_{1-x})_2\text{O}_7$) appearing often instead of the perovskite at low growth or anneal temperatures (137). The two typical pyrochlore diffraction peaks at 29.55° (222) and at

34.33° (400) with respectively 100 % and 55 % intensity as shown in Ref. (138) correspond less well to zone 2 peaks than ZrO_2 . Additionally, the diffraction peak from the (222) planes (at 29.55°) usually appears at first when this phase is present and for this film it is the other peak at 34.70° , which stays present in the other zones. Additionally, there is a clear stoichiometry difference (Zr rich, lead poor) in zone 2, indicating that the additional phase is most likely not pyrochlore.

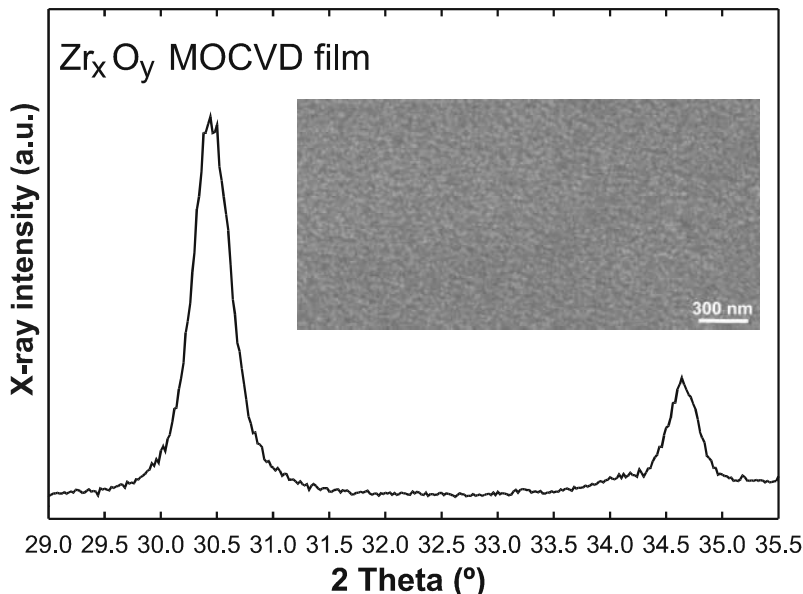


Figure 7-4: XRD spectrum and morphology (inset) observed by SEM for one of the MOCVD $\text{Xr}_{x}\text{O}_{y}$ film.

Table 7-2: d-spacings for the extra phase in zone 2, $\text{Zr}_{x}\text{O}_{y}$ MOCVD film, zirconium oxide compounds, and pyrochlore PZT.

Compounds	d-spacings; (relative peak intensity); (diffraction plane)
Zone 2	2.979; (85%)
PZT film	2.586; (100%)
$\text{Zr}_{x}\text{O}_{y}$	2.590; (100%)
MOCVD film	2.936; (30%)
ZrO_2	2.964; (50%); (011)
Orthorhombic (136)	2.619; (93%); (111)
ZrO_2	2.995; (100%); (101)
Tetragonal (135)	2.635; (39%); (002)
Pyrochlore	3.020; (100%); (222)
PZT (138)	2.610; (55%); (400)

7.1.2 Discussion

There are two phases observed in zone 2. The fine-grained phase is assigned to orthorhombic ZrO_2 from XRD measurements even though the 2θ positions do not match exactly the ones tabulated for orthorhombic ZrO_2 . In addition, the featureless granular morphology of this Zr_xO_y film, shown in Figure 7-4, is very similar to the granular phase in between the flat triangles in zone 2. It is in agreement with the composition measurements indicating that the granular phase of zone 2 contains less lead than the flat triangles. The other phase, composed of triangular flat crystals, corresponds therefore to the PZT signal observed in the XRD. As observed by SEM, the PZT bulky grains transform progressively to flat triangles as shown in Figure 7-1. In zone 1, the surface is completely covered by PZT grains, and no Zr_xO_y signature is observed in the XRD spectra, whereas for Zones 4 - 7, the wafer surface is covered with disparate PZT crystals with a sort of granular matrix and then the Zr_xO_y signature is also observed in the XRD spectra at $2\theta = 34.70^\circ$. It has not been further investigated by EDS, but part of this background could also be the ZrO_2 phase.

Attributing the granular phase observed in zone 2 to ZrO_2 is also in agreement with earlier results in Ref. (139), which indicate that MOCVD ZrO_2 films were smooth and fine grained. But their films were indexed as monoclinic ZrO_2 and it does not correspond to our indexing. Additionally, it was observed that zone 2 etched more slowly than the other zones and was never totally removed from the Pt substrates. It might be correlated to the observations of Balog et al. (139) who showed that the ZrO_2 films adhered strongly to the substrate (Pt was one substrate type used in their studies).

Even though the EDS measurement indicates a relatively low A ratio in the flat triangular crystals, PZT crystals are still formed in zone 2 but peculiar flat triangular crystals are formed instead of the standard PZT bulky multi-shape crystals. As the crystals are very flat, there is a clearly higher preferential growth rate in plane, which is not the case for the PZT crystals in the other zones. Similar flat PZT crystals had been observed by Shimizu et al. (125) (as discussed in section 5.3) for an A ratio of 0.5 and this peculiar shape disappeared for A ratio of 0.6. This is in agreement with our measurements indicating that flat triangular crystals are formed for low A ratio. Shimizu et al. (125) could show that the in-plane facet was a (111) plane, in agreement with our measurements on other PZT layers (Chapter 5). But the XRD for zone 2 did not allow any facet indexing, as there is a low XRD signal in Figure 7-3c and no additional PZT diffraction planes are seen with respect to the other zones.

Assuming that the flat triangular crystals in zone 2 observed at room temperature developed during growth, at 700°C in the cubic PZT phase, similarities can eventually be found with the formation of tabular crystals with a FCC lattice. In an earlier work, G. Bögels et al. (140) studied the growth mechanisms and twinning formation of tabular silver-halide crystals used in photographic emulsions and generalized their observations to FCC materials. They showed that for FCC crystals grown by vapor

phase, small sized crystals and supersaturation above a certain threshold enhanced twinning. Both these conditions are fulfilled in zone 2 with a considerable supersaturation in Zr; therefore we could assume that twins are formed during the growth of the PZT grains in zone 2. Additionally, PZT crystals seem to twin easily as Glazer et al. (15) reported that their $\text{PbZr}_{0.9}\text{Ti}_{0.1}\text{O}_3$ crystals were always twinned which prevent them from refining the PZT structure properly on crystals. G. Bögels et al. showed experimentally that there is a lateral growth preference by means of substep mechanisms leading to tabular (flat) crystals (140). The small sizes of the crystals in zone 2 prevent any detailed studies, but there is a lateral growth preference leading to flat PZT crystals in zone 2. The mechanisms might be the same for our cubic perovskite as for FCC crystals.

7.1.3 Conclusion

The run conditions for this layer were standard and in general this would result in relatively uniform and stoichiometric wafers (Color Figure 4). However, there was on average three times more zirconium in the layer than in the gas phase. This Zr problem created special lead-depleted conditions and unusual crystals grew in a specific zone on the wafer. In this zone, two phases grew together: ZrO_2 and perovskite PZT, whereas the remainder of the layer contains mainly perovskite PZT. The ZrO_2 has a fine-grain morphology whereas the PZT phase is composed of flat triangular crystals. PZT perovskite crystals do not usually have such preferential higher lateral growth rates. It is assumed that this peculiar PZT morphology is due to the lead deficiency and initial twinning during growth (in the perovskite cubic phase). It is in agreement with previous reports on MOCVD PZT films by other researchers showing that (111) texture triangular grains were formed in a lead deficient environment. The lateral growth is eventually due to a substep mechanism, in a similar fashion as for FCC crystals.

7.2 Lead oxide crystals on semi-epitaxial PT films grown on STO and polycrystalline PT films grown on platinized silicon wafers

Twelve PT films were grown simultaneously, in one run, on ten STO substrates and two platinized silicon substrates. The substrates were all 10 by 10 mm and placed in a 6" diameter Si wafer with laser cut spaces to hold them. This sample, placed at the middle of the Si wafer, was a smooth PT film with no additional phases. The films presented in this section displayed a very rich variety of crystals originating from Pb_xO_y phases as confirmed by XRD and Raman. The PT films were grown on substrates placed at the outermost radial position of the 6" diameter Si wafer during a PT run whereas the PZT films presented in Section 7.1 were obtained in non-reproducible conditions.

7.2.1 Results

Four PT samples are described here and listed in Table 7-3. There are two semi-epitaxial PT films grown on STO crystals. In this section, the orientation normal to the surface of the STO substrates is chosen as [001]. There are two polycrystalline PT films grown on platinized silicon wafer pieces. The 10 by 10 mm Pt substrate pieces were cleaved from a 6" diameter platinized silicon wafer, like the ones described in section 4. The thickness, estimated by ellipsometry, of the four films is $\sim 900 \pm 50$ nm. The substrates of the PT films presented here were all placed at the outermost radial position on the susceptor.

Table 7-3: List of the PT films.

PT film	Substrate	Specificities	Radial Position w.r.t center
Film 1 Semi-epitaxial PT	STO	Covered by different crystals	6 cm
Film 2 Semi-epitaxial PT	STO	Covered slightly by one type of crystal	5.5 cm
Film 3 Polycrystalline PT	Pt	Variety of crystals	6 cm
Film 4 Polycrystalline PT	Pt	Variety of crystals	6 cm

7.2.1.1 Morphology

The morphology of the PT film 1 is shown in the photograph in Figure 7-5a, where five zones can be clearly distinguished. Each zone corresponds nearly to one type of crystal morphology, but some crystals intermix with each other. Morphology of typical crystals in each zone is shown in the SEM pictures in Figure 7-5b-l. In Zone 1, the fine pattern of the a - c domains is visible with additional large disparate crystals. Two examples of these crystals are shown in Figure 7-5b-c. Zone 2 is a sort of small transition zone and contains several undefined multishaped crystals (Figure 7-5d-e). Zone 3 contains edgy crystals terminated like a line (Figure 7-5f), named line topped (l-t), oriented both along the STO [100] and [010] directions. This zone also contains patches of different crystals: square crystals ending in a point, called point terminated (p-t) (Figure 7-5g) and some kind of elongated outcrops with a lateral and normal preferential growth directions, like the ones seen in Zone 5 (Figure 7-5k). Crystals terminated by flat terraces, called terrace-topped (t-t) crystals, are characteristic of zone 4 (Figure 7-5i) and the transition between zone 3 and zone 4 is shown in Figure 7-5h where both t-t and l-t crystals are visible. Zone 5 is covered, not fully but much more than zone 1, by various crystals also observed in the other zones (Figure 7-5j-l).

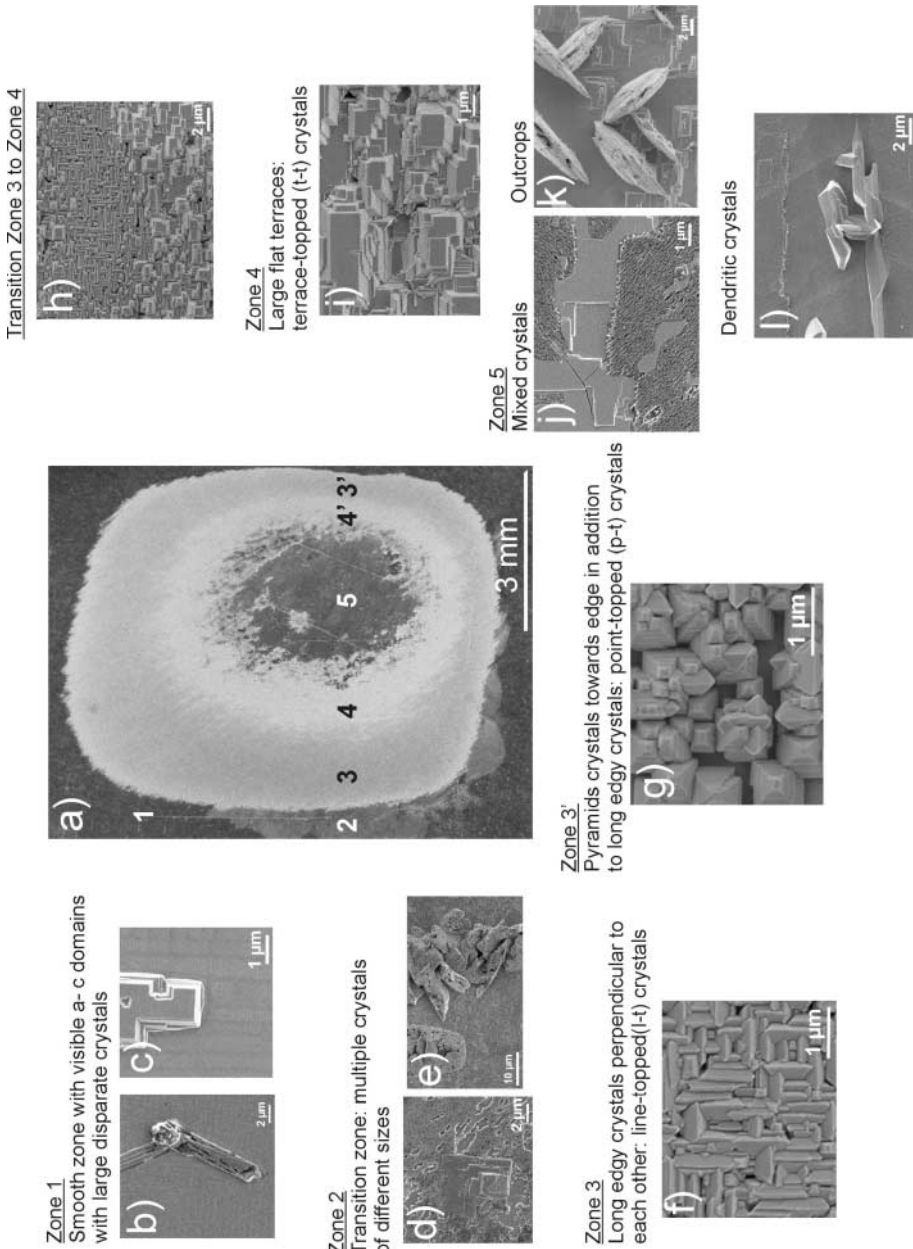


Figure 7-5: Lateral cross-view of the surface morphology of the PT film on STO.

The PT film 2 is very smooth and in addition to the typical a-c domain structure, dendritic crystals, similar to the ones shown in Figure 7-5l can be observed in the optical micrographs in Figure 7-6. The crystals were thinner at the edge of the film (Figure 7-6a) and thicker at the center of the film (Figure 7-6b). The majority of these crystals is oriented 45° from the STO [100] and [010] directions and give rise to a 45°

oriented stripped patch visible by naked eye, similarly to the 45° orientation, which can be seen in Figure 7-5a. Other PT films on STO were examined and when few crystals are visible in addition to the standard a-c domain structure, these dendritic are the first ones to appear in these non-PT favorable conditions.

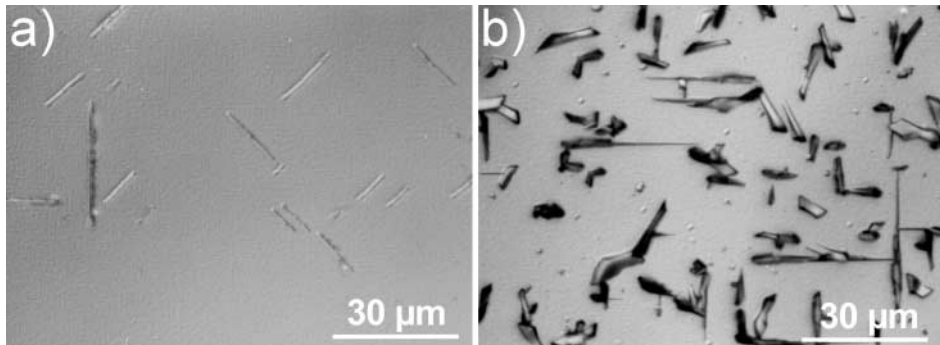


Figure 7-6: Optical microscopy images of the foreign crystals in PT film 2. a) Small "dendritic" crystals at the edge of the film and b) Developed "dendritic" crystals at the center of the film.

The morphology of the polycrystalline PT films was investigated by SEM. The surface of the films was not smooth at all and some kind of "bellies" could be observed, as shown in Figure 7-7a for PT film 3. It is unclear if these belly shapes come from the grown crystals or from the damage in the Pt layer after the five hours run at 700°C. On the top of these features, platelet-like crystals could be observed (Figure 7-7b). The rest of the layer (Figure 7-7c) was composed of the standard PT morphology (see section 5.5.2) and additional large crystals, similar to the outcrops shown in Figure 7-5k.

Some outcrops are very regular and oval (Figure 7-5k) and others are multi-shaped and multi-sized as in Figure 7-5e and Figure 7-7b. On the polycrystalline films, the outcrops are randomly oriented but they are ordered in plane, 45° from [100] and [010] STO for the PT film 2. Platelet-like crystals have been observed by Madsen et al. (141) on MOCVD lead oxide films grown on Si and SiO₂ / Si substrates. The films were composed of the litharge / scrutinyite and massicot / scrutinite lead oxide phases. Additionally, the same platelet crystals as the ones observed in Figure 7-7a have been observed by SEM by Hendriks (142) on lead oxide crystals grown on sapphire by MOCVD. He analyzed these platelet crystals as being litharge PbO and further TEM analysis revealed that the orientation of the side facets were normal to <201>. Both works reported in literature indicate that the platelet-like crystals, Figure 7-7a, are litharge PbO crystals.

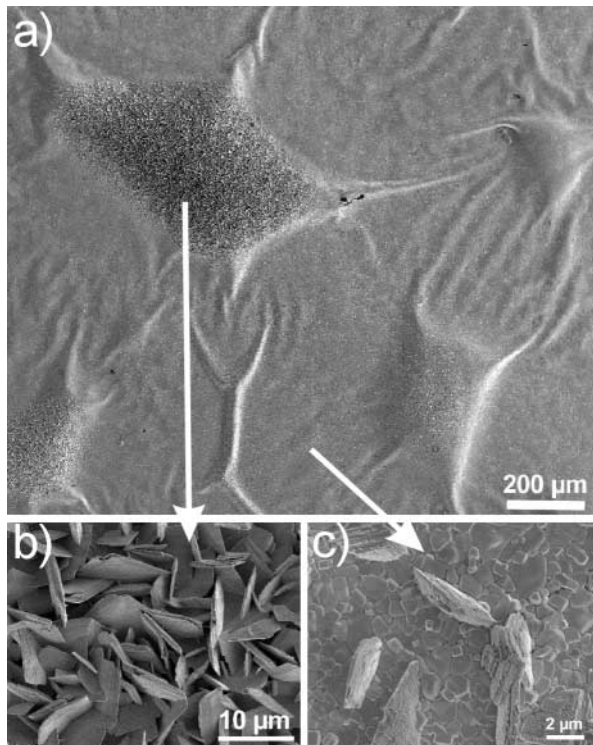


Figure 7-7: SEM picture of the crystals visible in PT film 3. a) overview of the film morphology. b) zoom in on the platelet crystals, c) zoom in on the PT crystals with outcrops. The platelet crystals were only observed on the “bellies” at the film surface.

The PT film 4 was cleaned successively in acetone and isopropanol prior to the SEM investigation. Unfortunately, the layer started to peel off after the cleaning and morphology observation was not possible anymore. Nevertheless, remainders of similar “bellies” were observed.

7.2.1.2 Composition in PT film 1

The compositions in the different zones of the PT film 1 were measured by EDS using an accelerating voltage of 9 kV. The composition is given as the A ratio in Table 7-4. Zone 1, with an A-ratio of ~ 1.1 corresponds well to the measurements on smooth samples having also an A-ratio of 1.1. On the other hand, there is a clear additional lead content in zones 2 to 5. In the t-t crystals, there is circa 22 times more lead than Ti. This doesn't directly mean that there is more lead in the t-t crystals than in the dendritic crystals. The penetration depth of the electron in the material for EDS is roughly 350 nm at 7 kV in a film of this type of material (Figure 3-6) and is higher at 9 kV. If the crystals grew on the top, or at a certain thickness, the A-ratio, determined by EDS, will depend on how much of the signal from the underlaying and surrounding PT is picked up. For the t-t crystals, the A ratio might simply be higher as

the film is completely covered by these crystals. On the other hand for the outcrops and the dendrites, the PT layer is only partly covered by these crystals and the A-ratio is lower as PT material is included in the probed volume.

Table 7-4: Composition measured by EDS on the PT film on STO.

Zones	EDS - A ratio
Zone 1 Smooth zone Figure 7-5b-c	1.1
Zone 2 Start of mixed terrace-like crystals Figure 7-5d-e	14.2
Zone 3 Concentration of special vertical platelets crystals Figure 7-5k	3.8
Zone 3' Blocky crystals Figure 7-5f	7.4
Zone 4-5 Terraces Figure 7-5i	21.7
Zone 5 Dendritic crystals Figure 7-5l	4.4

Only the lead and titanium elements were detected by EDS in the PT film 1, nevertheless, it is difficult to detect eventual contamination by EDS. For example Pb and Si lines overlap at 1.83 keV and eventual Si contamination measurements from the Si substrates holder or the Pt wafer is not possible. Therefore XRF was performed with different spot sizes on PT film 1. No contamination of Si, Pt, or Zr (above the 0.1 wt% detection limit of the instrument) was found. The A ratios measured by XRF, shown in Table 7-5, also indicate that the crystals are lead-rich. When a larger spot size is used, the A-ratio decreases as zone 1, corresponding to PT, is also measured. It is also true for zone 5, which is not totally covered by crystals. Additionally, using the XRF data and a density of 9 g/cm³, the layer thickness could be estimated as ~ 1 µm, corresponding relatively well with the ellipsometry estimation of 900 ± 50 nm.

Table 7-5: A-ratio measured by XRF in PT film 1.

Spot size - zone	A-ratio
5 mm - zone 4- 5	2.85
5 mm - zone 5	2.45
10 mm - whole sample	2.33

Both analysis techniques, EDS and XRF indicate that the additional crystals are lead-rich in PT film 1. This is in agreement with the morphology observation in PT film 3, compared to reports in literature, indicating that the platelet-like crystals are from litharge PbO.

7.2.1.3 Structure

XRD

$\theta - 2\theta$ scans were performed on all the films using the Powder diffractometer Philips PW1820 and the Bruker D8 (Figure 7-8a). In addition to the PT peaks and the substrate peaks, additional peaks are seen in both the semi-epitaxial and the polycrystalline films. Note that the PT(100) and STO (001) peaks overlap and that PT(100) peak is not visible for the hetero-epitaxial films grown on STO. For PT film 1, covered with a variety of crystals, there are several additional peaks, whereas there is only one type of crystal covering the PT film 2 and very few additional peaks to be seen. In the semi-epitaxial film, only PT (001) related peaks can be observed whereas PT (001), (100), (110), (111) related peaks can be seen in the polycrystalline films.

From the composition analysis and comparison of the crystal morphology from PT film 2 with results in literature, it was clear that Pb_xO_y phases were the most probable as additional phases. The peaks in the spectra were analyzed by comparing the d-spacings corresponding to the extra peaks to the different lead oxide phases reported in the ICSD database. As shown in Figure 7-8, several lead oxide phases, identified by different symbols, could be identified. The additional Pb_xO_y phases observed in the films are summarized in Table 7-6. PT film 1 displayed a large variety of crystals and contains three phases whereas one type of crystals was found in the PT film 2 and one additional phase. We therefore conclude that the dendritic crystals consist of PbO massicot. For both massicot textures, the c-axis is in plane. This corresponds well to the majority of the alignment of the dendritic crystals along the [110] STO as the mismatch is minimized along that direction for the c-axis (0.54%). In agreement with the platelet morphology compared to results in literature, PT film 3 contains PbO litharge, confirming that the platelet (Figure 7-7b) crystals are from PbO litharge in our film. The second phase $PbO_{1.57}$ observed might correspond to the large outcrop crystals, the second type of crystal observed in PT film 3. The morphology of the PT film 4 could not be investigated but three additional phases were detected and a few peaks did not correspond directly to any of these three phases. They probably correspond to another lead oxide phase. Both polycrystalline films were grown in the same conditions but additional phases were grown on PT film 4.

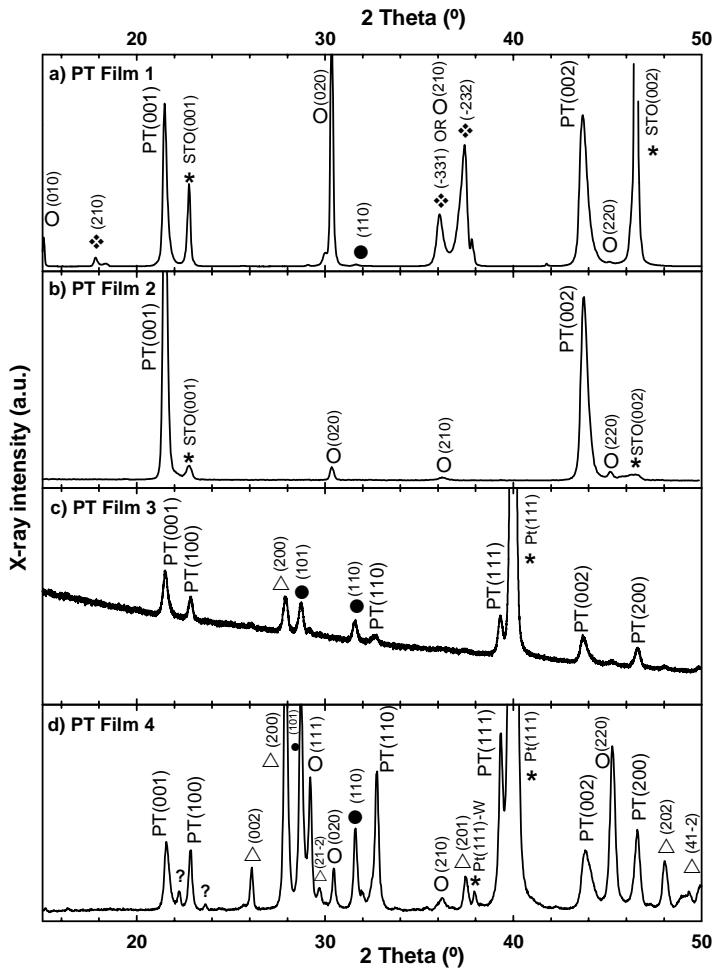


Figure 7-8: XRD θ - 2θ spectra of the a) PT film 1; b) PT film 2; c) PT film 3; and d) PT film 4. The asterisk * represents peaks from the substrate Pt or STO, O represents peaks due to the PbO massicot phase (143), ● represents peaks due to the PbO litharge phase (144), △ represents peaks due to the Pb_2O_3 phase (145), and ◆ represents peaks due to the $\text{Pb}_{2.05}$ (146). The assignment of the Pb_2O_3 and $\text{Pb}_{2.05}$ is tentative, as the presence of these phases was not confirmed by other techniques.

The PT film 1 and 2 were scanned laterally using the Bruker D8 as shown in Figure 7-9 and Figure 7-10. Again, only PbO massicot and $\text{Pb}_{2.05}$ were visible as main phase in PT film 1 and the weak peak of PbO litharge is hardly distinguishable in Figure 7-9.

At the center of the sample, the massicot (020) is weaker whereas the $\text{PbO}_{1.57}$ signal is strong. It indicates that the numerous I-t and t-t crystals in zone 3 and 4, not visible in zone 5, at the center of the sample, are probably originating from the Massicot phase.

Table 7-6: Additional Pb_xO_y phases observed in the PT films and the corresponding error on the d-spacings in Å, averaged on all the peaks observed.

Film	PbO Massicot	PbO Litharge	$\text{PbO}_{1.57}$	Pb_2O_3
PT film 1	YES - 0.003	YES - 0.02	YES - 0.03	NO
PT film 2	YES - 0.002	NO	NO	NO
PT film 3	NO	YES - 0.014	NO	YES - 0.0004
PT film 4	YES - 0.02	YES - 0.014	NO	YES - 0.02

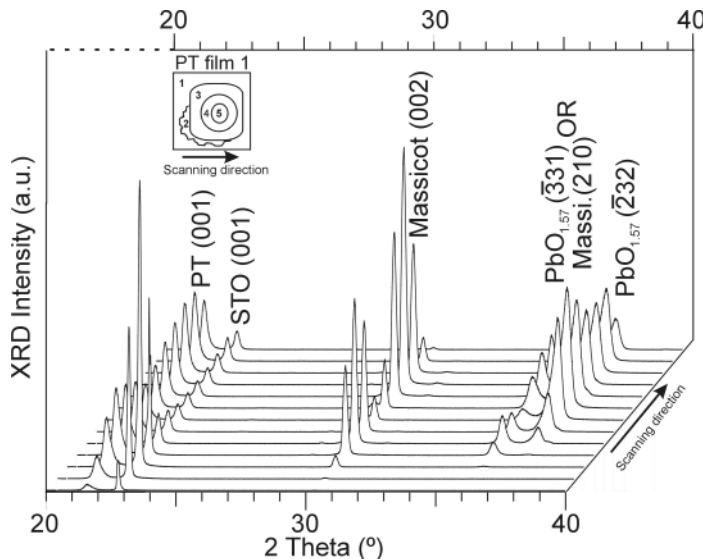


Figure 7-9: Lateral cross-section of the PT Film 1 grown on STO using XRD $\theta - 2\theta$ spectra. Zone 1 is first scanned and then zone 2, 3, 4 5, 4, 3, 2, and 1 as indicated in the schema in the left top corner of the figure and each scan corresponds to circa 1 mm displacement of the sample.

In the PT film 2, the non-PT XRD signal (Figure 7-10) is strong at the center corresponding well with the morphology observation (Figure 7-6) indicating a higher density and larger dendritic crystals at the center of the wafer.

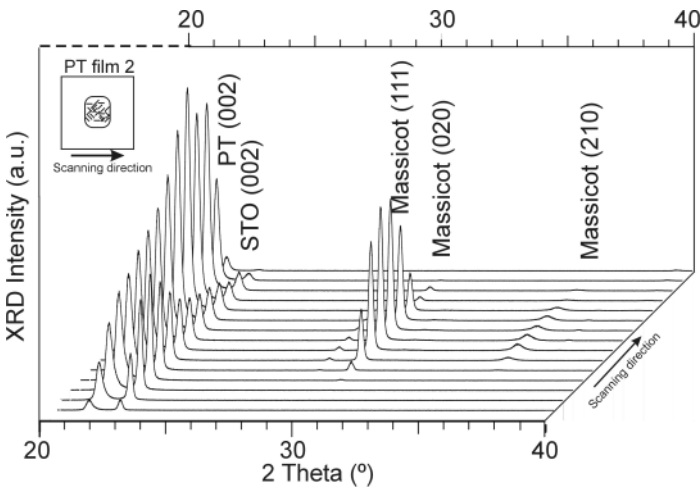


Figure 7-10: Lateral cross-section of the PT Film 2 grown on STO using XRD $\theta - 2\theta$ spectra. The smooth zone is first scanned and then the center with the high crystal density and then the edge again as indicated in the schema in the left top corner of the figure and each scan corresponds to circa 1 mm displacement of the sample.

Raman

Raman was used to distinguish peaks from the crystals in the different zones in PT film 1. The surface, of the films with crystals, was rough and gave the possibility to detect a Raman signal. As shown in Figure 7-11c and g, the smooth zones (1 and 1') give a specular reflection and only the STO signal is collected. On the other hand in zone 5, three bands at 220 , 288 , and 502 cm^{-1} correspond fairly well to the PT Raman signal shown in Figure 7-11b. The Raman signal from PT and PZT compounds is further described in Sections 3.1.5 and 5.4. In addition to the PT signal, an extra peak at 813 cm^{-1} is observed in zone 3, 3', 4, 4', and 5. The Raman signature of massicot, litharge, $\text{PbO}_{1.44}$, Pb_3O_4 , and PbO_2 compounds has been reported in the literature (147, 148, 149, and 150) but no peak around 813 cm^{-1} was found in the lead oxide literature. Though the high A ratio measured by EDS does not indicate a pyrochlore compound in these crystals, the pyrochlore Raman signature has been searched. Bersani et al. (151) reports that the pyrochlore phase is characterized by a sharp peak at 145 cm^{-1} in PZT films and they only observe a broad and low intensity peak at 837 cm^{-1} in their PT powders. Therefore we assign the peak at $\sim 813\text{ cm}^{-1}$ to the $\text{PbO}_{1.57}$ phase also observed by XRD for this film.

The PT film 4 was also investigated by Raman and the spectra measured on two different positions are shown in Figure 7-12. In both spots, the main signal is from PT but some PT peaks in the films are shifted down by $\sim 10\text{ cm}^{-1}$ except the PT peaks at 507 cm^{-1} , the peak at $\sim 448\text{ cm}^{-1}$ and the broad peak at 750 cm^{-1} . The strong peaks at 220 and 290 cm^{-1} are shifted down by $\sim 5\text{ cm}^{-1}$. This might be due to the nanocrystal

"finite-size" effect of the films as observed in nanocrystal powders versus single crystal (80). Such a shift was not observed for the PT single crystals peaks in Figure 7-11.

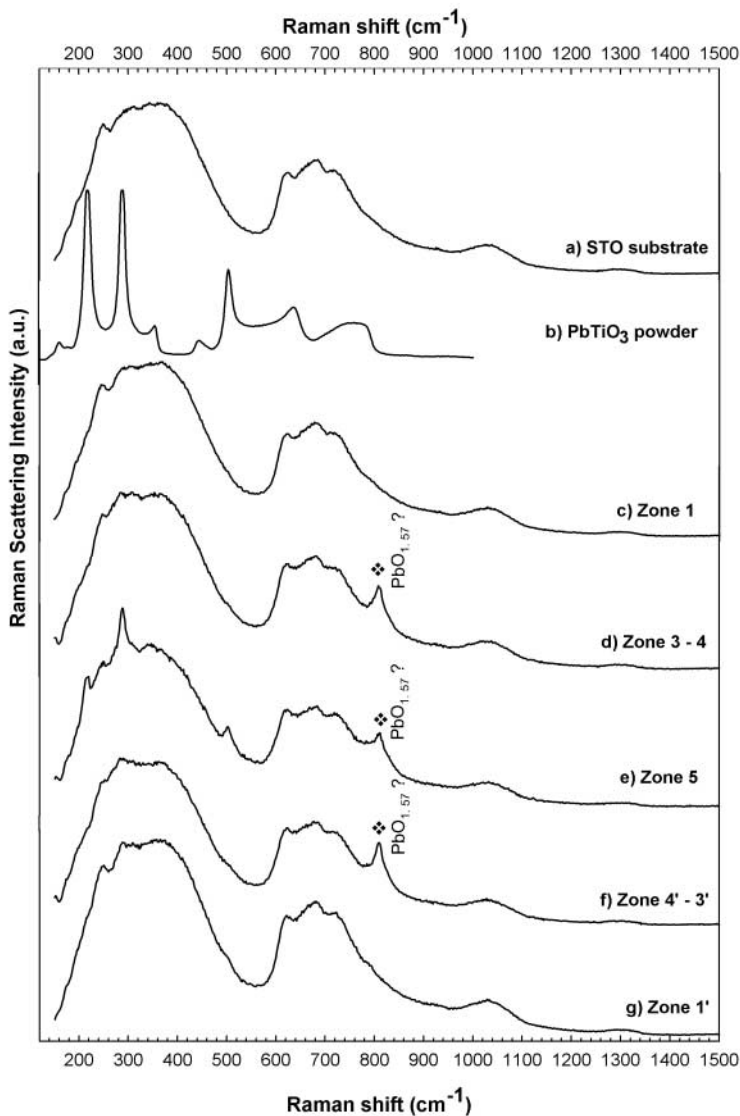


Figure 7-11: Raman spectra of a) STO substrate; b) PT powder; c) MOCVD PT film - Zone 1; d) MOCVD PT film - Zone 3-4; e) MOCVD PT film - Zone 5; f) MOCVD PT film - Zone 4'-3'; and g) MOCVD PT film - Zone 1'. The ♦ indicates a non-PT peak which might be due to the PbO_{1.57} phase.

In Figure 7-12a-b, a clear additional peak is detected at 385 cm^{-1} , a weak peak at $\sim 420\text{ cm}^{-1}$, and a weak broad peak at $809 - 815\text{ cm}^{-1}$. The peak at $\sim 385\text{ cm}^{-1}$ corresponds well to the main peak of the PbO massicot at 385 cm^{-1} as reported by Bullock (148) and to the 382 cm^{-1} massicot peak in sputtered film as reported by Venkataraj et al. (150). Additionally, it agrees well with the measured XRD spectrum of the film (Figure 7-8d) in which the massicot PbO was detected in addition to litharge PbO and Pb_2O_3 . The weak broad peak at $809 - 815\text{ cm}^{-1}$ corresponds to the same peak as the additional peak at 813 cm^{-1} in PT film 1 assigned to $\text{PbO}_{1.57}$. This is in agreement with the XRD results as no $\text{PbO}_{1.57}$ was detected in the XRD spectrum and the Raman signal is very weak and only observed in one spot, indicating that this phase is not dominant in the film. No lead oxide phases, corresponding to the peak at $\sim 420\text{ cm}^{-1}$, were found in literature and this peak might correspond to the Pb_2O_3 phase as the litharge (the third lead oxide phase detected by XRD in the film) Raman signature is known.

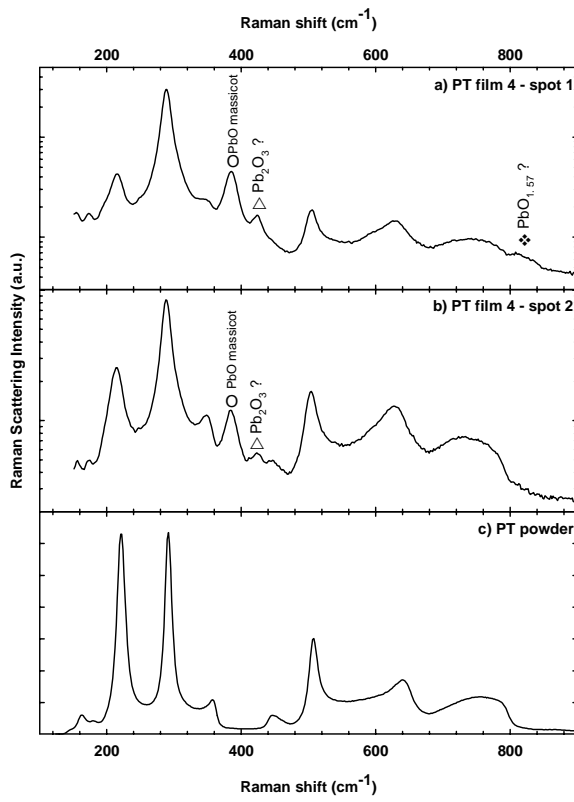


Figure 7-12: Raman spectra of a) PT film 4 spot 1, b) PT film 4 spot 2, and c) PT powder. The Raman scattering intensity is presented on logarithmic scale for the film spectra to show clearly all the non-PT peaks, indicated by symbols. O indicates the massicot PbO phase, Δ the Pb_2O_3 , and \blacklozenge the $\text{PbO}_{1.57}$. The last two phase-assignments are tentative.

The PbO litharge and massicot presence is measured by XRD and confirmed respectively by SEM morphology and Raman. These two phases had already been observed in MOCVD lead oxide films (141, 142). On the other hand the $\text{PbO}_{1.57}$ and Pb_2O_3 phases were only analyzed by XRD and only few peaks can be indexed. The $\text{PbO}_{1.57}$ phase was observed in lead oxide deposited on glass and stainless steel substrates with a high oxygen content in the gas-phase (152). In a more recent article (150), PbO , $\text{PbO}_{1.44}$, Pb_2O_3 , and PbO_2 were successively obtained by increasing progressively the oxygen flow rate for the deposition of lead oxide.

7.2.2 Summary - conclusion

Lead oxide phases (massicot and litharge PbO , $\text{PbO}_{1.44}$, and Pb_2O_3) were grown in addition to PT in polycrystalline films on platinized wafer and semi-epitaxial films on STO. The determination of the lead oxide phases present is confirmed with two techniques for the PbO massicot and litharge but only by d-spacings correspondence for the $\text{PbO}_{1.57}$ and Pb_2O_3 . The massicot PbO phase was detected by XRD in the two semi-epitaxial films and in one polycrystalline film. The phase massicot was confirmed by the detection of its main Raman peak at 385 cm^{-1} in the polycrystalline PT film 4. As only the massicot PbO phase is detected in PT film 2 covered only by dendritic crystals, it is concluded that the dendritic crystals (Figure 7-6) are massicot PbO . The phase litharge PbO was detected in one semi-epitaxial film and both polycrystalline films. The characteristic morphology of litharge crystals has been reported twice in literature and was observed on the polycrystalline film PT film 3 (Figure 7-7b). As this film contains only one other additional phase, Pb_2O_3 , and that only outcrops (Figure 7-7c) are observed in addition to the litharge and to PT, the outcrops are identified as Pb_2O_3 . It is difficult to assign a specific crystal morphology to $\text{PbO}_{1.57}$. In the lateral scan of PT film 1 a clear decrease of the massicot signal is detected at the center of the sample indicating that line-topped crystals and point-topped crystals are from massicot PbO (like the dendritic crystals) and that eventually the terrace-topped crystals are $\text{PbO}_{1.57}$.

Though the assignment of two phases and crystal morphology is tentative, it is clear that the additional phases are lead oxides. The formation of these crystals is not due to contamination as no Si, Pt, or Zr was found above the XRF detection limit for PT film 1. Additionally, the substrate surface does not play a role as these phases were observed on two different types of substrates. The origin of these lead oxide phases can therefore be the gas phase content or the growth mechanisms. It was observed for both polycrystalline and semi-epitaxial films that the nucleation rate of zirconium containing PZT was higher than for PT (see chapter 5). For this run, the partial pressure of the precursors in the reactor is high and all the lead precursor (or the evaporated PbO) might not be totally evacuated by the pump and therefore accumulated in the reactor and integrated in the layer. Only the samples placed at outermost radial positions on the susceptor were mainly covered by these crystals

indicating that, if this is a lead accumulation causing the problem, the lead is stocked at the liner sides. The issue of PbO formation in PT films is further discussed in Section 5.5.3. Above a certain threshold point, the additional lead might be integrated in the layer as lead oxide during growth or during cooling down. This is in agreement with the EDS analysis, for which Ti is still detected in surfaces totally covered by lead oxide terrace-topped crystals, indicating that the crystals should not have started growing at a depth deeper than ~ 350 nm (penetration depth for the accelerating voltage used) below the surface. But as no cross-sections were performed, it is not possible to estimate at which depth these crystals started growing.

Chapter 8

Optical Properties of MOCVD $\text{Pb}(\text{Zr}, \text{Ti})\text{O}_3$ Films¹⁴

¹⁴ The work presented in this chapter is based on "Optical Properties of PbTiO_3 , $\text{PbZr}_x\text{Ti}_{1-x}\text{O}_3$, and PbZrO_3 Films Deposited by Metalorganic Chemical Vapor Deposition" by M.P. Moret, M.A.C. Devillers, K. Wörhoff, and P.K. Larsen, J.Appl.Phys. 92, 468-474, (2002).

8 OPTICAL PROPERTIES OF MOCVD Pb(Zr,Ti)O₃ FILMS

PZT materials are under active consideration for optical applications (Section 1.4.3) as their properties are strongly dependent on x . Near the tetragonal/rhombohedral phase transition for x around 0.53, anomalously high dielectric constants have been measured and high electro-optic coefficients are expected. Detailed optical studies are available on PLZT ceramics (7, 153), but optical and dispersion data for thin films as a function of the x ratio are scarce. Three articles were found on PLZT ceramics and sol-gel films (69, 154, 155) and two on MOCVD PZT films (35, 53).

In this chapter, the optical properties of the epitaxial PZT films prepared by MOCVD on STO substrates are studied. Two sets of films, of thickness 50-100 nm and 700-1400 nm, containing 0%, 40%, 60%, and 100% Zr were prepared and investigated. The growth conditions of these films are shown in Table 2-2 and the growth of the PZ films is described in details in Chapter 6. The refractive index (n) was determined by ellipsometry for the thin films and by reflectivity for the thicker films. Results were obtained over the energy range from 1.55 eV to 3.72 eV, and with a Cauchy-fit extrapolation down to 0.62 eV. The refractive-index curves show a systematic variation with composition. For all compositions, n is close to 3.2 at 3.72 eV (333 nm), while at 1.55 eV (800 nm) n is 2.35 for PZ ($x=1$) and 2.61 for PT ($x=0$). In agreement with previous results we find that the optical bandgap is essentially independent of composition for PZT. We obtained $3.6 \text{ eV} \pm 0.1 \text{ eV}$. The $n(E)$ results were analyzed by a Wemple-DiDomenico dispersion analysis, yielding results for the dispersion region in the UV. Unlike the bandgap, which is insensitive to composition in PZT, the dispersion energy (E_d) decreases from PT to PZ in the same fashion as the refractive index in the transparent region.

8.1 Refractive index

Figure 8-1 presents our results for the dispersion of the refractive index of PZT. There are three different zones in the dispersion curves of the refractive index. Zone 2 is the refractive index as measured by ellipsometry on thin films at wavelengths of 500 nm, 600 nm, 700 nm, and 800 nm. Only hetero-epitaxial layers were used for this study: two series, a thin and a thick one, were used as shown in Table 8-1. The rms top-surface roughness coincides well with the top-surface roughnesses from the ellipsometry model, corresponding more to a peak-to-peak value. The thicknesses of the films were confirmed by other means as mentioned earlier (e.g. by X-ray reflectivity for the thin layers (36) and by optical reflectivity for the thick films). We determined the real part of the refractive index n with an error of ± 0.01 . Refractive indices for specific PZT compositions are available from the literature (Table 8-2). The values of the refractive index are in very good agreement at 633 nm with reported values (35, 69, 53, 156).

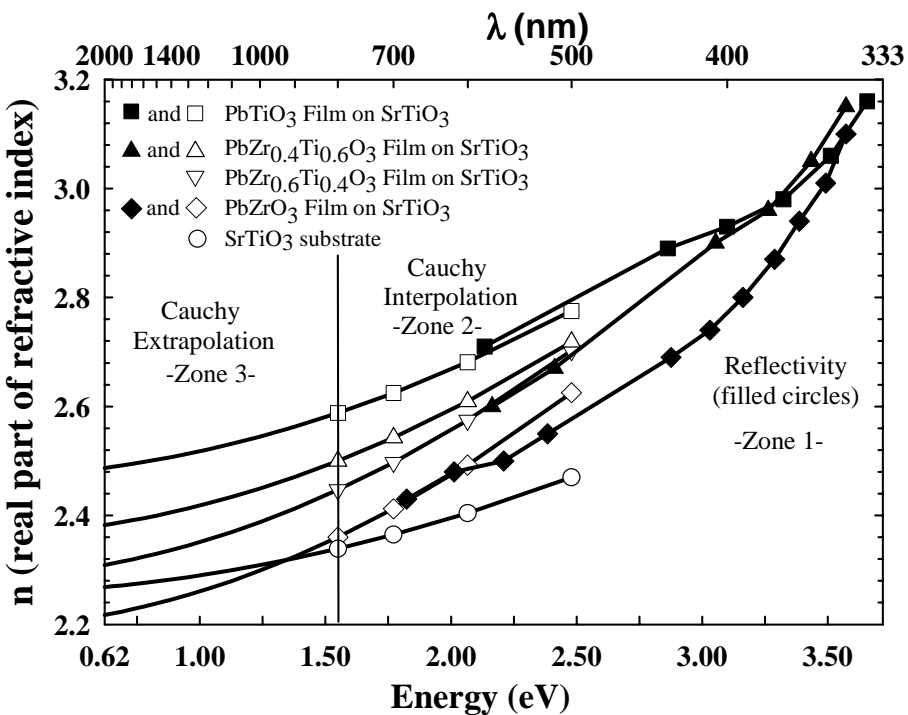


Figure 8-1: The refractive index of PZT as a function of composition and wavelength. Zone 1 contains the results of the reflectivity measurements (filled symbols). Zone 2 contains the results of the ellipsometry measurements (open symbols). The curves in zone 2 are Cauchy interpolations based on the experimental points. The curves in zone 3 are Cauchy extrapolations into the infrared.

Table 8-1: List of samples studied.

Composition	Thickness (nm)	rms surface roughness (nm)
PbTiO ₃	50 ± 5	4.2 ± 1.3
PbZr _{0.4} Ti _{0.6} O ₃	90 ± 5	0.55 ± 0.01
PbZr _{0.6} Ti _{0.4} O ₃	94 ± 5	0.89
PbZrO ₃	105 ± 5	0.57
PbZr _{0.6} Ti _{0.4} O ₃	340 ± 10	0.59 ± 0.01
PbTiO ₃	790 ± 10	4.17
PbZr _{0.4} Ti _{0.6} O ₃	800 ± 10	0.93
PbZr _{0.6} Ti _{0.4} O ₃	700 ± 10	1.05
PbZrO ₃	1420 ± 30	45.3
PbZrO ₃ dry-etched	1260 ± 30	18.4

Table 8-2: Refractive index values (at RT) of PZT films.

Film	λ (nm); n	Technique	Ref.
Sputtered PZT50/50 on (1-102) and on (0001) sapphire	633; 2.44 633; 2.54	Ellipsometry	(156)
PLZT (8/100/0) ceramics	633; 2.42	Ellipsometry	(69)
PLZT (8/80/20) ceramics	633; 2.479		
PLZT (2/65/35) ceramics	633; 2.523		
PLZT (16/40/60) ceramics	633; 2.552		
PLZT (8/10/90) ceramics	633; 2.644		
PLZT (0/0/100) ceramics	633; 2.668		
Sol-gel PZT (50/50) on platinized Si	650; \approx 1.9	Ellipsometer	(157)
Film PZT (x?) on $\text{LaNiO}_3/\text{LaAlO}_3$	400-800; 2.25-2.2	Reflectance	(158)
MOCVD PT on STO	633; \approx 2.67 450; \approx 2.85	Prism coupling	(53)
MOCVD PT on STO	633; \approx 2.675	Prism coupling	(35)
MOCVD PZT (20/80) on STO	633; \approx 2.607		
MOCVD PZT (80/20) on STO	633; \approx 2.505		
MOCVD PZ on STO	633; \approx 2.46		
Sol-gel PT	633; \approx 2.58	Transmittance	(154)
Sol-gel PZT 40/60	633; \approx 2.45		
Sol-gel PZT 60/40	633; \approx 2.40		
Sol-gel PZ	633; \approx 2.30		

Some reports indicate lower refractive index for thin films than the ceramics (158, 159). Optical characterization is used as a quality check for PZT films. In (159), the increase of the refractive index with increasing annealing time was monitored for sol-gel films. Other refractive index values are included in Table 8-2. The values given in the table are from films prepared by different techniques and from bulk ceramics. In (154), the linear variation of the refractive index, from PT to PZ, was used to determine the packing densities of the films. The lower refractive index (roughly 5% lower than for ceramics (69) or MOCVD films (36, our data)) is due to a 95% packing density of the sol-gel films. Similar results were found for sol-gel PLT films (155). The differences in the refractive index values (for samples with the same composition) result from variations in the details of the film structure (phase, interface, inhomogeneity, domains, microstructure, top roughness) and how these parameters were taken into account in the data analysis.

In Zone 2, the refractive index data as measured by ellipsometry on thin films at wavelengths of 500 nm, 600 nm, 700 nm, and 800 nm were fitted by a Cauchy fit of the form

$$n(\lambda) = n_0 + a \frac{(800)}{\lambda}^2.$$

A fit in $1/\lambda^2$ was found to be sufficient to extrapolate the data (zone 3) up to 2000 nm. The fit coefficients n_0 and a , shown in Table 8-3 for the different compositions are listed indicatively as they do not represent any physical quantities as the parameters of the other fit used below.

Table 8-3: Coefficients of the Cauchy fit for zone 2 and zone 3 in figure 2.

Composition	n_0	a
PbTiO_3	2.468	0.120
$\text{PbZr}_{0.4}\text{Ti}_{0.6}\text{O}_3$	2.360	0.140
$\text{PbZr}_{0.6}\text{Ti}_{0.4}\text{O}_3$	2.283	0.164
PbZrO_3	2.190	0.170
SrTiO_3	2.255	0.084

As mentioned in the introduction, few references reporting the refractive-index variation as a function of composition were found in the literature. An early paper on PLZT ceramics (69) showed that the refractive index decreases linearly from PT ($n=2.66$) to PZ ($n=2.46$) at $\lambda=633$ nm. Similar results were later found for MOCVD PZT films (69). The measurements are in agreement at 633 nm for MOCVD films and ceramics but the reference on MOCVD films does not contain dispersion data. In (69), it is also shown that the La content has little influence on the refractive index, which is mainly determined by x . Initially, the linear extrapolation of the refractive index as a function of x was used to determine the composition of our PZT films (36). The composition determination by ellipsometry was possible using the determination of the real part of the refractive index n , with ± 0.01 error, leading to ± 0.1 error in the x ratio. The composition estimation by ellipsometry is in good agreement with chemical analysis by XRF and EDS (TEM). The four compositions of PZT in zone 2 also indicate a linear decrease of n from PT (2.66) to PZ (2.46) at 633 nm for our films. It is only measured for four PZT compositions and large variation might be expected around the morphotropic phase boundary due to the presence of two phases in the film (36), or possibly even three (13). The linear variation of the refractive index from PT to PZ is preserved up to 2000 nm according to the Cauchy extrapolation. The linear relation (n to x) preservation is important for electro-optics devices, which function at 1500 nm.

8.2 Bandgap (E_g) and Dispersion Energy (E_d)

In Figure 8-1, Zone 1 shows the refractive index of the thick films as measured by reflectivity on thick films. All the $n(E)$ curves converge near the absorption edge at $3.6 \text{ eV} \pm 0.1 \text{ eV}$ ($340 \text{ nm} \pm 10 \text{ nm}$), which compares well with the convergence observed near 350 nm for the ceramics (69).

Table 8-4: Comparison of the dispersion of the refractive index for ceramics (13) and for our MOCVD films on STO.

Wavelength	PZ		PLZT 10/65/35	PZT (60/40)	PT	
	Ref (10)	films	Ref (10)	films	Ref (10)	films
450	2.56	2.66	2.64	2.76	--	2.86
500	2.50	2.60	2.58	2.66	2.78	2.82
600	2.46	2.50	2.50	2.60	2.70	2.70
700	2.44	2.41	2.46	2.52	2.66	2.62

Good agreement had also been found between ceramics and PZT films on sapphire (156) over the wavelength range from 400 to 750 nm. In (53), good agreement between MOCVD films and single crystals was reported for PT from $\lambda = 450$ to 635 nm . In Figure 8-1, the reflectivity and the ellipsometry results are consistent in the overlap region. For clarity, only the reflectivity results for PT, PZT ($x=0.4$), and PZ are shown.

While the refractive index varies systematically as a function of x , no absorption-edge variation was found as a function of composition. In Table 8-5, reported bandgap values for PZT are listed. Our estimation of the gap is in reasonable agreement with previous ceramic estimates (69) and differs from film estimates (154, 158, 160). The insensitivity of bandgap to composition is in agreement with results in reference 69, but in disagreement with reference 154. The endpoint values of the bandgap variation claimed in (154) fall within our measured $3.6 \text{ eV} \pm 0.1 \text{ eV}$. No PZT composition determination is therefore possible by band-gap determination.

In addition to the Cauchy extrapolation described above, which was done to provide reasonable estimates for n in the infrared region, we have also carried out a Wemple-DiDomenico single-oscillator dispersion analysis using all of the experimental data of Figure 8-1. Both Cauchy and Wemple-DiDomenico fits provide useful parameterizations of the experimental results. But the Wemple-DiDomenico fit additionally provides physically significant quantities, which characterize the strong interband-transition absorption band in the ultraviolet that causes the refractive-index dispersion in the visible.

Table 8-5: Bandgap values for PZT.

Film	Band Gap (eV)	Technique	Ref.
MOCVD PT to PZ	$3.63 \text{ eV} \pm 0.11 \text{ eV}$	Reflectivity	This work
Film PZT(x?)on LaNiO ₃ /LaAlO ₃	3.07	Reflectance	(158)
Ceramics PLZT	≈ 3.5	ellipsometry	(69)
Sol-gel PZT(65/35)	Main absorption at 3.37 eV and two secondary at 2.6 eV and 1 eV	Transmittance/reflection	(160)
Sol-gel PT Sol-gel PZT 40/60 Sol-gel PZT 60/40 Sol-gel PZ	~ 3.45 ~ 3.6 ~ 3.65 ~ 3.70	Transmittance	(154)

The widely-used Wemple-DiDomenico dispersion relation (161) for $n(E)$, the refractive index at photon energy E , is:

$$n(E)^2 - 1 = \frac{E_d E_0}{(E_0^2 - E^2)},$$

where E_0 is the energy of the effective dispersion oscillator, which is expected to correspond to the photon-energy position of the center of gravity of the ultraviolet band. E_d , called the dispersion energy, is a measure of the average strength of the interband optical transitions. The data ($(n(\lambda)^2 - 1)^{-1}$ versus $1/(\lambda)^2$ (in cm⁻²)) can be fitted by a straight line to obtain E_0 and E_d . The corresponding fits from the experimental data are shown in Figure 8-2. Wemple-DiDomenico parameters obtained from these fits are shown in Table 8-6. This table also includes, for discussion, the refractive index value at 1.55 eV (800 nm) in the transparent region.

Table 8-6: Wemple-DiDomenico dispersion parameters for our MOCVD PZT films.

MOCVD Film	E_0	E_d	$n(1.55 \text{ eV})$
PbTiO ₃	4.67	25.1	2.59
PbZr _{0.4} Ti _{0.6} O ₃	4.27	20.7	2.50
PbZr _{0.6} Ti _{0.4} O ₃	4.10	18.6	2.45
PbZrO ₃	4.09	17.3	2.36

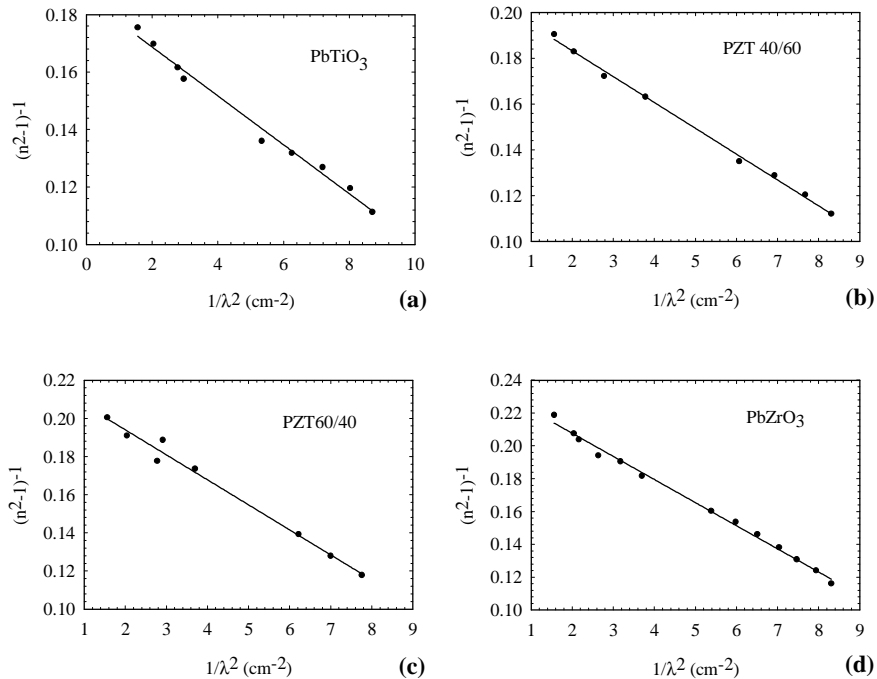


Figure 8-2: Fit of the experimental data (Zone 2 - Figure 8-1) by the Wemple-DiDomenico fit.

The usual situation in insulators and semiconductors is to find an inverse correlation between the refractive index and the characteristic interband energy E_0 . In semiconductors, this correlation works very well, and even extends to an analogous correlation with the bandgap energy (162) because the bandgap in semiconductors is closely correlated with E_0 . But in PZT, we find the surprising result that the transparent-region refractive index is not inversely correlated with E_0 , which decreases slightly from PT to PZ. Instead, the behavior is dominated by the very strong composition dependence of the absorption-strength parameter E_d . We therefore conclude that the larger refractive index in PT arises primarily from stronger interband transitions in this material, rather than from a significant difference in interband energies between PT and PZ. This conclusion is also consistent with the finding that there is little difference between the bandgaps of PT and PZ.

There is a 30% decrease in E_d from PT to PZ. If an error of ± 1.5 eV (which is reasonable, from the data) is taken for E_d , there is a linear decrease in E_d as function of decreasing x . The relationship E_d to x is very similar to the one for the refractive index (n) to x in the transparent regime, as shown in Figure 8-3.

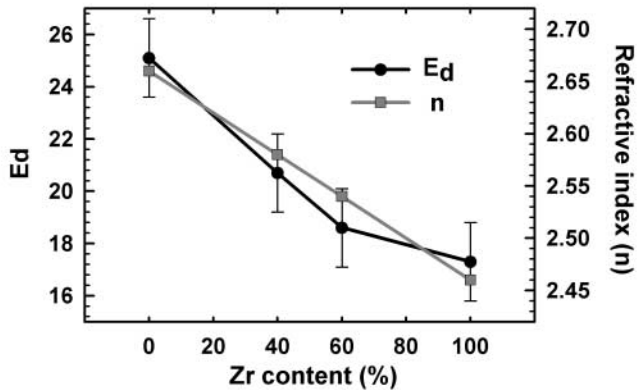


Figure 8-3: The interband strength parameter (E_d) from the Wemple fit and the refractive index (n) at $\lambda = 633$ nm as a function of Zr content.

Table 8-7 shows reported values of the Wemple-DiDomenico E_d and E_o for PLZT ceramics (69). The E_o and E_d values of ceramic PT correspond fairly well with the results for our MOCVD PT film, but the E_d decrease as a function of x is small for PLZT ceramics (6%) and can not be convincingly interpreted as a trend due to the error in these measurements.

Table 8-7: Reported dispersion parameters for ceramics.

Sample	E_o (eV)	E_d (eV)	Reference
Ceramics			
PLZT (8/90/10)	6.26	28.0	(69)
PLZT (8/80/20)	6.11	28.1	
PLZT (2/65/35)	5.85	27.8	
PLZT(16/40/60)	5.89	28.9	
PLZT (8/10/90)	5.59	29.4	
PLZT (0/0/100) = PT	5.59	30.0	
SrTiO_3	5.8	23.7	(161)
BaTiO_3	5.8	24.5	(161)
PbTiO_3	5.6	29.6	(161)

The unclear modification of E_d for PLZT as a function of the x ratio might be due to an effect of the La dopant or to the correction for surface roughness in the measurements. Similar conclusions can be drawn for PLT sol-gel films (155), which showed no consistent variation for E_d and/or E_o as a function of La content. However, our results for MOCVD PZT films clearly show (Figure 8-3) a definite decrease in E_d with increasing Zr content. Wemple and DiDomenico (161) noted that

E_d was roughly constant (around 23 eV) for most oxides and oxygen-octahedra ferroelectrics, though the trend could not apply to lead-based ferroelectrics as lead does not have a d-band (used for the classification) (163). Recent calculations by Robertson¹⁵ (164) indicate that states derived from the Pb⁺⁺ ions enter differently into the conduction bands of PT and PZ, which might account for the smaller interband-transition E_d in PZ.

8.3 Waveguide experiments¹⁶

Light was coupled into rhombohedral PZT layers by 633 nm prism coupling using a rutile prism. Two TE modes, TE₀ and TE₁, were found to be excitable in a 700 nm thick PZT ($x=0.6 \pm 0.1$) layer. From the uncoupling angles, assuming a homogenous PZT-core layer and inserting $n_{\text{prism}}=n_e=2.872$ and $n_{\text{substrate}}=n_{\text{SrTiO}_3}=2.389$ and a refractive index $n_{\text{layer}}=2.505$, a layer thickness $d_{\text{layer}}=705 \pm 5$ nm could be calculated. This corresponds well with $n_{\text{layer}}=2.50 \pm 0.01$ and $d_{\text{layer}}=700 \pm 10$ nm determined by ellipsometry. It has to be noted that, because of the relatively low modal field at the outside regions of the PZT-core layer, the coupling angles are very insensitive to the potential presence of a thin interface layer or somewhat lower refractive index and the 1 nm rms surface roughness. Because both measurement methods are applying completely different field distribution inside the PZT layer, this good correspondence indicates good thickness homogeneity of the PZT core layer. TM light could not be coupled into the films by prism coupling, although the TM₀ and TM₁ modes are accessible using a TiO₂ prism. Similar difficulties were reported for MOCVD PZT films on STO (35, 53). We ascribe this to an insufficient coupling strength as a result of surface roughness, though the rms roughness is only 1 nm for these films. The small dimensions of the substrate (1 by 1 cm) did not allow for quantitative loss measurements of the TE modes. By usual inspection (microscope), strong bulk scattering could be observed into the PZT layer outside the propagating beam area.

8.4 Conclusion

Optical characterization was carried out on our PZT films grown by MOCVD on STO, structures of interest for future optical-modulator applications. The top roughness of the PZT films was within the requirements for waveguiding, and two TE modes were coupled in a 700 nm film. For applications, poling of the films might decrease the bulk scattering, which appeared high by visual inspection. The refractive-index dispersion was measured from 1.55 eV (800 nm) to 3.72 eV (333 nm) by ellipsometry and reflectivity, as a function of composition. A Cauchy extrapolation was used to estimate the refractive index down to 0.62 eV (2000 nm). It indicates that the refractive index is close to linear in x not only at 633 nm, as shown in previous

¹⁵ J. Robertson (Cambridge University) is acknowledged for making his PZT-band-structure calculations available.

¹⁶ Kerstin Worhoff, Henck van Wolferen, and Paul Lambeck (Twente University) are acknowledged for the prism-coupling measurements.

reports, but also up to 2000 nm. The refractive-index determination is thus a convenient measure of composition. The absorption edge is insensitive to composition, and is located at 3.6 ± 0.1 eV (340 ± 10 nm). This is in good agreement with earlier results on ceramics. The interband absorption-strength parameter E_d , extracted from a Wemple fit to the refractive-index dispersion $n(E)$ decreases linearly from PT to PZ. It is the composition dependence of E_d , rather than that of the average interband gap E_0 , which is the dominant factor in the composition dependence of $n(E)$. This is an unusual behavior compared to semi-conductors and to other oxides. The smaller infrared refractive index of PZ arises from the smaller E_d for this material.

Reference

-
- 1 "Ceramics" in: D.M. Considine and G.D. Considine (Eds.), Van Nostrand's Scientific Encyclopedia, International Thompson Publishing Inc., New-York, 598-601, 1995.
 - 2 R. Lundberg, M.P. Moret, L. Garguet-Duport, ASME 98-GT-566, 1998.
 - 3 B.D. Stojanović, Science of Sintering 28, 21-34, 1996.
 - 4 Yuhuan Xu, "Ferroelectric Materials and their Applications", Elsevier Science Publishers, New-York, 1991; S. Trolier Mc-Kinstry and D. Damjanovic, Tutorial Courses on Ferroelectrics, ISIF2000, Aachen, 2000.
 - 5 S.A. Rössinger and S.I. Misat, unpublished results.
 - 6 W.P. Mason, J.Ac.Soc.Am. 50, 1281-1298, 1971; G. Bush, Ferroelectrics 74, 267-284, 1987.
 - 7 G.H. Haertling, Ferroelectrics 75, 25-55, 1987; G.H. Haertling, J.Vac.Sci.Technol. A9, 414-420, 1991.
 - 8 G.A. Smolenskii, V.A. Bokov, V.A. Isupov, N.N. Krainik, R.E. Pasynkov, and A.I. Sokolov, "Ferroelectricity and Related Phenomena", Gordon & Breach Science Publishers, Amsterdam, 1984.
 - 9 <http://www.webmineral.com>
 - 10 R.W.G. Wyckoff, "Crystal Structures", 2nd Edition, Interscience Publishers, (p390-408), 1963.
 - 11 M. Sayer and V. Chivukula "Ferroelectric Materials", in: "Handbook of Thin Film Process Technology", Institute of Physics, Bristol, X4.0:1-X4.0:14, 1985.
 - 12 B. Jaffe, W. Cook, and H. Jaffe, "Piezoelectric Ceramics", Academic Press, London, 1971.
 - 13 B. Noheda, J.A. Gonzalo, L.E. Cross, R. Guo, S.-E. Park, D.E. Cox, and G. Shirane, Phys. Rev. B. 61, 8687-8695, 2000; B. Noheda, D.E. Cox, G. Shirane, R. Guo, B. Jones, and L.E. Cross, Phys. Rev.B 63, 014103-1-9, 2000.
 - 14 A.M. Glazer, Acta Cryst. A31, 756-762, 1975.

-
- 15 A.M. Glazer, S.A. Mabud, and R. Clarke, *Acta.Cryst.* B34, 1060-1065, 1978.
- 16 P.K. Larsen, G.A.C.M. Spierings, R. Cuppens, and G.J.M. Dormans, *Microelectronic Engineering* 22, 53-60, 1993.
- 17 R. Ramesh, "Thin Film Ferroelectric Materials Devices", Kluwer Academic Publishers, Boston, 1997.
- 18 N. Nagel, T. Mikolajick, I. Kasko, W. Hartner, M. Moert, C-U. Pinnow, C. Dehm, and C. Mazure, *Mat. Res. Symp.Proc.* 655, CC1.1.1- CC1.1.10, 2001.
- 19 International Symposium on Integrated Ferroelectrics, Colorado Springs, March 2001.
- 20: <http://www.mems-exchange.org/>; [http://www.memsccenter.com/memsc](http://www.memscenter.com/memsc); "Industrial Physicist" p10-11 and 20-25, December 2001/January 2002.
- 21 P. Muralt, *MME* 99, 203-213, 1999.
- 22 M. Elwenspoek, T.S.J. Lammerink, R. Miyake, and J.H.J. Fluitman, *J.Micromech.Microeng.* 4, 227-245, 1994.
- 23 D.K. Fork, F. Armani-Leplingard, and J.J. Kingston, *MRS Bulletin*, 53-58, 1996.
- 24 C. Buchal and M. Siegert, "The Physics of Modulators", Proceedings of the International School of Physics "Enrico Fermi", IOS Press, Amsterdam, 1999.
- 25 F. Niu, B.H. Hoerman, and B.W. Wessels, *Applied Surface Science* 161, 74-77, 2000.
- 26 <http://www.motorola.com/mediacenter/> (press release 4th September 2001); *Photonics Spectra* October, 22, 2001.
- 27 C. Buchal and M. Siegert, *Integrated Ferroelectrics* 35, 1-10, 2001.
- 28 B.W. Wessels, *J.Crystal Growth* 195, 706-710, 1998.
- 29 E. Dogheche, B. Jaber, D. Remiens, and B. Thierry, *Microelectronic Engineering* 29, 315-318, 1995; E. Dogheche and D. Remiens, *Integrated Ferroelectrics* 25, 71-82, 1999; E. Dogheche, B. Jaber, X. Lansiaux, and D. Remiens, *J.Phys.IV France* 8, Pr9-277-280, 1998; A. Boudrioua, J.C. Loulergue, E. Dogheche, and D. Remiens, *J.Appl.Phys.* 85, 1780-1783, 1999.
- 30 K. Nashimoto, S. Nakamura, T. Morikawa, H. Moriyama, M. Watanabe, and E. Osakabe, *Jpn.J.Appl.Phys.* 38, 5641-5645, 1999.

-
- 31 W.H. Steier, A. Chen, S-S Lee, S. Garner, H. Zhang, V. Chuyanov, L.R. Dalton, F. Wang, A.S. ren, C. Zhang, G. Todorova, A. Harper, H.R. Fetterman, D. Chen, A. Udupa, D. Bhattacharya and B. Tsap, *Chem. Phys.* 245, 487-506, 1999.
- 32 D.M. Gill, C.W. Conrad, G. ford, B.W. Wessels, and S.T. Ho, *Appl.Phys.Lett.* 71, 1783-1785, 1997.
- 33 G. Teowee, J.T. Simpson, T. Zhao, M. Mansuripur, J.M. Boulton, and D.R. Uhlmann, *Microelectronic Engineering* 29, 327-330, 1995.
- 34 M. Hoekman, "Design of an Integrated Optical Electro-Optical Modulator Based on PZT Containing Multilayer-Stacks", Thesis, Twente University, May 2001.
- 35 C.M. Foster, G.-R Bai, R. Csencsits, J. Vetrone, R. Jammy, L.A. Wills, E. Carr, and J. Amano, *J.Appl.Phys.* 81, 2349-2357, 1997.
- 36 M.P. Moret, M.A.C. Devillers, A.R.A. Zauner, E. Aret, P.R. Hageman, P.K. Larsen, *Integrated Ferroelectrics* 36, 265-274, 2001.
- 37 T. Schneller, Ferroelectric Chemical Deposition Method, Tutorial International Symposium on Integrated Ferroelectrics, Aachen, 2000.
- 38 D. Schlom, Ferroelectric Physical Deposition Method, Tutorial International Symposium on Integrated Ferroelectrics, Aachen, 2000.
- 39 R.E. Leuchtner and K.S. Grabowski, in: D.B. Chrisey and G.K. Hubler (Eds), *Pulsed Laser Deposition of Thin Films*, Wiley-Interscience, New-York, 473-500, 1994.
- 40 M.S. de Keijser, "Organometallic Chemical Vapour Deposition of Lead Zirconate Titanate", PhD thesis, University of Nijmegen, 1995.
- 41 P.R. Hageman, G.J. Bauhuis, S.M. Olsthoorn, *J.Crystal Growth* 194, 272-275, 1998; P.L. Bastos, M.J. Anders, M.M.G. Bongers, P.R. Hageman, L.J. Giling, *J.Crystal Growth* 170, 710-714, 1997.
- 42 A.R.A. Zauner, F.K. De Theije, P.R. Hageman, W.J.P. van Enckevort, J.J. Schermer, and P.K. Larsen, *Mat.Res.Soc.Symp.Proc.* 572, 345-350, 1999; A.R.A. Zauner, "Homo- and hetero-epitaxial growth of Gallium Nitride by metalorganic chemical vapor deposition", PhD Thesis, University of Nijmegen, Nijmegen 2001.
- 43 R.D. Dupuis in: D.A. Glocker and S.I. Shah (Eds), *Handbook of Thin Film Process Technology*, Institute of Physics, Bristol, B1.1:1-B1.1:18, 1997.

-
- 44 H.M. Manasevit, *Appl.Phys.Lett.* 12, 156-159, 1968.
- 45 T. Nakagawa, J. Yamaguchi, M. Okuyama, and Y. Hamakawa, *Jpn.J.Appl.Phys.* 21, L655 - L656, 1982.
- 46 M. Okada, K. Tominaga, T. Araki, S. Katayama, and Y. Sakashita, *Jpn.J.Appl.Phys.* 29, 718-722, 1990.
- 47 C.M. Foster, in "Thin Ferroelectric Materials and Devices" Ed. R. Ramesh, Kluwer Academic Publishers, Dordrecht, 1997, p.175.
- 48 T. Matsuzaki and H. Funakubo, *J.Appl.Phys.* 86, 4559-4564, 1999.
- 49 K. Tokita and H. Hoshi, *Jpn.J.Appl.Phys.* 39, 5399-5402, 2000.
- 50 K. Nagashima, M. Aratani, and H. Funakubo, *Jpn.J.Appl.Phys.* 39, L996-L998, 2000.
- 51 K. Nagashima and H. Funakubo, *Jpn.J.Appl.Phys.* 39, 212-216, 2000; H. Funakubo, K. Nagashima, K. Shinozaki, and N. Mizutani, *Thin Solid Films* 368, 261-265, 2000.
- 52 M. Aratani, T. Oikawa, T. Ozeki, and H. Funakubo, *Appl.Phys.Lett.* 79, 1000-1002, 2001.
- 53 C.M. Foster, Z. Li, M. Buckett, D. Miller, P.M. Baldo, L.E. Rehn, G.R. Bai, D. Guo, H. You, and K.L. Merkle, *J.Appl.Phys.* 78, 2607-2622, 1995.
- 54 R.E. Koritala, M.T. Lanagan, N. Chen, G.R. Bai, Y. Huang, and S.K. Streiffer, *J.Mater.Res.* 15, 1962-1971, 2000.
- 55 C.H. Lin, P.A. Friddle, X. Lu, H. Chen, Y. Kim, and T.B. Wu, *J.Appl.Phys.* 88, 2157-2159, 2000.
- 56 C.H. Lin, B.M. Yen, H.C. Kuo, H. Chen, T.B. Wu, and G.E. Stillman, *J.Mater.Res.* 15, 115-124, 2000.
- 57 H. Fujisawa, M. Yoshida, M. Shimizu, and H. Niu, *Jpn. J. Appl. Phys.* 37, 5132-5136, 1999.
- 58 H. Fujisawa, S. Nakashima, K. Kaibara, M. Shimizu, and H. Niu, *Jpn.J.Appl.Phys.* 38, 5392-5396, 1999.
- 59 M. Shimizu, S. Nakashima, K. Kaibara, H. Fujisawa, and H. Niu, *Ferroelectrics* 241, 183-190, 2000.

-
- 60 H. Fujisawa, K. Morimoto, M. Shimizu, H. Niu, K. Honda, and S. Ohtani, Jpn.J.Appl.Phys. 39, 5446-5450, 2000.
- 61 W. Ma, M. Zhang, T. Yu, Y. Chen, and N. Ming, Appl.Phys. A 66, 345-349, 1998.
- 62 T. Yu, Y.-F. Chen, Y.-Y. Zhu, Z.-G. Liu, N.-B. Ming, and X.-S. Wu, Appl.Surface Science 138-139, 609-612, 1999.
- 63 A. Sakurai, X. Min Li, K. Shiratsuyu, K. Tanaka, and Y. Sakabe, Jpn.J.Appl.Phys. 39, 5441-5445, 2000.
- 64 E. Hong, J.C. Shin, J. Choi, C.S. Hwang, and H.J. Kim, J.Mater.Res. 5, 1284-1290, 2000.
- 65 C.H. Wang, D.J. Won, and D.J. Choi, J.Mater.Science 36, 815-820, 2001.
- 66 M. Miyake, K. Lee, S. Kawasaki, Y. Ueda, S. Okamura, and T. Shiosaki, Jpn.J.Appl.Phys. 41, 241-244, 2002.
- 67 K. Nassau, "The Physics and Chemistry of Colors – The fifteen causes of colors", John Wiley & Sons, Inc., New-York, 2001.
- 68 Harland G. Tompkins, "A User's Guide to Ellipsometry", Academic press Inc., Boston, 1993.
- 69 P. Thacher, Applied Optics 16, 3210-3213, 1977.
- 70 E.D. Palik, "Handbook of optical constants of solids", Academic Press Inc., San Diego, 1998.
- 71 M.P. Moret, S.A. Rössinger, P.R. Hageman, M.A. Devillers, H. van der Linden, E. Haverkamp, P.K. Larsen and N. Duan, Ferroelectrics 241, 149-158, 2000.
- 72 B.D. Cullity, "Elements of X-ray diffraction", Addison-Wesley Publishing Co, Inc., London, 1978.
- 73 ICSD card for PbTiO₃: 06-452.
- 74 ICSD card for Pb(ZrTi)O₃ tetragonal: 33-784.
- 75 ICSD card for Pb(Zr,Ti)O₃ rhombohedral: 70-738/73-2022.
- 76 ICSD card for PbZrO₃: 75-1607.

-
- 77 P.F. Fewster, J.Mat.Science: Materials in Electronics 10 , 175-184, 1999.
- 78 Program Win-Refsim (2.0) from Bruker.
- 79 G. Burns and B.A. Scott, Phys.Rev.B 7, 3088-3101, 1973.
- 80 J.F. Meng, R.S. Katiyar, G.T. Zou, and X.H. Wang, Phys.Stat.Sol. 164, 851-862, 1997.
- 81 C.M. Foster, Z. Li, M. Grimsditch, S.-K. Chan, and D.J. Lam, Phys.Rev. B 48, 10160-10167, 1993.
- 82 Y.I. Yuzyuk, R. Fahri, V.L. Lorman, L.M. Rabkin, L.A. Sapozhnikov, E.V. Sviridov, and I.N. Zakharchenko, J.Appl.Phys. 84, 452-457, 1998.
- 83 S.A. Rössinger, M.P. Moret, S.I. Misat, P.R. Hageman, H.A. van der Linden, E. Haverkamp, W.H.M. Corbeek, and P.K. Larsen, Integrated Ferroelectrics 30, 71-79, 2000.
- 84 O. Auciello, A. Gruverman, H. Tokumoto, S.A. Prakash, S. Aggarwal, and R. Ramesh, MRS Bulletin 23, 33-42, 1998; E.D. Mishina, N.E. Sherstyuk, K.A. Vorotilov, A.S. Sigov, R. Barberi, M.P. Moret, F. Manders, M.P. De Santo, P.K. Larsen, and Th. Rasing, Applied Physics B 74, 783-788, 2002.
- 85 H. N. Al-Shareef and A. Kingon in: "Ferroelectric thin films: Synthesis and Basic Properties" Eds C.P. de Araujo, J. F. Scott, and G.W. Taylor, Gordon and Breach Publishers, Amsterdam, 1996.
- 86 J.M. Bell, P.C. Knight, and G.R. Johnson, in: "Ferroelectric thin films: basic properties" Eds C.P. Araujo, J.F. Scott, and G.W. Taylor, Gordon and Breach Publishers, Amsterdam, 1996.
- 87 G.R. Fox, S. Trolier-McKinstry, S.B. Krupanidhi, and L.M. Casas, J.Mater.Res. 10, 1508-1515, 1995.
- 88 D. Kim, T-Y. Kim, I. Chung, C.W. Chung, and J.S. Lee, Integrated Ferroelectrics 17, 67-79, 1997.
- 89 V.P. Afanas'ev, E.Yu Kaptelev, G.P. Kramar, and I.P. Pronin, Crystallography Reports 43, 322-325, 1998.
- 90 J.G.E. Gardeniers, M. Elwenspoek, and C. Cobianu, Mat.Res.Soc.Symp. 343, 451-456, 1994.

-
- 91 P. Muralt, T. Maeder, L. Sagalowicz, S. Hiboux, S. Scalese, D. Naumovic, R.G. Agostino, N. Xanthopoulos, H.J. Matieu, L. Patthey, and E.L. Bullock, *J.Appl.Phys.* 83, 3835-3841, 1998.
- 92 P.K. Larsen, G.J.M. Dormans, D.J. Taylor, and P.J. van Veldhoven, *J.Appl.Phys.* 76, 2405-2413, 1994.
- 93 M.P. Moret, S.A. Rössinger, P.R. Hageman, M.A. Devillers, H. van der Linden, E. Haverkamp, P.K. Larsen, and N. Duan, *Ferroelectrics* 241, 149-158, 2000.
- 94 G.R. Fox, S. Trolier-McKinstry, S.B. Krupanidhi, and L.M. Casas, *J.Mater.Res.* 10, 1508-1515, 1995.
- 95 S. Itabashi, I. Okada, T. Kaneko, S. Matsuo, and H. Yoshihara, *J.Vac.Sci.Technol. A.*, 10, 3312-3317, 1992.
- 96 Y.-M. Sun, D.N. Belton, and J.M. White, *J.Phys. Chem.* 90, 5178 (1986); M.S. Spencer, *Journal of Catalysis* 93, 216-223, (1985); M.S. Spencer, *Surface Science* 145, 145 - 158, 1984.
- 97 S. L. Firebaugh, K.F. Jensen, and M.A. Schmidt, *Journal of Microelectromechanical Systems* 7, 128-135, 1998.
- 98 H. Tokura, B. Window, D. Neely, and M. Swain, *Thin Solid Films* 253, 344 -348, 1994.
- 99 M.S. Spencer, *J. of Catalysis* 93, 216-223, 1985.
- 100 T. Michely, M. Kalff, G. Comsa, M. Strobel, and K-H. Heinig, *Phys. Rev. Lett.* 86, 2589-2592, 2001.
- 101 D. Gupta and P.S. Ho, "Diffusion Phenomena in Thin Films and Microelectronic Materials", Noyes Publications, 1988.
- 102 A. Tsuzumitani, Y. Okuno, M. Yamanaka, and Y. Mori, *Integrated Ferroelectrics* 38, 239-247, 2001.
- 103 T.B. Massalski (editor-in-chief), *Binary Alloy Phase Diagrams*, ASM International, Ohio, 1990.
- 104 <http://srdata.nist.gov/xps>
- 105 E. Comforto and P.E. Schmid, *Philos. Mag. A* 81, 61-82, 2001.

-
- 106 G.A.C.M. Spierings, G.J.M. Dormans, W.G.J. Moors, M.J.E. Uleners, and P.K. Larsen, *J.Appl.Phys.* 78, 1926-1933, 1995.
- 107 ICSD card 4-802.
- 108 M. Ohring, "The Materials Science of Thin Films", Academic Press, Boston, 1992.
- 109 J.G.E. Gardeniers and A. Prak, unpublished results.
- 110 W.P. Pennebaker, *J.Appl.Phys.* 40, 394-399, 1969.
- 111 D. K. Bowen and B.K. Tanner, "High Resolution X-ray Diffractometry and Topography", Taylor & Francis, London, 1998.
- 112 H.G. Tompkins, S. Tasic, J. Baker, and D. Convey, *Surf. Interface Anal.* 29, 179-187, 2000.
- 113 K. Postava, M. Aoyama, T. Yamaguchi, *Appl. Surf. Sci.* 175-176, 270-275, 2001.
- 114 H.Tang, H. Berger, P.E. Schmid, and F. Levy, *Solid State Commun.* 92, 267-271, 1994.
- 115 C.V. Thompson, *Annu. Rev. Mater. Sci.* 20, 245-268, 1990.
- 116 L.D. Madsen, L. Weaver, H. Ljungcrantz, and A. Clark, *J.Electron.Mat.* 27, 418-426, 1998.
- 117 T. Maeder, L. Sagalowicz, and P. Muralt, *Jpn.J.Appl.Phys.* 37, 2007-2012, 1998.
- 118 A.L. Roytburd, "Elastic domains in ferroelectric epitaxial films" in: "Thin film ferroelectric materials and devices" Ed. R. Ramesh, Kluwer Academic Publishers, Dordrecht 1997.
- 119 K.S. Lee, J.H. Choi, J.Y. Lee, and S. Baik, *J.Appl.Phys.* 90, 4095-4102, 2001; V. Nagarajan, C.S. Ganpule, H. Li, L. Salamanca-Riba, A.L. Roytburd, E.D. Williams, and R. Ramesh, *Appl.Phys.Lett.* 79, 2805-2807, 2001.
- 120 A.L. Roytburd, S.P. Alpay, L.A. Bendersky, V. Nagarajan, and R. Ramesh, *J.Appl.Phys.* 89, 553-556, 2001.
- 121 S.K. Streiffer, C.B. Parker, A.E. Romanov, M.J. Lefevre, L. Zhao, J.S. Speck, W. Pompe, C.M. Foster, and G.R. Bai, *J.Appl.Phys.* 83, 2742-2753, 1998; A.E. Romanov,

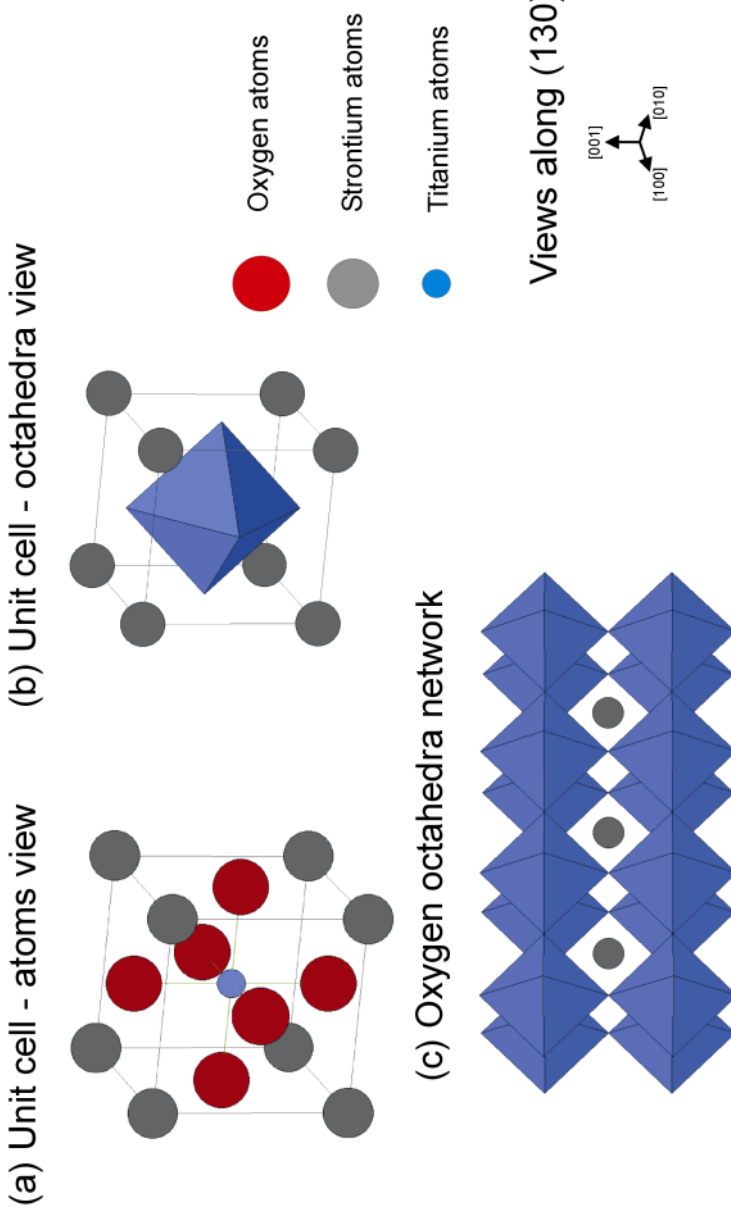
-
- M.J. Lefevre, J.S. Speck, W. Pompe, S.K. Streiffer, C.M. Foster, *J.Appl.Phys.* 83, 2754-2765, 1998.
- 122 T. Mitsui and S. Nomura, in: "Landolt-Börnstein: Numerical data and functional relationships in science and technology - Ferroelectrics and related substances" Vol. 16, Ed. K.-H. Hellwege, Springer-Verlag, Berlin, 1981.
- 123 N. Chen, G.R. Bai, O. Auciello, R.E. Koritala, and M.T. Lanagan, *Mat.Res.Soc.Symp.* 541, 345-350, 1999.
- 124 D. Kim, T.-Y. Kim, J. Key Lee, W. Tao, and S.B. Desu, *Mat.Res.Soc.Symp.* 433, 213-224, 1996.
- 125 M. Shimizu, M. Sugiyama, H. Fujisawa, and T. Shiosaki, *Jpn.J.Appl.Phys.* 33, 5167-5171, 1994.
- 126 M. Shimizu, H. Fujisawa, H. Niu, and K. Honda, *J.Crystal Growth* 237-239, 448-454, 2002.
- 127 G.R. Bai, H.L.M. Chang, D.J. Lam, Y. Gao, *Appl.Phys.Lett.* 62, 1754-1756, 1993.
- 128 K. Yamakawa, S. Trolier-McKinstry, J.P. Dougherty, S.B. Krupanidhi, *Appl.Phys.Lett.* 67, 2014-2016, 1995; H. Maitwa and N. Ichinose, *Jpn.J.Appl.Phys.* 40, 5507-5510, 2001.
- 129 F. Wang, K. K. Li, and G. Haertling, *Appl.Phys.Lett.* 65, 2507-2509, 1994.
- 130 L. Čakare, B. Malič, M. Kosec, and A. Sternberg, *Ferroelectrics* 241, 107-114, 2000; S.S.N. Bharadwaja and S.B. Krupanidhi, *J.Appl.Phys.* 86, 5862-5869, 1999.
- 131 International Centre for Diffraction Data: Card ICSD 75-1607.
- 132 C.M. Foster, W. Pompe, A.C. Daykin, and J.S. Speck, *J.Appl.Phys.* 79, 1405-1415, 1996.
- 133 Crystal Morphology Editor and Viewer – JCystal 1.02.
- 134 Y.S. Touloukian, R.K. Kirby, R.E. Taylor, and T.Y.R. Lee, "Thermophysical properties of matter: thermal expansion nonmetallic solids" Volume 13, IFI/Plenum, 1977.
- 135 ICSD 73-1441; ICSD 42-1164; and ICSD 79-1763.
- 136 ICSD 79-1796; ICSD 34-1084; and ICSD 83-809.

-
- 137 C.-H. Peng, "Optical Property Studies and Metalorganic Chemical Vapor Deposition of Ferroelectric Thin Films", PhD Thesis, Virginia Tech, 1992.
- 138 ICSD card 26-142; F.W. Martin, Phys.Chem.Glasses 6, 143-146, 1965.
- 139 M. Balog, M. Schieber, M. Michman, and S. Patai, Thin Solid Films 47, 109-120, 1977.
- 140 G. Bögels, "Growth Mechanism of (111)-Twinned fcc Crystals", PhD thesis, University of Nijmegen, 1999.
- 141 L.D. Madsen and L. Weaver, J.Am.Ceram.Soc. 81, 988-996, 1998.
- 142 W.C. Hendricks, "Metalorganic Chemical Vapor Deposition of Lead Oxide and Lead Titanate", Master of Science Thesis, Virginia Tech, 1993.
- 143 Massicot PbO (orthorombic) - ICSD card 38-1477.
- 144 Litharge PbO (tetragonal) - ICSD card 5-561.
- 145 Pb_2O_3 (monoclinic) - ICSD card 73-1284.
- 146 $\text{PbO}_{1.56}$ (monoclinic) - ICSD card 73-1284.
- 147 L. Burgio, R.J.H. Clark, and S. Firth, Analyst 126, 222-227, 2001.
- 148 K.R. Bullock, J. Electroanal.Chem. 222, 347-366, 1987.
- 149 L. Madsen and L. Weaver, J.Amer.Ceram.Soc. 81, 988-996, 1998.
- 150 S. Venkataraj, J. Geurts, H. Weis, O. Kappertz, W. Njoroge, R. Jayavel, and M. Wuttig, J.Vac.Sci.Technol. A 19, 2870-2878, 2001.
- 151 D. Bersani, P.P. Lottici, A. Montenero, S. Pigoni, and G. Gnappi, J.Non-Crystalline Solids 192&193, 490-493, 1995.
- 152 Y. Pauleau and E. Harry, J.Vac.Sci.Technol. A 14, 2207-2214, 1996.
- 153 C.E. Land, P.D. Thacher, and G.H. Haertling, in: "Applied Solid State Science: Advances in Materials and Devices Research" Vol. 4, Ed. R. Wolfe, Academic Press, New-York 137-233, 1974; G.H. Haertling, Ferroelectrics 131, 1-12, 1992.
- 154 C. H. Peng, J-F. Chang, and S. Desu, Mat.Res.Soc.Symp.Proc. 243, 21-26, 1992.

-
- 155 S. Bhaskar, S.B. Majumder, M. Jain, P.S. Dobal, and R.S. Katiyar, Mat. Sc. Eng., B87, 178-190, 2001.
- 156 S. Trolier-McKinstry, H. Hu, S.B. Krupanidhi, P. Chindaudom, K. Vedam, and R.E. Newnham, Thin Solid Films 230, 15-27, 1993.
- 157 X.Meng, Z. Huang, H. Ye, J. Cheng, P. Yang, and J. Chu, Mat.Res.Soc.Symp.Proc 541, 723-728, 1999.
- 158 J.D. Klein and S.L. Clauson, Mat.Res.Soc.Symp. 361, 147-152, 1995.
- 159 D.R. Uhlmann, G. Teowee, J.M. Boulton, S. Motakef, and S.C. Lee, J. Non-Crystalline Solids 147&148, 409-423, 1992.
- 160 I. Boerasu, M.I. Vasilevskiy, M. Pereira, M.F. Costa, and M.J.M. Gomes, Ferroelectrics 268, 187-192, 2002.
- 161 S. H. Wemple and M. DiDomenico, Phys.Rev. B 3, 1338-1345, 1971; S.H. Wemple, Phys.Rev. B 7, 3767-3777, 1973; M. DiDomenico M. and S.H. Wemple, J.Appl.Phys. 40, 720-734, 1969; S.H. Wemple, J.Chem.Phys. 67, 2151-2168, 1977.
- 162 D.J. Chadi and M.L. Cohen, Physics Letters 49A, 381-382, 1974.
- 163 Wemple and DiDomenico also use their (E_0 , E_d) values to classify materials as "covalent-type" and "ionic-type". Using their system, PT is covalent and PZ is ionic, even though both solids are oxides with perovskite-based structures and are usually considered to be ionic.
- 164 J. Robertson, private communication. A part of this has appeared in J. Robertson, Appl.Surf.Sc. 190, 2-10, 2002.

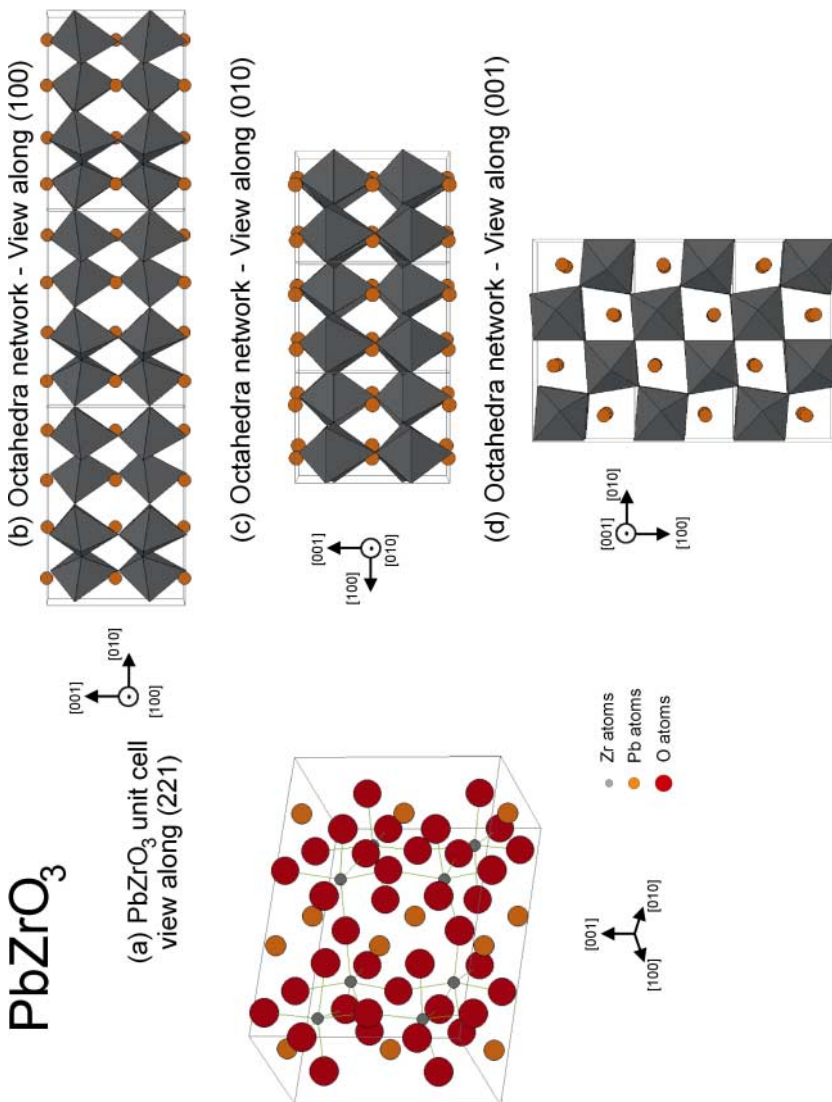
Appendix 1: Color Figures

Perovskite - SrTiO_3

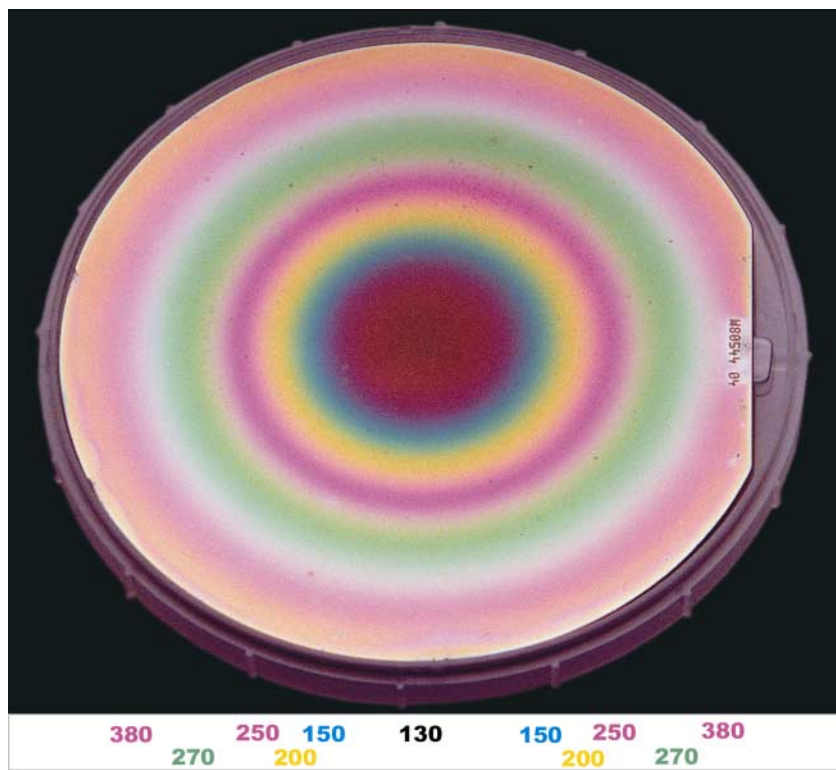


Color Figure 1: Perovskite structure of STO. (a) unit cell with the different atoms (b) unit cell with the octahedron (c) oxygen octahedral network.

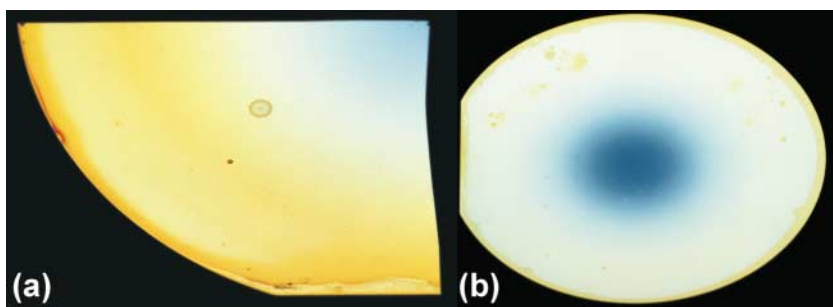
PbZrO_3



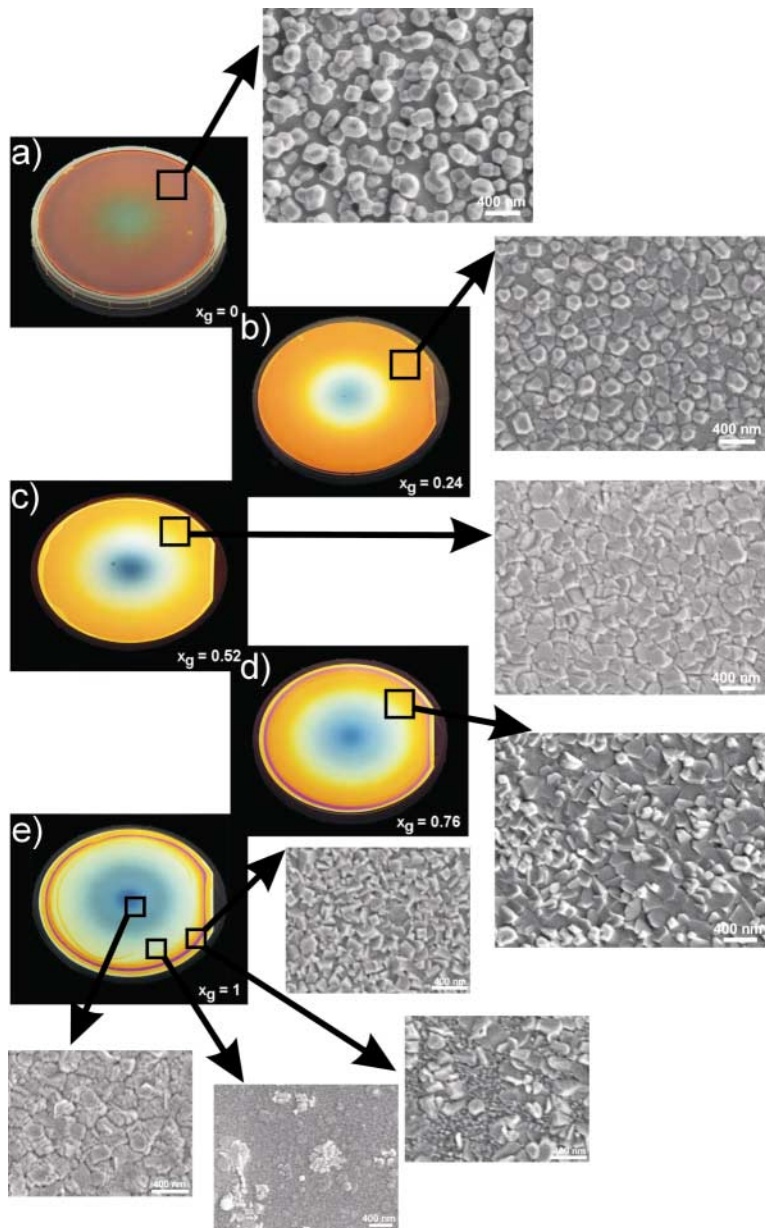
Color Figure 2: Orthorhombic PbZrO_3 . (a) unit cell, (b-d) oxygen octahedral network.



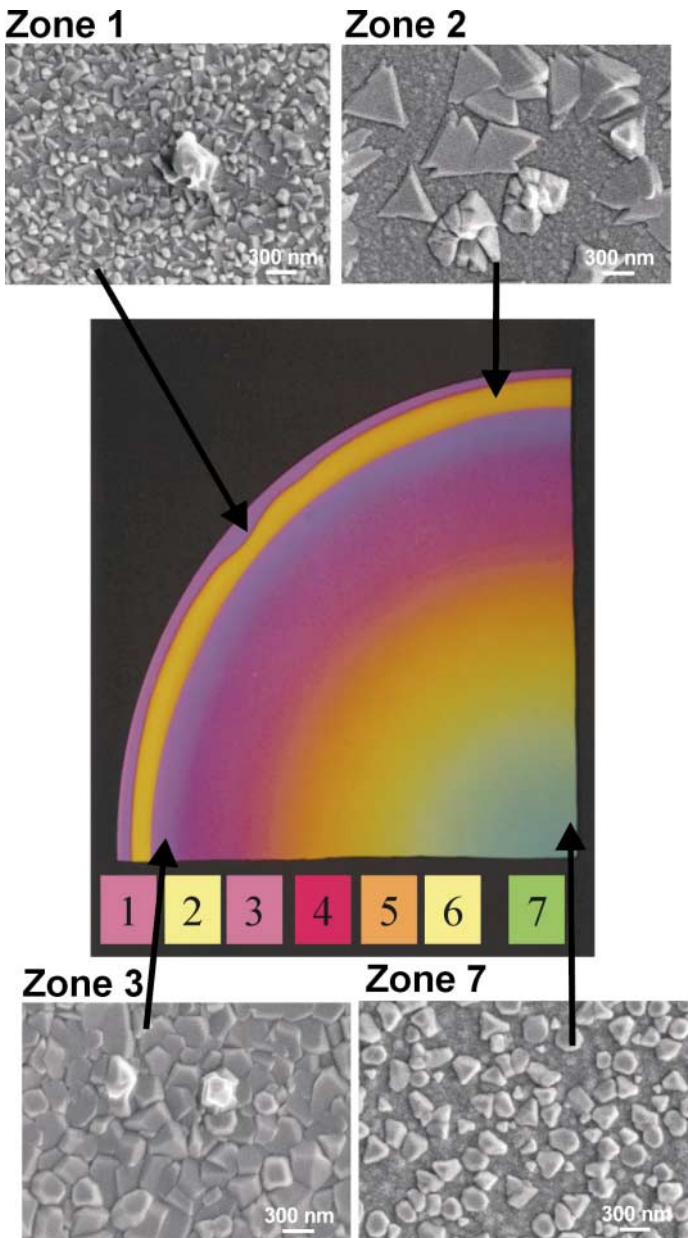
Color Figure 3: A PT film deposited on a 6" diameter platinized silicon substrate displaying large radial thickness variation. The thickness (in nm) of each color ring is indicated in the same color.



Color Figure 4: PZT film on platinized silicon substrate with the typical radial homogeneity, which could be obtained in the MOCVD reactor. a) a quarter of the reference run deposited on a 6" diameter platinized silicon wafer and b) the reference run repeated on another 6" diameter platinized silicon wafer.



Color Figure 5: Overview of the polycrystalline composition-variation growth series as a function of the gas phase x ratio (x_g). a) $x_g = 0.00$ (PT), b) $x_g = 0.24$, c) $x_g = 0.52$, d) $x_g = 0.76$, and e) $x_g = 1.00$ (PZ). The color photographs correspond to an overview of the 6" wafers and a SEM photograph of the morphology at ~ 3.8 cm radial distance from the center is shown for each wafer. For $x_g = 1.00$ (PZ layer), the morphology in additional positions is shown as this wafer contains two phases.



Color Figure 6: Overview of a quarter of a 6" PZT film grown on a platinized silicon substrate. The different zones are labeled as zone 1 to zone 7 from the edge to the center of the wafer according to the colored rings. The morphology observed by SEM is shown for the zones 1, 2, 3, and 7. The growth parameters were the same as for the film shown in Color Figure 4, but non-reproducible conditions (Chapter 2) lead to very large non-uniformity and different morphologies.

S a m e n v a t t i n g

In dit proefschrift staan de resultaten beschreven van vier jaar onderzoek aan dunne lagen van $Pb(Zr,Ti)O_3$ (PZT), uitgevoerd aan de Universiteit van Nijmegen bij de vakgroep Experimentele Vaste Stoffysica III. In het eerste hoofdstuk wordt een algemene beschrijving gegeven van de oxidische, elektro-ceramische PZT materialen en hun eventuele toepassingen in de vorm van dunne lagen. Het onderzoek was voornamelijk gericht op micromechanische- en optische applicaties. Deze zijn respectievelijk op de piezoelectrische- en elektr-optische eigenschappen van het PZT materiaal gebaseerd. De PZT lagen zijn gedeponeerd, " gegroeid ", vanuit de gasfase met behulp van de Metalorganic Chemical Vapor Deposition (MOCVD) techniek. Een algemene beschrijving van deze specifieke groeimethode wordt gegeven, met de nadruk op de details welke van belang zijn voor de depositie van het PZT materiaalsysteem. Er wordt ook ingegaan op de bijzonder- en eigenaardigheden van de reactor die in dit onderzoek is gebruikt. De structuur, morfologie en optische eigenschappen van de gegroeide lagen zijn uitgebreid bestudeerd en geanalyseerd met meerdere karakteriseringtechnieken.

De PZT lagen zijn gedeponeerd op twee geheel verschillende typen substraten, te weten geplatineerde siliciumwafers (4" and 6" diameter) voor de depositie van polykristallijne lagen voor micromechanische toepassingen, en $SrTiO_3$ (STO) éénkristallen (1 bij 1 cm) waarop hetero-epitaxiale lagen voor optische toepassingen gegroeid zijn. De geplatineerde silicium-substraten bestaan uit een multi-laag structuur Pt / Ti / SiO_2 / Si. De multi-laag structuur van het substraat veranderde tijdens de opwarmprocedure, voorafgaand aan de depositie, waarbij de optredende modificaties (beschadigingen genoemd) afhankelijk zijn van de opwarmomstandigheden. De modificaties die voorafgaand aan de eigenlijke groei optreden zijn tot in de details bestudeerd om de invloed hiervan op de PZT laag zorgvuldig te kunnen onderzoeken. De beschadigingen zijn van dien aard dat de geplatineerde silicium substraten niet bruikbaar zijn voor groei bij 700°C gedurende langere tijd, voornamelijk omdat de platina laag van de siliciumwafer afbladdert waardoor de PZT laag niet verder kan worden gebruikt. Door het kiezen van speciale omstandigheden tijdens het opwarmen, onder andere door het gebruik van stikstof als dragergas, bleek het desondanks mogelijk groeistudies op deze substraten uit te voeren.

De beheersing van de compositie van de gedeponeerde PZT lagen is niet eenvoudig omdat de verschillende oxides elk een andere, specifieke rol spelen in het groeiproces van PZT. Dit kan geïllustreerd worden aan de hand van enkele voorbeelden. Tijdens de groei van PT ($x = 0$) moet rekening gehouden worden met het feit dat TiO_2 veel minder gemakkelijk nucleert dan PbO terwijl dit laatst genoemde oxide relatief erg gemakkelijk desorbeert van het oppervlakte tijdens de groei (vooral bij hoge temperaturen). Dit heeft tot gevolg dat de vorming van PT met een enkelvoudige fase eenvoudig is. Aan de andere kant, wanneer de partiële drukken van de precursors hoger zijn, waarbij wel dezelfde stoichiometrische verhouding in de gasfase wordt

gehandhaafd, kan er additioneel PbO gevormd worden naast PT. De extra PbO fase in de PT lagen zijn geanalyseerd. Voor de depositie van PZ ($x = 1$) ligt de situatie compleet anders, voornamelijk omdat ZrO_2 zeer gemakkelijk nucleert waardoor er naast PZ een ZrO_2 fase gevormd wordt tijdens experimenten met lage precursor partiële drukken. Met het opvoeren van de partiële drukken verdwijnt de extra ZrO_2 fase en wordt er alleen PZ gevormd. Tijdens de groei van PZT vindt er een competitief proces plaats tussen de vorming van PbO en van ZrO_2 , waarbij Zr-rijk PZT wordt gevormd bij hoge partiële drukken. Naast het aspect van de beheersing van de samenstelling wordt de morfologie en de structuur van de polykristallijne lagen bestudeerd. De slechte reproduceerbaarheid van de groeiruns, veroorzaakt door een combinatie van technische onvolkomenheden en chemische eigenschappen van de diverse precursors, bemoeilijkte de groeistudies aanzienlijk. Het was hierdoor niet mogelijk om grondige experimenten uit te voeren die kunnen leiden tot de vorming van een groeimodel. Een interessante PZT laag die werd gegroeid onder Pb-arme en niet geheel reproduceerbare condities vertoonde een merkwaardige morfologie met vlakke driehoekige PZT kristalletjes als ook de ZrO_2 fase.

PZT hetero-epitaxiale lagen gegroeid bij 700°C zijn interessant omdat deze tijdens de groei een kubische structuur (para-elektrische fase) bezitten die tijdens de afkoeling verandert in een tetragonale, rhombohedrale of orthorhombische structuur (ferroelectrische / anti-ferroelectrische fase). Welke fase na het afkoelen onstaat is afhankelijk van de PZT compositie. Deze verandering in structuur veroorzaakt verstoringen in de laag welke opgevangen worden door de formatie van domeinen met verschillende kristallografische richtingen. Dit verklaart het ontstaan van de verschillende domeinen welke bij kamertemperatuur gevonden worden in de diverse lagen. In de vakliteratuur is al uitgebreid gepubliceerd over de domeinen, welke ontstaan als de PZT laag bij afkoeling transformeert tot een tetragonale of een rhombohedrale structuur. In dit proefschrift worden de morfologie en structuur van hetero-epitaxiale orthorhombische PZ lagen bediscussieerd. De PZ lagen zijn samengesteld uit (120) georiënteerde domeinen, in combinatie met (002) domeinen voor lagen die dikker zijn dan 260 nm, beiden met respectievelijk 2 en 4 varianten. Deze varianten corresponderen met de zes verschillende vervormingsrichtingen van de para-elektrische kubische structuur bij de vorming van de anti-ferroelectrische orthorhombische structuur.

Tenslotte wordt er nader ingegaan op de optische eigenschappen van hetero-epitaxiale lagen met verschillende composities en laagdiktes. Met behulp van ellipsometrie en reflectie metingen is de dispersie (of wel de golflengte afhankelijkheid) van de brekingsindex, afhankelijk van de compositie, tussen 1.55 eV (800 nm) en 3.72 eV (333 nm) bepaald. Een Cauchy extrapolatie is gebruikt om de brekingsindex te berekenen tot en met 0.62 eV (2000 nm). Het onderzoek laat zien dat de brekingsindex vrijwel lineair is in x , niet alleen bij 633 nm (zoals aangetoond in de vakliteratuur), maar ook tot en met 2000 nm. Tevens blijkt dat de absorptieband onafhankelijk is van de samenstelling en dat deze zich bevindt bij 3.6 ± 0.1 eV (340 ± 10 nm).

Met dit promotieonderzoek is er inzicht verkregen in de complexiteiten en subtiliteiten van PZT groei in een klassieke horizontale MOCVD reactor. Hieruit zijn verschillende interessante resultaten voortgekomen. Samen met de gedetaillerde analyses van de structuur en morfologie, van typisch MOCVD gegroeide PZT lagen, zou dit nuttig moeten zijn voor toekomstige onderzoekers. Zo zijn de beperkingen en grenzen van het gebruik van geplatineerde silicium wafers als substraten voor de groei van PZT lagen zorgvuldig geëxamineerd. Verder zijn de vorming en analyse van domeinen in hetero-epitaxiale PZT lagen op STO beschreven. Ondanks het feit dat PZT lagen potentiële kandidaten zijn voor elektro-optische applicaties was er tot nu toe nauwelijks informatie beschikbaar over de optische eigenschappen van dunne lagen. Met dit onderzoek is de brekingsindex nu over een groot golflengtebereik bepaald voor hetero-epitaxiale PZT lagen met uiteenlopende samenstellingen.

Summary

The work described in this thesis is the result of four years research on $\text{PbZr}_x\text{Ti}_{1-x}\text{O}_3$ (PZT) thin films at the University of Nijmegen in the Experimental Solid State Physics III group. PZT materials are of high interest for their ultimate applications in thin film form. The two of main interest for our studies were micromechanical and optical devices based on their piezoelectric and electro-optic properties. The PZT layers were grown by MOCVD, Metalorganic Chemical Vapor Deposition. This specific vapor-phase growth technique is described in the thesis both generally and in the detailed context of the reactor used for this study. The structure, the morphology, and the optical properties of the grown layers were intensively analyzed with a variety of characterization techniques.

The layers were of two main types: polycrystalline layers grown on platinized silicon wafers (4" and 6" diameter) for eventual micromechanical devices, and hetero-epitaxial layers grown on SrTiO_3 (STO) crystals (1 by 1 cm) for eventual optical devices. The platinized silicon substrates were not inert to the warming-up procedure prior to growth, and the initial multilayer Pt / Ti / SiO_2 / Si structure of the substrate was modified in the warming-up procedure with the modifications (called damage) dependent on the warming-up ambient. Damage could not be suppressed, but nitrogen was found to be a less harmful environment and the modifications prior to growth were investigated in order to characterize the PZT-substrate stack properly. The damages are such that these platinized silicon substrates are not suitable for growth at 700°C for an extended time, as the platinum layer peels off the silicon wafer and the PZT layer can not be further processed. Nevertheless several growth studies could still be performed on such substrates.

Composition control of the PZT layers is not straightforward because several oxides are involved in the PZT formation. For PT ($x = 0$) growth, TiO_2 does not nucleate easily in these films and PbO desorbs relatively easily at 700°C. Therefore a PT single phase is easily formed. On the other hand, if the precursor partial pressures are too high, PbO can be formed in addition to PT. The PbO phases present in the PT films were analyzed. For PZ growth ($x = 1$), it is different as ZrO_2 nucleates very easily. ZrO_2 by-phases are formed with PZ at standard precursor partial pressures and single phase PZ is formed when high partial pressures are used. Growth of PZT is a competitive process between ZrO_2 and TiO_2 to form perovskite PZT, and Zr-rich PZT is formed at high precursor partial pressures. In addition to composition-control-aspects, the morphology and the structure of the polycrystalline layers were carefully studied. The growth studies performed in this research were complicated by poor run reproducibility due mainly to the Zr and Pb precursor flows. It was therefore not possible to perform a study adequate for creating a growth model. An interesting polycrystalline film obtained in non-reproducible Pb-deficient conditions exhibited peculiar flat triangular PZT crystals, as well as the ZrO_2 phase.

PZT hetero-epitaxial layers grown at 700°C are interesting as, during growth, the PZT lattice is cubic (paraelectric phase) and transforms upon cooling to tetragonal, rhombohedral, or orthorhombic (ferroelectric / antiferroelectric phase) depending on composition. Therefore domains of different crystallographic orientation are formed to accommodate the distortion of the lattice and are present in the layers at room temperature. Studies of these domains have already been discussed in the literature for tetragonal and rhombohedral PZT. The morphology and structure of the hetero-epitaxial orthorhombic PZ layers were investigated in this thesis. The PZ layers are composed of (120) oriented domains, as well as (002) domains for layers thicker than about 260 nm, with respectively 2 and 4 variants each. These variants correspond to the 6 different elongation directions of the paraelectric cubic structure to form the antiferroelectric orthorhombic structure.

Finally, the optical properties of the hetero-epitaxial layers for different compositions and thicknesses were studied. The refractive-index dispersion, sensitive to composition, was measured from 1.55 eV (800 nm) to 3.72 eV (333 nm) by ellipsometry and reflectivity, as a function of composition. A Cauchy extrapolation was used to estimate the refractive index down to 0.62 eV (2000 nm). It indicates that the refractive index is close to linear in x not only at 633 nm, as shown in previous reports, but also up to 2000 nm. The absorption edge is insensitive to composition, and is located at 3.6 ± 0.1 eV (340 ± 10 nm).

To conclude, several points can be highlighted. Insight was gained into the complexities and subtleties of PZT growth in a classical horizontal MOCVD reactor. Careful analyses of the structure and morphology of typical MOCVD-grown PZT films were carried out, which should be helpful to future researchers. Additionally, the limits of the platinized silicon substrates for the growth of such films were clearly detailed. Domain formation and morphological analysis of hetero-epitaxial PZ layers on STO are described. Though PZT films are eventual candidates for optical devices further information about thin film optical properties is required. The refractive index of these MOCVD PZT hetero-epitaxial PZT layers was measured as a function of composition and wavelength.

R é s u m é

Les résultats présentés dans cette thèse proviennent de quatre ans de recherche sur les couches minces de $PbZr_xTi_{1-x}O_3$ (PZT), zircono titanate de plomb, à l'université de Nimègue (Pays-Bas) dans le département de physique expérimentale du solide III. Dans le premier chapitre, le PZT est présenté en tant qu'oxyde électro-céramique et les utilisations éventuelles de couches minces de ce type de matériaux sont décrites. Deux applications étaient principalement envisagées pour ce projet: des dispositifs micromécaniques et optiques basés respectivement sur les propriétés piézo-électriques et électro-optique du matériau PZT. Dans cette étude, la technique de dépôt par phase vapeur (MOCVD) a été utilisée pour faire croître les couches. Cette technique de dépôt, ainsi que le réacteur utilisé, sont détaillés. La structure, la morphologie et les propriétés optiques des couches minces produites ont été systématiquement analysées avec différentes techniques de caractérisation.

Deux sortes de couches de PZT ont été déposées: des couches polycristallines déposées sur des galettes de silicium platinées (4" et 6" de diamètre) pour d'éventuels dispositifs micromécaniques et des couches hetero-épitaxiales sur des cristaux de $SrTiO_3$ (STO) (de 1 sur 1 cm) pour d'éventuels dispositifs optiques. Les galettes de silicium platinées n'étaient pas inertes à la procédure de chauffe et la structure initiale des ces substrats Pt / Ti / SiO_2 / Si est modifiée et se transforme en un substrat endommagé avant la croissance du PZT. Bien que ces modifications du substrat n'aient pas pu être supprimées, il a été observé qu'un chauffage sous azote était moins nocif que sous oxygène. Les modifications du substrat avant la croissance ont été analysées en détails et la caractérisation de l'ensemble PZT / Pt a été possible. Bien que ces substrats ne soient pas adaptés à de longues croissances à 700°C car la couche de platine se décolle de la galette de silicium, plusieurs séries de croissance ont été effectuées sur ces substrats.

Le contrôle de la composition des couches de PZT n'est pas simple car pour la croissance de PZT plusieurs oxydes sont présents. Pour la croissance de PT ($x = 0$), le TiO_2 ne germe pas facilement et le PbO désorbe relativement facilement à 700°C, donc seul l'oxyde PT est formé. Néanmoins, si les pressions partielles des précurseurs sont augmentées, une phase parasite PbO est présente avec le PT. L'analyse des différentes phases de PbO observées dans ce type de couches est présentée. Pour la croissance de PZ ($x = 1$), c'est différent car le ZrO_2 est formé très rapidement. Une phase parasite de ZrO_2 est présente pour de pressions partielles standard mais seul le PZ croît pour des hautes pressions partielles. Donc pour la croissance de PZT, le TiO_2 et le ZrO_2 sont en compétition pour former la phase perovskite PZT. Pour une composition gazeuse constante, plus les pressions partielles sont augmentées, plus la phase PZT sera riche en Zr. En plus des aspects de contrôle de composition des couches, la morphologie et la structure des couches polycristallines sont aussi présentées. Ces études de croissance ont été compliquées par le fait que la reproductibilité est faible dû à l'instabilité des écoulements de Zr et de Pb. Il n'a donc

pas été possible de faire une étude plus approfondie sur la croissance et d'éventuellement développer un modèle. Une couche de PZT obtenue dans des conditions non-reproductibles déficientes en Pb est composée de cristaux de PZT plats et triangulaires non-standards et d'une phase parasite de ZrO_2 .

Les couches hétero-épitaxiales de PZT sur des substrats STO qui poussent à 700°C sont intéressantes car le PZT est cristallisé dans le système cubique et la croissance est cube-sur-cube à cette température sur de tels substrats. Après la croissance, pendant le refroidissement, le PZT passe par une transition de phase: de paraélectrique (système cubique) à ferroélectrique / antiferroélectrique (système quadratique ou rhomboédrique / orthorhombique suivant la composition du PZT). Des domaines de différentes orientations cristallographiques sont donc formés pour accommoder ces transformations et sont présents dans la couche finale. L'étude de ces domaines a été reportée dans la littérature pour le système de maille quadratique ou rhomboédrique mais pas pour le système orthorhombique. L'étude des couches minces de PZ (orthorhombique) est détaillée dans cette thèse. Les couches de PZ finales sont composées de domaines (120), combiné à des domaines (002) pour les couches dépassant les 260 nm d'épaisseur. Chaque domaine est composé respectivement de 4 et 2 variantes. Ces variantes correspondent aux 6 élongations différentes du système de maille quadratique (en phase paraélectrique) pour former le système de maille orthorhombique (en phase antiferroélectrique).

Les propriétés optiques des films hétero-épitaxiaux de PZT, de différentes compositions et épaisseurs, ont été étudiées et sont présentées. La dispersion de l'indice de réfraction, dépendant de la composition, a été mesuré de 1,55 eV (800 nm) à 3,72 eV (333 nm) par ellipsométrie et réflectivité en fonction de la composition. Une extrapolation de Cauchy a été utilisée pour estimer l'indice de réfraction jusqu'à 0,62 eV (2000 nm). Il est observé que l'indice de réfraction est linéaire en fonction de la composition à 633 nm, comme observé dans d'autres études, mais également jusqu'à 2000 nm. Contrairement à l'indice de réfraction, le bord d'absorption n'est pas dépendant de la composition du PZT et est à $3,6 \pm 0,1$ eV (340 ± 10 nm).

Pour conclure, plusieurs résultats intéressants ont pu être mis à jour par ce travail. Un aperçu pratique de la croissance de PZT dans un réacteur horizontal classique est donné. Plusieurs études détaillées de la morphologie et la structure de films PZT polycristallins produits dans ce réacteur peuvent être utiles pour une recherche ultérieure. Les limites de galettes de silicium platinées en tant que substrat pour la croissance de tels films sont clairement détaillées. La formation et l'analyse des domaines dans les couches hétero-épitaxiales de PZ sur substrat STO sont décrites. De plus, bien que les couches de PZT aient le potentiel d'être intégrées à des dispositifs électro-optiques, très peu de données sont disponibles sur les propriétés optiques des couches minces. L'indice de réfraction des couches MOCVD de PZT hétero-épitaxiales a été mesuré en fonction de la composition et de la longueur d'onde.

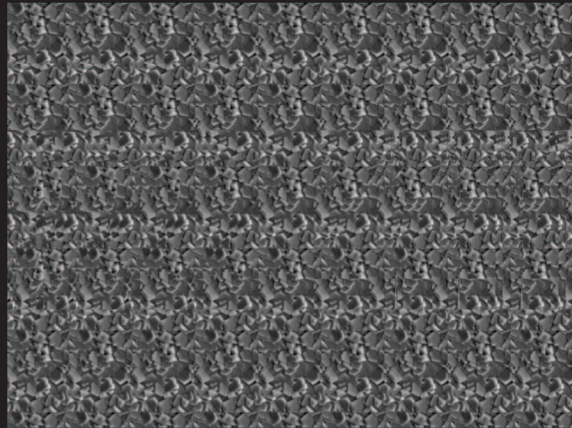
List of publications

1. "Damage after Annealing and Aging at Room Temperature of Platinized Silicon Substrates", M.P. Moret, M.A.C. Devillers, F.D. Tichelaar, E. Aret, P.R. Hageman, P.K. Larsen, accepted in Thin Solid Films.
2. "Structure and Morphology of Epitaxial PbZrO₃ Films Grown by Metal Organic Chemical Vapor Deposition" M.P. Moret, J.J. Schermer, F.D. Tichelaar, E. Aret, and P.R. Hageman, *J.Appl.Phys.* 92, 3947-3957, (2002).
3. "Optical Properties of PbTiO₃, PbZr_xTi_{1-x}O₃, and PbZrO₃ Films deposited by Metalorganic Chemical Vapor Deposition", M.P. Moret, M.A.C. Devillers, K. Wörhoff, and P.K. Larsen, *J.Appl.Phys.* 92, 468-474, (2002).
4. "MOCVD PbZr_xTi_{1-x}O₃ Thin Films on Platinized Silicon Wafers and SrTiO₃ Crystals: Growth and Optical Properties", Mona P. Moret, Marijn A.C. Devillers, Andy R.A. Zauner, Edwin Aret, Paul R. Hageman, Poul K. Larsen, *Integrated Ferroelectrics* 36, 265-274, (2001).
5. "MOCVD Growth and Characterization of PbTiO₃ Thin Films on Pt/Ti/SiO₂/Si Substrates", M.P. Moret, S.A. Rössinger, P.R. Hageman, S.I. Misat, M.A.C. Devillers, H.van der Linden, E. Haverkamp, W.H.M. Corbeek, P.K. Larsen, *Integrated Ferroelectrics* 31, 305-314, (2000).
6. "Interfacial Layer Observed by Ellipsometry in MOCVD Grown Pb(Zr,Ti)O₃ Thin Films" M.P. Moret, S.A. Rössinger, P.R. Hageman, M.A. Devillers, H.van der Linden, E. Haverkamp, P.K. Larsen, and N. Duan *Ferroelectrics* 241, 149-158 (2000).
7. "Brookite-rich titania films made by pulsed laser deposition" M.P. Moret, R. Zallen, D.P. Vijay, and S.B. Desu, *Thin Solid Films* 366, 8-10, (2000).
8. "Infrared Activity in the Aurivillius layered ferroelectric SrBi₂Ta₂O₉", M.P. Moret, R. Zallen, R.E. Newnham, P.C. Joshi, and S.B. Desu, *Phys. Rev. B* 57, 5715-5723, (1998).
9. "New ferroelastic phase in SrBi₂Ta₂O₉ and study of the ferroelectric phase-transition dynamics", S. Kamba, J. Pokorný, V. Porokhonskyy, and J. Petzelt, M.P. Moret, A. Garg, Z.H. Barber, and R. Zallen, *Appl.Phys.Lett.* 81, 1056-1058, (2002).
10. "Non-linear optical and electrostatic force microscopy for ferroelectric polarization imaging" E.D. Mishina, N.E. Sherstyuk, K.A. Vorotilov, A.S. Sigov, R. Barberi, M.P. Moret, F. Manders, M.P. De Santo, P.K. Larsen, and Th. Rasing, *Applied Physics B* 74, 783-788, (2002).

11. "Local Probing of the polarization state in thin $\text{Pb}(\text{ZrTi})\text{O}_3$ films during polarization reversal" E.D. Mishina, N.E. Sherstyuk, E.Ph. Pevtsov, K.A. Vorotilov, S.A. Sigov, M.P. Moret, S.A. Rössinger, P.K. Larsen, and Th. Rasing, *Appl.Phys.Letters* 78, 796-798, (2001).
12. "Incorporation of Pb, Ti and Zr into MOCVD Grown $\text{PbZr}_x\text{Ti}_{1-x}\text{O}_3$ thin films" S.A. Rössinger, M.P. Moret, S.I. Misat, P.R. Hageman, H. van der Linden, E. Haverkamp, W.H.M. Corbeek, and P.K. Larsen, *Integrated Ferroelectrics* 30, 71-79, (2000).
13. "HIP'ed Silicon Nitride Components for Agata - Properties and Evaluation", R. Lundberg, M.P. Moret, L. Garguet-Duport, ASME 98 98-GT-566, Proceedings International Gas Turbine & Aeroengine Congress and Exhibition in Stockholm, (1998).

Curriculum Vitae

Born in Besançon, France in August 1972, Mona P. Moret received her first degree (DUT, Diplôme Universitaire Technologique) in Electrical Engineering at the University of Franche-Comté in Belfort, France in June 1992. A motivating training period at the company Turbomeca encouraged her to pursue her studies in applied physics. She received a B.Sc. Honours, First Class, in Applied Physics from the University of Portsmouth, England in July 1994. She then enrolled at Virginia Tech, USA, to pursue graduate studies. Her thesis involved the optical and structural characterization of $\text{SrBi}_2\text{Ta}_2\text{O}_9$ and TiO_2 crystals, pellets and laser-ablation-deposited thin films. She received her Master's degree in Applied Physics from the Physics Department in July 1996. Back in Europe, she spent a year and half as a materials scientist at Volvo Aero in Trollhättan, Sweden, working on the development of Si_3N_4 ceramics for automotive applications. In order to deepen her knowledge in materials science and participate scientifically in the development of materials from their growth to their applications, she decided to go back to university. In April 1998, she started to work in the ferroelectric $\text{Pb}(\text{Zr},\text{Ti})\text{O}_3$ films project at the University of Nijmegen, Experimental Solid State Physics III group. Most of the work she carried out for this project is reported in the present PhD thesis. After the completion of her thesis, she returned to France in September 2002 to work as a postdoc at the ESRF in Grenoble.



Stereogram Relax and don't focus on the picture